

University of Southampton Research Repository

Copyright © and Moral Rights for this thesis and, where applicable, any accompanying data are retained by the author and/or other copyright owners. A copy can be downloaded for personal non-commercial research or study, without prior permission or charge. This thesis and the accompanying data cannot be reproduced or quoted extensively from without first obtaining permission in writing from the copyright holder/s. The content of the thesis and accompanying research data (where applicable) must not be changed in any way or sold commercially in any format or medium without the formal permission of the copyright holder/s.

When referring to this thesis and any accompanying data, full bibliographic details must be given, e.g.

Thesis: Author (Year of Submission) "Full thesis title", University of Southampton, name of the University Faculty or School or Department, PhD Thesis, pagination.

Data: Author (Year) Title. URI [dataset]

UNIVERSITY OF SOUTHAMPTON

FACULTY OF PHYSICAL SCIENCES AND ENGINEERING

Electronics and Computer Science

Electromagnetic Modelling of Switched Reluctance Machines Exploiting Flux Tubes

by

Aleksas Stukys

Thesis for the degree of Doctor of Philosophy

February 2018

UNIVERSITY OF SOUTHAMPTON

ABSTRACT

FACULTY OF PHYSICAL SCIENCES AND ENGINEERING

Electronics and Computer Science

Thesis for the degree of Doctor of Philosophy

ELECTROMAGNETIC MODELLING OF SWITCHED RELUCTANCE MACHINES EXPLOITING FLUX TUBES

Aleksas Stuikys

A new and computationally efficient algorithm for the design and analysis of switched reluctance machines is proposed. At the heart of the rapid analysis and design methodology is the reduced order computational method based on a flux tube model which has been refined, extended and formalised. The new flux tube method is a combination and important extension of the existing flux tubes and tubes-and-slices modelling techniques used for quantifying magnetic fields in electromechanical devices. The new method is applied to translating and rotating switched reluctance machine topologies in order to obtain the flux-linkage maps for the machines. Original analytically derived numerical error analysis of the improved flux tube method is presented which shows that the numerical accuracy afforded by the method is high despite the fact that the method is classed as a reduced order computational method. It is demonstrated how the improved model enables consistent and accurate analysis and design optimization of switched reluctance machines. The new technique is also validated against finite element simulation results.

Instead of manually laborious geometry based analytical derivations; an automatic generation of cubic splines is introduced to model the magnetic flux using the improved flux tube method. The improved flux tube method exploits cubic-spline approximations for construction of constant flux lines in the magnetic and non-magnetic parts of electromechanical devices. To make the magnetic field modelling of the devices practical the saturation effects of ferromagnetic materials are included in the cubic-spline based flux tube method. Furthermore, the new flux tube method enables, in principle, the modelling of the magnetic leakage flux effects that are important from the machine performance

results accuracy point of view. It is shown that in order to account for the leakage flux effects it is necessary to assume and construct probable, yet representative, leakage flux paths which are not known beforehand. An argument is put forward to support the assumption that the assumed probable leakage flux paths, even if approximate, will accurately account for the majority of leakage flux effects in the device. In order to perform rapid initial design search and optimization of switched reluctance machines the improved flux tube method was combined with the genetic algorithm based multi-objective optimization.

The flux-linkage functions pertinent to a particular optimized switched reluctance machine topology obtained from the improved flux tube method indicate that the method offers good accuracy compared to finite element based analysis, but with significantly improved computational efficiency. It is demonstrated that the new modelling technique can accurately capture the important magnetic saturation and leakage flux effects occurring in the modelled machine parts. Furthermore, the new flux tube method is seen to be computationally efficient and reduces ambiguity and number of parameters used to define flux tubes in the electromagnetic devices. Pareto fronts obtained from the multi-objective genetic algorithm based optimization of a selected number of distinct topology switched reluctance machines indicate that the new flux tube method leads to the accurate and consistent estimation of these Pareto fronts. The proposed analysis and design approach based on flux tubes is applicable to translating and rotating switched reluctance machines of various topologies and therefore enables rapid design search and optimization of novel topologies.

Table of Contents

Table of Contents	i
Table of Tables	v
Table of Figures	vii
List of Accompanying Materials	xiii
Academic Thesis: Declaration Of Authorship.....	xv
Acknowledgements.....	xix
Definitions and Abbreviations	xxi
Chapter 1 Introduction.....	23
1.1 The Need for Rapid Electromagnetic Modelling of the Switched Reluctance Machines	23
1.2 Research Objectives	30
1.3 Organisation of the Work	32
Chapter 2 Literature Review.....	35
2.1 Estimating Flux Path Permeance - Roters Method.....	35
2.2 Magnetic Equivalent Circuit Method	40
2.3 The Method of Assumed Flux Tubes	46
2.4 The Tubes and Slices Approach.....	53
2.5 Analytical Air Gap Field Solutions	57
2.6 Chapter Summary	62
Chapter 3 Proposed Modelling of the Flux Tubes and Slices Utilising Cubic-Splines.....	63
3.1 Translating (Linear) SR Machine Flux Paths Modelling Using Cubic-Splines	64
3.1.1 Unaligned Translator Position Modelling	64
3.1.2 Refining the Unaligned Air Gap	68
3.1.3 Aligned Translator Position Modelling	69
3.1.4 Intermediate Translator Position Modelling	71
3.2 Rotating SR Machine Flux Paths Modelling Using Cubic-Splines.....	73
3.2.1 Unaligned Rotor Position Modelling.....	73

Table of Contents

3.2.2	Aligned Rotor Position Modelling	74
3.3	Numerical Accuracy and Robustness of the Flux Tubes Modelling	75
3.3.1	Flux Tubes and Slices Air Gap Reluctance Accuracy	76
3.3.2	Flux Tubes and Slices Iron Circuit Reluctance Accuracy	78
3.3.3	Flux Tubes and Slices Dual Bounds Estimations	82
3.3.4	Geometric Modelling Aspects of the Flux Tubes and Slices Techniques	85
3.3.5	Further Sources of Modelling Error	90
3.4	Chapter Summary	91
Chapter 4 Cubic Splines Based Flux Tubes and Slices Error Results...		93
4.1	Geometric Modelling of Flux Tubes using TAS Technique	93
4.2	SR Machine Electromagnetic Modelling Error of Flux Tubes and Slices Technique	97
4.3	Flux Tubes and Slices Flux Linkage Results Sensitivity Analysis ...	102
4.3.1	Aligned Flux Linkage Results Sensitivity Analysis	102
4.3.2	Unaligned Flux Linkage Results Sensitivity Analysis	106
4.4	Chapter Summary	110
Chapter 5 Flux Tubes and Slices Based SR Machine Analysis and Design Optimization Results.....		111
5.1	General SR Machine Performance Analysis Approach	111
5.1.1	3D Flux-Linkage Map Determination	111
5.1.2	Optimum Angle-Of-Advance Determination	112
5.1.3	SR Machine Output Power Curves	114
5.1.4	Optimization of SR Machines using Genetic Algorithm	114
5.2	Translating Switched Reluctance Machine Analysis and Design Results	116
5.2.1	LSRM Analysis – Defining the Variables	116
5.2.2	LSRM Flux Linkage Analysis Results	117
5.2.3	LSRM Optimum Angle-Of-Advance Determination	119
5.2.4	LSRM Output Power Curves Determination	121
5.2.5	LSRM GA Optimization and Pareto Front	123

5.3	Rotating Switched Reluctance Machine Analysis and Design Results	126
5.3.1	Rotary SR Machine Analysis – Defining the Variables	127
5.3.2	Rotary SR Machine Flux Linkage Analysis Results	129
5.3.3	Rotary SR Machine Optimum Angle-Of-Advance Determination	135
5.3.4	Rotary SR Machine Output Power Curves Determination	136
5.3.5	Rotary SR Machine GA Optimization and Pareto Front	138
5.4	Chapter Summary	143
Chapter 6	Discussion and Conclusions	145
6.1	Results Discussion	145
6.1.1	Flux Tubes and Slices Model Sensitivity Discussion	145
6.1.2	SR Machine Optimization Results Discussion	146
6.2	Conclusions	148
6.3	Scientific Contributions	151
Chapter 7	Extensions and Future Work	153
7.1	On the Capability of 2D Leakage Flux Estimations using Flux Tubes and Slices Modelling Techniques	154
7.2	On the Capability of Modelling 3D Flux Distributions using Flux Tubes and Slices Techniques	159
7.3	On the Capability of Modelling Flux Distributions in Synchronous Reluctance Machines using Flux Tubes and Slices Techniques	163
Appendix A		167
Appendix B		177
Glossary of Terms		207
List of References		209

Table of Tables

Table 1: Analytical inductance solution error compared with FEM solution for three distinct machine frame sizes. Taken from [87].	60
Table 2: Analytical inductance contributions of the rotor and stator parts of the machine compared to FEM solution. Taken from [87]	61
Table 3: Summary of the dual bound reluctance values of the flux tubes and slices equations	84
Table 4: Flux tubes and slices geometric errors and their combinations.	86
Table 5: Geometric error effect on the numerical accuracy on the equivalent reluctance of the flux tubes and slices method	87
Table 6: GA optimization parameters and their numeric ranges of the three LSRM topologies	116
Table 7: GA based optimization settings for the LSRM topologies	117
Table 8: Numerical Error analysis of the 16-20 LSRM GA optimization results	125
Table 9: Rotary 18/12 SR machine design variables. Adapted from [2].	127
Table 10: Rotary 18/12 SR machine geometric design variables and their ranges	128
Table 11: GA based optimization settings for the rotary 18/12 SR machine topology	129
Table 12: Feature comparison table of the 3D flux tubes and slices approach and 3D FEM for the Optimization of SR machines	161

Table of Figures

Figure 1: Hierarchical design optimization process of an electromechanical device. Taken from [69].....	28
Figure 2: The proposed SR machine design optimization cycle exploiting reduced order computational method of flux tubes. Adapted from [70].	29
Figure 3: Two infinitely thick magnetic plates with an air gap. Adapted from [72]	36
Figure 4: Semi-circular cylinder and its mean path length definition. Adapted from [72]	38
Figure 5: Definition of flux tube (a) and an equivalent reluctance element formed by the flux tube (b). Taken from [73].....	41
Figure 6: General 3D reluctance MEC model without any active elements. Taken from [73]	42
Figure 7: Induction motor MEC reluctance elements subdivision into 1302 such elements. Taken from [73]	44
Figure 8: Comparison of the machine performance results obtained with reluctance MEC method and with alternative analytical and numerical methods to the measured values. Taken from [73]...	45
Figure 9: Single sided LSRM for propulsion of levitation and guidance systems. Taken from [7].....	47
Figure 10: FEM based solution of the magnetic flux distributions in the LSRM circuit. Taken from [7]	49
Figure 11: Normal force component of the LSRMs as obtained with 2D FEM and laboratory measurements. Taken from [7].....	51
Figure 12: Normal force component of the LSRMs as obtained with 2D FEM and 2D flux tube analysis. Taken from [7].....	51
Figure 13: Four phase radial flux SR machine with the assumed flux path distribution. Taken from [83]	52

Table of Figures

Figure 14: Example TAS electric current flow and resistance computations. Taken from [84].....	54
Figure 15: Subdivision of the trapezoidal plate into slices. Taken from [84]....	55
Figure 16: Subdivision of the trapezoidal plate into tubes. Taken from [84]....	56
Figure 17: Transformed radial SR machine geometry and the air gap subdivision into distinct regions shown in red. Adapted from [87]	58
Figure 18: Analytical (upper) and FEM (lower) field solutions of the rotor air gap. Adapted from [87].....	59
Figure 19: Air gap field solutions of the stator slot region, outlined in red, using (a) analytical method and (b) FEM. Adapted from [87]	60
Figure 20: LSRM flux distribution obtained from 2D FEM analysis	64
Figure 21: FEM analysis based magnetic field density plot for a symmetry segment of the LSRM.....	66
Figure 22: LSRM subdivision into five slices along the lengths of the flux paths	67
Figure 23: LSRM subdivision into tubes of flux (red arrow) and slices of equipotentials (blue arrow) of the air gap region.....	69
Figure 24: FEM analysis based magnetic field solution of the aligned translator position of the LSRM.....	70
Figure 25: Modelled aligned position LSRM flux paths based on cubic-spline interpolation.....	71
Figure 26: Flux-linkage map and gauge curves, not to scale, used to deduce candidate intermediate rotor positions.....	72
Figure 27: Flux tubes and slices superimposed onto 2D FEM solution for the 18/12 three phase SRM2 design at the unaligned rotor position.	74
Figure 28: Flux Tubes and Slices superimposed onto 2D FEM solution for the 18/12 three phase SRM2 design at the aligned rotor position..	75
Figure 29: A system of magnetic flux tubes arranged in parallel. Taken from [69]	76

Figure 30: An approximation of a true tube introducing the errors in length and area. Taken from [50]	77
Figure 31: A typical magnetization curve of a saturable iron circuit and the resulting errors in the non-saturated and saturated regions.....	79
Figure 32: Dual bounds approximations of the true flux linkage functions for the aligned and the unaligned rotor (or translator) position of SR machine.....	84
Figure 33: Flux tubes and slices area error generation	88
Figure 34: Flux tube length error term λ minimization using cubic splines	89
Figure 35: TAS implementation of the flux tubes technique for the aligned rotor position of the radial SR machine	94
Figure 36: TAS implementation of the flux tubes technique for the unaligned rotor position of the radial SR machine	96
Figure 37: Comparison of the flux TAS technique to the series flux tubes technique and the FEM solutions for the aligned and the unaligned rotor positions of the radial SR machine	97
Figure 38: Flux TAS and series flux tubes comparison of the flux linkage and the absolute error.....	98
Figure 39: Sensitivity analysis of the aligned flux linkage as a function of the number of tubes m	103
Figure 40: Speed-up of the aligned flux linkage computations as a function of the number of tubes m	104
Figure 41: Sensitivity of the aligned flux linkage as a function of the number of segment slices n	105
Figure 42: Speed-up of the aligned flux linkage computations as a function of the number of slices n	106
Figure 43: Sensitivity of the unaligned flux linkage as a function of the number of tubes m	107
Figure 44: Speed-up of the unaligned flux linkage computations as a function of the number of tubes m	108

Table of Figures

Figure 45: Sensitivity of the unaligned flux linkage as a function of the number of slices n	108
Figure 46: Speed-up of the unaligned flux linkage computations as a function of the number of slices n	109
Figure 47: General speed-torque characteristic of SR motor. Adapted from [93]	112
Figure 48: Speed-torque envelopes resulting from AoA parameter sweep.....	113
Figure 49: Graphical representation of the GA objective function.....	115
Figure 50: Flux-linkage map of the 16-20 LSRM obtained with flux tubes and slices approach and FEM.....	117
Figure 51: Comparison of instantaneous current and torque waveforms obtained with the flux tube method and FEM at the rated machine speed of 1000 rpm.....	119
Figure 52: Speed-torque envelopes of the 16-20 LSRM obtained with the improved flux tube approach and FEM	120
Figure 53: Speed-power envelopes of the 16-20 LSRM obtained with the flux tubes approach and FEM.....	122
Figure 54: GA optimization Pareto front of the 16-20 LSRM obtained with the flux tube method and FEM	124
Figure 55: Comparison of the aligned and unaligned flux-linkage functions of the 18/12 SR machine.....	129
Figure 56: Calibrated flux tubes and slices flux linkage functions with respect to FEM results	131
Figure 57: Unaligned air gap flux tube distribution of SRM1 18-12 SR machine	133
Figure 58: Uncalibrated flux tubes and slices based instantaneous current and torque profiles of the 18-12 rotary SR machine compared to FEM	134
Figure 59: Calibrated flux tubes and slices based instantaneous current and torque profiles of the 18-12 rotary SR machine compared to FEM	135

Figure 60: Speed-torque envelopes of the 18-12 rotary SR motor obtained with the improved flux tube approach and FEM.....	136
Figure 61: Speed-power envelopes of the 18-12 rotary SR motor obtained with the flux tubes and slices approach and FEM	137
Figure 62: GA optimization Pareto front of the 18-12 rotary SR motor obtained with the flux tube method	139
Figure 63: 3D-RadVis technique used to visualise the GA obtained 3D pareto front of the 18-12 rotary SR machine	140
Figure 64: Numerical error analysis of the 18-12 rotary SR motor GA optimization results obtained with the uncalibrated and calibrated flux tubes and slices method and FEM	141
Figure 65: Leakage flux effect on the accuracy of the modelled flux linkage curves for the rotary 18-12 SR machine.....	155
Figure 66: Ideal LSRM flux tube distribution under low levels of excitation current	156
Figure 67: LSRM with the probable leakage flux paths.....	157
Figure 68: Proposed exemplary 3D flux distribution implementation using the flux tubes and slices approach	162
Figure 69: Typical radial flux fractional slot synchronous reluctance machine. Taken from [117].....	164
Figure 70: The radial flux fractional slot synchronous reluctance machine flux distribution of flux tubes method. Taken from [117]	165

List of Accompanying Materials

NONE.

Academic Thesis: Declaration Of Authorship

I, Aleksas Stukys.....

declare that this thesis and the work presented in it are my own and has been generated by me as the result of my own original research.

Electromagnetic Modelling of Switched Reluctance Machines Exploiting Flux Tubes.....

.....

I confirm that:

1. This work was done wholly or mainly while in candidature for a research degree at this University;
2. Where any part of this thesis has previously been submitted for a degree or any other qualification at this University or any other institution, this has been clearly stated;
3. Where I have consulted the published work of others, this is always clearly attributed;
4. Where I have quoted from the work of others, the source is always given. With the exception of such quotations, this thesis is entirely my own work;
5. I have acknowledged all main sources of help;
6. Where the thesis is based on work done by myself jointly with others, I have made clear exactly what was done by others and what I have contributed myself;
7. Parts of this work have been published as: References [69], [70], [94], [117].

Signed: Aleksas Stukys.....

Date: 12 February 2018.....

*Jesus Christ you are the Author of life, the Prince of peace, the eternal Priest, the
Light for the world to see, the Beginning and the End.*

Amen.

Acknowledgements

I would like to dedicate the entire work and effort over the years which resulted in the present research piece to my family who so patiently supported me through this great journey.

First and foremost a sincere expression of gratitude goes to my supervisor Professor Jan Sykulski. His guidance and support was thoroughly felt throughout the research work and was critical to its successful completion. Therefore his support and help during this time will be dearly remembered.

Further thanks are to my co-supervisor Dr Mihai Rotaru for his ongoing academic support during the entire research project. His ability to see the bigger picture helped deliver the research project to its successful completion and helped to prevent the project being caught up in the small but too numerous technical matters that so often distract. His helpful discussions helped the understanding of the more important goals and milestones of the entire research effort.

Further acknowledgements and thanks are to the many academics and staff at the University of Southampton and wider community who were always ready to extend a helping hand and were very supportive during this intense time. Similar support was felt from many of the colleagues, those who have completed their own research degrees as well as those who were in the writing up stage.

Definitions and Abbreviations

Switched Reluctance (SR)

Direct-current (DC)

Magnetic Equivalent Circuit (MEC)

Finite Element Method (FEM)

Genetic Algorithm (GA)

Three-dimensional (3D)

Tubes-and-slices (TAS)

Linear Switched Reluctance Machine (LSRM)

Magnetomotive force (mmf)

Maxwell Stress Tensor (MST)

Angle-of-advance (AoA)

Revolutions per minute (rpm)

Synchronous Reluctance Machine (SynRel)

Torque-per-Ampere (TPA)

Chapter 1 Introduction

1.1 The Need for Rapid Electromagnetic Modelling of the Switched Reluctance Machines

Switched reluctance (SR) machine, a type of electromechanical energy converting device technology, has attracted substantial attention from researchers and engineers in the past 40 years [1], both in academia and industry, due to its simple, low cost and robust construction. SR machines are as versatile, from the industrial application point of view, as the well-established induction, direct-current (DC) brushed, brushless permanent magnet synchronous and synchronous reluctance electric machines. The SR machine technology spans the following topologies: radial flux [2], axial flux [3], [4], and transverse flux rotating machines [5], [6]; translating (linear) machines [7], [8], and tubular translating (linear) machines [9], [10]. SR machines can be DC as well as AC fed depending on the application requirements [11], [12], as well as a single phase or multi-phase [13]. SR machine technology is suitable to as diverse industrial applications as the more traditional electric machine technologies mentioned earlier and, therefore, spans output power levels from few *mW* [14] to hundreds of *kW* [15], [16]. For example, the radial and axial flux SR machines have been used in many industrial drives, traction motors and pumping applications [17]–[19]. The novel SR translating machines have been used as magnetic propulsion and levitation devices for railway systems in transportation [20]. The tubular translating SR machines were successfully tested in medical applications as artificial heart pump actuators [21]. The field of industrial applications of the SR machines, and more importantly their distinct suitability, is truly remarkable as is shown with the above spelled non-exhaustive list of examples.

However, the constructional advantages of the SR machines translate into quite complex task of the engineering analysis and design of SR machines, the task which is compounded by their non-linear electromagnetic behaviour. That is to say; the mechanical design, manufacturing and assembly tasks of the SR machine are relatively uncomplicated, however the electromagnetic analysis and design of the machine is very complex. Despite some effort to formalise [22]–[25], the SR machine analysis and design calculations have not yet been developed into convenient and versatile design tools (with a few historical special case exceptions [26], [27]) that could be comparable to the closed form solution

Chapter 1

methods available for the more traditional types of rotating electric machines such as induction or brushless permanent magnet. The main difficulty with the analysis and design of SR machines is the magnetic non-linearity caused by the heavily saturated iron parts of the machine circuit even while in the steady state operation. The purely non-saturating SR machines, as used in some niche industrial applications, do not pose the non-linearity challenge and are therefore not considered in this work, however the interested reader can refer to the engineering or academic research literature, for example [28].

Furthermore, the disadvantages of the SR machine, whether it is saturating or non-saturating machine, are also numerous starting with high levels of torque ripple [29]–[31] and high levels of acoustic noise emission [32], [33], [34], complexity of control [35], high levels of current ripple, unsatisfactory EMC issues to name a few. If left unresolved, these disadvantages can completely outweigh the main advantages of the SR machine technology and render it unsuitable for many industrial applications. Although the simultaneous technical resolution of all of the above mentioned issues is extremely difficult in practice [36] there remains ample evidence of industrial applications in which some of the SR machine disadvantages can be reduced and tolerated while others are completely resolved thus resulting in highly economical electric motor drive system [37].

Given the wide variety of topological arrangements of the SR machine technology [38]–[49], which is expected to grow substantially in the near future as the demand for the new and challenging industrial applications increases, it is important to establish analysis and design methods that are reliable, accurate and computationally efficient for the prediction of SR machine performance. Therefore the concept of this work is that the quest for novelty in the generation of the versatile SR machine topologies must not be limited or prevented due to the absence of practical analysis and design methods used to analyse and design such machines. However, the design task could be made much easier if such practical analysis and design methodologies existed and were available. Thus, the aim is to make the SR machine electromagnetic design task more systematic, formal and far less complex which in turn will help to discover new industrial application areas for this highly versatile electric machine technology and potentially will aid the discovery of many new and practical SR machine topologies.

The above expressed point has important industrial implications and a further perspective is given as follows.

One particular application area in which SR machines will proliferate even more so is the automotive electric propulsion application where the SR machine will act as the main traction motor-generator [2], [50]–[52]. The automotive industry is set to benefit from the SR motor technology due to the already mentioned favourable qualities of robust mechanical construction and absence of any permanent magnet components which, in contrast to most other types of electrical machines used in the automotive electric propulsion applications, are not possible to avoid. Let us expand on the advantage of SR machines for the automotive electric propulsion applications compared to permanent magnet machines.

In the recent past there has been an upsurge in demand for the permanent magnet materials, (e.g. neodymium iron-boron, etc.) obtainable from the excavated rare-earth ores, due to the automotive and other industry requirements to supply mostly the permanent magnet based motor technologies [53]. This has resulted in the global demand exceeding the global supply thus giving rise to highly unstable market prices for the rare-earth material based permanent magnets [54], [55]. This, in turn, has led to a wide scepticism amongst the automotive industry experts [56] questioning the notion that only the permanent magnet based automotive traction motors will suffice for the ongoing effort of mass-electrification and hybridisation of passenger cars [57] and of transport more generally. The absence of the permanent magnet components is the principal reason why the SR machine technology is set to increase in importance so rapidly in the automotive electric traction motor sector [58]. The attractive SR machine constructional features offer unparalleled mechanical and electrical robustness [59], in addition to complete immunity from the unforeseen price fluctuations of the permanent magnet components in the highly competitive high volume automotive electric traction motor sector.

However, once the SR machine is considered for a particular high volume automotive electric traction motor application the requirement to optimize the given SR machine topology becomes of overriding importance in order not to compromise the complete electric traction drive system [60]. This is the case since SR machines are exclusively designed simultaneously in combination with their power converters in turn requiring sophisticated as well as accurate, yet rapid design optimization methods in order to meet the stringent high volume automotive electric traction motor design goals. The high volume electric traction motor application is considered to be of such high importance precisely due to the total amount of energy consumed during the entire useful life of such electric

vehicles with the direct economic impact to the transportation. This calls for electromagnetic analysis methods which exhibit high fidelity of the physical phenomena of the pertinent SR machine topology, as may be considered suitable for a particular vehicular electric traction application, since the number of design objectives and constraints in such applications is unusually very large [36]. The need for such analysis methods and their economic benefits, albeit in more general case, have already been noted previously [61]. Therefore it is anticipated that the electromagnetic analysis and design methods presented in this work will largely meet the requirements for the rapid design optimization of novel SR machine technology based electric traction motors as may be deemed suitable for the propulsion of the electric and hybrid vehicles.

We now briefly turn our attention to the currently most widely accepted design and analysis tools for the electromagnetic devices and their suitability for the electromagnetic performance predictions of the novel topology SR machines.

Reduced order computational methods, the most notable example being the magnetic equivalent circuit (MEC) approach, have been successfully employed in the past for the various types of electric machines [62]. The main advantage of the MEC based electromagnetic models is that they are relatively accurate given their computational efficiency. On the contrary, the finite element method (FEM) based computational technique is very useful for most-accurate analysis and design of the established electric machine technologies and topologies, but the technique does not offer the cause-and-effect insights of numerous and interrelated design variables when novel and unfamiliar electric machine topologies are being considered for optimization [63], [64]. This is precisely the difficulty an SR machine designer is facing due to the absence of relatively fast yet accurate and intuitive electromagnetic modelling techniques suitable for most exacting electromagnetic design calculations. In such cases the best choice, although a compromise in itself, is the accurate yet time consuming FEM analysis which, as was mentioned before, does not offer insights into the numerous complexly interrelated SR machine design parameters. Therefore, by using the FEM techniques the designer is left with uncertainty as to the optimality of the analysed SR machine design while facing the very large design objectives response surface space. What is needed, in the ideal scenario, is the accuracy afforded by the FEM and the computational efficiency of MEC methods. Of course such scenario is not attainable since the computational efficiency of a given method is inversely related to its accuracy. That is to say, it is difficult to have

very fast and yet very accurate electromagnetic analysis method as a single design tool. In practical terms what is needed is at least a partial compromise between the computational efficiency and accuracy. Express it differently, the need to bridge the currently present gap between the accuracy and computational efficiency of the electromagnetic methods used for SR machine analysis and design tasks. It is anticipated that the electromagnetic approach presented in this work, and directed mainly but not exclusively to the analysis and design of SR machines, will enable such compromise to be made for the design and optimization tasks.

The above presented argument is further supported by the fact that most of the available 2D or 3D FEM based analysis and design software packages, although very versatile as to the variety of problems being solved, are available only under the commercial licensing options. The availability of computationally capable FEM based analysis tools can help speed up the discovery and generation effort of innovative SR machine designs considerably. However, there are few instances of fairly versatile 2D FEM analysis packages that are distributed under the open source license, one noteworthy example can be found in [65].

Since the SR machine is a classical electromechanical energy converting device [66]–[68] its design optimization process largely follows the hierarchical design optimization paradigm presented in Fig. 1 which could be termed “the classical” electromechanical device design optimization process.

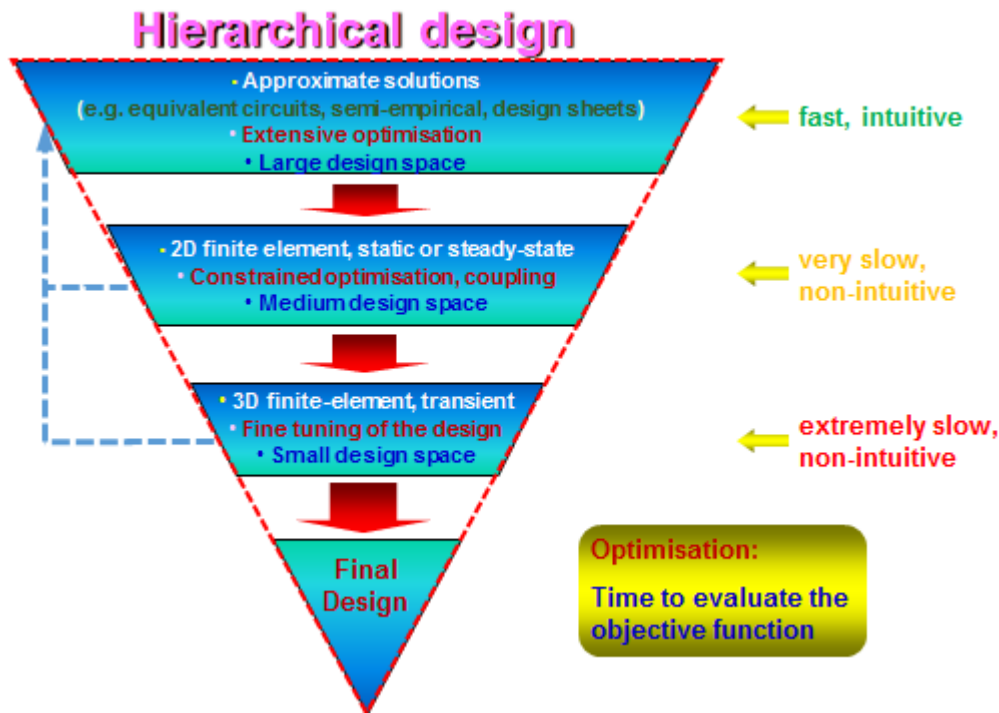


Figure 1: Hierarchical design optimization process of an electromechanical device. Taken from [69]

As can be seen from Fig. 1, the typical design optimization process of an electromechanical device progresses through distinct design steps where generally the solution time increases whereas the solution accuracy improves. Once the satisfactory design solution accuracy is reached, or alternatively the available solution time is exhausted, the final design solution is obtained. The hierarchical design process in Fig. 1 does benefit from the internal information communication paths (punctured directed lines) whereby the information obtained in the subsequent design solution step is not lost but can be used in the previous design solution step if it is found that the design optimization process has to be repeated in the previous rung of the pyramid again. Such scenario is likely to occur when the initially specified SR machine design objectives or constraints have to be modified or updated to reflect newly formulated requirements for the optimized device. However, the main point about the hierarchical design process in Fig. 1 is that the intermediate step between the fast approximate solutions and the very slow 2D FEM solutions would be a desirable addition to the existing design optimization process as applied to the SR machine electromagnetic design optimization. This is the case since the SR machine non-linear electromagnetic behaviour requires much more accurate as well as fast and intuitive methods whereas the 2D FEM fall short of this requirement since the intuition is not preserved in these methods and the speed of solution is low.

Therefore, bearing in mind the mentioned advantages of the MEC and the FEM based electromagnetic analysis, the SR machine design optimization cycle is proposed as illustrated in Fig. 2.

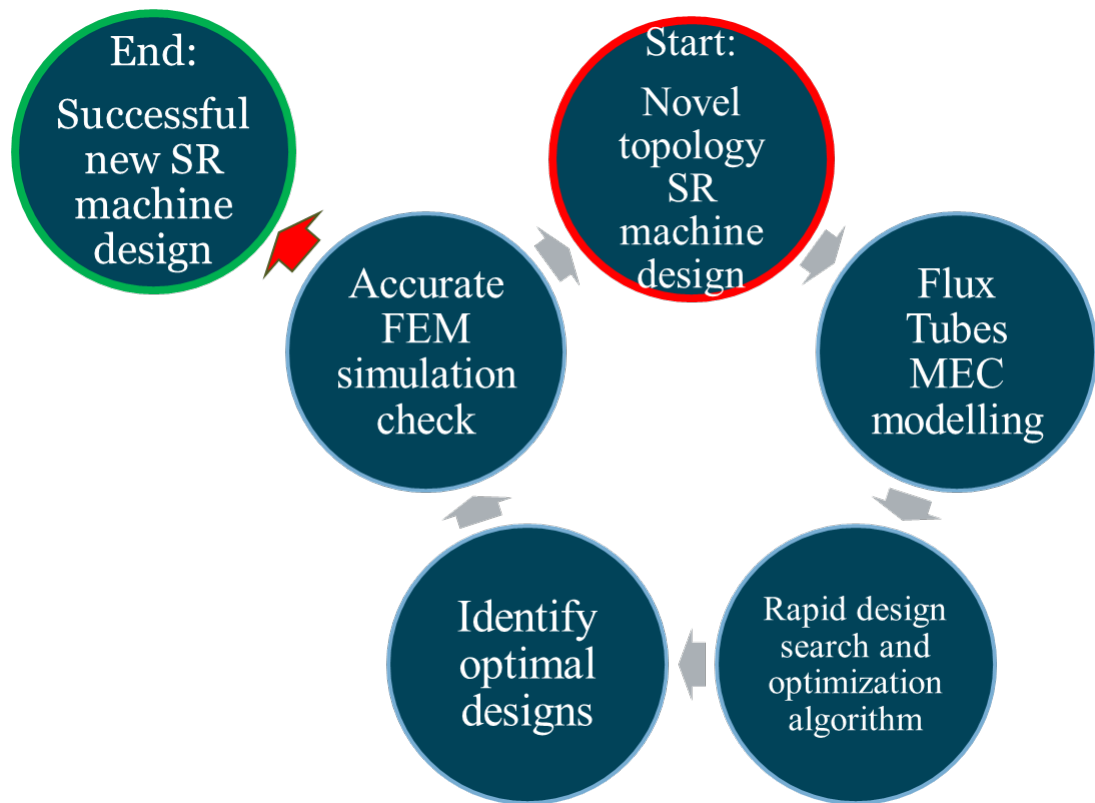


Figure 2: The proposed SR machine design optimization cycle exploiting reduced order computational method of flux tubes. Adapted from [70]

By executing the proposed design cycle in Fig. 2 in the predetermined manner can result in speedy design optimization of an SR machine. As a first step of the cycle a novel topology SR machine is identified and considered for a certain application because that particular machine topology meets some specific requirements imposed by the application, for example: cost, volume and mass, mechanical, etc. In the next step of the cycle, the improved flux tube based method, which we propose in this work, is employed in order to construct and evaluate the electromagnetic model of the machine and is subsequently used in conjunction with a design search and optimization algorithm, for example the genetic algorithm (GA). Once a set of near optimal solutions (i.e. a Pareto front) is established from the previous design optimization cycle step in Fig. 2, a few designs are selected for further analysis and optimization using an order of magnitude more accurate analysis technique, such as FEM. If FEM confirms that indeed the selected designs are near optimal, the design optimization cycle can conclude as the SR machine which satisfies all the design constraints has been

found. If, however, the FEM proves otherwise, the knowledge and insights gained from the flux tube modelling are fed back into the novel topology SR machine generation stage and the design cycle is repeated. The situation in which the reconsideration of the chosen SR machine topology is initiated after the full design cycle in Fig. 2 is completed can be triggered by a broad range of practical considerations. These practical considerations should not concern us in this work since we are investigating the computational efficiency and accuracy afforded by the proposed electromagnetic analysis methods and therefore are not primarily concerned in listing these practical design considerations in the exhaustive manner.

This report is therefore an investigative work of SR machines analysis and design using electromagnetic computational simulation and modelling tools. As is known from prior work, for example [63] and [71], the SR machine performance can be completely described by a three-dimensional (3D) flux-linkage map (see Fig. A1, Appendix A for an example). The flux-linkage map is a function of simultaneously the both the electric current in the active phase windings and of the translator or rotor pole position with respect to the poles of active phases on the stator part of the SR machine. Such flux-linkage map will contain all the information to quantify the machine performance – the instantaneous torque it can produce at a particular phase current level for a particular speed of rotation or translation if it is a linear machine, operating voltage level and the maximum useful rotational speed. Obtaining the flux-linkage map is not an easy task since, as has already been underlined above, SR machine operation can take place in the saturated as well as in non-saturated regions of magnetisation curve of a ferromagnetic steel from which the machine is constructed – thus material properties are critically important. Therefore, this research work is focused on the development of computational techniques which enable such non-linear flux-linkage map to be estimated with reasonable accuracy and computational efficiency. In this work it is demonstrated that by using well known but substantially improved and extended magnetic field modelling and simulation techniques such desirable computational performance is attained.

1.2 Research Objectives

Therefore, given the above discussed SR machine design and optimization requirements the following research objectives are set in order to investigate,

propose and formalise reduced order computational methods suitable for rapid and accurate electromagnetic analysis and design of the SR machines.

1. Investigate the currently available reduced order, and other more widely used, computational methods for the electromagnetic analysis of SR machines
2. Perform qualitative review of the presently available reduced order computational methods and consider their advantages and disadvantages for the rapid electromagnetic analysis and design of the SR machines
3. Having identified the favourable computational and modelling features of the currently available electromagnetic analysis methods propose an alternative and highly improved reduced order computational method which will exhibit the favourable computational and modelling features of the alternative computational methods as applied to the SR machines
4. Formalise the newly proposed SR machine electromagnetic analysis approach by demonstrating the computational performance and modelling advantages the method offers, identifying the factors and the severity due to which the method is likely to underperform compared to alternative methods using practical SR machine electromagnetic circuits as computational examples

The first objective will present the overview of the currently best known and most practical electromagnetic analysis methods that are applicable to the SR machine analysis. This will be followed by the detailed review of these methods and the assessment of their advantages and disadvantages as applied to the rapid analysis of the SR machines. At this stage the favourable qualities of the modelling approaches will be identified and used as desirable benchmarking goals to be achieved by the newly proposed modelling approach. Finally, once the newly proposed method is demonstrated to be practicable the modelling and analysis performance characteristics of the method will be formalised in terms of the factors which affect the computational performance of the method and the likely strategies to control these factors in practice.

It is anticipated that the above listed research objectives will help to direct the research effort towards the discovery and formalisation of the computationally efficient and numerically accurate reduced order computational methods which will complement the industry standard tools, such FEM analysis approach, used for the design of the SR machines as discussed in the previous section.

1.3 Organisation of the Work

The scientific research work contained in this document is organised as follows.

First a literature review is presented in the report which covers prior and current art of reduced order computational modelling and simulation of electromagnetic fields with applications to rotating and translating electric machine analysis and design. This material is covered in Chapter 2.

Next, the methodology section introduces and describes the improved flux tubes and slices method used for modelling and simulation of SR machine performance. The improved flux tube method itself is based on the following methodologies: estimation of permeances of probable flux paths [72], MEC [62] and [73], assumed flux tubes [63], [74] and [75], and tubes-and-slices (TAS) [76]. The improved flux tubes and slices method is a combination and extension of the aforementioned methods for the electromagnetic analysis and design of SR machines. This is covered in Chapter 3.

Further methodology chapter describes in detail the properties of the flux tubes and slices model in terms of its accuracy and computational efficiency. Certain guidelines are given as to the expected performance of the flux tubes method when applied to the analysis and design optimization of the SR machines. This is covered in Chapter 4.

The results chapter of the report presents the computational simulation results of a translating (linear) SR machine (LSRM) and rotating SR machine obtained through the improved electromagnetic simulation approach of the flux tubes and slices. The new method is applied to particular topologies of LSRM and rotating SR machines and the simulation results compared with FEM results. This is in line with the prescribed steps in the proposed design optimization cycle in Fig. 2. This is covered in Chapter 5.

The conclusions chapter of the report summarises the main findings of the electromagnetic simulations using the improved flux tubes and slices modelling techniques. Conclusions chapter of the report also indicates advantages and disadvantages of the new method compared to other electromagnetic field simulation and modelling approaches for the analysis and design of SR machines. This is covered in Chapter 6.

Finally, the future work chapter of the report contains discussion and recommendations on further SR machine 3D electromagnetic modelling approaches in order to realise rapid design optimization of such machines for the energy efficient, torque and power dense SR machines suitable for high volume pure-electric and hybrid-electric vehicle traction and industrial applications. The improved flux tubes and slices method is put into perspective of this requirement in terms of the inherent modelling advantages. This is covered in Chapter 7.

Chapter 2 Literature Review

The electromagnetic modelling of SR machines has received substantial academic and industry led research effort which has resulted in a number of newly developed as well as adopted existing electromagnetic analysis techniques. In order to appreciate more fully the many analysis techniques and their advantages and disadvantages when applied specifically to SR machines electromagnetic analysis the following literature review is presented.

2.1 Estimating Flux Path Permeance - Roters Method

A method of estimating 2D magnetic field flux path permeances of gapped electromagnets was proposed by Roters [72]. The method known as “Estimating the Permeances of Probable Flux Paths” is based on a concept that 2D magnetic fields occurring in gapped magnetic circuits of tractive electromagnets can be quite accurately quantified and analysed by use of properties of simple geometric shapes in order to compute average lengths and areas of cross-sections of flux tubes therein (see Fig. 29 for most general definition of a flux tube). As reported in [72] as well as other sources [63] the device performance results accuracy can be within 5% of measurements of the actual devices when the Roters method is used. Due to the nature of operation of SR machine and its resulting flux-linkage map, which in principle is very similar to that of gapped tractive electromagnet flux-linkage map, the Roters method is a valuable method in estimating the flux-linkage function for the unaligned stator and rotor poles position as described, for example, in detail in [3], [7], [8], [74], [75] and [77]. The unaligned poles position corresponds to minimum inductance state of SR machine and should be made as low as possible in order to maximise instantaneous torque production for the rated phase current level [78].

A simple case of two parallel and infinitely thick (along the z-axis) magnetic plates separated by an air gap, shown in Fig. 3, can be used to illustrate the application of the method of Estimating the Permeances of Probable Flux Paths. The accuracy attainable with the Roters method can then be compared to an alternative method of reasonable accuracy.

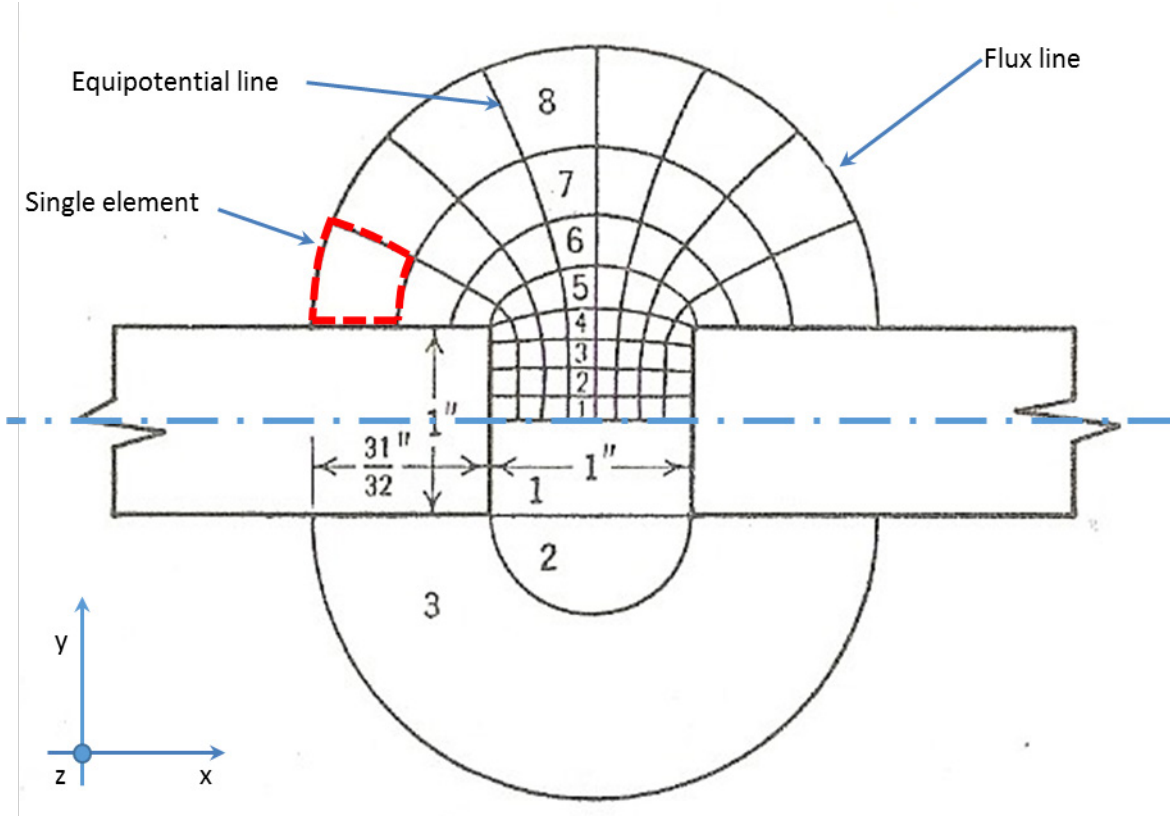


Figure 3: Two infinitely thick magnetic plates with an air gap. Adapted from [72]

Considering the upper part of the system in Fig. 3 - depicting the 2D magnetic field equipotential lines and their associated flux lines. These lines are constructed by the manual method of “field mapping”, which can be likened to the conformal mapping analysis techniques in mathematics, in an air gap between two magnetically soft metallic plates. By the method of field mapping each of the elements in the upper part of the magnetic field is made a curvilinear square (which in row 1 reduces to a simple square) permeance of which will be equal to permeance of any other element in that system due to orthogonality principle. The orthogonality principle ensures that each curvilinear square in the system will have numerically equal ratios of their lengths (along the x-axis) to their areas of cross-section (in the z-axis). The orthogonality principle therefore implies that any one square element, of a unit depth, from the first row of elements in Fig. 3 will have permeance value numerically equal to any other square element in that same row or any other curvilinear element in any other row (row 2, 3, 4, 5, etc.). By calculating permeance of any one square therefore will enable value of the total permeance of the system to be found. Defining permeance of a magnetic flux tube as a reciprocal of flux tube reluctance R [40]:

$$\text{Permeance} = P = \frac{\mu_0 \cdot S}{l} = \frac{1}{R} \quad (1)$$

where μ_0 is the permeability of free space, S is the cross-sectional area and l is the length of the element under consideration.

For the given dimensions in Fig. 3 it can be shown by substituting that the permeance of a single square element, in row 1, per inch of plate thickness is equal to

$$P = \frac{\mu_0 \cdot S}{l} = \frac{3.2 \times \left(\frac{1}{8} \times 1\right)}{\frac{1}{8}} = 3.2 \left(\frac{\text{maxwell}}{\text{ampere-turn}} \right) \quad (2)$$

Due to the orthogonality principle this permeance value will be the same for all the elements in the system in Fig. 2 provided that all the elements were drawn to their true shape in the first instance. And as there are in all 8 such elements connected in series (along the x-axis) and 16 such elements connected in parallel (along the y-axis) the total permeance of the air gap is equal to

$$P_{total} = \frac{3.2 \times 16}{8} = 6.4 \left(\frac{\text{maxwell}}{\text{ampere-turn}} \right) \quad (3)$$

In contrast to the above demonstrated field mapping method the application of the Roters method of Estimating the Permeances of Probable Flux Paths proceeds as follows: the lower half of the air gap magnetic field in Fig. 3, which in an actual device would be identical to the upper half, is subdivided into three simple geometric shapes of a rectangle, semi-circle and half annulus (denoted 1, 2 and 3 respectively). If the problem is to be described in 3D then these geometries would become a right angle prism, semi-circular cylinder and half annulus cylinder. Permeance of the first geometry, per inch of depth of the plates, can be readily calculated by the standard permeance formula, Eq. 1, as

$$P_1 = \frac{3.2 \times \left(\frac{1}{2} \times 1\right)}{1} = 1.6 \left(\frac{\text{maxwell}}{\text{ampere-turn}} \right) \quad (4)$$

Next, the semi-circular geometry based magnetic permeance of Fig. 3 is evaluated by assuming that the true path length lp of the flux line acting therein will be numerically close to the mean (not the average) path length l' of the semi-circle in the air gap as shown in Fig. 4.

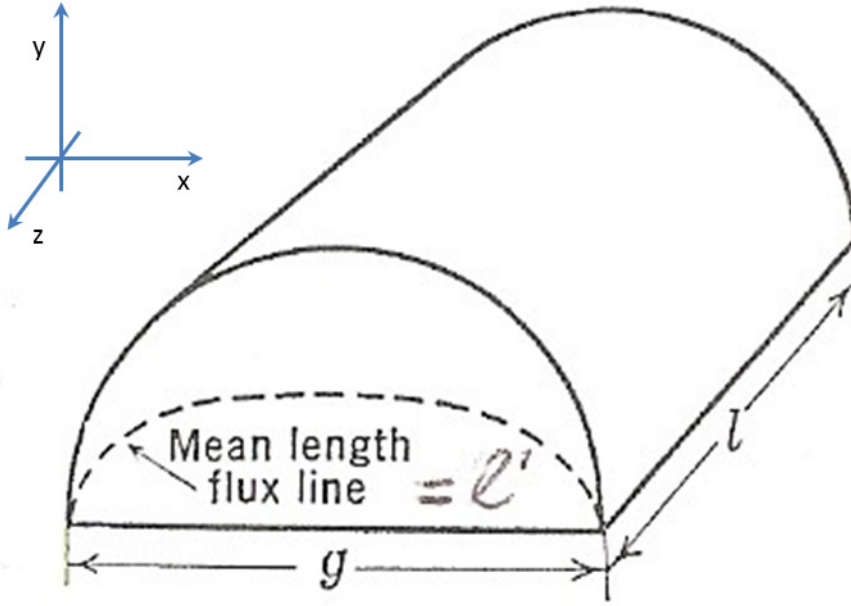


Figure 4: Semi-circular cylinder and its mean path length definition. Adapted from [72]

Furthermore, the cross-sectional area S of the true magnetic flux path will be approximated by a probable flux path mean area S' which will be numerically close to the value of the true flux path. For the accurate estimation of these two probable values, l' and S' , the volume formula of the semi-circular cylinder is used and the mean path length l' of the semi-circle is computed which is equal to $1.22 \times g$, where g is the diameter of the semi-circle. Now it follows that the mean area of the semi-circular cylinder is equal to the ratio of the volume, V , to the mean path length l' as follows

$$S' = \frac{V}{l'} = \frac{l \times \pi \times g^2}{8} \div (1.22 \cdot g) = 0.322 \cdot g \cdot l \quad (5)$$

where letter l in the above calculation denotes one unit of depth along the z -axis in Fig. 4. Having obtained these two probable values the permeance of the semi-circle, per unit depth, is computed by the use of the standard permeance formula defined earlier as follows

$$P_2 = \frac{\mu \cdot S'}{l'} = \frac{3.2 \times 0.322 \cdot g}{1.22 \cdot g} = 0.84 \left(\frac{\text{maxwell}}{\text{ampere-turn}} \right) \quad (6)$$

Finally, the semi-circular annulus, geometric shape 3 in Fig. 3, is treated in a similar way to find the probable mean length and area of cross-section of the geometry of the true flux path therein. Once these quantities are found the

permeance of this geometric shape is computed by the standard permeance formula and is numerically equal to [72]

$$P_3 = 1.08 \left(\frac{\text{maxwell}}{\text{ampere-turn}} \right) \quad (7)$$

Thus the total permeance of all the probable flux paths, in Fig. 3, is composed of individual permeances arranged in parallel

$$P_{total} = 2 \times (P_1 + P_2 + P_3) = 2 \times (1.6 + 0.84 + 1.08) = 7.04 \left(\frac{\text{maxwell}}{\text{ampere-turn}} \right) \quad (8)$$

where the multiplication factor is due to the symmetry of the system being considered.

Roters method of Estimating the Permeances of Probable Flux Paths gives, in this example, an answer which is within 10% of the alternative method of field mapping considered first. Of course there is no guarantee that the first method gives the actual values as would be found by accurate laboratory measurement of the real system. However, it is reasonable to assume that if the number of curvilinear squares in the system in Fig. 3 is reasonably large then the answer given by the first method of analysis will be close to the actual value encountered in a practical device. Nevertheless, the results comparison of the two methods indicates that there is close agreement of the results for approximate estimation of air gap permeance with relatively straightforward calculations and with the effort of obtaining the orthogonal squares by tedious hand sketching eliminated altogether in the Roters method.

From the preceding numerical example it is possible to generalise the Roters method for more complex air gap flux paths which nevertheless will always be a combination of straight lines and circular arcs [63] whether arranged in series or parallel. What is required to arrive at a reasonably close estimate of the true air gap permeance is an ability (which can be enhanced by careful study and experience of the subject of the magnetic fields) to split the total air gap flux into geometrically simple shapes, as in the lower part of Fig. 3. Once the subdivision step is performed the calculation of permeances of individual components of the overall flux path can be performed by deducing the true volume V of that particular geometry and finding the mean path length l' which will correspond to the path length of the actual flux in the air gap. Next, the mean cross-sectional area S' corresponding to the mean path length of that particular geometry will be

found by the ratio of the actual volume to the mean path length. Thus the probable component permeance of one of the true flux paths will be found as

$$P_u = \frac{\mu \times V}{(l')^2} = \frac{\mu \times S'}{l'} \quad (9)$$

It is therefore evident that only one estimated value - that of mean length of the assumed flux path - is required with all the other quantities being exact in the calculation in Eq. 9. Such calculation has a merit of reducing error of the final result.

Although the Roters method is well suited for the air gap magnetic permeance or reluctance calculations its application cannot be directly extended to ferromagnetic materials with the non-linearly varying permeability such as magnetically soft iron. The reason for this is that accurate representation of each of the overall flux path components in a practical magnetic steel circuit, except the most simplest cases such as well-proportioned u-core inductor or similar, would demand very fine subdivision of component flux path lengths in order to fit mean lengths of simple geometric shapes that closely mimic true flux path geometries. The number of calculations, although in principle not complicated, would be prohibitively large and the computational efficiency of the method would be low. On the other hand a courser number of subdivisions would produce only approximate estimates of the probable flux path lengths and this in turn would make the results less precise when saturation effects are taken into account. Precision and computational efficiency of magnetic field analysis method is of considerable importance if rapid design of electromagnetic devices under consideration, SR machines of various topologies in particular, with near optimal characteristics are to result.

2.2 Magnetic Equivalent Circuit Method

As was mentioned in the previous sub-section the electromagnetic devices producing useful work are constructed with magnetic circuits that contain variable length air gaps inside them. Although accurate estimation of the magnetic reluctances (or permeances) of these air regions is an important task additional consideration becomes of significance when determining the performance of an electromechanical device itself – consideration of whether the ferromagnetic steel parts of the magnetic circuit are likely to saturate significantly and in the non-linear manner under the normal (rated) operating conditions of the

device. If such magnetic saturation is expected then the overall reluctance of the magnetically saturable parts of the machine must be accurately accounted for. To perform such analysis it is possible to utilise FEM that can be accurate in most cases, yet these methods have shortcomings of lengthy simulations and non-intuitive cause-and-effect analysis [79].

An approach used to compute saturable sections of electromagnetic circuits was proposed in [62] using magnetic equivalent circuit (MEC) approach. The MEC approach has been applied for the analysis of electric machines, such as rotating induction machines, as well as power transformers and similar electromagnetic devices. References [73] and [80] give detailed account of 2D and 3D MEC model implementation for the analysis of fractional horsepower induction machine. The MEC method is based on the concept of a flux-tube as a basic modelling block of each reluctance element in the magnetic circuit as shown in Fig. 5.

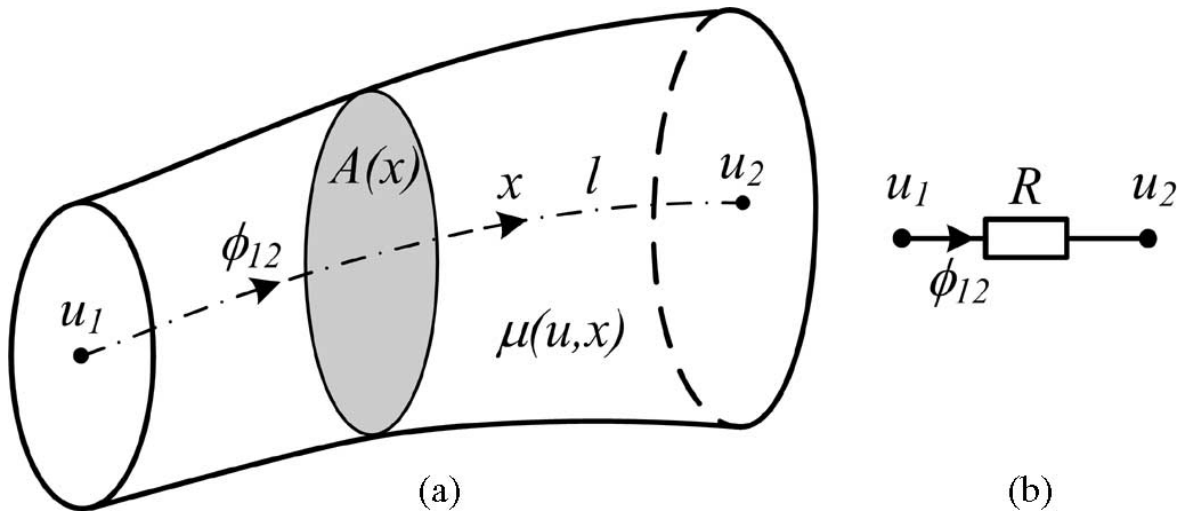


Figure 5: Definition of flux tube (a) and an equivalent reluctance element formed by the flux tube (b). Taken from [73]

Flux tube can be geometrically defined as a magnetic flux line of certain length and its geometry of cross-section can be other than round section to suit geometry of a specific part of electromagnetic device under consideration. Referring to Fig. 5, the reluctance of a single flux tube is defined as follows [73]

$$R = \frac{u_1 - u_2}{\phi_{12}} = \frac{1}{\mu(u, x)} \int_0^l \frac{1}{A(x)} dx \quad (10)$$

where u_1 and u_2 are the node magnetic scalar potentials, $\mu(u, x)$ is the magnetic permeability which can vary along the length l of the flux tube as well as due to intensity of the magnetic field, $A(x)$ describes area of cross-section of the flux

tube and ϕ_{12} indicates constant magnetic flux value along the length of the flux tube. One or more of the flux tubes can be used to model a particular section of electric machine, stator tooth or yoke for example, in order accurately to capture distribution of magnetic flux lines occurring in an actual device. Of course the flux tube can be used to represent air gap reluctance as well and this is easily accomplished by use of constant permeability of free space μ_0 . The resulting reluctance elements are connected in parallel or series to form a network of reluctances in that part of the device.

Extension of the MEC method to 3D elements is accomplished by combining six equivalent reluctance elements to form orthogonal axes of 3D space as shown in Fig. 6.

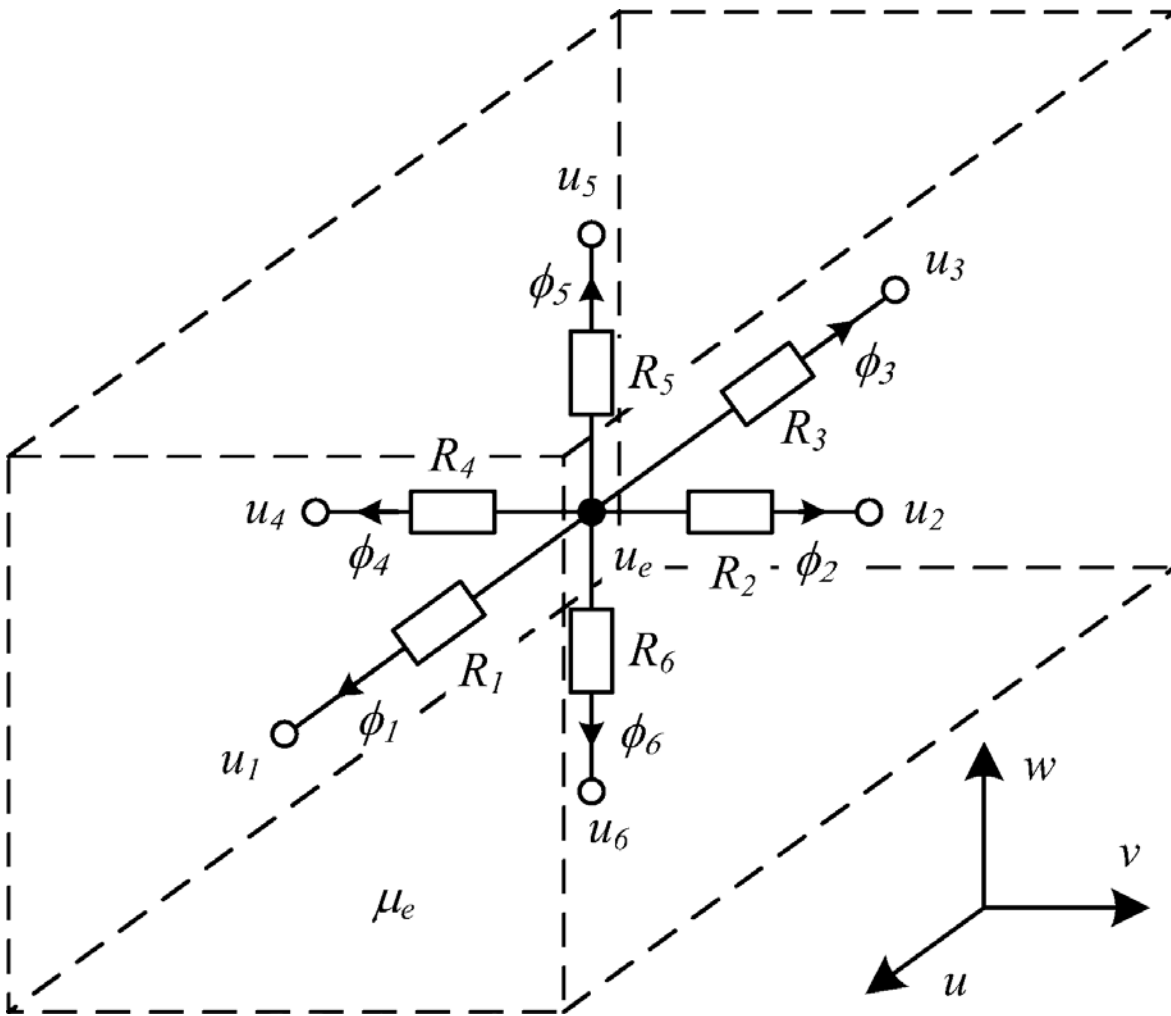


Figure 6: General 3D reluctance MEC model without any active elements. Taken from [73]

In addition to the passive reluctance network shown in Fig. 6, active magneto motive forces (*mmfs*) as well as constant magnetic flux sources can be added to the reluctance elements placed in series and parallel to the individual reluctance

elements in question in order to model the electromagnet and permanent magnet sources respectively. Such 3D extension of the reluctance MEC method is suitable for the 3D modelling of electromagnetic fields provided the subdivision of the modelled system is sufficiently small thus enabling accurate magnetic analysis and results. Alternatively the 3D equivalent reluctance element can be made of irregular hexahedron shape to suit intricate geometry of electromagnetic device; this reduces overall number of otherwise rectilinear elements, as in Fig. 6, with decreasing number of unknown potentials to be solved and thus resulting lower computation time. However, transformation of the irregular hexahedrons back into parallelepiped elements for flux intensity estimation will add computational penalty to the efficiency of the method.

An attractive feature of the reluctance MEC modelling is that the translational and or rotational motion can be incorporated into time-stepping analysis of electromechanical device [73]. This can be achieved by overlapping reluctance components of stationary and moving reluctance elements which are adjacent to each other during that time step. New reluctance value is then a sum of two reluctance values of the stationary and moving reluctance elements. If the mechanical motion of parts of the modelled electromagnetic device is present then there must be a useful work production as a result of this motion. To calculate translational force or torque of the modelled system accurately Maxwell Stress Tensor (MST) is used which is one of few alternative force calculation methods used in magnetic FEM. The MST is used because the computational mesh of such analyses is often dense enough to facilitate accurate integration of air gap regions where electromagnetic force is produced [66].

Fig. 7 shows 2D representation of the MEC reluctance elements distribution of the fractional horsepower induction motor.

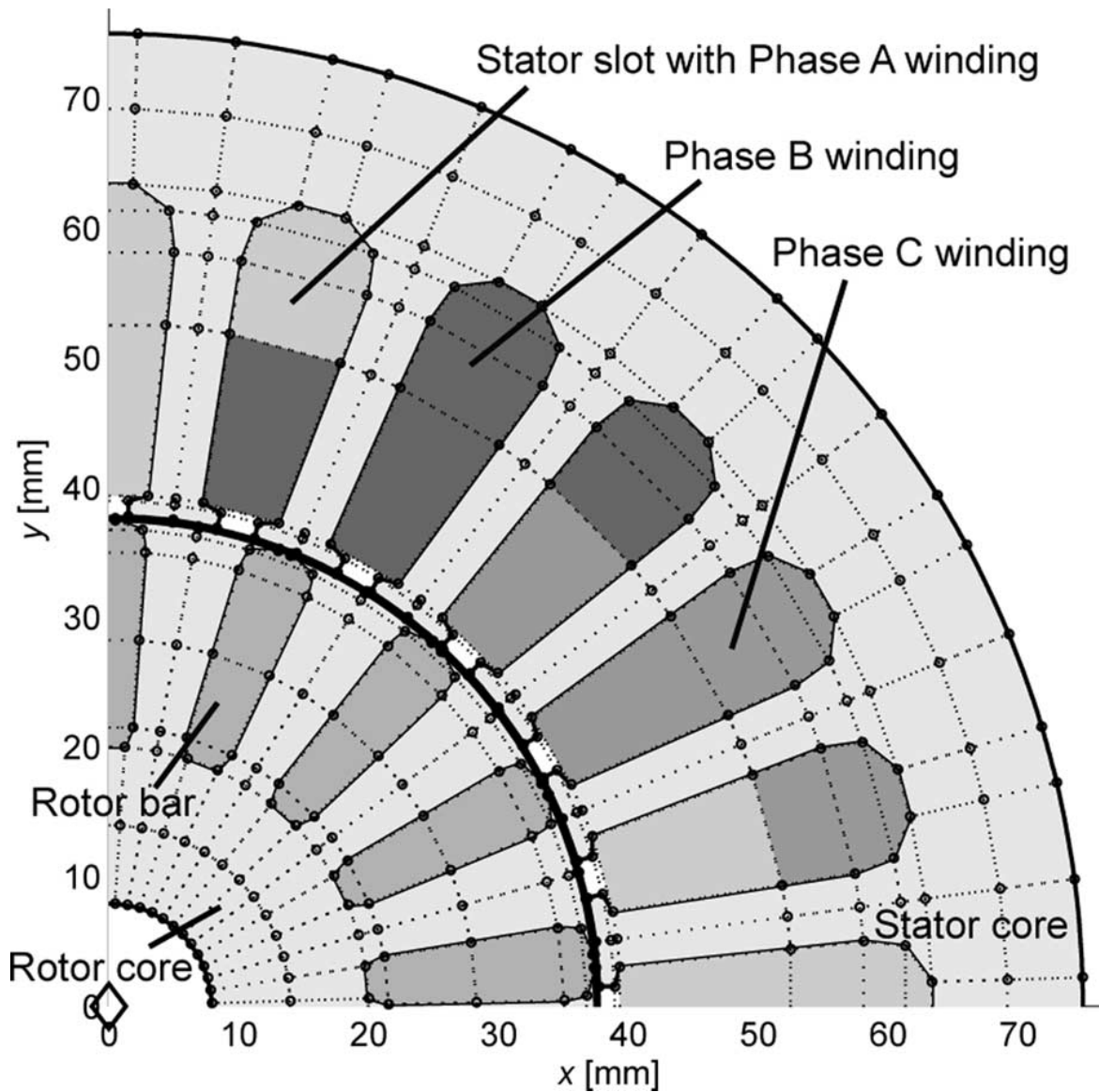


Figure 7: Induction motor MEC reluctance elements subdivision into 1302 such elements. Taken from [73]

Dashed lines in the above figure indicate boundaries of adjacent reluctance elements in the machine steel parts with the solid lines representing the element and air gap boundaries. It is understood that each reluctance element contains single magnetic flux tube of Fig. 5. The induction machine was reported to have excessive magnetic saturation of stator and rotor poles under normal operating conditions; the design flaw not captured by standard FEM analysis, and as such presented modelling challenge to the reluctance element based MEC method.

With the level of geometry subdivision, as shown in Fig. 7, the induction machine steady-state torque results were obtained [73] and are compared with the alternative analytical and numerical methods as shown in Fig. 8.

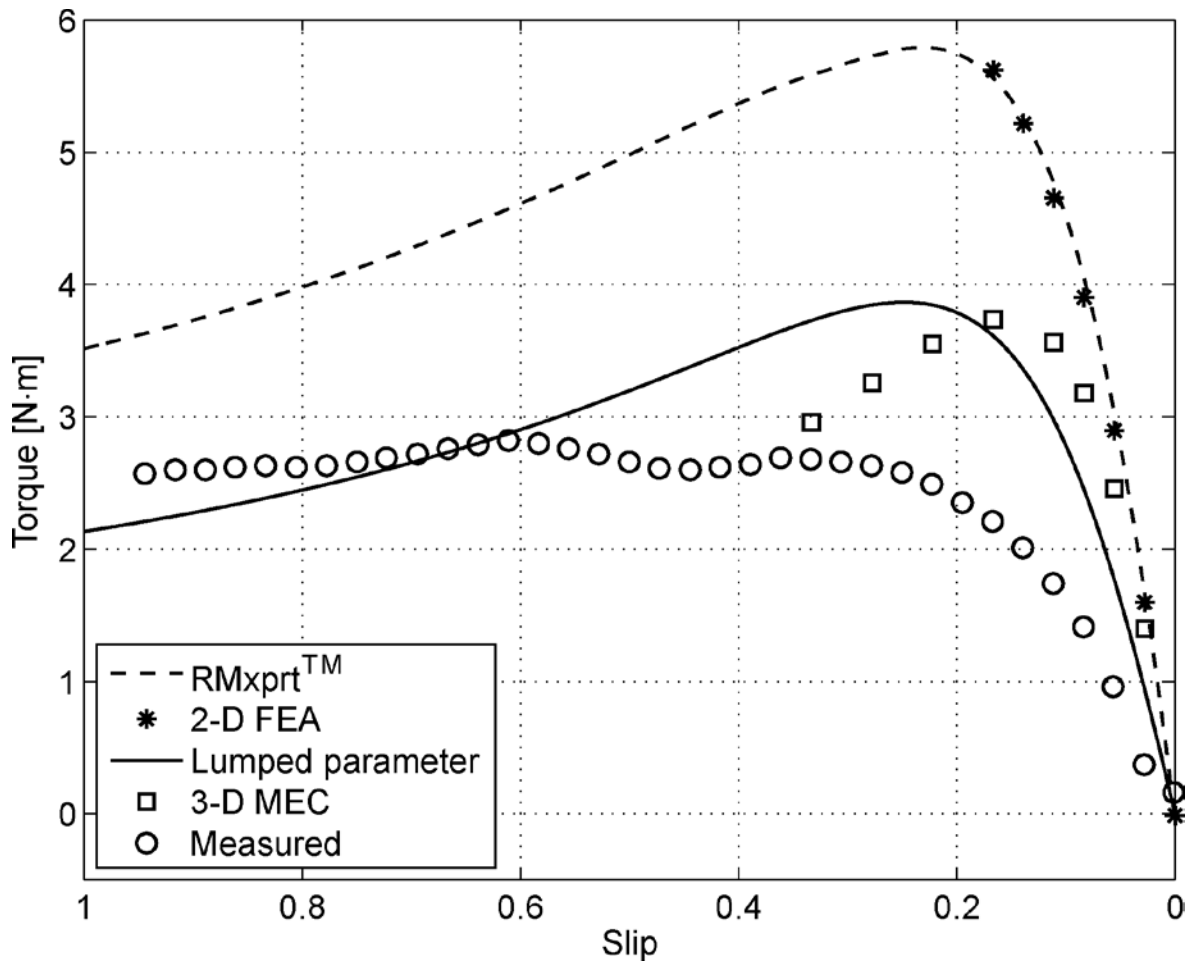


Figure 8: Comparison of the machine performance results obtained with reluctance MEC method and with alternative analytical and numerical methods to the measured values. Taken from [73]

Fig. 8 shows that the measured values of the steady-state torque of the induction machine are indeed affected by the above mentioned design flaw and that even 3D FEM modelling (dashed line in Fig. 8) was not able to capture the machine performance accurately. The 3D MEC model torque values at the low slip region (0.4 to 0.2) were closer in agreement to the measured and lumped parameter model results (for example for a description of this method see [81]). Reference [73] attributes the discrepancy of the MEC model and lumped parameter model results to the skin effect in rotor bars of the induction machine in Fig. 7 which was not modelled in the MEC model but was included in the lumped parameter model.

From the preceding discussion it can be concluded that the MEC modelling approach has certain advantages over FEM or lumped parameter based methods. For example the MEC modelling has lower computational effort compared to FEM and is easily extendable to 3D geometries. The accuracy of the MEC method can

be improved with finer subdivision of the modelled device. Furthermore motion effects can be captured by the reluctance MEC model and forces or torques found by Maxwell Stress Tensor – quantities which are most important in complete characterisation of electromechanical devices which produce useful work.

However, in general, the reluctance MEC method discussed so far cannot predict localised saturation effects, as would be expected in SR machine operation, unless the region under consideration is subdivided into large number of the reluctance elements. Fine geometric subdivisions are possible, however if these occur in intricate geometry of electromagnetic device this will necessitate irregular hexahedron reluctance elements with the necessity of transformation of the hexahedron planes back into parallelepiped reluctance elements for accurate magnetic field intensity values. As reported in [73] it is not yet clear if large number of subdivisions of the reluctance elements will increase the overall simulation time unacceptably and this is the subject of further research.

Finally, it is possible to work with much improved field-circuit formulation [82], where electromagnetic field effects are taken into account simultaneously with the MEC circuit. Such formulations require more advanced theory and are thus beyond the reduced order computational methods and the computing effort is higher. Nevertheless, these extended MEC and field-circuit methods form continuity between the reduced order computational methods and other more sophisticated methods for the modelling of electric machines.

2.3 The Method of Assumed Flux Tubes

Detailed flux tube modelling of magnetically saturable parts of electromechanical devices was investigated in [7] for rectilinear propulsion of levitation and guidance systems. Single sided LSRM topology was analysed with single stator (active) and single translator part as shown in Fig. 9.

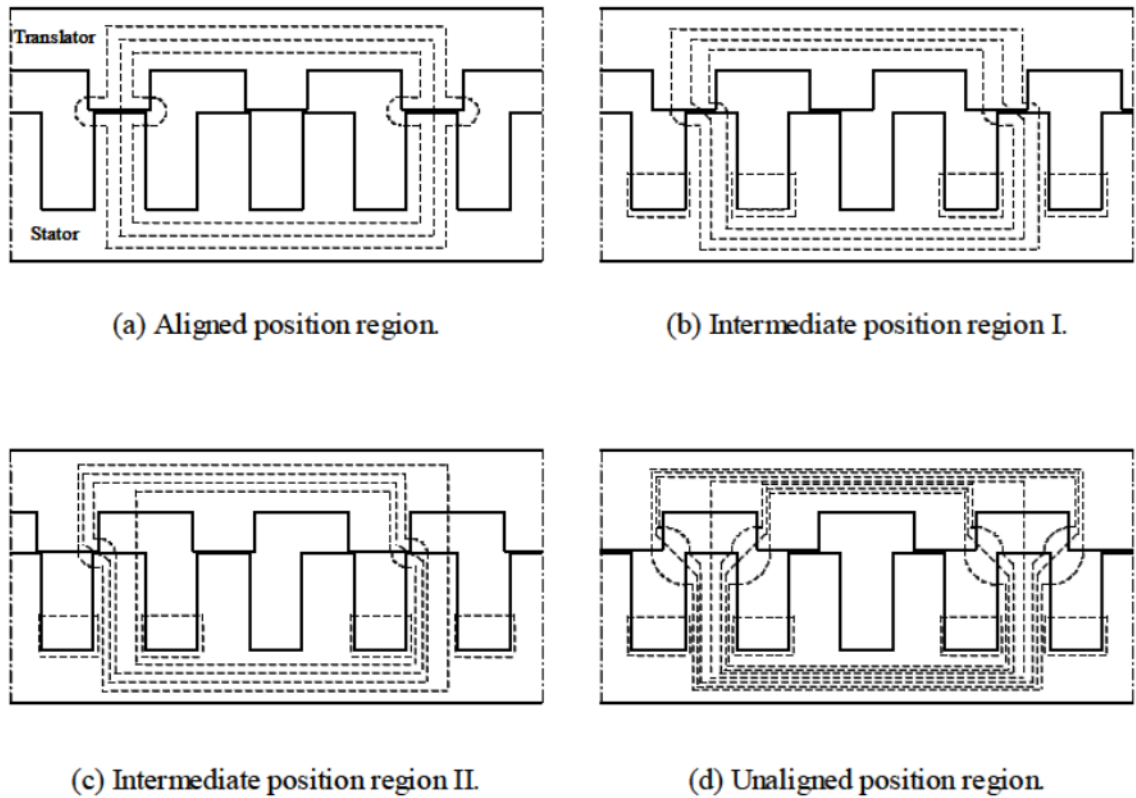


Figure 9: Single sided LSRM for propulsion of levitation and guidance systems.

Taken from [7]

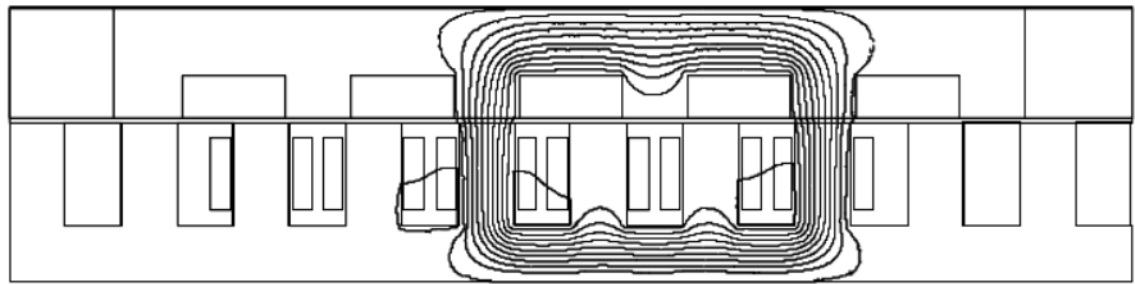
As can be seen in Fig. 9 the SR machine magnetic flux analysis is split into discrete positions of the translator with respect to the stator from the fully aligned position (also referred to as the conjunction position) to the fully unaligned position as magnetic field distributions in all of these positions are quite distinct. It should be understood that the number of translator position instances is infinite in practice, however a reasonably accurate extrapolation between the finite number of the chosen points can be made once the chosen translator positions are analysed using the assumed flux tubes method.

Due to simple geometric and spatial (i.e. 2D planar) arrangement of the machine shown in Fig. 9 the magnetic flux lines in the ferromagnetic steel parts of the SR machine can be accurately analysed using straight line representations of flux tubes of the true flux paths (neglecting corner radius of the flux tubes between vertical and horizontal lines in Fig. 9). Since the linear SR machine arrangement contains well-proportioned magnetic steel sections of constant cross-sectional area the analysis can be less complex compared to rotary SR machines that are of more intricate geometry. Therefore by finding lengths and mean cross-sectional areas of the modelled flux tubes it is possible to analyse the SR machine

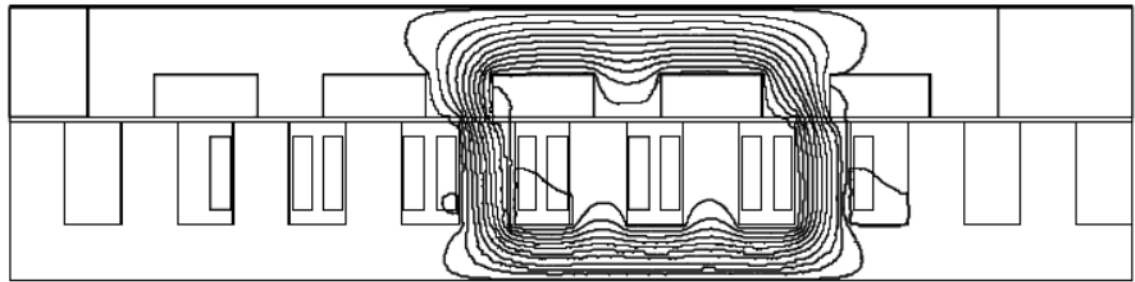
Chapter 2

performance with reasonable accuracy including onset of uniform saturation of saturable sections of the machine.

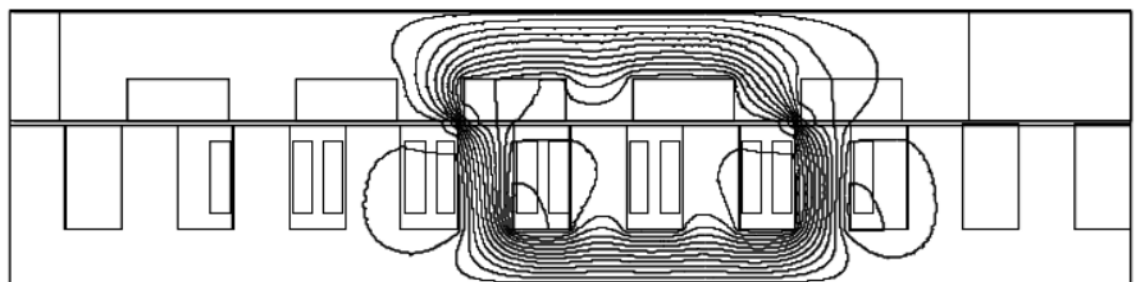
The method of assumed flux tubes was demonstrated in [7] by splitting the stator and translator parts of the SR machine, the poles and back iron sections, into simple rectangular shapes. It was assumed that there is a fixed number of flux lines, seven reported in [7], for each instant of the translator position with respect to the stator position and allowance for the constant leakage flux for all but the fully aligned translator position is assumed as in Fig. 9. The SR machine part dimensions are then used to derive expressions of the geometric quantities of the modelled flux paths and, if known, numerical values are substituted to find the reluctance values. With this approach the parameterisation of the SR machine dimensions with respect to the number of conductor turns and phase count of the machine can be made and extensive sweep of parameters performed. This has an advantage of rapid computations with non-linear saturation effects, albeit of simple geometric shapes, of the SR machine. The FEM based magnetic flux distribution of Fig. 10 can be compared with the assumed flux tube distributions in Fig. 9.



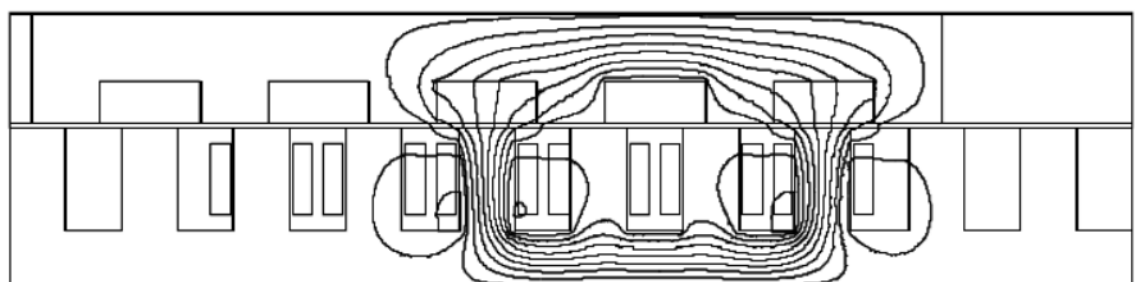
(a) Fully aligned position.



(b) Intermediate position I: 20 mm shifting of translator from fully unaligned position.



(c) Intermediate position II: 10 mm shifting of translator from fully unaligned position.



(d) Fully unaligned position.

Figure 10: FEM based solution of the magnetic flux distributions in the LSRM circuit. Taken from [7]

Inspection of the flux distributions of the two figures reveals that the FEM based flux distribution is much more complex, especially for the unaligned cases of the translator position, and that the most accurate representations of the assumed

Chapter 2

flux paths in Fig. 9 are only approximately close to the flux path distributions in Fig. 10. It should be recognised that Fig. 9 and Fig. 10 represent flux path distributions for a single valued excitation current and that these distributions are certain to change with variation of the exciting phase current and the level of magnetic saturation. Therefore the parameterisation of the flux-linkage values with respect to the current will be only approximate. However, by making use of Roters assumed probable flux path definition [72], as discussed in section 2.1 this method of analysis will yield consistent and accurate results.

Once the flux tubes are quantified the reluctances of the individual parts of the SR machine can be computed and overall magnetic circuit reluctances found by application of series and parallel network rules. Next, the resulting flux-linkage map can be found with respect to the phase excitation current taking translator position as a parameter. In general each of the flux-linkage functions, for the range of currents, is defined as [63]

$$\psi = \frac{N^2 \cdot I}{R}. \quad (11)$$

where N is the number of conductor turns, I is the phase current and R is the total circuit reluctance. Having determined the 3D flux-linkage map of the SR machine in question normal and tractive force component values can be found. Normal force component values were obtained and reported in [7] using 2D FEM and the assumed flux tube method and both compared to measurements of prototype machine as shown in Fig. 11 and Fig. 12.

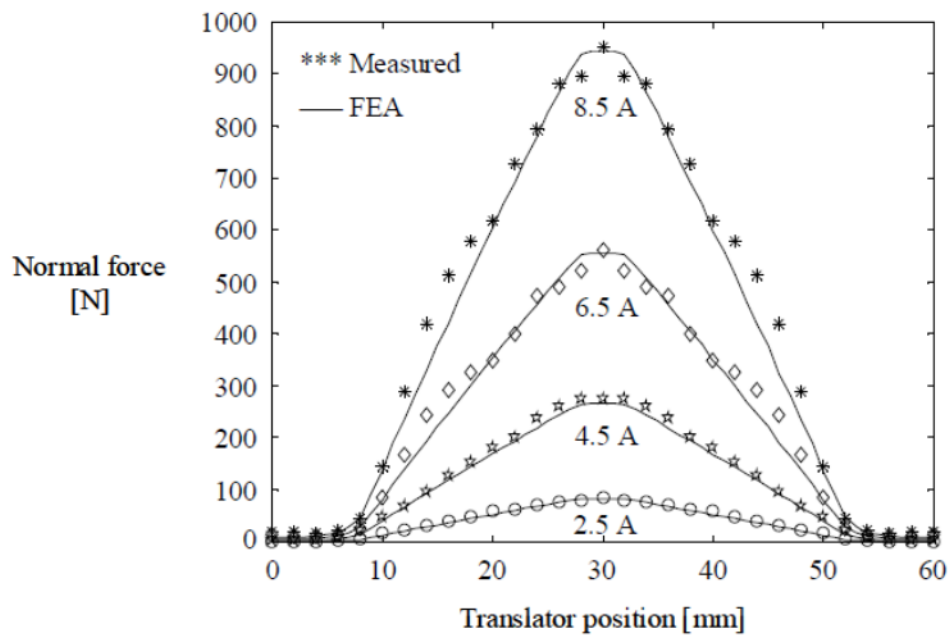


Figure 11: Normal force component of the LSRM as obtained with 2D FEM and laboratory measurements. Taken from [7]

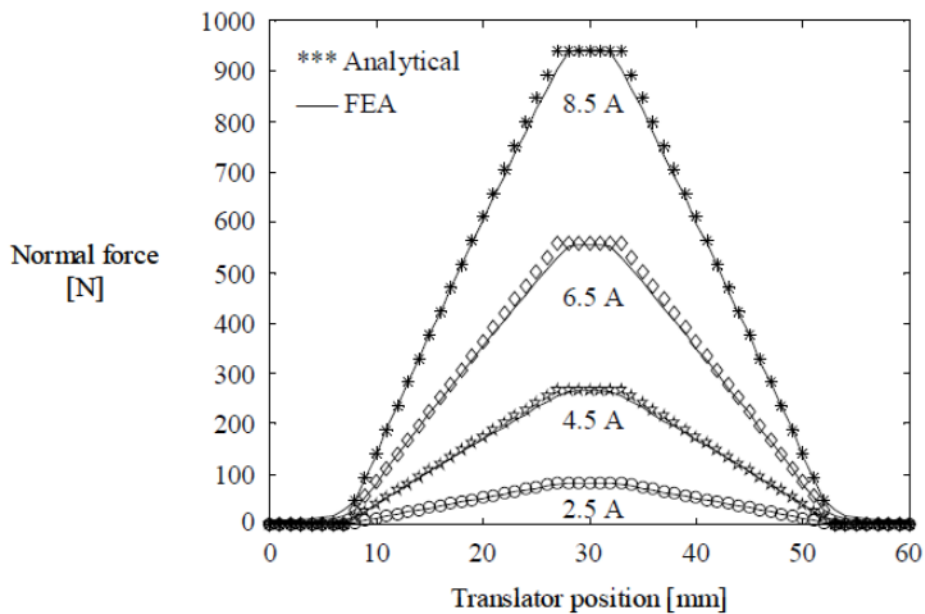


Figure 12: Normal force component of the LSRM as obtained with 2D FEM and 2D flux tube analysis. Taken from [7]

Fig. 11 indicates that the measured values of normal force acting in the LSRM tend to be affected by the saturation and leakage flux at the higher phase excitation currents and therefore do not follow linear slope of the force with respect to translator position as is predicted by the FEM analysis. Fig. 12 indicates that 2D FEM and flux tube method results are in very close agreement for the

whole range of phase excitation currents and translator positions thereby validating the 2D flux tube based modelling approach in this particular case. In order for the 2D flux tubes based modelling to mimic the saturation effects more closely, as shown by the measurements in Fig. 11, localised saturation effects of the SR machine sections should be taken into consideration. Localised saturation of pole tips of SR machines is an important factor in accurate prediction of force or torque production of these machines and must be modelled accurately as discussed in [78] and [83]. Finally the propulsion forces arrived at by the 2D flux tubes modelling, that are equally important for the linear SR machine characterisation, were not reported in [7] although 2D FEM and measured values were compared and were found to be in close agreement for practical purposes. Of course the tractive force component values can be indirectly calculated once the normal force component values are available.

Recognising the advantages of the discussed flux tube modelling of linear SR machines Krishnan [63] applied the same method to rotating SR machines for accurate determination of 3D flux-linkage maps and instantaneous torque values from these maps. The assumed flux tubes were modelled by combination of straight line and circular arc segments as shown in Fig. 13.

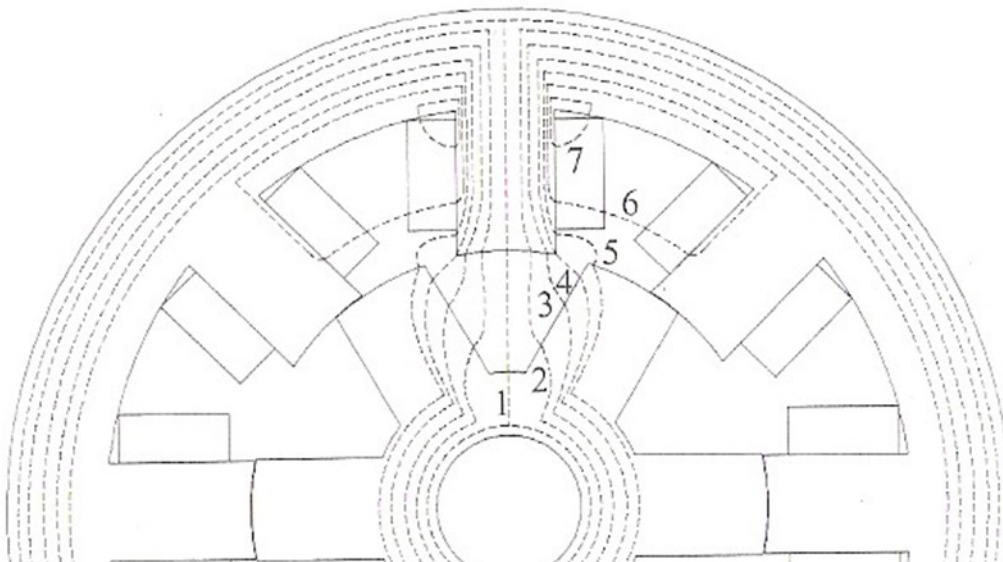


Figure 13: Four phase radial flux SR machine with the assumed flux path distribution. Taken from [83]

The 2D flux tubes analysis of the radial flux SR machines requires an order of magnitude larger number of geometrically based variables for the accurate representation of the assumed flux paths in the air region as well as in the

ferromagnetic steel sections of the device compared to the flux tube analysis of the LSRM as reported in [7]. This demands considerable experience and judgment to be exercised when deciding which SR machine dimensions (in Cartesian and Cylindrical coordinates) should be chosen in order fully to describe the flux paths. For example it is not a straightforward matter to deduce which major machine dimensions should be used to express in mathematical form the arc of flux path 5, Fig. 13, occurring in the air gap region between unaligned stator and rotor poles. General FEM based analyses are helpful in such situations in deducing the flux path distributions, however once the geometric scaling of the design is performed with, at the same time, varying excitation currents the true flux path distributions are likely to depart from the fixed assumed flux path distributions. This in turn impacts on the accuracy of the assumed flux tube method and introduces numerical uncertainty in the final results of the analysis. The main advantage of the assumed flux paths modelling is that once the task of expressing the flux paths in a mathematical form is accomplished the design and optimization of the device can be performed with considerable computational efficiency and speed and intuitive cause-and-effect analysis [63]. Furthermore, the relationship between the number of phases and conductor turns per phase, operating voltage, angular speed and instantaneous torque becomes explicit when the assumed flux paths are defined in geometric form analytically.

The flux tubes based results reported in [63] for two distinct radial SR machine design studies were encouraging and indicate close correlation with FEM based studies of the same devices as well as laboratory measurements of the prototype SR machines. For example the average electromagnetic torque values of the analysed three phase radial flux SR machine were reported to be within 10% of the measured values. The aligned and unaligned rotor position inductance results of the analysed four phase machine were also consistent with FEM and were reported to be within 5% accuracy. It should be noted that these results were obtained with 2D analyses in the FEM and the assumed flux paths cases and did not take into account the end effects of the SR machine windings – effects that become dominant as the radial machine stack length becomes shorter compared to the machine diameter.

2.4 The Tubes and Slices Approach

The tubes-and-slices technique, similarly to the above approaches, falls into the spectrum of electromagnetic analysis techniques which could be described as

reduced order computational techniques. As described in detail in [76] and [84], by using most elegant mathematical descriptions, the accuracy of the lower and upper bounds method (later termed tubes and slices, or TAS, method in [76]) can be increased by use of Lagrangian multipliers to optimize the placement of the tubes and the slices thus reducing the dual bounds numerical error. To keep the description of the TAS formulation simple the mathematics is left out, but interested reader can refer to [84] and [85] for examples.

Since the TAS method is primarily directed to practical systems of engineering importance the following example will be used to describe the physical principles that make the TAS approach so intuitive. Considering the trapezoidal plate as in Fig. 14 having thickness t and where the vertical edges of the plate are charged with the potentials V_1 and V_2 . In this particular example the potentials are assumed to be those due to the applied voltage.

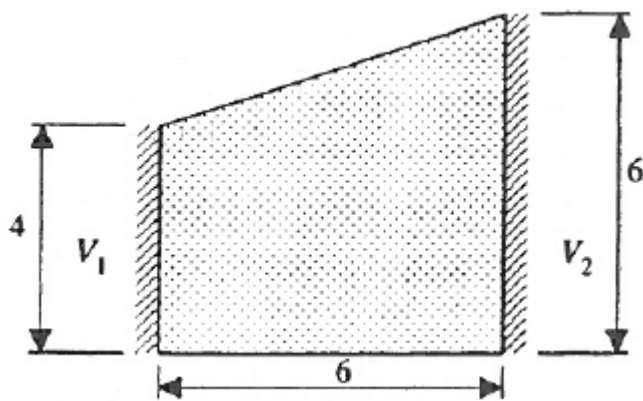


Figure 14: Example TAS electric current flow and resistance computations. Taken from [84]

Since the plate is of non-uniform cross section along its length the determination of electrical resistance of the plate is difficult, if not impossible, using the classical expressions involving electrical conductivity σ and only the major dimensions of the plate.

However, we can attempt the problem of finding the effective resistance of the trapezoidal plate by using, as a starting point, the geometric subdivisions of the plate as in Fig. 15, termed subdivision into slices that are nothing more than subdivisions parallel to the equipotentials.

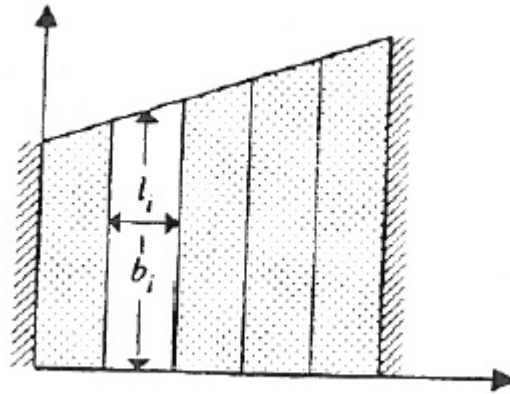


Figure 15: Subdivision of the trapezoidal plate into slices. Taken from [84]

The subdivision of the plate into slices in Fig. 15 is fairly coarse however the determination of the effective resistance of each of the slice is now a much easier task since we have the approximation of the rectangle instead of the entire trapezoid. Therefore, the effective resistance of each of the slices is approximately equal to $R \approx b/\sigma l$. An alternative and more physical interpretation of the subdivision into slices in Fig. 15 can be put forward as follows. Let us assume that we know the resistance of each of the slices in Fig. 15 individually and it is known that the total resistance of the trapezoidal plate will be the individual resistances added in series. However since the boundary conditions of the slices are not exactly correct at the upper and lower sides along the length of the trapezoidal plate this will introduce some error in the final values of the total resistance. It also effectively means that if we join the slices in series as to form the original trapezoidal plate as in Fig. 14 will necessitate the inclusion of infinitesimally thick sheets of infinitely conducting material. However, since in practise it is not possible to introduce the infinitely conducting sheets into the trapezoidal plate perfectly, this will tend to produce lower resistance of the plate. Hence the total resistance of the slices in series will be lower than the true resistance of the trapezoidal plate. We leave the discussion of the slices to consider the subdivision into tubes.

Considering the same plate in Fig. 16 where instead of the subdivision into slices we have now subdivided it into tubes of possible, yet not exact, electric current flow. This is only an approximation since the current must leave the plate at a right angle to the vertical line V2 as in Fig. 14 and Fig. 16. Nevertheless, if the subdivision into tubes is fairly extensive the assumption of the condition of perpendicularity of the current flow along the equipotential slices can be justified.

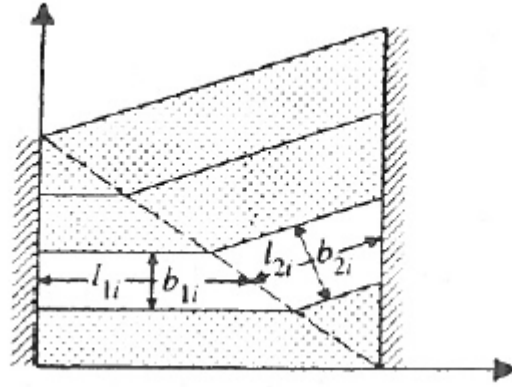


Figure 16: Subdivision of the trapezoidal plate into tubes. Taken from [84]

As before, since the conductivity σ is known the approximate resistance of each of the tubes can be estimated to be equal to $R \approx l/\sigma bt$. However, in this case of subdivision the total resistance of the trapezoidal plate will be that of the individual tube resistances arranged in parallel if we are to end up with the shape of the plate as in Fig. 14. By joining the tubes in parallel we will inevitably introduce some error, but to preserve the electric current flow in each of the tubes in proportion to the total current in the plate it is necessary to insulate the tubes from each other using imaginary sheets of infinitesimally thin yet infinitely resistive material. Nevertheless, since the subdivision into tubes can never be perfect this parallel combination of resistances will introduce some error. Therefore the placement of the infinitesimally thin sheets of infinitely resistive material between the tubes will increase the equivalent resistance of the trapezoidal plate which effectively means a higher equivalent resistance compared to the true resistance of the plate.

From the ensuing non-mathematical description of the TAS approach it is apparent that by performing the geometrically simple subdivisions into tubes and slices it is possible to obtain upper and lower bounds of the electrical quantities of interest; be it resistance, inductance or capacitance in the linear media [76]. In the case of the trapezoidal plate the average equivalent resistance of the plate is therefore equal to $R \approx (b^2 + l^2)/2\sigma btl$. The TAS method therefore avoids the solutions of the field equations based on Laplace's or Poisson's equations which, though give the exact answer, require extensive mathematical operations even for the simple geometric shapes as in Fig. 14. The dual bounds answer afforded with the TAS approach can be averaged, since it is normally a single value that is needed in the engineering analysis. Similarly, the dual bounds techniques directly

comparable to the TAS approach were also observed to yield useful results in the thermal equivalent circuit analysis as discussed in [86].

As stated in [84] however, the true answer is much more difficult to determine and the TAS formulation might not be capable of achieving this. However, reconsidering the advantages of intuitive derivations based on direct physical quantities and least effort to perform the computations merit TAS method for the effective solution of wide range of electric and magnetic field problems.

Although the nonlinear magnetic field analysis was not attempted to date using the above described dual bounds method, the TAS formulation has all the capabilities to perform such calculations provided that the nonlinearly varying quantities, such as the magnetic reluctance, are properly accounted for in the computations of the dual bounds.

2.5 Analytical Air Gap Field Solutions

From the preceding literature review it is imperative to ask if it is at all possible to obtain an exact analytical model which is relatively simple to apply, yet is not lacking in generality, for the magnetic field analysis of gaped electromagnetic devices. Specifically, analytical model which would be capable of the following: handling complex geometric shapes of the electromagnetic device, accounting for leakage flux resulting from interactions of various components of the electromagnetic device and accurate determination of the overall reluctance of an air gap. An attempt to construct such a model for the electromagnetic analysis of SR machines was made by Radun [87]. The method is based on the analytical series solution of the Laplace's and the Poisson's partial differential equations in 2D. The analytical model therefore requires sound knowledge of the correct application techniques of these equations to the intricate SR machine geometries.

In [87] the analytical method is applied to 2D radial flux SR machines. However, to make the radial SR motor geometry amenable to the analytical reluctance calculation it is first necessary to subdivide the air gap region into distinct sub regions and subsequently transform these sub regions from the Polar-coordinate system to the Cartesian-coordinate system, as shown in Fig. 17.

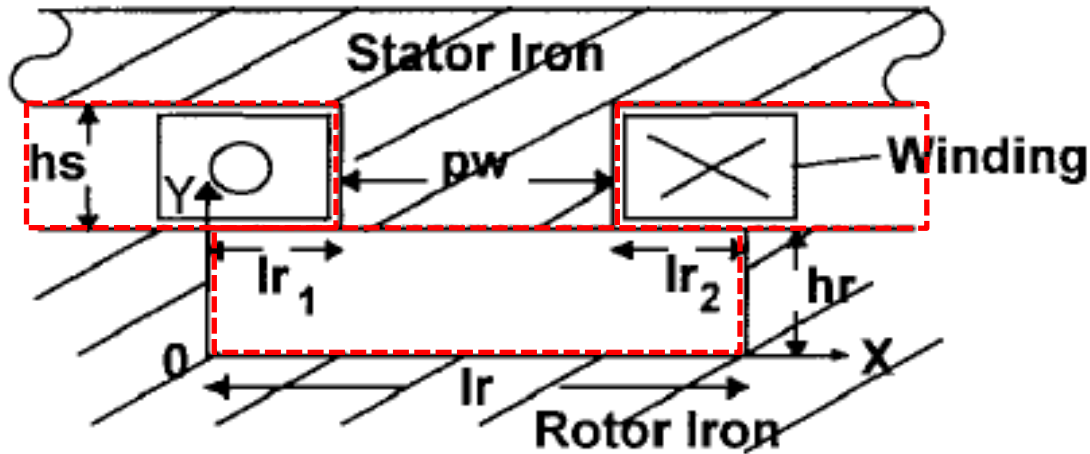


Figure 17: Transformed radial SR machine geometry and the air gap subdivision into distinct regions shown in red. Adapted from [87]

The analysis further assumes that the iron permeability is infinite in order to simplify boundary conditions of the air regions and to simplify Laplace's and Poisson's equations. As stated in [87] the assumption of infinite permeability of the iron can be valid provided that the stator and rotor poles of the machine do not overlap. Thus the analytical method is capable of modelling rotor pole position anywhere between the completely unaligned and the onset of overlap of the poles.

From the solved example given in [87] it is clear that the most critical part of the analysis is the ability to identify and apply correct boundary conditions to the subdivided air gap regions as these boundary conditions will not be identical everywhere and will strongly depend on the relative position of the machine components and their geometries. Once the correct boundary conditions are applied the solution of the partial differential equations can be obtained with a small number of series terms to arrive at a reasonably accurate air gap field solution. Fig. 18 shows the constant magnetic flux line plots comparison of the analytical and FEM method.

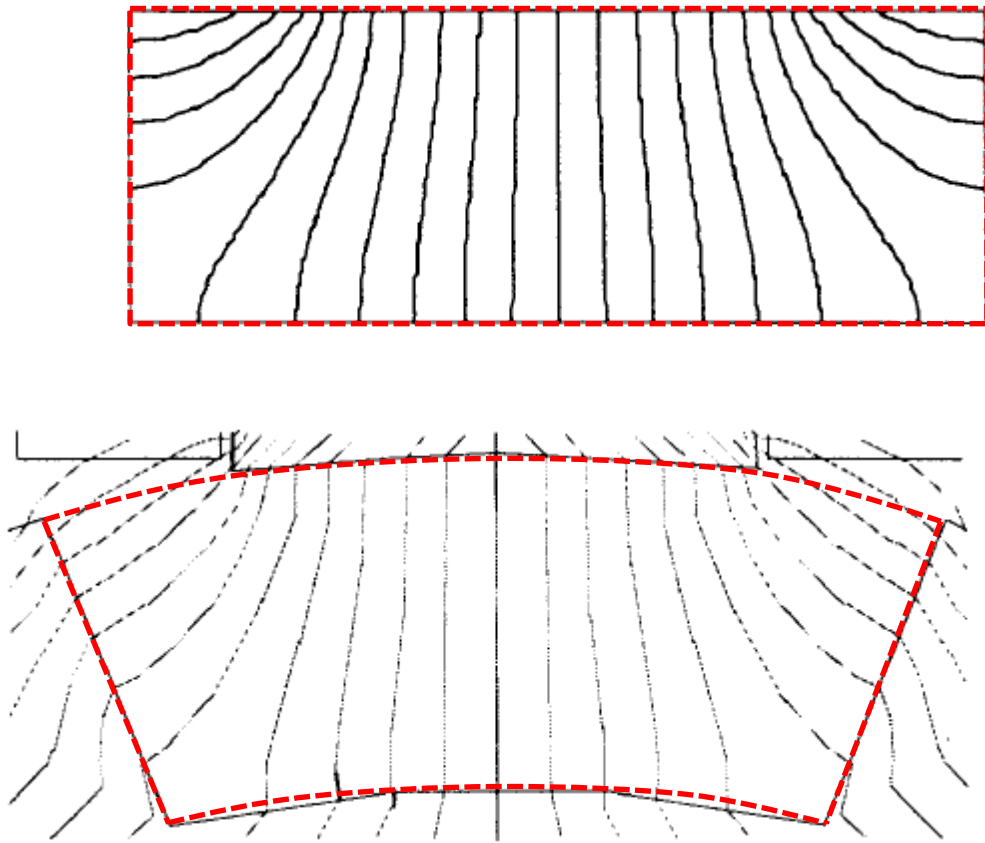


Figure 18: Analytical (upper) and FEM (lower) field solutions of the rotor air gap.
Adapted from [87]

The pictorial similarity of the two alternative magnetic field solutions in Fig. 18 is satisfactory and encouraging. In a similar way the rest of the subdivided air gap regions of Fig. 17 are compared in Fig. 19.

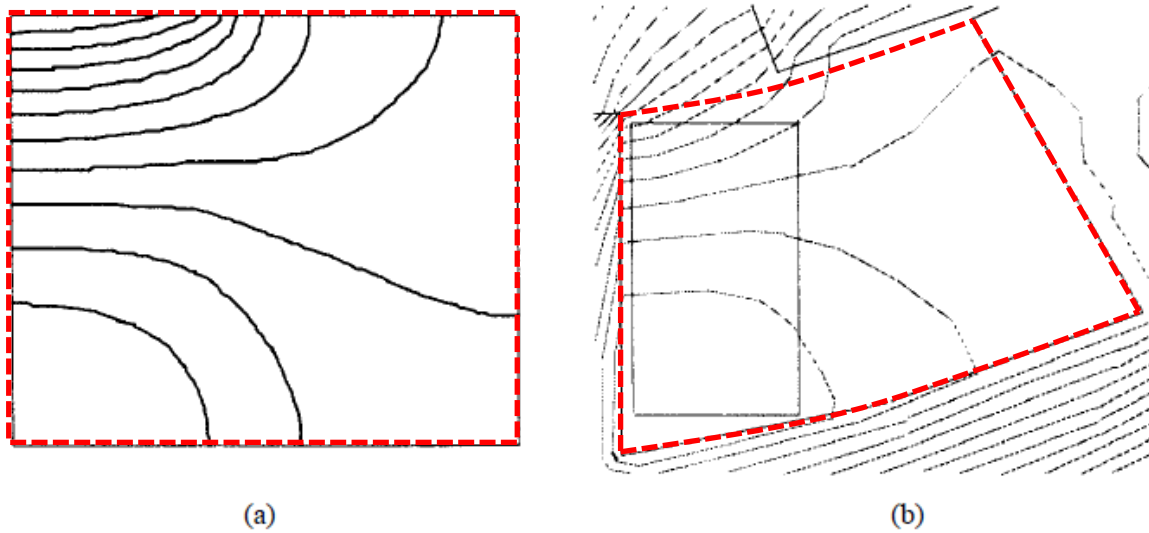


Figure 19: Air gap field solutions of the stator slot region, outlined in red, using (a) analytical method and (b) FEM. Adapted from [87]

As was demonstrated in the previous figures, Fig. 19 shows that the two alternative solutions produce similar results of the air gap field distributions. The absolute error of the analytical method, compared against FEM solution, is summarised in Table 1.

Table 1: Analytical inductance solution error compared with FEM solution for three distinct machine frame sizes. Taken from [87]

SRM	FE uH	Analytical uH	error %	Rotor OD inches
6/4	57.36	63.91	11.42	3.25
12/8	21.48	24.36	13.41	6.25
18/12	21.46	23.81	10.95	5.82

Table 1 indicates that for a range of machine sizes the analytical method error does not exceed 14% which compared to all the previously review air gap reluctance calculations is the most accurate.

The advantages of the analytical method are threefold. First, the method gives numerical answer of the air gap inductance values for a range of excitation currents as in Table 1. Therefore a check can be made on numerical values against alternative analysis techniques such as FEM or any other thus far discussed method. Second, the equations obtained for each of the subdivided air gap regions can be used to plot the magnetic field solutions in these regions as the 2D plots seen in Fig. 18 and Fig. 19. This is very useful when checking the

validity of the derived air gap solutions and when comparing the obtained flux distributions with alternative approximate field solution methods or FEM. Thirdly, once the solution equations are derived, for a particular machine geometry, it is advantageous to separate and find the individual inductance contributions of all the individual air gap regions as was demonstrated in [87], shown in Table 2, for the corresponding three SR machine geometries of Table 1.

Table 2: Analytical inductance contributions of the rotor and stator parts of the machine compared to FEM solution. Taken from [87]

SRM	Rotor			Stator		
	FE	Analytical	error	FE	Analytical	error
	μH	μH	%	μH	μH	%
6/4	45.51	51.61	13.40	11.85	14.40	21.54
12/8	16.79	18.12	7.94	4.69	6.24	32.96
18/12	15.20	16.05	5.26	6.26	7.76	23.96

The information in Table 2 is very useful as it enables analytical insights to be gained as to the magnitude of inductances contributed by each air gap sub region. Knowing the relative difference of these inductance values can help to design low inductance machine which is advantageous in high speed applications as will be seen in the results section of this report. Or else an inverse problem could be attempted with this knowledge; having set the unaligned machine inductance value, in order to extend the machine speed range for example, the analytical expression parameters of each air gap region could be analytically derived and optimized to achieve the desired inductance. However, once more it is stated that the present method, although very advantageous when analysing an SR machine, demands sound knowledge of application of the Laplace's and the Poisson's equations in 2D with appropriately assigned boundary conditions that are critical to the validity and accuracy of the final results.

The final remark regarding the proposed analytical method is as follows. Since the assumption of the infinitely permeable iron of the SR machine circuit is assumed in addition to the non-overlapping poles the analytic model is capable of predicting the unaligned inductance, as demonstrated in [87], for a single valued phase excitation current. This is sufficient for most purposes as in practise it is observed most of the time that the unaligned flux linkage function of the SR machines is customarily treated as a straight line whose slope is the self-inductance of the phase. However, since the assumption of the straight line of the unaligned flux linkage function is the necessary condition of the analytical model

reviewed in this section it then follows that machines which exhibit narrow unaligned air gap region are unlikely to be modelled accurately since the phase excitation current can be substantial for the given air gap which will produce considerable saturation and therefore the nonlinearity. Of course it could be argued that in practise there is little chance of having such design in the first instance, yet the analytical model would be much more versatile if the range of phase current values could be used to check for such onset of saturation. As it appears the author did not consider this aspect of modelling in his work in [87].

2.6 Chapter Summary

The literature review chapter can be summarised as follows.

Most of the selected and presently reviewed electromagnetic analysis methods fall under the definition of the reduced order computational method since the computational accuracy is partly forfeited for the speed of solution of the electromagnetic model. Such compromise between the speed and accuracy of solution can be seen as an advantage when the electromagnetic model to be solved, even in the reduced form, can nonetheless capture the governing physical phenomena of the system sufficiently accurately. The speed of solution brings further advantage in the extensive design optimization task of the system under the consideration. Therefore there is the need to bring together as completely as possible the above reviewed advantages of the reduced order computational methods so as to enable most efficient, yet sufficiently accurate computations of quite complex electromagnetic circuits and systems. By achieving this goal the novel topologies of SR machine technology can be discovered which can lead to highly disruptive innovations in most critical industrial environments of the present times such as effective electrification of the transportation sector.

In the proceeding chapter an attempt is made to combine together the advantages of the above discussed computational methods since it appears that there is a substantial scope for improvements of the above discussed methods in order to benefit as much as possible from their modelling flexibility, efficient computational performance and physical fidelity and physical intuition while completely eliminating or effectively controlling their disadvantages.

Chapter 3 Proposed Modelling of the Flux Tubes and Slices Utilising Cubic-Splines

From the preceding literature review regarding the magnetic field modelling of electromagnetic devices it is evident that all the methods are based on the construct of a magnetic flux tube, Fig. 5, as a most basic concept of these methodologies. The flux tube concept will contain all the necessary variables such as material properties and geometry of the respective flux path to quantify magnetic flux value as well as magnetic field density for a given mmf . It is then a matter of judgment and experience to assume a probable flux path which will be a reasonably accurate representation of flux path occurring in the analysed part of an actual electromagnetic device. It is also necessary to make a judgement as to the number of subdivisions of each of the modelled flux paths along their cord lengths so as to arrive at reasonably close estimates of magnetic field densities in the intricate geometries of electromechanical devices being analysed. It is possible to achieve accurate magnetic flux and magnetic field density values in the intricate geometries of electromechanical devices by use of FEM techniques. Yet, the FEM will not reveal explicitly cause-and-effect relationships resulting from the numeric variation of numerous design variables and therefore will not aid alone in the effective design and optimization of the device as is envisaged in Fig 1.

A new flux tubes modelling method proposed in this report adopts some of the modelling techniques covered thus far (i.e. [63], [72], [74], [75]) and extends them in such a way that the ambiguity of definition of the modelled flux paths (the terms “assumed” and “probable” in the context of flux paths modelling are still used) is reduced with the use of cubic-spline interpolation techniques. The new method could be termed the improved flux tubes and slices model to reflect the improvements and extensions made based on the previous flux tube based methods. In this particular case a commercial scientific scripting language was used, Matlab, but many others, including the open source package Octave [88], can also be used with no deterioration of the performance or the functionality to the flux tubes and slices method.

3.1 Translating (Linear) SR Machine Flux Paths Modelling Using Cubic-Splines

3.1.1 Unaligned Translator Position Modelling

The first machine to be investigated in this report is of double translator LSRM of the 12-8 topology (12 stator and 8 rotor poles), section of which is shown in Fig. 20. It should be noted that the abbreviation of the linear switched reluctance machine (LSRM) does not imply the ferromagnetic linearity, but refers to the mode of the mechanical operation of the machine. The figure shows the machine components and constant magnetic flux distribution plot of the device arrived at by use of industry standard commercial FEM package [89], however the same quality results could have been obtained with open source 2D FEM packages such as *femm* [65] or more powerful 3D FEM software [90].

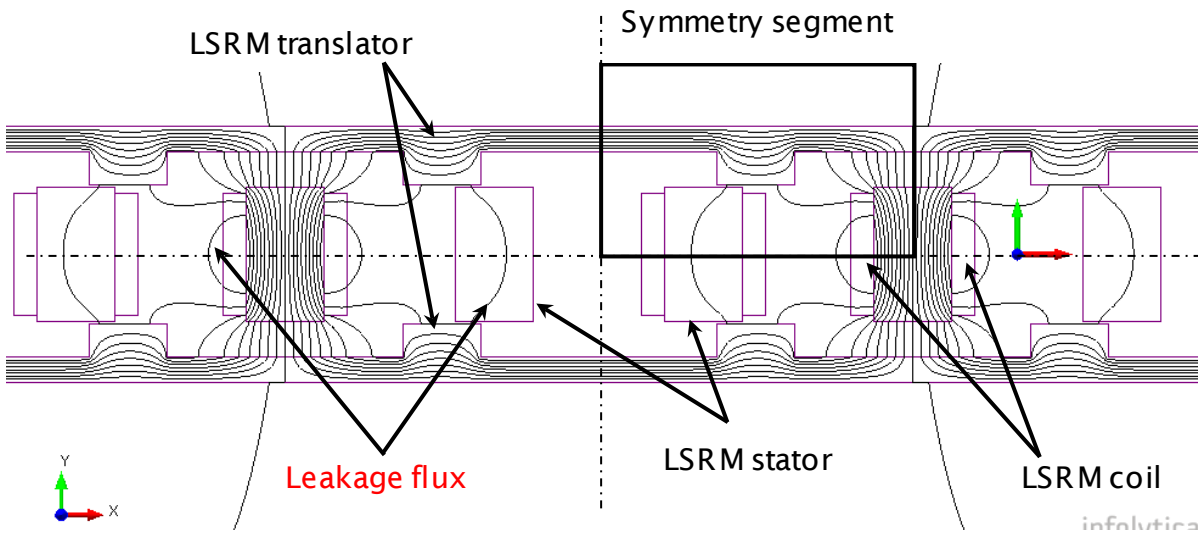


Figure 20: LSRM flux distribution obtained from 2D FEM analysis

Again, each of the flux paths occurring in the machine steel and the surrounding air regions can be modelled by a combination of straight line and circular arc segments along the cord lengths of the respective paths as in Fig. 5. Of course the exact shapes of actual flux paths can be attained by subdivision of the flux tubes into infinite number of segments and then fitting straight line approximations to these segments which in the limit will approach the true shapes of the paths. However, by revisiting the definition of the probable flux paths as defined in [72], relaxation of the condition of infinite number of segments along the flux path length can be made with only slight departure from actual performance results of the real device as will be shown in the results

section of this report. Further assumption, found in [72], is followed which states that: provided that most (i.e. 80%) of the flux tubes are modelled in the immediate vicinity of the air gap this will accurately represent large proportion of the air gap permeance. Therefore, there is no need to model the magnetic leakage flux precisely, as in Fig. 12, but only approximately.

The next step in the reasoning of how reasonably accurately to approximate the true flux paths without excessively large number of geometric variables the convenient method of fitting cubic-spline polynomials (requiring only three sets of coordinate points in 2D) presents itself as a candidate method. Therefore, to fit any one chosen segment along the length of the modelled flux path cord it is necessary and sufficient to know three coordinate points on that flux path segment. Once such coordinates are defined in 2D Cartesian coordinate system cubic-spline fitting can take place and the true flux path segment can be approximated by the cubic-spline curve pertinent to the set of coordinate points defined earlier. The only guess (educated or otherwise) to be made at this point is the selection of accurate or convenient coordinate points on each of the modelled flux paths so as to reduce the interpolation error between the coordinate points to an acceptable level. In other words, the selected flux path segment should be smooth and continuous without any abrupt changes or abrupt points of inflection the fitted cubic-splines will not be able to mimic accurately enough.

The only satisfactory method of finding the start and the end coordinate points along the cord lengths of modelled flux paths was found to be that based on equipotential lines of a magnetic field occurring in the analysed device as is extensively used in [76] and [84]. By utilization of FEM analysis, accurate magnetic field density plots can be produced to illustrate the approach, as shown in Fig. 21, containing the exact symmetry segment of the machine in Fig. 20.

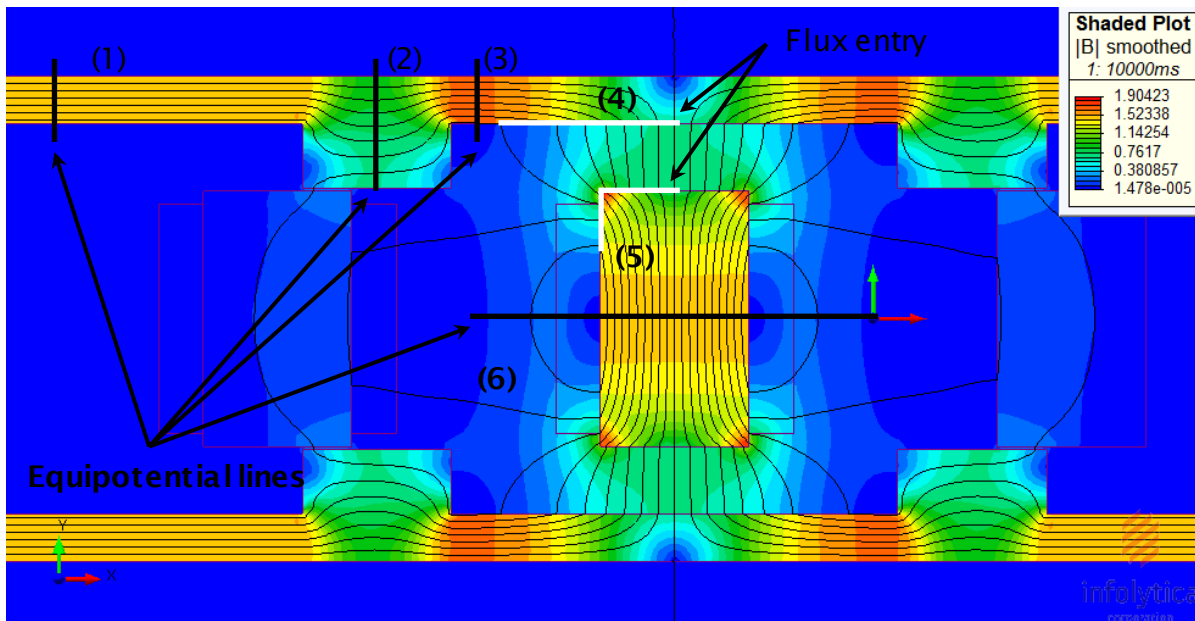


Figure 21: FEM analysis based magnetic field density plot for a symmetry segment of the LSRM

By visual inspection of Fig. 21 it is possible to locate equipotential lines on the shaded plot as indicated by the straight lines (termed “slices” in [84]) – these lines will be orthogonal to all the modelled flux paths in the respective parts of the machine. It is evident, from the above figure, that if an attempt was made to fit smooth and continuous cubic-spline segments between the aforementioned equipotential lines, given only three coordinate points between them, there would be large interpolation errors introduced due to geometric discontinuities and abrupt points of inflection that describe the true flux paths. Therefore it is necessary to subdivide the remaining flux path segments (in between the equipotential lines) still further to facilitate accurate cubic-spline interpolation. This is achieved by recognising the very important property of magnetic flux paths that was successfully used in the TAS method described in [84]: the property that each flux path normally enters magnetic material at a right angle (orthogonally) to the surface of the material. Once the magnetic flux lines are in the magnetic material they divert in such a way so as to assume least resistant paths. Such magnetic flux path entry points are indicated in Fig. 21.

Flux paths in Fig. 21 have been, thus far, subdivided into five segments as indicated by the straight lines. Any two neighbouring slices can now be used to define a pair of 2D Cartesian coordinate points (number of which will correspond to the number of flux paths being modelled) with one or more intermediate coordinate points chosen so as to minimize cubic-spline interpolation errors between all of the coordinate points. Fig. 22 illustrates an implementation of the

above described technique whereby the symmetry segment of the LSRM was subdivided into five slices.

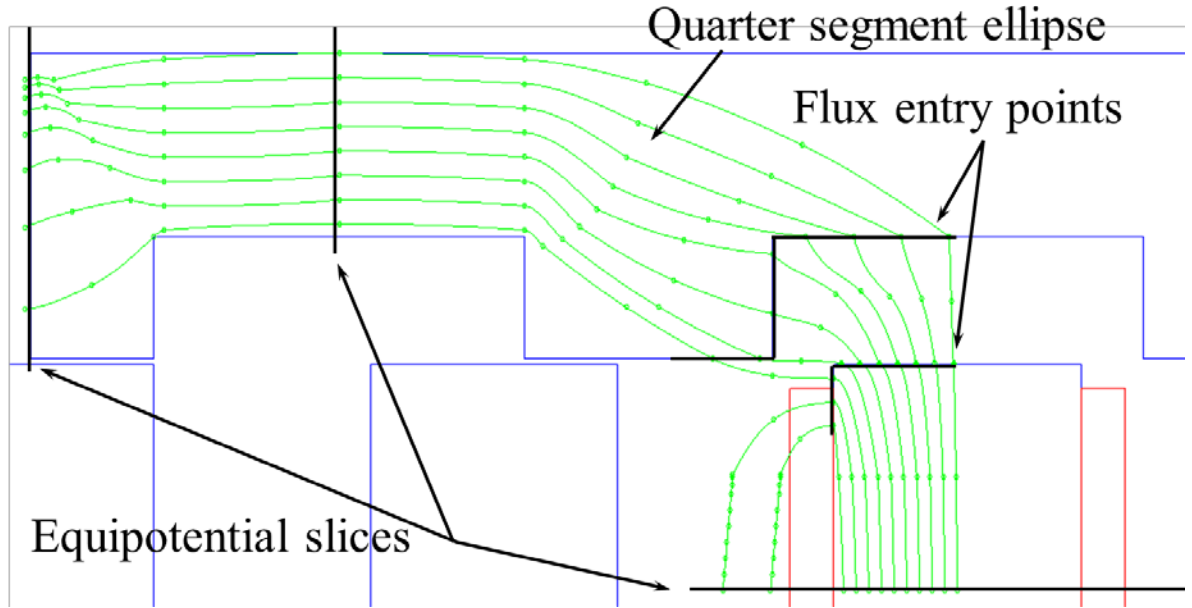


Figure 22: LSRM subdivision into five slices along the lengths of the flux paths

The above figure demonstrates that some of the flux paths can be reasonably accurately approximated by only the three coordinate points whereas others will require a minimum of four such points. Comparing Fig. 21 and Fig. 22 it can be seen that the flux tube segment between slice 2 and slice 3 cannot be accurately interpolated by only the three sets of coordinate points. Furthermore, the flux paths segment between these two slices contains equipotential magnetic field lines which are not straight lines, but combinations of straight lines as well as circular arcs. For this reason some of the equipotential slices in Fig. 22 were constructed as quarter segment ellipses in order to produce more accurate results. Of course this adds computational penalty as computation of ellipses presents mathematical challenge [91]. However, if the modelled machine geometry is novel and the magnetic equipotential lines in the magnetic circuit are of complex shape, which presents difficulty in modelling them accurately, then the straight line approximations of these equipotential lines can be used. This simplification might appear to be fairly crude, yet by revisiting the “probable flux path” formulation in [72] justification of this simplification can be made if the final results are in close agreement with more traditional magnetic field analysis techniques. This enables simplified mathematical functions of the coordinate points to be defined with only major machine dimensions.

Finally, once the cubic spline approximations to the true flux tube paths are complete, their individual reluctances (or permeances) can be found from (1) as all the geometric information in relation to the flux tubes is known from the polynomial equation coefficients, specifically; the cross-sectional areas, cord lengths and material properties. Therefore, flux-linkage functions, as given by (11), for the aligned and unaligned translator cases are readily found.

3.1.2 Refining the Unaligned Air Gap

As is emphasized in the large number of already cited publications on magnetic analysis of SR machines and those in [92] and [93] accurate determination of the total reluctance of the unaligned case air gap region is important when determining overall performance of the machine. This region is most important as it influences large proportion of unaligned case flux-linkage function value with respect to the phase excitation current. The lower this function value is, all else being equal, the higher the amount of instantaneous electromagnetic torque can be produced by the machine [92]. This value will have a direct influence on the machine rating and performance metrics of specific-power and specific-torque - these should be made as high as possible for the given machine dimensions.

In order to achieve high numerical accuracy of reluctance values of the flux paths in the air gap region for the unaligned case of SR machine it is possible to adopt the dual-bounds based estimation technique, presented in detail in [84], whereby the modelled air region flux paths are subdivided into a larger number of tubes (flux lines) and slices (equipotential lines) and abbreviated as TAS method. Such technique enables upper and lower bounds of the reluctance of the air region to be found. The upper and lower bounds are then averaged to give a single reluctance value needed for further machine design and analysis. The confidence interval, namely the upper and lower bound reluctance values, guarantees that the true reluctance value will be somewhere in between the upper and the lower limit. Fig. 23 depicts TAS technique applied to the air gap region of the analysed LSRM using the improved flux tube approach.

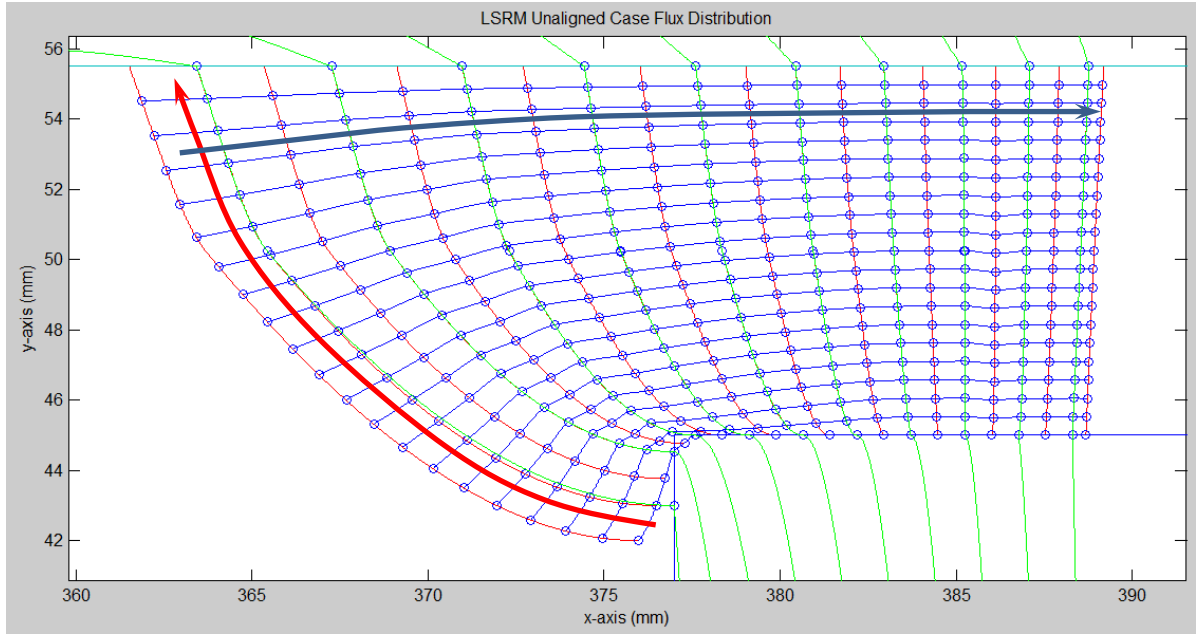


Figure 23: LSRM subdivision into tubes of flux (red arrow) and slices of equipotentials (blue arrow) of the air gap region

To get the exact upper and lower bound values of reluctance of the air gap this region must be subdivided in such a way so that the slices of equipotential lines are orthogonal to the tubes of flux they cut across. As the number of flux tubes and equipotential slices tends towards infinity the orthogonality condition can be approached. However, in practice it is not necessary to approach such a limit as the solution accuracy will converge asymptotically towards the exact values as the number of tubes and slices grows larger [84]. The TAS method was adopted in the current LSRM analysis with only a small number of such subdivisions in order to get the dual-bound estimate of the unaligned translator position flux-linkage function with respect to phase excitation current and was seen to be effective [94].

3.1.3 Aligned Translator Position Modelling

The aligned translator position is modelled in a similar manner to the unaligned translator position case and is somewhat easier to implement. The same assumptions are followed when defining the probable flux paths in the air region surrounding the LSRM as well as in the magnetic material parts of the machine. Fig. 24 shows the flux path distribution obtained from industry standard FEM analysis [34]. Magnetic leakage flux surrounding the energised stator coil or emanating from the translator back iron were not modelled.

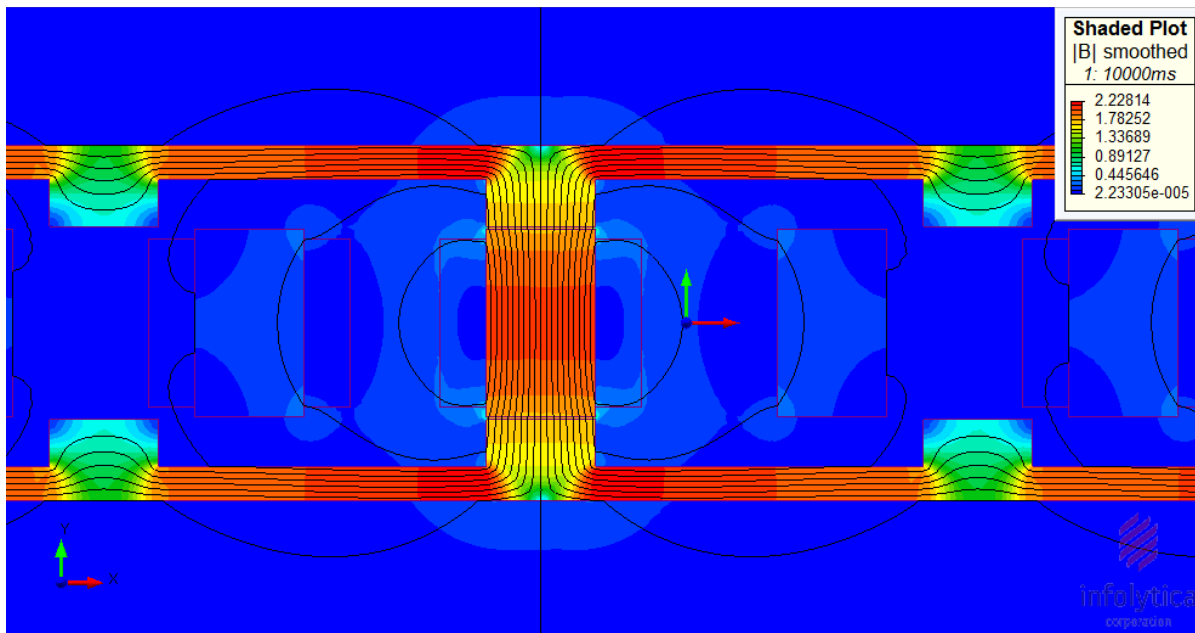


Figure 24: FEM analysis based magnetic field solution of the aligned translator position of the LSRM

Magnetic field intensity plot of Fig. 24 was obtained with the excitation current levels set at 1.2 *p.u.* of the maximum design excitation current of the analysed machine. The high level of excitation current produces highly saturated iron parts of the machine as well as leakage flux around the energised stator pole. Visual inspection of the above figure reveals the equipotential magnetic field density values in the ferromagnetic steel parts of the machine. As discussed in Section 3.1.1, these will form initial slices of equipotentials between which cubic-spline interpolation can be performed in order to model the actual flux paths. Further subdivision into slices might be necessary, depending on the level of intricacy of the machine geometry, and can be performed readily with straight line slice approximations. Fig. 25 shows such subdivision of the LSRM and the modelled cubic-spline based flux paths.

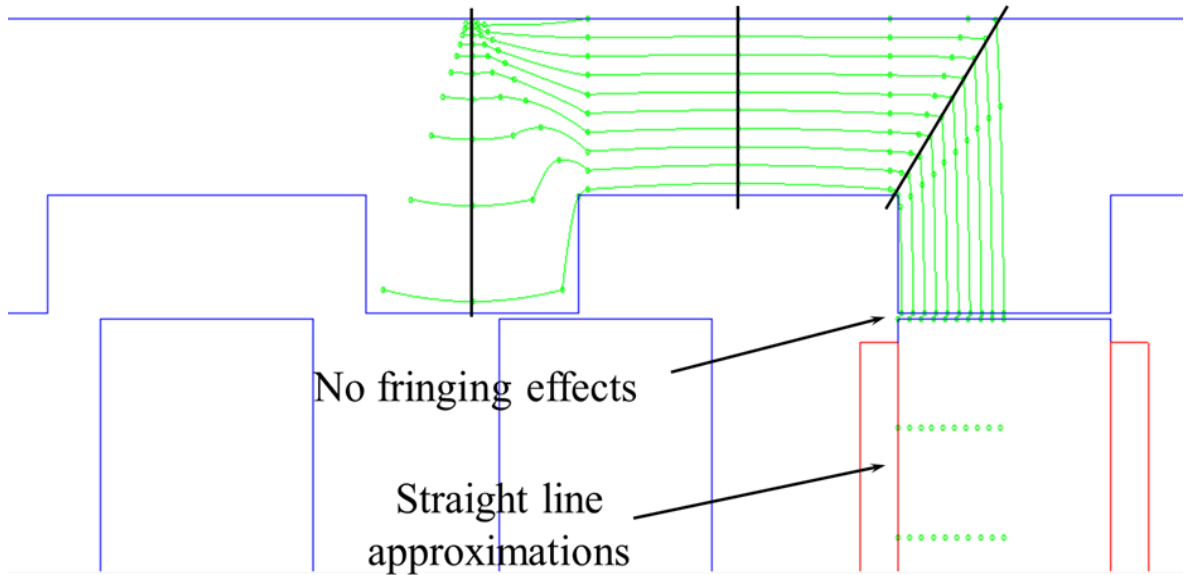


Figure 25: Modelled aligned position LSRM flux paths based on cubic-spline interpolation

Fig. 25 shows that some of the assumed flux paths were modelled with more than three coordinate points for more accurate mapping of the actual flux paths in these parts of the machine. It is further assumed that the flux paths in the stator pole (not shown in Fig. 25) can be approximated by vertical straight line segments between two adjacent equipotential slices. Furthermore, magnetic fringing effect is neglected in the existing flux paths modelling to simplify the method, however if needed, an empirical factor, albeit of constant value, which accounts for the fringing effect can be added to the final magnetic circuit reluctance result as is recommended in [63]. Finally, it is evident from the comparison of Fig. 24 and Fig. 25 that the modelled flux paths in the latter figure form ideal paths – there are no leakage flux paths in the modelled flux paths under varying excitation current levels. This assumption, as will be shown in the results section of the report, is valid and does not lead to significant deviations from the FEM analysis results.

3.1.4 Intermediate Translator Position Modelling

The intermediate translator positions can, in the most general sense, be modelled by the same equipotential slice construction techniques and cubic-spline approximations of the actual flux paths as presented in Section 3.1.1. However, the intermediate translator positions can be numerous and it is necessary to reduce the number of instances to be modelled to a minimum without introducing too large errors in the final results of the machine performance

analysis. Once this number of distinct translator positions is known the probable flux paths cubic-spline fitting can be performed to each instance and it will be a combination of aligned and unaligned translator position modelling specifics presented earlier.

Fig. 26 can aid in determining the number and spacing of intermediate translator positions to be modelled. In general each of the flux-linkage functions, for the range of currents, is given by (11) which for convenience is rewritten here

$$\psi = \frac{N^2 \cdot I}{R}. \quad (11)$$

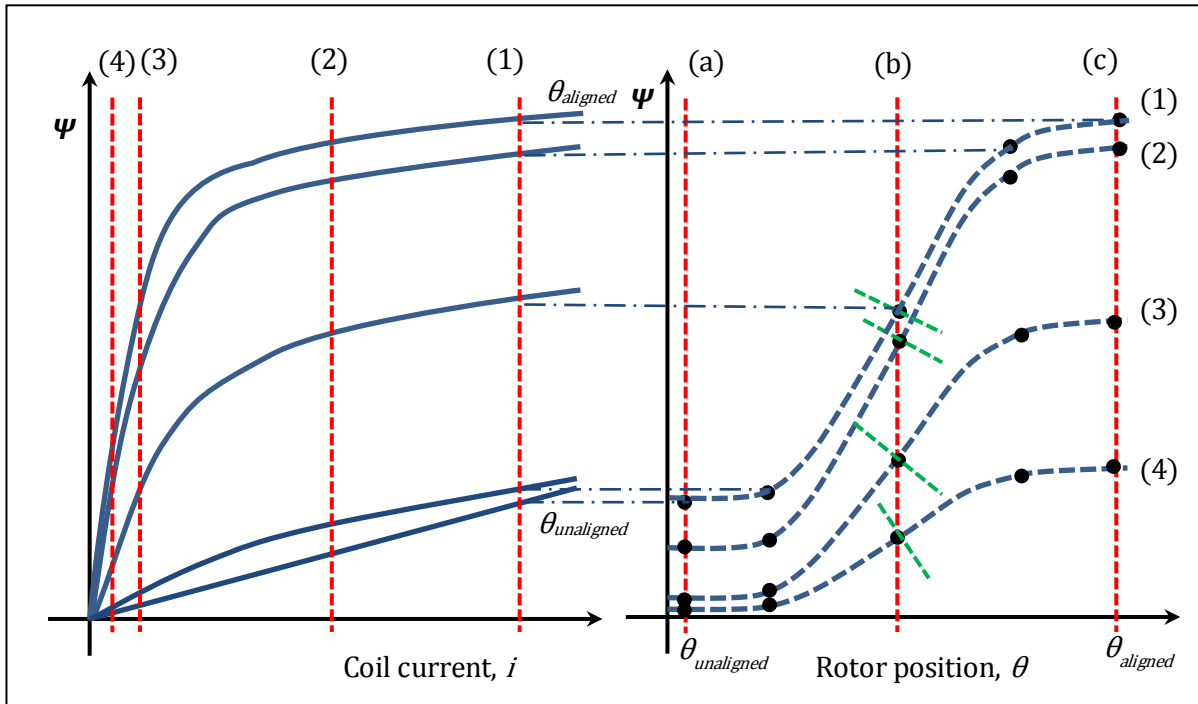


Figure 26: Flux-linkage map and gauge curves, not to scale, used to deduce candidate intermediate rotor positions

In the above figure the left hand side graph represents typical non-linear flux-linkage map projection with respect to phase excitation current and with rotor position or equivalently translator position as a parameter (with only five such rotor increments shown for illustration). This graph is subdivided by the four vertical dashed lines numbered 1 to 4 (more generally these lines are edges of 2D planes in the Ψ - θ plane). Right hand side of the figure shows the same flux-linkage map rotated by 90 degrees clockwise around the flux-linkage axis. This map would in principle contain as many gauge curves (curves 1 to 4) as there are vertical dashed lines in the left-hand side of the figure. Therefore, the sliced left-

hand side figure (which results in four gauge curves) is projected onto the Ψ - θ plane on the right-hand side. From the right-hand side of the figure it is evident that each of the gauge curves can in effect be modelled by a certain minimum number of points to preserve their mathematically defined shape. There is no need, at least from machine performance computation point of view, to fit continuous gauge curves from a large number of coordinate points [71]. Therefore cubic-spline interpolation can be utilised for each gauge curve by selecting three convenient coordinate points that fall exactly on the respective gauge curve. Firstly it is recognised that; all the gauge curves will be periodic with respect to the angle of rotation of rotor, between unaligned and aligned angles, and that the gauge curves at these two angles will have zero derivative values (horizontal tangents). Secondly: the inflection points of the gauge curves (dashed green lines in Fig. 26), that coincide with half-aligned rotor position points, will define half-cord length of each gauge curve. From these two boundary conditions it will be possible to select other convenient coordinate points for cubic-spline fitting of the two-halves of each gauge curve. Thus, from Fig. 26 it is evident that a minimum of three intermediate rotor position points will be required in order to interpolate each gauge curve accurately (preserving the mathematically defined shape) with a single cubic-spline along the gauge curve length.

Once the described gauge curve fitting, by means of cubic-splines, is accomplished the 3D flux-linkage map for the analysed machine can be reconstructed readily because all other variables were obtained by the flux tube analysis or were given as machine design variables. Generic 3D flux-linkage map of an SR machine, 2D projection of which is shown in Fig. 26, is shown in Fig. A2 in the Appendix A.

3.2 Rotating SR Machine Flux Paths Modelling Using Cubic-Splines

3.2.1 Unaligned Rotor Position Modelling

Similarly to the translating SR machine circuit subdivision into the flux tubes the rotating SR machine geometry was subdivided first into the approximate equipotential slices along the length of the unaligned magnetic circuit as in Fig. 27.

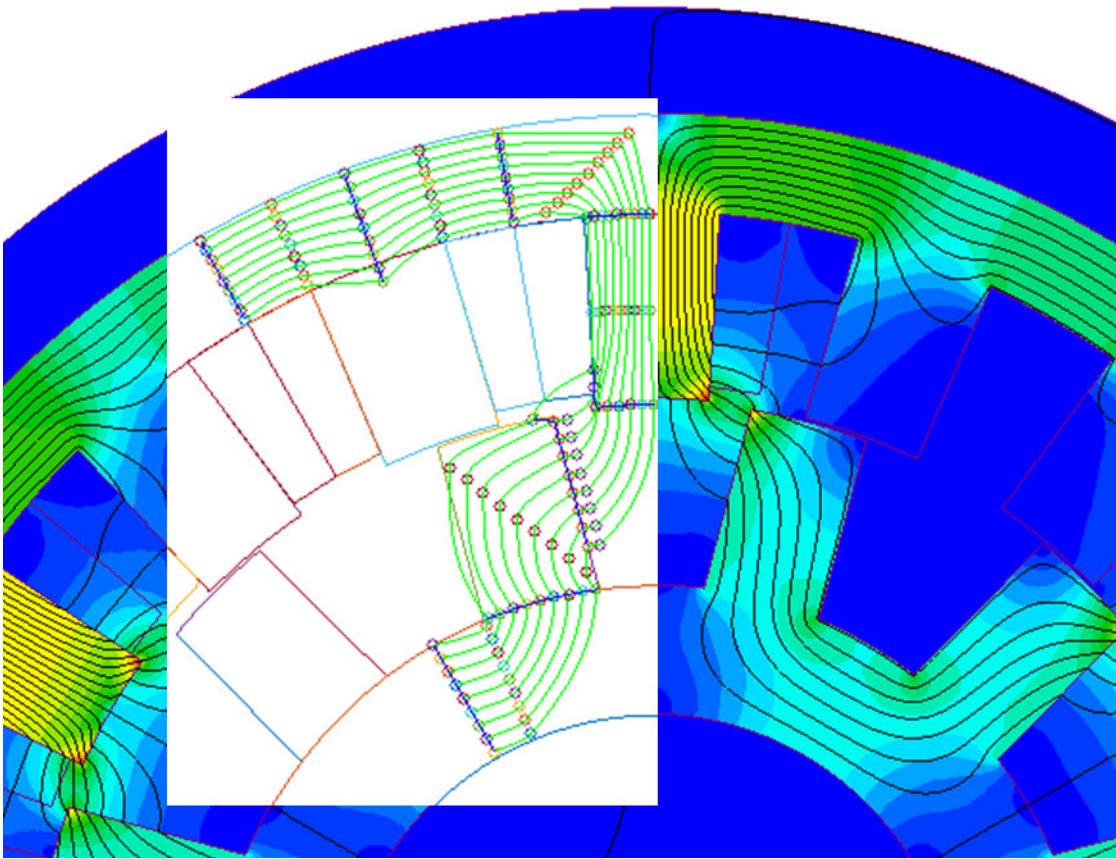


Figure 27: Flux tubes and slices superimposed onto 2D FEM solution for the 18/12 three phase SRM2 design at the unaligned rotor position.

As can be seen from Fig. 27 the symmetry of the magnetic circuit greatly simplifies the subdivision task into slices. Compromise is made when deciding which major machine dimensions to use for the construction of the slices and the accuracy with which such slices are approximated as the magnetic field equipotentials. Visual examination of the flux tubes and slices of the circuit in Fig. 27 reveal that the path accuracy is somewhat compromised due to the inability to model the leakage flux paths. This is the case since FEM obtained flux function distribution shown in Fig. 27 was for the phase current value well above the design point which produces much higher magnetic saturation and flux leakage as a result.

3.2.2 Aligned Rotor Position Modelling

Compared to the unaligned rotor position flux tubes and slices distribution in Fig. 27 with the aligned rotor position flux distribution in Fig. 28 it is evident that the slices construction is markedly easier to fit.

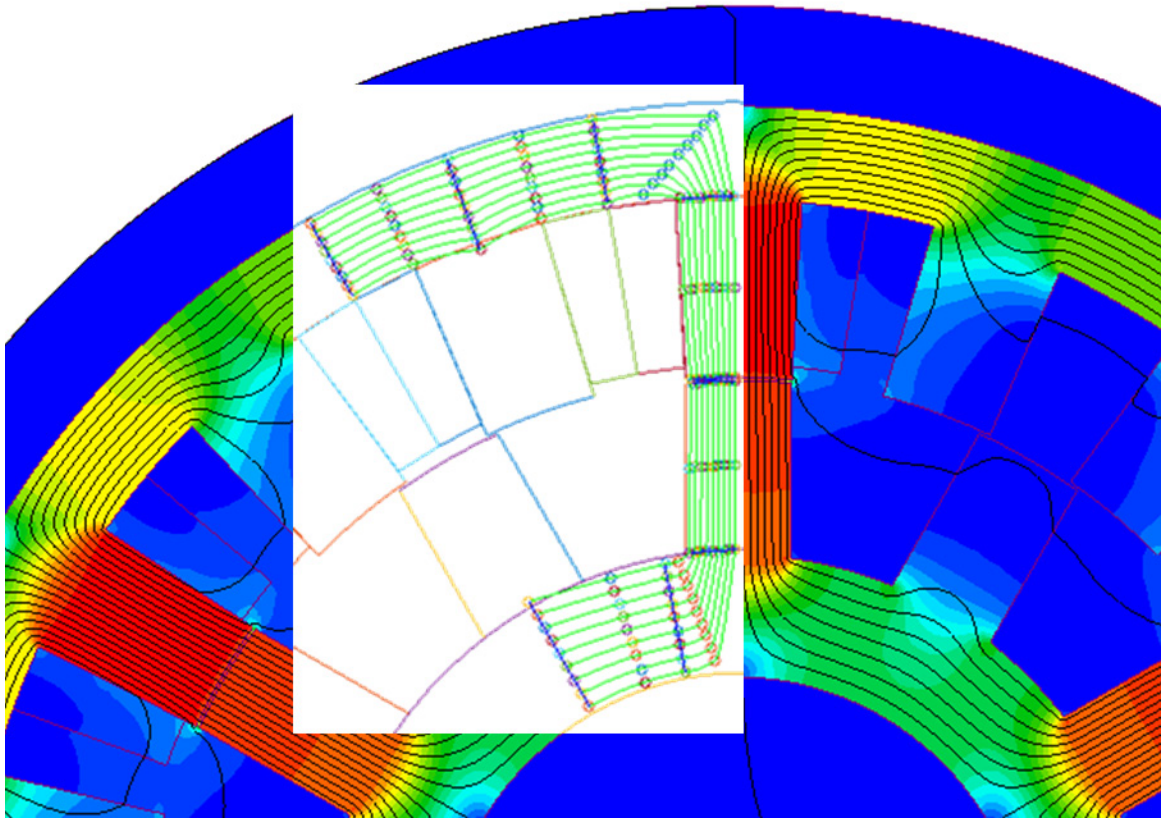


Figure 28: Flux Tubes and Slices superimposed onto 2D FEM solution for the 18/12 three phase SRM2 design at the aligned rotor position.

As was the case in Fig. 27 the flux function distribution in Fig. 28 was produced with the machine phase excitation current higher than the specified peak current for this particular design. This level of excitation inevitably produces higher magnetic saturation and as a result excessive flux leakage. On the contrary, the flux tubes and slices distribution is ideal regardless of the level of phase current excitation. Since it was not attempted to model the complex leakage and fringing flux patterns with the comparably simple flux tube and slice placement techniques it is anticipated that the resulting flux linkage values of the flux tubes and slices approach will yield lower values compared to FEM values.

3.3 Numerical Accuracy and Robustness of the Flux Tubes Modelling

In order to illustrate the accuracy and robustness of the improved flux tubes method, from the computational and numerical error propagation point of view, analytical formulation is employed. Fig. 29 can be used to describe what is meant by the system of flux tubes.

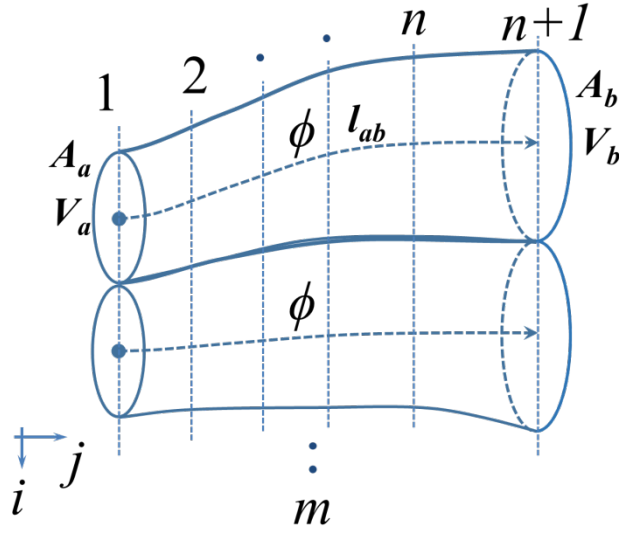


Figure 29: A system of magnetic flux tubes arranged in parallel. Taken from [69]

However, due to the resulting error terms being somewhat different in the distinct parts of the magnetic circuit of an SR machine each such error term derivation is undertaken separately as presented below.

3.3.1 Flux Tubes and Slices Air Gap Reluctance Accuracy

From Fig. 22 and or Fig. 27 it is assumed that the flux tube system is in the air gap or other non-magnetic region of the SR machine. The flux tubes have been subdivided into n slices, as shown in Fig. 29, along their lengths and cross-sectional areas of each such slice averaged

$$A_j \leftarrow (A_j + A_{j+1}) \div 2, \quad j = 1, 2, \dots, n \quad (12)$$

where the arrow in (12) indicates the substitution.

Therefore, the individual reluctance of each of the m flux tubes can be expressed as

$$R_{ab} = r_t = \sum_{j=1}^n \frac{l_{ij}}{\mu_0 \cdot A_{ij}}. \quad (13)$$

Now, because the system of flux tubes in Fig. 22 is arranged in parallel, as in Fig. 29, the total flux tube system reluctance will be

$$\frac{1}{R_{parallel}} = \frac{1}{r_{t1}} + \frac{1}{r_{t2}} + \dots + \frac{1}{r_{tm}} = \sum_{i=1}^m \left(\sum_{j=1}^n \frac{l_{ij}}{\mu_0 \cdot A_{ij}} \right)^{-1}, \quad i = 1, 2, \dots, m \quad (14)$$

As argued in the previous section, the resulting flux tube system of Fig. 22 approximates the FEM solution in Fig. 21 well, but is not exact. The flux tubes method considers discretized systems rather than continuous. Thus it is necessary to take two neighbouring cross-sectional areas of each tube-slice and average them to produce a mean value for that particular flux tube slice as in (12). This averaging of cross-sectional areas, however, will introduce some numerical error. The error itself will vary from slice to slice, and from tube to tube, and even from system to system. Taking into account the numerical error thus created, (13) can be expressed as follows

$$r'_t = \frac{l_1 \cdot \varepsilon_{l1}}{\mu_0 \cdot A_1 \cdot \varepsilon_{A1}} + \frac{l_2 \cdot \varepsilon_{l2}}{\mu_0 \cdot A_2 \cdot \varepsilon_{A2}} + \dots + \frac{l_n \cdot \varepsilon_{ln}}{\mu_0 \cdot A_n \cdot \varepsilon_{An}}. \quad (15)$$

It is assumed that each error term ε in (15) will be in the region of, and unlikely to exceed, ± 1.1 (or put in other words will overestimate or underestimate by 10%) for the averaged cross-sectional areas and cord lengths of each slice. If the number of terms n in (15) is increased, the errors resulting from the estimated cord lengths and cross-sectional areas of the tube slices can be averaged, namely

$$r'_t = \left(\frac{l_1}{\mu_0 \cdot A_1} + \frac{l_2}{\mu_0 \cdot A_2} + \dots + \frac{l_n}{\mu_0 \cdot A_n} \right) \times \frac{\varepsilon_{l \cdot av}}{\varepsilon_{A \cdot av}}. \quad (16)$$

For convenience, the averaged errors of the cross-sectional areas and cord lengths of each slice in (16) can be written as

$$A_j \cdot \varepsilon_{A \cdot av} = A_j + A_j \cdot \alpha; \quad l_j \cdot \varepsilon_{l \cdot av} = l_j + l_j \cdot \lambda. \quad (17)$$

Where the meaning of the errors can be more clearly interpreted in Fig. 30.

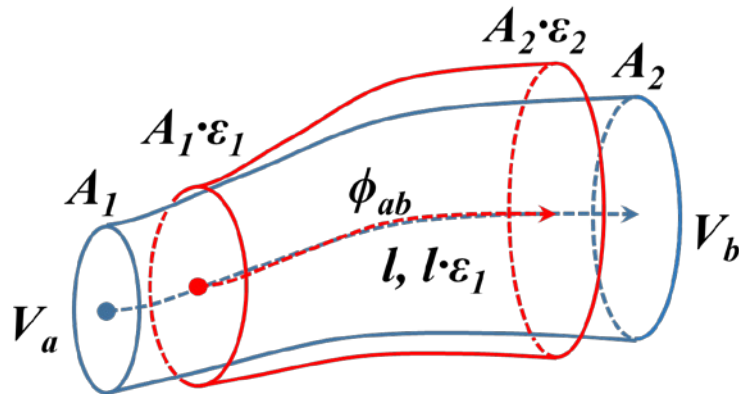


Figure 30: An approximation of a true tube introducing the errors in length and area. Taken from [50]

Chapter 3

It is now possible to show what impact the errors of the estimated geometric features of the tube will have on the reluctance value of the whole system of tubes of Fig. 29. Rewriting (16) in terms of (17)

$$r'_i = \frac{l_1 \cdot (1 + \lambda)}{\mu_0 \cdot A_1 \cdot (1 + \alpha)} + \frac{l_2 \cdot (1 + \lambda)}{\mu_0 \cdot A_2 \cdot (1 + \alpha)} + \dots + \frac{l_n \cdot (1 + \lambda)}{\mu_0 \cdot A_n \cdot (1 + \alpha)} = \left(\sum_{j=1}^n \frac{l_{ij}}{\mu_0 \cdot A_{ij}} \right) \times \frac{(1 + \lambda)}{(1 + \alpha)} \quad (18)$$

and rewriting (14) in terms of (18)

$$\frac{1}{R'_{parallel}} = \sum_{i=1}^m \left(\sum_{j=1}^n \frac{l_{ij}}{\mu_0 \cdot A_{ij}} \right)^{-1} \times \frac{(1 + \alpha)}{(1 + \lambda)} \quad (19)$$

results in the total equivalent reluctance of the system of tube-slices in series and combined in parallel to be

$$R'_{parallel} = \left(\sum_{i=1}^m \left(\sum_{j=1}^n \frac{l_{ij}}{\mu_0 \cdot A_{ij}} \right)^{-1} \right)^{-1} \times \frac{(1 + \lambda)}{(1 + \alpha)}. \quad (20)$$

The result in (20) indicates that the estimated parallel equivalent reluctance of the air gap tubes will scale linearly with the quotient of the two errors. Thus it could be argued that if the two error terms are both either positive or negative this will tend to minimize the total error of the parallel reluctance. The worst case scenario occurs if the two errors are of equal magnitude but opposite sign, that is the cross-sectional areas are underestimated whilst the cord lengths of the tubes are overestimated, or vice versa. Even the worst case scenario is considered to be tolerable provided the errors α and λ are not larger than $\pm 10\%$ as stated earlier. Under such conditions the total error can be no more than $\pm 22\%$ of the true reluctance value.

3.3.2 Flux Tubes and Slices Iron Circuit Reluctance Accuracy

In a similar way the reluctance of the magnetically nonlinear iron circuit of the SR machine can be estimated and effects of the errors accounted for. Considering Fig. 29 again, this time however with the magnetic permeability no longer constant but varying according to the magnetization curve of the material as portrayed in Fig. 31.

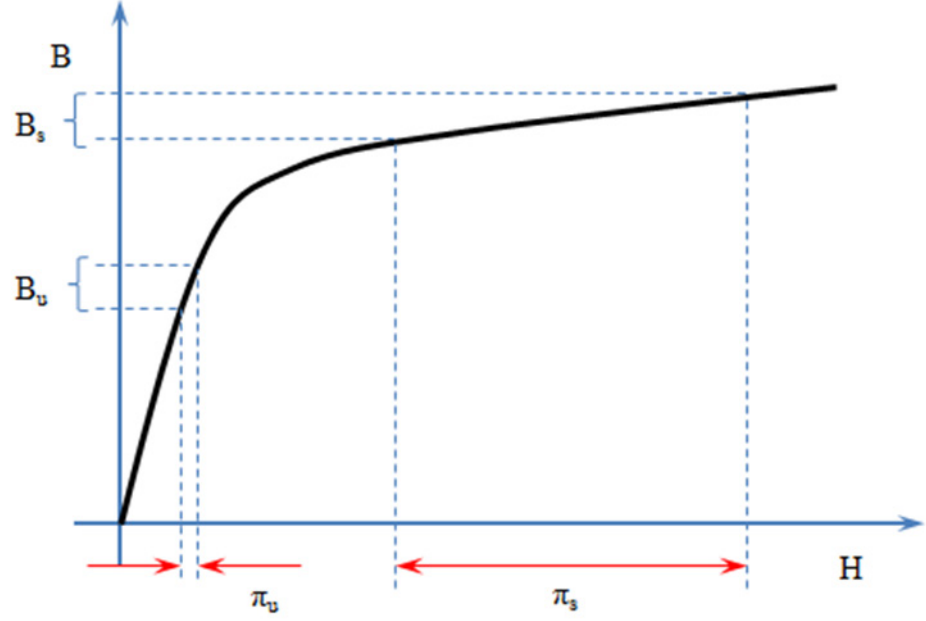


Figure 31: A typical magnetization curve of a saturable iron circuit and the resulting errors in the non-saturated and saturated regions

Therefore (13) may be rewritten, taking saturation into account, as

$$R_{ab} = \frac{H_{ab} \cdot l_{ab}}{B_{ab} \cdot A_{ab}} = r_t = \sum_{j=1}^n \frac{H_{ij} \cdot l_{ij}}{B_{ij} \cdot A_{ij}}. \quad (21)$$

Assuming that the flux of each tube is of constant value the estimated magnetic field density occurring at each given slice is

$$B'_j = \frac{\phi}{A'_j} = \frac{\phi}{A_j(1 + \alpha)} \quad (22)$$

and from (22) the following can be deduced

$$\begin{aligned} \text{if } \alpha > 0 \text{ then } B'_j &< B_j \\ \text{if } \alpha < 0 \text{ then } B'_j &> B_j. \end{aligned} \quad (23)$$

In other words, if the area error α is positive the magnetic field density will be underestimated compared to the true value and vice versa. From the magnetization curve of Fig. 31 it follows that the relationship between the erroneous magnetic field density estimate and the resulting magnetic field strength can be stated as

$$\begin{aligned} \text{if } B'_j < B_j \text{ then } H'_j &< H_j \\ \text{if } B'_j > B_j \text{ then } H'_j &> H_j. \end{aligned} \quad (24)$$

Chapter 3

The resulting erroneous magnetic field strength for each of the flux tube slices along the lines of (17) can be expressed, for convenience, as

$$H'_j = H_j + \pi \cdot H_j = H_j(1 + \pi). \quad (25)$$

The estimated values in the denominators of (21) imply that

$$B'_j \cdot A'_j = \frac{\phi}{A'_j} \times A'_j = \frac{\phi \times A_j(1 + \alpha)}{A_j(1 + \alpha)} = \phi \quad (26)$$

which is trivial, however it does show that the estimated flux, that is the denominator in (21), is not affected by the cross-sectional area error α . Expression (26) can be shown to yield such results due to the particular computational iterative algorithm used in this work. The flowchart of the algorithm, which employs the bisection root finding method, is shown in Fig. A2 in the Appendix A.

Equation (21) can now be expressed in terms of (25), also remembering to include the tube slice cord length error term derived in (17), as follows

$$\begin{aligned} r'_t = & \frac{H_1 \cdot (1 + \pi) \times l_1 \cdot (1 + \lambda)}{B_1 \cdot A_1} + \frac{H_2 \cdot (1 + \pi) \times l_2 \cdot (1 + \lambda)}{B_2 \cdot A_2} + \dots + \\ & + \frac{H_n \cdot (1 + \pi) \times l_n \cdot (1 + \lambda)}{B_n \cdot A_n} = \left(\sum_{j=1}^n \frac{H_j \cdot l_j}{B_j \cdot A_j} \right) \times (1 + \pi) \cdot (1 + \lambda) \end{aligned} \quad (27)$$

and the parallel reluctance of the system of tubes in the iron circuit is

$$R'_{parallel} = \left(\sum_{i=1}^m \left(\sum_{j=1}^n \frac{H_{ij} \cdot l_{ij}}{B_{ij} \cdot A_{ij}} \right)^{-1} \right)^{-1} \cdot (1 + \pi) \cdot (1 + \lambda). \quad (28)$$

Equation (28) indicates that the cross-sectional area estimation error α has no influence on the final result of the total reluctance of the iron circuit. However, a new error term appears in (28) due to the estimation of magnetic field strength from the non-linear iron magnetization curve in Fig. 31. Therefore, the total saturating iron reluctance will scale as a product of the two errors. In contrast to the total air gap reluctance, as in (20), the iron circuit reluctance value is affected less by the equal magnitude but opposite signs of the errors (that is when one is positive and the other is negative). The worst case scenarios occur when both error terms are of equal magnitude and either both positive, or both negative.

Attention is now turned towards the discussion of the errors in (28) when the iron circuit is in the non-saturated and when it is in the fully saturated regions of the magnetization curve. As can be seen from Fig. 31, the π_u error term, which corresponds to the unsaturated state, for the magnetic field strength will be very small when the flux-linkage values of the SR machine are estimated at low phase excitation currents. The situation is very different when flux-linkage values of the SR machine are estimated at high phase excitation current levels where most of the iron circuit is fully saturated. At this condition the π_s error term is significantly larger, even if uncertainty associated with the magnetic field density value B_s is the same as in the non-saturated region B_u .

Due to the magnetic circuit design of the SR machine used here for illustrative purposes, the air gap and iron circuit components are arranged magnetically to be in series. Thus for the both the aligned and unaligned flux-linkage function estimations, the reluctances given by (20) and (28) will be additive, while the error terms for the unaligned flux-linkage curve will be an order of magnitude smaller compared to the error terms of the aligned flux-linkage curve. This effect is due to the point made above, but to repeat: the saturated reluctance error of the aligned SR machine circuit will be exacerbated due to error terms in (28), whereas in (20) the error will be negligible as the length of the air region is small as in Fig. 25. On the other hand, the reluctance error of the unaligned SR machine circuit will be made worse due to increased error terms in (20) as the length of the air-gap region is relatively large, whereas in (28) the error will be much smaller because of the non-saturated state of the iron as in Fig. 22.

The final note is made with regards to the preceding derivation of the geometric error terms in relation to the MEC based electromagnetic computations as discussed in Section 2.2. From the discussion in Section 2.2 it is evident that the original MEC formulation is liable to the same geometric modelling errors as the presently proposed flux tubes and slices method since the same basic construct of the flux tube is assumed. Therefore, although not covered in the extensive literature of MEC techniques for the modelling of electric machines, the geometric errors are the main cause of the uncertainties and the requirement for the calibration parameters of MEC based analysis. Therefore it is likely that the preceding geometric error derivation will be used to improve the classical MEC based electromagnetic analyses in the future.

3.3.3 Flux Tubes and Slices Dual Bounds Estimations

The preceding error analysis of the flux tube approach, and in particular expressions (20) and (28), can be directly compared to the TAS method used to analyse electric and magnetic fields in the linear media [84]. The analytical TAS derivation, in addition to using the tubes, makes use of the construction of a system of slices along the lines of Fig. 29, leading to the creation of dual bounds. The tubes result in a lower bound of the permeance, whereas the slices in an upper bound. There is similarity to the calculation of a resistance or capacitance, with the analogue of the permeability, μ , being the conductivity, σ , or permittivity, ϵ , respectively. The dual bounds are guaranteed for a particular tube-slice system and thus the true answer always lies between the two values. Taking an average often results in a good approximation.

It may be possible to adapt the TAS approach to the flux tubes in the non-linear media if the resulting error of the entire system of tubes and slices is to be minimized. A possible strategy would compare the resulting flux-linkage function based on a particular flux tube system with a FEM analysis solution and use the numerical error found to correct the subsequently generated systems of flux tubes when SR machine design variables are changed. Such a strategy would be likely to be most effective when a large number of the flux tube systems is being generated, as in GA based optimization.

The following derivation is used to complement the expression (14), which will apply to both the air gap region as well as the iron region of the magnetic circuit, in order to make the full use of the dual bounds theory fully derived and explained in [84] and [95] and reviewed in Section 2.4.

Therefore, starting with the parallel reluctance of each slice n of all the tubes that are arranged in series in Fig. 29 the following expression results

$$\frac{1}{R_j} = \frac{1}{r_{t1}} + \frac{1}{r_{t2}} + \dots + \frac{1}{r_{tm}} = \sum_{i=1}^m \left(\frac{l_{ji}}{\mu_0 \cdot A_{ji}} \right)^{-1}, \quad j = 1, 2, K, n \quad (29)$$

Equation (29) considers the tube slices to be in parallel which can be compared with (13) where the tube slices are first considered in series.

Finally, using (29) to account for all the n slices arranged in series in the system of tubes in Fig. 29 the following expression for the equivalent parallel-series reluctance of the system is obtained

$$R_{series} = \sum_{j=1}^n \left(\sum_{i=1}^m \left(\frac{l_{ji}}{\mu_0 \cdot A_{ji}} \right)^{-1} \right)^{-1}. \quad (30)$$

Equation (30) will give a lower bound value of the equivalent reluctance value of the system of tubes in Fig. 29 whereas (14) will give an upper bound value of the equivalent reluctance in the magnetically linear medium.

Similar reasoning is applied for the derivation of the lower bound equivalent reluctance value considering ferromagnetic circuit parts of the SR machine. Rewriting (21) in terms of the parallel m terms results in the following expression of the system of tubes in Fig. 29

$$\frac{1}{R_j} = \frac{1}{r_{t1}} + \frac{1}{r_{t2}} + \dots + \frac{1}{r_{tm}} = \sum_{i=1}^m \left(\frac{H_{ij} \cdot l_{ij}}{B_{ij} \cdot A_{ij}} \right)^{-1}, \quad j = 1, 2, K, n \quad (31)$$

Finally summing the n slice terms to arrive at the equivalent parallel-series reluctance of the system of tubes of Fig. 29

$$R_{series} = \sum_{j=1}^n \left(\sum_{i=1}^m \left(\frac{H_{ij} \cdot l_{ij}}{B_{ij} \cdot A_{ij}} \right)^{-1} \right)^{-1}. \quad (32)$$

Equation (32) can be compared with (28), and summarised in Table 3, not taking into account the error terms derived in (17) and (25) since these errors were averaged for simplicity. Nevertheless, the dual bounds obtainable from the above derived equations can aid the accurate computational effort of SR machine design greatly as illustrated in Fig. 32.

Table 3: Summary of the dual bound reluctance values of the flux tubes and slices equations

Flux linkage bound ()	Air region	Ferromagnetic Region
Series-parallel (lower)	$R_{parallel} = \left(\sum_{i=1}^m \left(\sum_{j=1}^n \frac{l_{ij}}{\mu_0 \cdot A_{ij}} \right)^{-1} \right)^{-1} \cdot (14)$	$R_{parallel} = \left(\sum_{i=1}^m \left(\sum_{j=1}^n \frac{H_{ij} \cdot l_{ij}}{B_{ij} \cdot A_{ij}} \right)^{-1} \right)^{-1} \cdot (28)$
Parallel-series (upper)	$R_{series} = \sum_{j=1}^n \left(\sum_{i=1}^m \left(\frac{l_{ji}}{\mu_0 \cdot A_{ji}} \right)^{-1} \right)^{-1} \cdot (30)$	$R_{series} = \sum_{j=1}^n \left(\sum_{i=1}^m \left(\frac{H_{ij} \cdot l_{ij}}{B_{ij} \cdot A_{ij}} \right)^{-1} \right)^{-1} \cdot (32)$

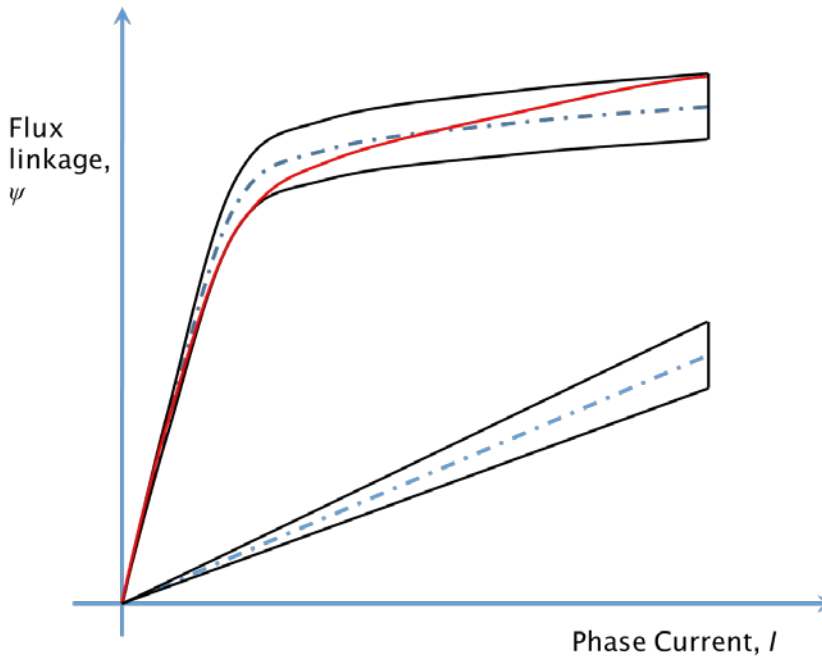


Figure 32: Dual bounds approximations of the true flux linkage functions for the aligned and the unaligned rotor (or translator) position of SR machine

In order to illustrate the dual bounds usefulness in the design of SR machines it is assumed in Fig. 32 that the true values of the aligned and unaligned flux linkage functions are as depicted by the central punctured curves in the non-linear and linear region respectively and are generally unknown at the time of the flux tubes based SR machine design stage. The dual bounds of the non-linear flux linkage will be obtained with expressions (28) and (32) for the upper and lower reluctance

bounds respectively. The two resulting flux linkage curves are joined together to indicate the area between them so formed in Fig. 32. In a similar fashion, the dual bounds of the linear flux linkage will be obtained with expressions (14) and (30) for the upper and lower reluctance bounds respectively. These two flux linkage curves are also joined together in Fig. 32 to indicate the area between them so formed.

Given such situation as depicted in Fig. 32 the following strategy can be adopted in order for the flux tubes and slices analysis to result in a conservative SR machine design which is considered here to be more advantageous when only the approximate analysis tools, such as the flux tubes method, are used. The dual bounds of the aligned flux linkage functions can be combined in such a way so as to give worst case scenario, which in Fig. 32 is shown as a red solid line. Adopting this strategy of the aligned flux linkage estimation will result in the higher inductance SR machine design. In a similar way the dual bound values of the linear flux linkage functions can be combined in such a way so as to arrive at a higher inductance SR machine design. However, since the unaligned flux linkage is a linear function selecting only the upper unaligned flux linkage curve in Fig. 32 will result in higher inductance SR machine. Therefore overall the resulting SR machine will produce lower output torque if the conservative estimates described above are chosen.

Of course such scenario as described above and in Fig. 32 is contingent upon the true flux linkage curves falling somewhere in between the respective aligned and unaligned dual bounds – the information which is not known beforehand. Nevertheless, such strategy will still prove effective if the given entire flux tube system is calibrated beforehand using FEM analysis results.

3.3.4 Geometric Modelling Aspects of the Flux Tubes and Slices Techniques










Since the derived equations in Section 3.3.3 are very important from the numerical error propagation point of view when the flux tubes and slices computations are performed it is necessary to fully describe the approaches with which these errors can be predicted, controlled and minimized.

Reconsidering expressions (20) and (28) with respect to Fig. 30 we are able to make the following general predictions as to the influence of the error terms α

Chapter 3

and λ as is shown in Table 4, for all possible geometric error combinations, where it is assumed that the magnetic potential is from left to right.

Table 4: Flux tubes and slices geometric errors and their combinations

Length, l Area, A	Under ($\lambda < 0$)	Over ($\lambda > 0$)	Equal ($\lambda \equiv 0$)
Under ($\alpha < 0$)			
Over ($\alpha > 0$)			
Equal ($\alpha \equiv 0$)			

Using the manual flux tube slice placement techniques described in Sections 3.1 and 3.2 will result in one of the following geometric error combinations as in Table 4. The ideal case scenario is when both errors are equal to zero producing exact geometric match between the actual flux tube slices and those constructed manually resulting in the accurate reluctance values and under such conditions the dual bounds will converge to a single value. However, it should be understood that the manual slice placement procedure statistically can never be exact in practice and will most of the time deviate from the true flux tubes and slices as obtainable with FEM analysis. In addition, the rotor position and the amount of the magnetic saturation in the entire circuit will also have a profound effect on the resulting equivalent reluctance as summarised in Table 5.

Table 5: Geometric error effect on the numerical accuracy on the equivalent reluctance of the flux tubes and slices method

Aligned Unsaturated Iron Lambda error = low Phi error = low Aligned Air Lambda error = low Alpha error = low	Aligned Saturated Iron Lambda error = low Phi error = high Aligned Air Lambda error = low Alpha error = low
Unaligned Unsaturated Iron Lambda error = low Phi error = low Unaligned Air Lambda error = low Alpha error = high	Unaligned Saturated Iron Lambda error = low Phi error = low Unaligned Air Lambda error = low Alpha error = high

It can be seen from Table 5 that dependent on the state of saturation of the magnetic circuit and the likely geometric error variations from Table 4, occurring due to the manual slice placement techniques, will result in the listed worsening effects to the accuracy of the final flux linkage function. The combination of the error terms in Table 4 and the worsening effects in Table 5 pose a computational accuracy challenge since the inherently random manual placement of slices will give rise to random fluctuations of flux linkage functions of a given SR machine geometry, but not due to the phase current values, and will make it rather more difficult to ascertain the true flux linkage functions.

Fig. 33 illustrates an exemplar mechanism by which the flux tube slice area error is introduced in the modelling stage.

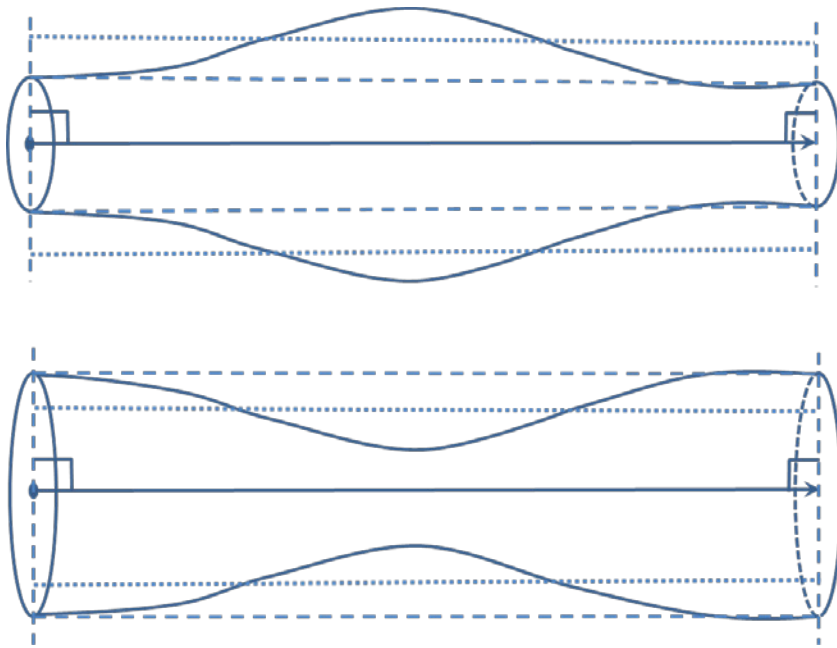


Figure 33: Flux tubes and slices area error generation

Considering the upper tube in Fig. 33 it can be seen that if the two slices happen to be manually placed at each extreme end of the tube will result in the actual cross-sectional area to be averaged which is an underestimate of the true average value. Likewise if the two slices happen to be manually placed at each extreme end of the lower tube in Fig. 33, this will result in the actual cross-sectional area to be averaged which is an overestimate of the true value. However, the resulting erroneous reluctance value, in addition to the area errors, will also be affected by the amount of magnetic saturation occurring in that particular slice which in turn depends on the intricacy of the magnetic circuit geometry. Therefore to remedy such gross underestimation or overestimation of the flux tube cross-sectional areas it is necessary to control the number of slices n the system of tubes should be subdivided into, as was shown in Fig. 29 in Section 3.3. Therefore it is reasonable to expect that given an intricately shaped magnetic circuit of a given SR machine will require much larger number of slices n compared to a simpler shaped magnetic circuit.

Turning our attention now to the flux tube length error term λ with respect to expressions (20) and (28) and Fig. 30 it can be seen that the flux tubes method has favourable error minimization qualities since it utilises the cubic splines in order to estimate the flux tube cord lengths independent of the number of the slices n as shown in Fig. 34.

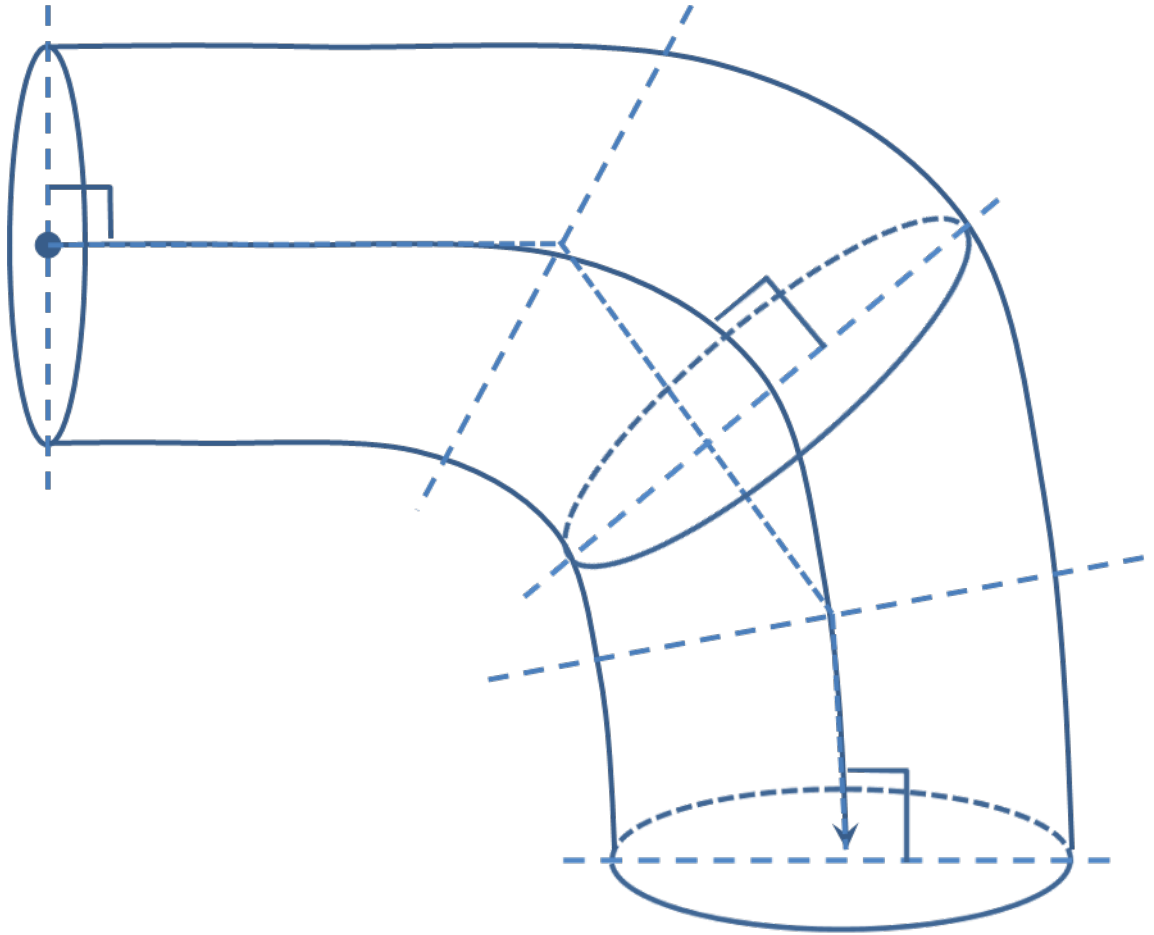


Figure 34: Flux tube length error term λ minimization using cubic splines

Figure 34 shows that by utilising the cubic splines to interpolate between three coordinate points (i.e. three slices) will produce negligible mean tube cord length error λ whereas if the mean tube cord length was approximated with the straight line segments this would necessitate much larger number of slices n , yet the length error λ would still remain significant. In other words, the linear mean cord length approximation is not feasible technique as the mean cord length error term λ would be highly dependent on the number of slices n . Therefore it is deduced from the preceding argument that the flux tubes and slices method based on cubic splines is far superior from the numerical accuracy point of view compared to the classical MEC techniques as used in [62] or [73] for example, especially for non-rectilinear magnetic circuit geometries.

Therefore it could be deduced that the following advantages are pertinent to the flux tubes and slices based method compared to the classical MEC based electromagnetic modelling techniques. Since the flux tubes and slices cord length calculation is numerically more accurate, as it corresponds more closely to the SR machine geometry under consideration, the cord length error λ is reduced upon the construction of the cubic spline based flux tubes. The only other error which

is left uncertain is the flux tube area error α which is not known at the time of the flux slices construction for the geometry under consideration. The classical MEC method has both of the geometric errors left uncertain since the classical MEC method in itself can produce tube area and cord length errors independent of each other and also independent of the geometry to which it is constructed. This results in inherently larger error and error variation of the classical MEC method as the modelled geometries are varied parametrically. Flux tubes and slices method on the contrary will always underestimate the flux tube areas with respect to the true values, as found by FEM analysis for example, which will help to establish the required calibration coefficient for the flux tubes and slices model being constructed. Likewise, the cord length values are most likely to be underestimated, still by considerably much lower factor than the slice areas, with respect to the true values, as found by FEM analysis for example, which will help to establish the required calibration coefficient to compensate the error.

3.3.5 Further Sources of Modelling Error

Having established the main sources of errors in the flux tubes and slices method it is also advantageous to consider other sources of error in the modelling and analysis process of SR machines. This consideration is important since the electromagnetic modelling of SR machines with the flux tubes and slices method can be made more accurate and aid in the correct interpretation of the modelling results when other sources of error are known and their effects can be interpreted correctly. Therefore, below is the list of likely sources of modelling errors that should be taken into account when using the flux tubes and slices method to analyse and design practical SR machines:

1. Magnetic material property variations due to manufacturing processes, i.e. $B = H(\mu)$, however this only taken into consideration once a practical device is built, tested and compared to the design
2. Approximation of the ampere-turns, $N \times I$, parameter of the SR machine to the magnetomotive force, mmf , or the approximation to the Ampere's law
3. Non-uniform air gap between the moving and stationary parts of the practical SR machine circuit, e.g. two opposite rotor poles of not equal length
4. Variation of material properties due to operating temperature variations of the SR machine

5. Variation of the geometric parameters of the magnetic circuit due to manufacturing inaccuracies and tolerances and displacement due to the internal forces
6. Leakage flux and fringing flux occurring in the magnetic circuit of the analysed SR machine not being modelled with the simple flux tube and slice placement techniques

All the above listed additional sources of errors will add to the uncertainty of the SR machine performance results obtainable with the flux tubes and slices method. Complete and simultaneous elimination of these errors is not possible in practice, however their ranges are normally known with reasonable confidence from the previous SR machine analysis and design experience. The prior experience can help to manage the errors associated with the above described factors and predict their impact upon the modelling results.

The next chapter outlines some of the numerical accuracy results obtainable with the flux tubes and slices techniques using cubic splines as proposed in this work.

3.4 Chapter Summary

The proposed modelling using flux tubes and slices techniques based on the cubic spline approximations can be summarised as follows.

As was demonstrated above the cubic-spline based flux tube construction to replicate the actual magnetic flux tubes occurring in the SR machine circuits is a versatile technique for a number of the different machine topologies presented. In particular, the unaligned position air gap flux distribution modelling is markedly simplified compared to previously demonstrated and published manual air gap region subdivision techniques. The aligned and unaligned ferromagnetic circuit flux distribution also modelled conveniently using only the major SR machine circuit geometric parameters to construct slices after which the automatic generation of the cubic-splines is performed.

The flux tubes and slices method is not completely immune from the modelling errors and mainly depends on the assumptions made as to the placement of the equipotential slices in the magnetic circuit. The two major modelling errors of the flux tubes and slices method are; the flux tube cross-sectional area estimation α and the flux tube cord length estimation λ . These two particular geometric errors

Chapter 3

were shown to be largely responsible for the numerical errors of the estimated reluctance values of the magnetic circuits in question.

The two main factors to be used for the control of the geometric errors of the flux tubes and slices method were identified in order to counteract the error propagation effects. Namely, the total number of flux tubes in parallel m , and the number of slices n of the flux tubes along their cord lengths. It is anticipated that by varying these two parameters the flux tubes and slices reluctance estimates can be controlled to an acceptable error bounds for accurate flux linkage estimation. Further technique which has a potential to greatly simplify the modelling error handling is the TAS technique whereby the two bounds resulting from the modelling errors are averaged in a way that minimizes the total modelling error in favour of the model accuracy.

Next chapter presents numerical error sensitivity analysis results of the improved flux tubes and slices method.

Chapter 4 Cubic Splines Based Flux Tubes and Slices Error Results

This chapter summarises the main findings of the flux tubes and slices method implemented as TAS technique in order to estimate the dual bounds of the flux linkage functions of SR machines being investigated.

4.1 Geometric Modelling of Flux Tubes using TAS Technique

Starting with the TAS implementation of the flux tubes and slices it is first necessary to decide a particular method of subdividing the flux tubes along their lengths in order to increase the number of subdivisions n . Figure 35 shows the adopted method of the cord length subdivisions for the flux tubes at the aligned rotor position of the radial SR machine where the number of tubes $m = 9$.

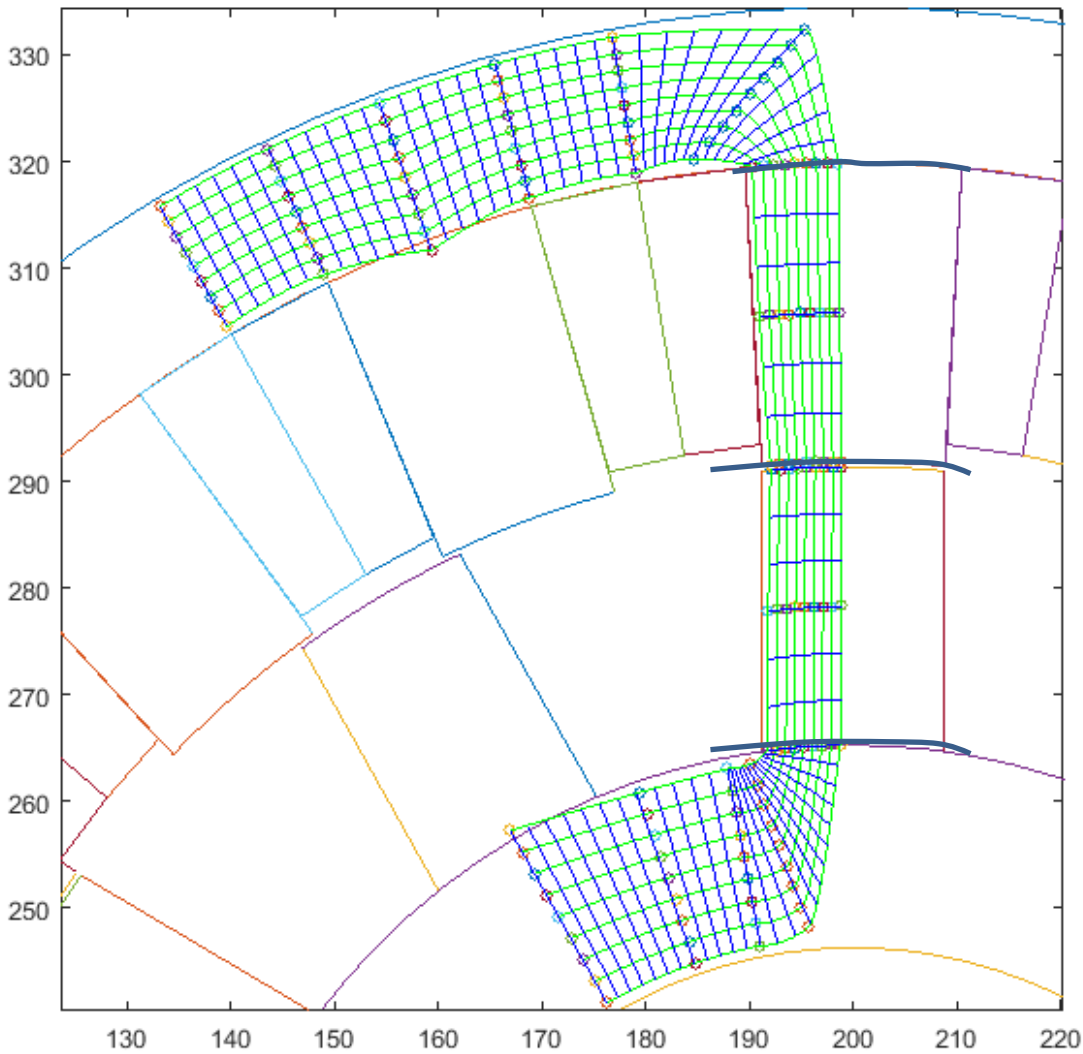


Figure 35: TAS implementation of the flux tubes technique for the aligned rotor position of the radial SR machine

Figure 35 indicates that before the slices were constructed the fitted flux tubes were first subdivided into four segments along their entire cord lengths (please note that the cord lengths of the segments are not equal but were chosen for convenience of modelling). This was done for the possibility of varying the coarseness of the number of final TAS slice subdivisions n in different parts of the machine circuit where it is known from the general FEM simulations that these regions have quite different levels of magnetic saturation. In this case the four segments were subdivided into, from top to bottom; 12, 6, 6 and 12 tube slices n . Fig. 35 shows the original construction slices alongside the tube slices n . It was anticipated that if the magnetic saturation is not so great in the back iron of the stator for example then there is no particular reason to have very fine subdivision in this part of the machine since the magnetic field density error π in such regions was reasoned to be lower as shown in Fig. 31. Therefore if the magnetic

steel in such regions is unsaturated the error term π is likely to be lower and there is therefore little benefit in increasing the number of TAS subdivisions n in that particular part of the machine. The scope for numerical error minimisation and computation efficiency gain using the flux tubes and slices method are obvious.

Second important point to make with regards to the TAS based slice subdivisions in Fig. 35 and more generally is a particular geometric reference where the subdivisions start and where they end – or in other words – considering which magnetic circuit segments to select for such subdivisions to accomplish. From the original TAS approach [84] it is seen that the best way to accomplish this is by assuming the unit cord length of the entity being subdivided. Therefore it was assumed that each tube in the particular segment has a unit cord length and then subdivide such unit length using the specified number of subdivisions n . In this way it was anticipated that the resulting TAS equipotential slices of the ‘real’ magnetic field density will be reconstructed more realistically. As can be seen from Fig. 35 certain segments of the geometry approached closely the curvilinear squares as discussed in Section 2.1. However, contrary to the previously mentioned method the curvilinear squares were generated automatically using the cubic spline fitting routines which is marked advantages over the laborious manual method.

In a similar way the unaligned rotor position of the machine is being subdivided using variable levels of subdivisions n dependent on the particular location of the SR machine magnetic circuit as shown in Fig. 36.

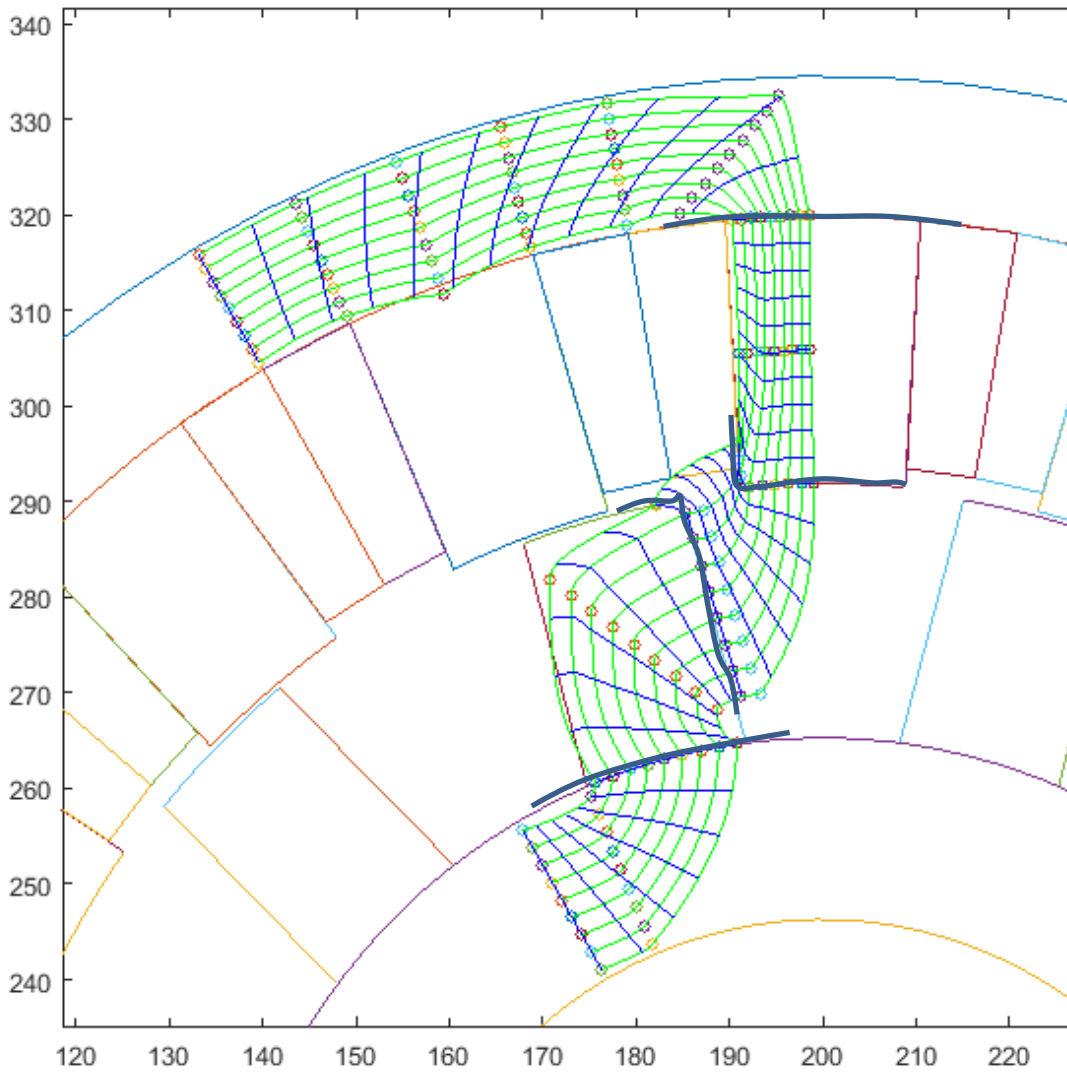


Figure 36: TAS implementation of the flux tubes technique for the unaligned rotor position of the radial SR machine

Again, as can be seen in Fig. 36, the entire magnetic circuit is subdivided into five initial segments and the number of subdivisions n in each such segment is independent of others due to the saturation error π identified in Fig. 31. In Fig. 36 the segments were subdivided, from top to bottom, into 12, 10, 6, 6 and 6 TAS subdivisions respectively. In this way the number of subdivisions in more saturating segments of the circuit, for example the stator and rotor pole tips, can be analysed with higher precision while at the same time giving consideration for the overall efficiency of the computational model.

Given the successful geometric subdivision of the flux tubes for the two rotor positions of the SR machine using TAS technique it is now necessary to investigate to what extent the TAS subdivision is better from the numerical error minimization point of view compared to the simple flux tubes subdivision – that

is only the series subdivision of the flux tubes as well as compared to the FEM solutions.

4.2 SR Machine Electromagnetic Modelling Error of Flux Tubes and Slices Technique

To start the electromagnetic modelling of the nonlinear radial SR machine using TAS technique it is first necessary to decide the nonlinear solution iterative approach to be taken in order to estimate the flux linkage. Therefore given the TAS based geometric subdivisions it is now necessary to choose between the series or parallel reluctance of the particular rotor position to be iteratively solved. In this particular study it was decided to use the series reluctance value at a given current level as the iteration progresses through the error minimisation routine since it is a more physical approach to select the series reluctance due to the physical meaning of the flux tubes. Once the series reluctance value has converged to an acceptable level the parallel reluctance is computed for that particular phase current level using the simple parallel circuit formulation and the two reluctance values are averaged to get a final answer of the flux linkage. Figure 37 shows the results of such studies where the TAS technique is compared to the simple series flux tubes method and the FEM solution of the aligned and the unaligned rotor positions of the radial SR machine.

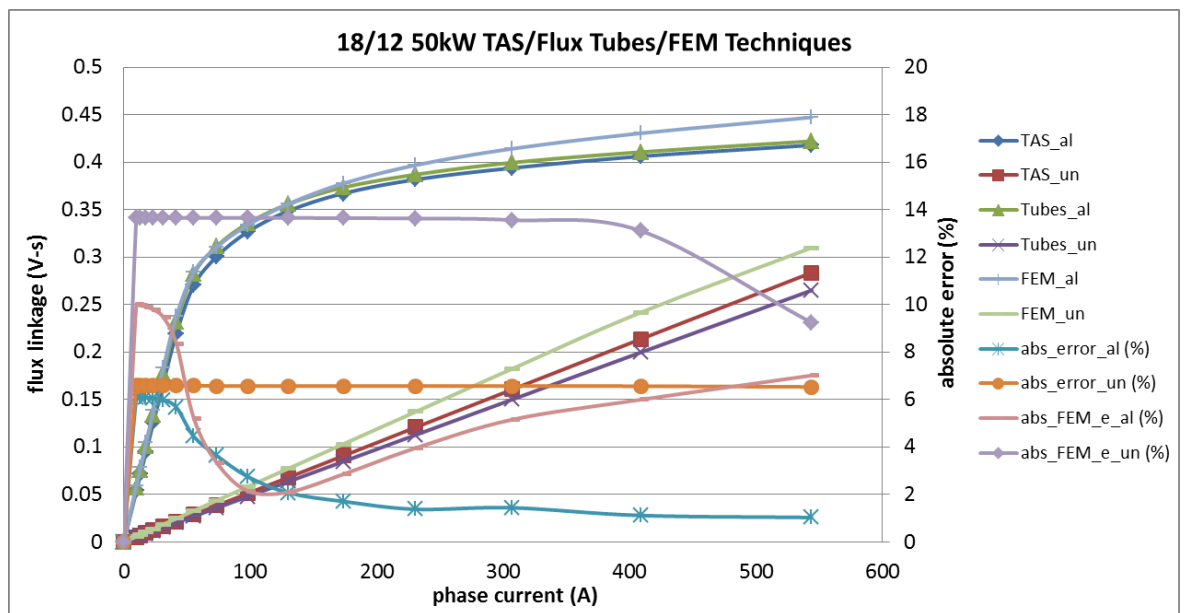


Figure 37: Comparison of the flux TAS technique to the series flux tubes technique and the FEM solutions for the aligned and the unaligned rotor positions of the radial SR machine

The results in Fig. 37 will be considered in turn and discussed in detail.

To start with the aligned rotor position of the SR machine is considered and the flux TAS as well as the series flux tubes techniques are compared. As can be seen in Fig. 37 the two techniques produce very close numerical results of the flux linkage for the entire SR machine phase current range. It can be seen that the flux TAS technique somewhat underestimates the aligned flux linkage value compared to the series flux tubes method. However it must be remembered that the flux TAS generated flux linkage is the average of the two bounds of the technique. Therefore it can be reasoned that one of the dual bounds of the flux TAS result is actually higher than the series flux tubes result which was confirmed in the current study but shown in Fig. 38 for the sake of clarity.

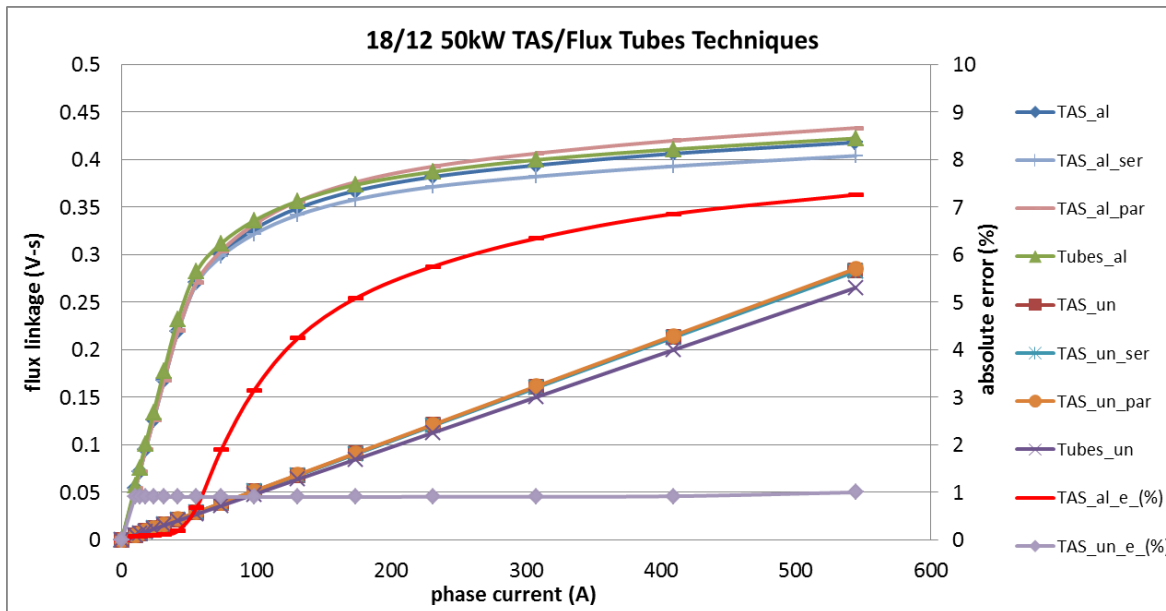


Figure 38: Flux TAS and series flux tubes comparison of the flux linkage and the absolute error

Furthermore the flux TAS technique used very fine subdivision of the flux tube cord lengths - n subdivisions being equal to 36 whereas the series flux tubes method used only $n = 16$. The computing time difference of these two techniques is significant with the flux TAS method taking 5 s whereas the series flux tubes method took only 1.5 s to obtain the aligned flux-linkage in Fig. 37 and Fig. 38.

It is also useful to obtain and plot the numerical error of the flux TAS and the series flux tubes method over the entire range of phase currents. The following equation is used to compute absolute error of the two methods

$$\text{Abs.error}(\%) = \text{abs}\left(\frac{100}{\text{flux_TAS}} \times \text{Flux_tubes} - 100\right). \quad (33)$$

Fig. 37 shows such error curve for the two flux tube techniques for the aligned rotor position flux linkage. It can be seen that the error starts at about 6% value when the phase current level is very low and decreases monotonically to a value of around 1% at the maximum phase current level where the magnetic saturation of the entire magnetic circuit is relatively very high.

Next we compare the flux TAS technique and the 2D FEM flux linkage values for the aligned rotor position in Fig. 37. Here we can see that the flux TAS technique, although underestimates the flux linkage values compared to the FEM solution, preserves the shape of the aligned flux linkage curve quite well over the entire phase current range. Again, (33) is used to compute the numerical error of the TAS and FEM techniques which is shown in Fig. 37. The absolute error curve of the TAS/FEM techniques is similar to the previously discussed flux TAS/series flux tubes error curve as it also starts at a highest level of error at the lowest phase current level which is 10%. The error is then decreased as the phase current is increased but only to increase again as the level of saturation of the magnetic circuit becomes severe at a value of 7%.

The comment regarding the TAS/FEM aligned flux linkage error curve is as follows. As prior experience indicates [70] the error values up to the phase current level of about 200A for this particular machine in Fig. 37 are insignificant to the accurate calculation of the *rms* phase current and the average instantaneous torque values. The flux linkage error past the 200A phase current point increases due to inability of the TAS method to take into account the magnetic flux leakage in the magnetic circuit which is perfectly well captured by the FEM solution (which we assume is the 'true' solution). Thus the TAS/FEM error starts rising again just after the aligned flux linkage knee-point when the saturation of the magnetic circuit increases to the level of flux leakage occurring.

The 7% error at the peak current value in Fig. 37 is relatively small and translates into negligible error of the *rms* current and the average instantaneous torque values, as the past experience showed, for the series flux tubes flux linkage.

Continuing with the absolute error estimation discussion we now turn to consider the unaligned flux linkage estimates from the flux TAS and series flux tubes methods. Fig. 37 indicates that this time it is the series flux tubes method which underestimates the unaligned flux linkage. We note at this point that the TAS

technique had a very fine level of the initial ‘segments’ subdivision n being equal to 40 whereas the series flux tubes were subdivided into 15 segments. Given the levels of subdivisions the TAS method took 6 s to compute the unaligned flux linkage curve whereas the series flux tubes took only 1.5 s to compute the same curve. Using the absolute error expression (33), the error is computed for the TAS and series flux tubes methods and is shown in Fig. 37. The unaligned absolute error curve of the two methods is very different compared to the error curve of the aligned case in Fig. 37. The error of the unaligned case appears to be constant at a value of $<7\%$ since the level of magnetic saturation is not reached due to the very large air gap region of the magnetic circuit as can be seen in Fig. 36. Hence this is exactly what TAS and series flux tubes methods predict since both flux linkage curves are straight lines.

We now turn to compare the TAS/FEM methods absolute error for the unaligned flux linkage curves. Fig. 37 shows the unaligned error curve which overall has a higher error value, contrasting to the previous unaligned error comparison, starting at 14% at very low level of phase current and remaining at this level until the level of the phase current reaches the 300A value. After this phase current point the error term decreases somewhat to a final value of 9% at the maximum phase current level in Fig. 37. The constant TAS/FEM error region can be easily interpreted as that due to the constant numerical discrepancy in the computed reluctance values of the two methods - since the heavy saturation is not achieved the error remains constant as per Fig. 31. However the error beyond the 300A level starts decreasing and this is due to the saturation effect actually appearing in the FEM flux linkage result at this high level of the phase current. Therefore it can now be seen that the unaligned flux linkage curve obtained with the FEM method is not straight line but has a turning point at the 300A phase current level where its gradient is now lower thus approaching the straight TAS curve which does not capture the saturation at that point. This is where the two results start converging thus decreasing the absolute error between the two methods in Fig. 37.

Again it should be remembered that in the unaligned TAS/FEM comparison in Fig. 37 the TAS flux linkage is the average of the two bounds and therefore one of the bounds is actually higher than this average thus approaching the flux linkage values that of the FEM method. The upper bound of the TAS method is always the parallel-series computation which is nothing more than the finely subdivided original series flux tubes evaluated in parallel as in Table 3. Therefore we could

reason that it would suffice to use such finely subdivided series flux tubes in parallel for the aligned and unaligned flux linkage estimations as can be seen from the unaligned flux TAS result in Fig. 38. However this argument is as yet unsupported by the experimental investigations and there is therefore no proof that all the finely subdivided series flux tubes taken in parallel will always perform better compared to the simple series flux tubes computation in the large number of generated SR machine design points on or near the pareto front using the genetic algorithm as envisaged in Fig 2.

To conclude, the unaligned flux linkage error comparison of the TAS/FEM methods in Fig. 37 we can say that overall the error is insignificant since the 14% error in the unaligned flux linkage values translates into negligible error of the *rms* currents and the average instantaneous torque values [70]. This argument is repeated from the above discussed aligned error comparison in Fig. 37, but it is also supported by the fact that both TAS curves are underestimated compared to the both FEM curves thus comparatively preserving the actual surface area value between the two sets of curves and making the *rms* current and the average instantaneous torque values acceptable for rapid initial design search.

One further important point regarding the absolute error of the TAS method in Fig. 38 is as follows. The shape of the error curve with respect to the phase current can be explained by considering the error argument in Fig. 31 where it is seen that the saturation error π is small when the estimated B is uncertain and this translates into small dual bounds error in Fig. 38 up to the 50A phase current value. However once the SR machine circuit starts saturating even the smallest error in the estimated B value in Fig. 31 translates into large π which in turn increases the dual bounds TAS error as in Fig. 38 past the 50A phase current. The unaligned dual bounds TAS error is of constant and small value in Fig. 38 since the machine circuit is not saturated and the saturation error π therefore has no effect – only the α and λ geometric errors of area and length are important. Therefore, from the preceding discussion the ramifications of Table 4 and Table 5 are apparent for the flux tubes and slices approach and could be argued to be even worse in practice if the classical MEC techniques were used instead for the SR machine analysis.

Finally it should be pointed out that the entire flux tube modelling has a certain degree of randomness since it is down to a particular interpretation of where the initial flux tube slices are to be located on the particular magnetic circuit of the modelled SR machine. This component of randomness in turn introduces the

numerical error in the final values of the equivalent reluctance thus making the flux linkage values less certain. However, by revisiting the earlier made argument that the pareto front generation is the result of highly repetitive generation of SR machine design points this repetitiveness can have the random error minimization effect since inevitably some of the flux linkage curves will be overestimated and some will be underestimated compared to the 'true' flux linkage values as obtained with highly accurate FEM solutions. The average accuracy of the flux TAS method is therefore much more important in such pareto front generating scenarios as the TAS errors will, on average, cancel out thus contributing very little effect on the final values of the *rms* phase currents and the average instantaneous torque values of the SR machine as envisaged in Fig. 2.

4.3 Flux Tubes and Slices Flux Linkage Results Sensitivity Analysis

Next avenue of enquiry regarding the flux tubes and slices implementation is the sensitivity of the results accuracy of the method when the number of subdivisions m and n , as defined in Fig. 29, are varied. In addition, such sensitivity information will help to assess the computational resources requirements in order to gain optimal computational efficiency and minimal numerical error ratio for the analysis of SR machines.

The geometric information of the rotary SR machine used for the sensitivity analysis, presented in Fig. 35 and Fig. 36, is placed as Fig. A3 in the Appendix A.

4.3.1 Aligned Flux Linkage Results Sensitivity Analysis

As a check on the aligned flux linkage function sensitivity the number of initial tubes m (defined in Section 4.1) was decreased by a factor of two compared to the number of slices in Fig. 35. Fig. 39 shows the plot of the flux tubes system where the number of tubes was 15.

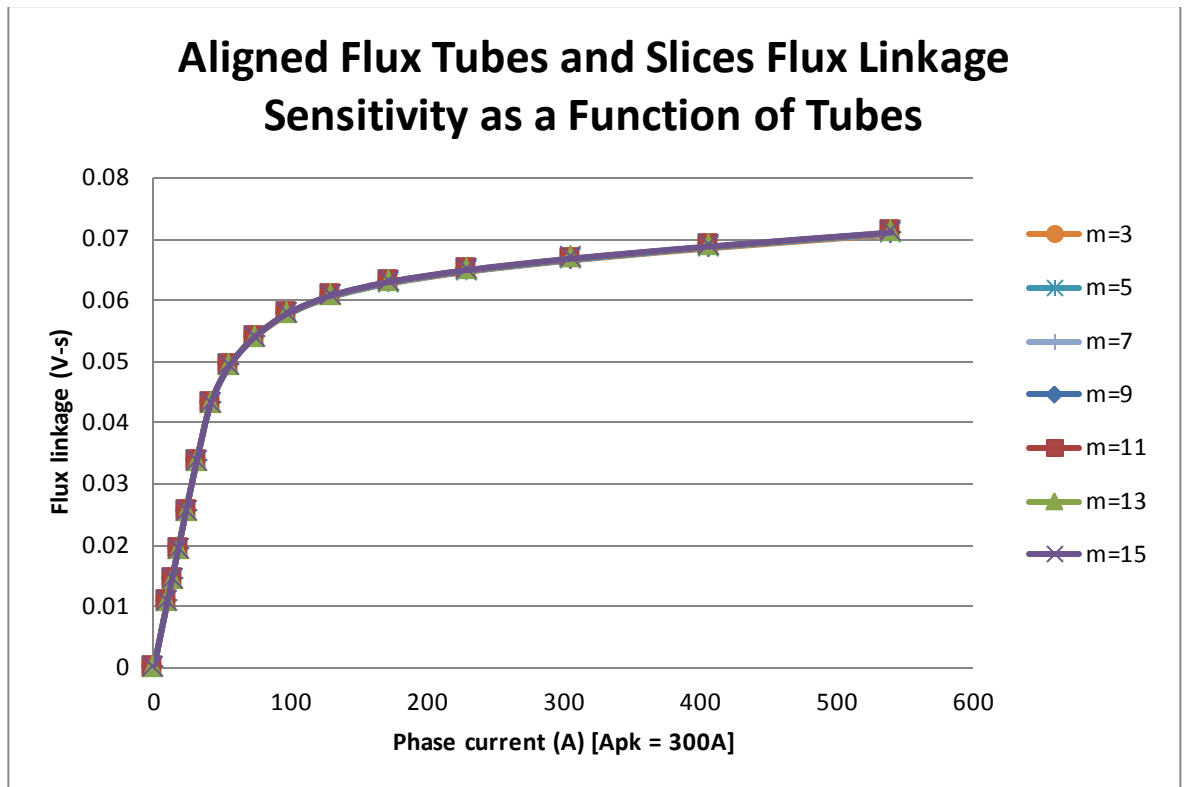


Figure 39: Sensitivity analysis of the aligned flux linkage as a function of the number of tubes m

From the Fig. 39 it can be deduced that the number of tubes m has very little effect on the results sensitivity of the aligned flux linkage function. However, since it was reasoned in the previous chapter that the flux TAS technique error depends not only on the flux tube cord length error λ , but also on the number of slices n the result in Fig. 39 must be taken with caution before the results sensitivity due to the number of slices n is also assessed.

Considering further the implications of the results in Fig. 39 it is now necessary to assess to what extent will the reduction in the number of tubes m will have on the computational efficiency of the solution. Figure 40 plots such computational efficiency gains when the number of tubes m is varied.

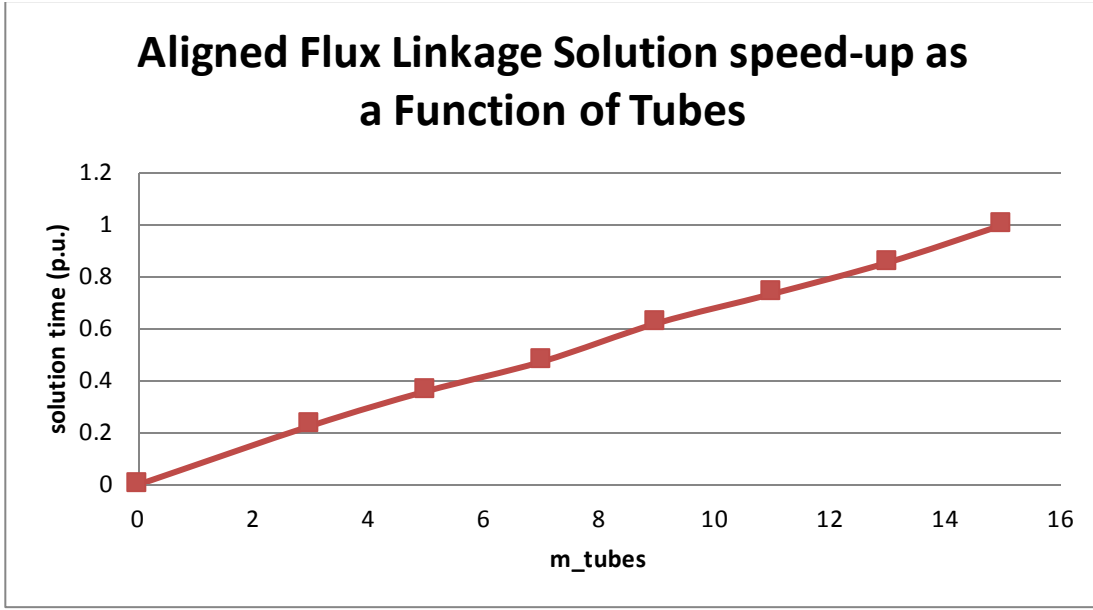


Figure 40: Speed-up of the aligned flux linkage computations as a function of the number of tubes m

From Fig. 40 it can be deduced that if the number of tubes is reduced from its maximum, e.g. $m = 15$, to its minimum this will result in the linear variation on the speed-up of the solution. Therefore, by using the ‘*Big O*’ notation the variation of the number of tubes m will have a linear variation of solution time T provided the number of slices n is fixed, and can be expressed as follows

$$T(m) \in O(m). \quad (34)$$

which indicates that the flux tubes algorithm has linear order with respect to the input m .

Next we compare the flux linkage result sensitivity when the number of tube slices n is varied in each chunk of the magnetic circuit as discussed in Section 4.1. Figure 41 indicates that similarly to the trend in Fig. 40 the sensitivity of the aligned flux linkage results is very small and can be safely neglected when the speed of computations are a primary goal.

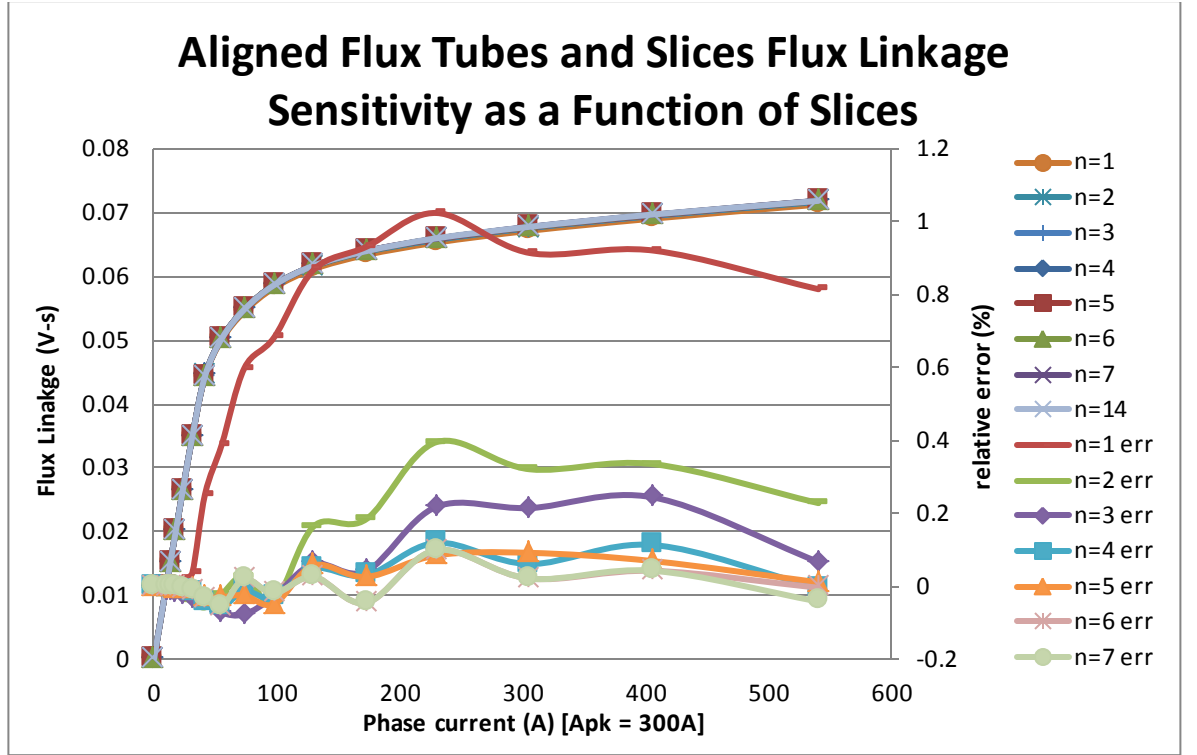


Figure 41: Sensitivity of the aligned flux linkage as a function of the number of segment slices n

Using (33) the absolute error with respect to the $n = 14$ case in Fig. 41 indicates that the largest error does not exceed 1% in this particular case which is very encouraging as far as the computational efficiency is compared.

To quantify the solution time performance of the flux TAS method with respect to the number of flux tube slices n the same notation as in (34) is used to express the algorithm performance, assuming the number of tubes m is fixed

$$T(n) \in O(n). \quad (35)$$

Therefore it is deduced that the flux TAS algorithm will perform linearly and this is confirmed in Fig. 42 where the speed-up is linear, however this time keeping the number of tubes m constant, as was the case in Fig. 41.

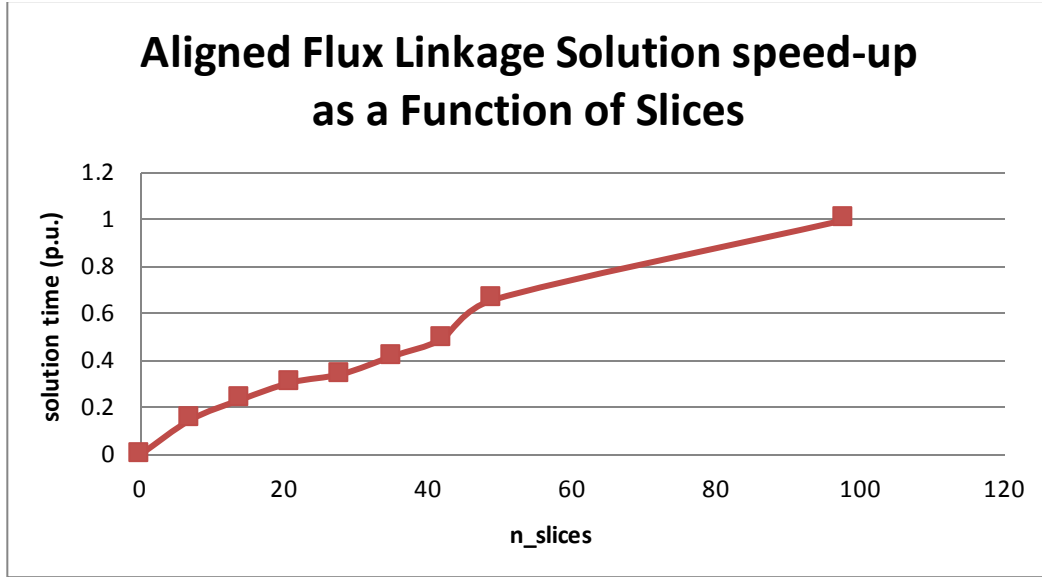


Figure 42: Speed-up of the aligned flux linkage computations as a function of the number of slices n

Therefore by combining the results for the number of tubes m and slices n and (34) and (35) the overall runtime of the algorithm can be expressed as

$$T(m, n) \in O(m \times n). \quad (36)$$

Thus the runtime of the algorithm will scale as a product of the two factors m and n . Therefore it is highly beneficial, from the computational efficiency point of view, to reduce the number of tubes m and slices n to the levels at which the flux linkage result error is nonetheless tolerable for the accurate and meaningful estimation of the analysed SR machine performance.

4.3.2 Unaligned Flux Linkage Results Sensitivity Analysis

As a check on the unaligned flux linkage sensitivity the number of initial segment slices n , as defined in Section 4.1, was decreased by a factor of two compared to the number of slices in Fig. 36. Fig. 43 shows the plot of the flux tubes system where the initial segments were subdivided into 12, 10, 6, 6 and 6 TAS subdivisions respectively.

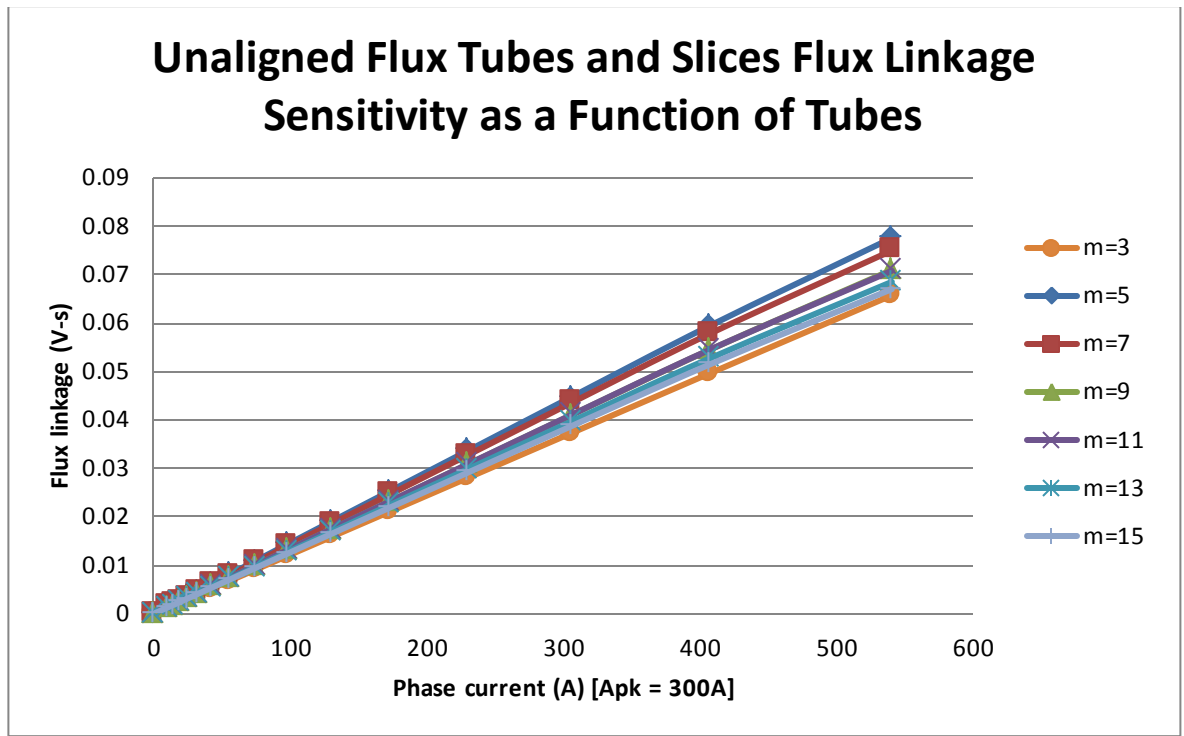


Figure 43: Sensitivity of the unaligned flux linkage as a function of the number of tubes m

The relationship between the resulting flux linkage error and the number of tubes m in Fig. 43 is not as simple compared to the aligned flux linkage results in Fig. 39. In Fig. 42 it is seen that when the number of tubes is low, e.g. $m = 3$, the flux linkage function is quite low which indicates relatively high reluctance of the system of tubes. However, as the number of flux tubes m is increased incrementally the flux linkage function is increased to a maximum value followed by the convergence of the flux linkage function when $m = 15$.

The above described behaviour of the flux TAS method is most likely to be attributable to the specific implementation of the fitting of the flux tubes for the given SR machine geometry. Therefore when the flux tube number approaches the borderline minimum value, e.g. $m \approx 3$ or less, the method results in unsatisfactory performance and for this reason, specifically for the unaligned rotor position, the number of tubes m should be increased to as large a value as reasonably practical.

In addition to the result sensitivity analysis as the number of tubes m is varied the solution speed-up is also investigated and is shown in Fig. 44.

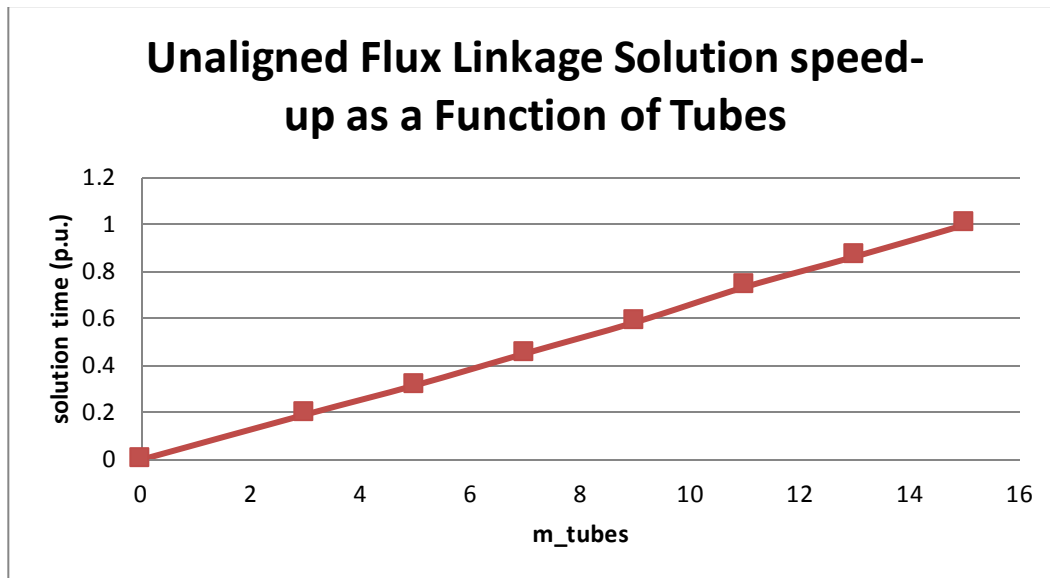


Figure 44: Speed-up of the unaligned flux linkage computations as a function of the number of tubes m

From Fig. 44 it can be deduced that the flux tubes algorithm run time scales linearly with respect to the number of tubes m . This result is expected and closely comparable to the result in Fig. 40.

The investigation of the results sensitivity analysis for the unaligned flux linkage when the number of slices n is varied is depicted in Fig. 45.

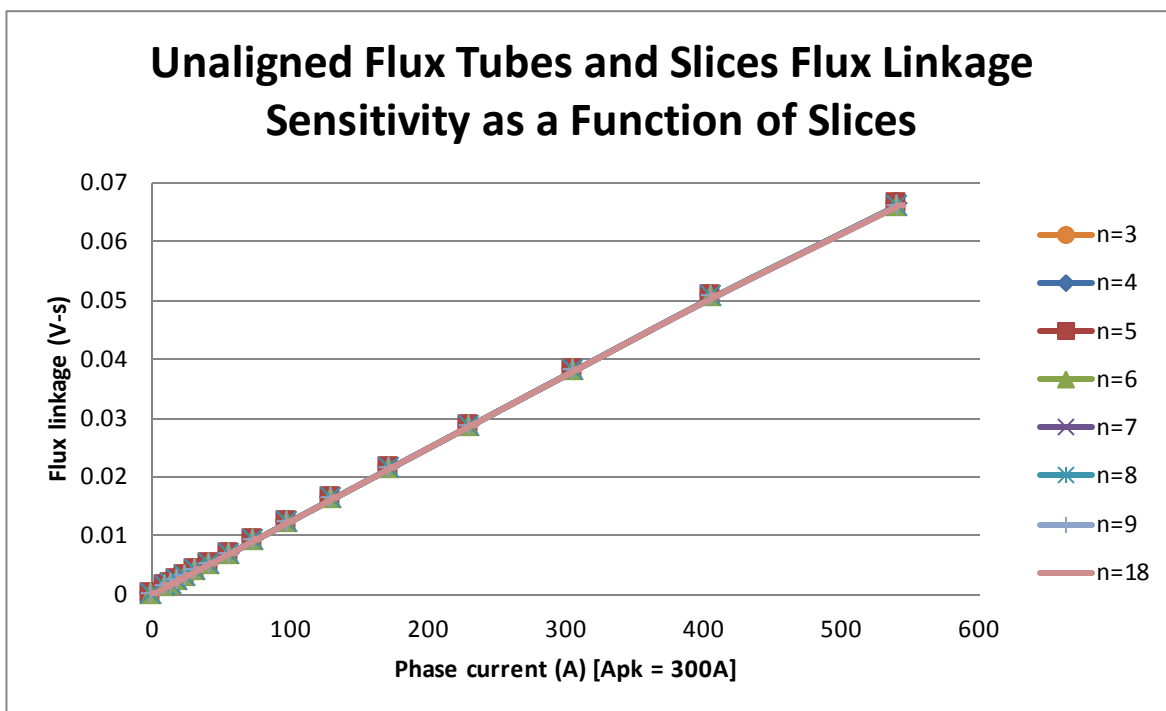


Figure 45: Sensitivity of the unaligned flux linkage as a function of the number of slices n

Since the magnetic saturation in the unaligned rotor position of an SR machine is small, due to the relatively large air gap, the unaligned flux linkage is almost always linear except when the phase current values are extremely large and outside the practically achievable range. Therefore the linear unaligned flux linkage function in Fig. 45 enables clearly and simple indication of the absolute error between the different unaligned flux linkage functions when the number of tube slices n is varied. Figure 45 indicates that the sensitivity is very small with respect to the parameter n and the number of slices therefore can be reduced to as low a value as reasonably practicable provided that the final flux linkage value is still accurate enough to obtain meaningful performance results of the analysed SR machine.

In the similar way to the aligned case the unaligned case speed-up as a function of the number of tube slices n is investigated and shown in Fig. 46.

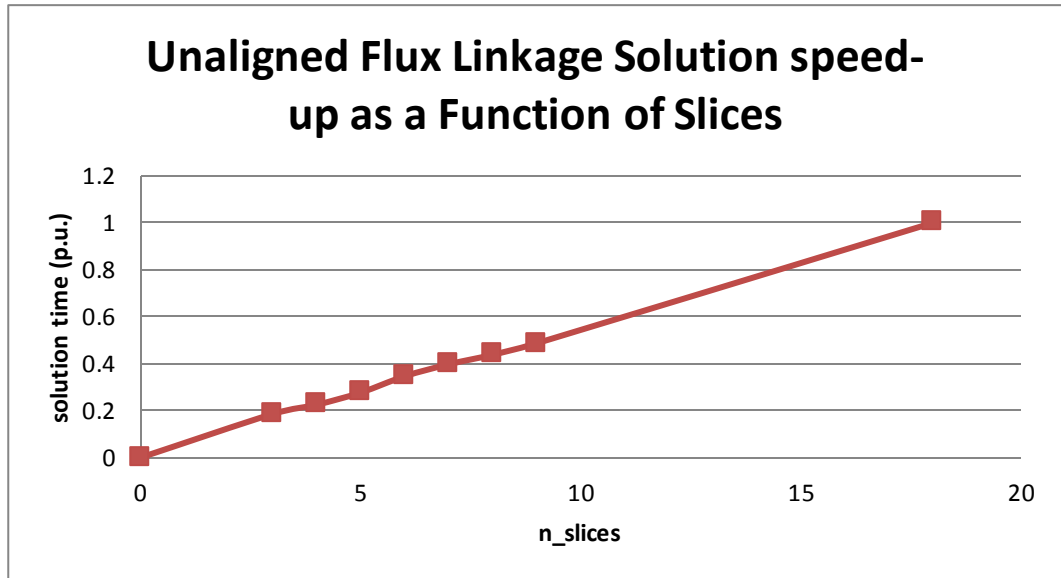


Figure 46: Speed-up of the unaligned flux linkage computations as a function of the number of slices n

The speed up trend of the flux tubes and slices algorithm is linear and compares closely with the aligned flux linkage case. Therefore overall the solution time of the flux TAS method will scale as a product of the number of tubes m and slices n , as indicated by (36). Thus it is most beneficial, from computational efficiency and numerical error minimization point of view, to reduce the number of slices n to a minimum, but not the number of tubes m since it was shown in Fig. 43 that there is a definite minimum number of the tubes beyond which the accuracy becomes highly uncertain. Finally, it should be recognised that the sensitivity analysis presented here was obtained for a single SR machine geometry and not a

range of geometries with varying geometric feature proportions. Therefore, the sensitivity analysis results are taken with caution since it is not known if the same results would have been obtained for widely different SR machine geometries.

4.4 Chapter Summary

Collecting the initial result from the above error sensitivity analysis and Chapter 3 it is now possible to summarise the main advantages of the flux tubes and slices technique compared to the reviewed techniques of comparable computational order.

Features and advantages of using flux TAS compared to the previously reviewed reduced order computational methods:

1. Magnetically nonlinear media supported, not in the original TAS although in principle that could have been implemented, enabling highly saturable sections of the SR machine circuit to be modelled with relatively high numerical accuracy
2. Automatic generation of flux tubes once the equipotential slices, often in a form of straight lines, are constructed, contrary to the published manual flux tube construction techniques in the 'assumed flux paths' and other methods, thus simplifying and speeding up the flux tubes and slices modelling process considerably
3. Automatic generation of TAS slices once the tubes are constructed, not in the original TAS although in principle that could have been implemented, thus further contributing to the flexibility in the control of the geometric modelling errors in terms of the dual bounds
4. Independently controlled numerical accuracy of the cord lengths of the tubes and the cross-sectional areas of the slices, not possible with classical MEC approach, thus allowing the control of the speed of the solution versus numerical accuracy
5. Physical fidelity and intuition of the flux TAS method enables rapid post processing of the magnetic field results, as these are inherent in the analysis of the flux tubes and slices, for accurate estimations of hysteresis and eddy current ferromagnetic core losses

Chapter 5 Flux Tubes and Slices Based SR Machine Analysis and Design Optimization Results

Having established the computational capabilities of the proposed electromagnetic modelling technique of flux tubes and slices the next step in the process of validation is to test the approach for a selected range of SR machine topologies. It is anticipated that the analysis and design optimization based on flux tubes and slices approach of a number of different SR machine topologies will test the modelling capabilities of the approach more systematically. This in turn will have a positive impact upon the wider adoption of the flux tubes and slices method as a computationally accurate and efficient electromagnetic analysis tool.

5.1 General SR Machine Performance Analysis Approach

Before the detailed performance analysis and design of an SR machine is undertaken it is important clearly state the methodology to be used in such analyses. This section will define and briefly review the main techniques used to assess the SR machine performance.

5.1.1 3D Flux-Linkage Map Determination

Once the aligned, unaligned and a suitable number of intermediate translator and stator positions is chosen and the flux-linkage functions for these instances are obtained through the utilisation of the flux tubes and slices approach the complete 3D flux-linkage map of the SR machine can be constructed. Therefore the flux linkage values will be expressed as functions of rotor position, expressed in degrees, and the phase current values. The efficient computational aspects of the construction of the complete 3D flux-linkage map are extensively covered in [71] and [92] among others. From discussion in [92] it is clear that not all excitation current levels need to be considered for each of the flux-linkage functions. This is advantageous from computational efficiency point of view as it reduces the number of computations without any appreciable error in the analysis results. The flux linkage map method of construction based on [92] is adopted in the present analysis of SR machines. The critically important point in the

construction of the flux-linkage map is that of interpolation of gauge curves as was shown on the right-hand side of Fig. 26 in Section 3.1.4. In order to reduce the number of stator-translator instances to be modelled with the improved flux tube modelling method it is assumed, for the present study, that a total of 2 stator-translator/rotor positions are needed. These stator-translator/rotor positions are the fully aligned and fully unaligned. It will be shown in the results section of this report that this assumption, although underestimating the instantaneous electromagnetic torque values of the modelled SR machines, does offer computational efficiency and consistency of the results compared to FEM.

5.1.2 Optimum Angle-Of-Advance Determination

In order to determine the optimum angle-of-advance (AoA) θ_A of an SR motor use of Fig. 47 can be made which depicts the most general speed-torque curve of the machine.

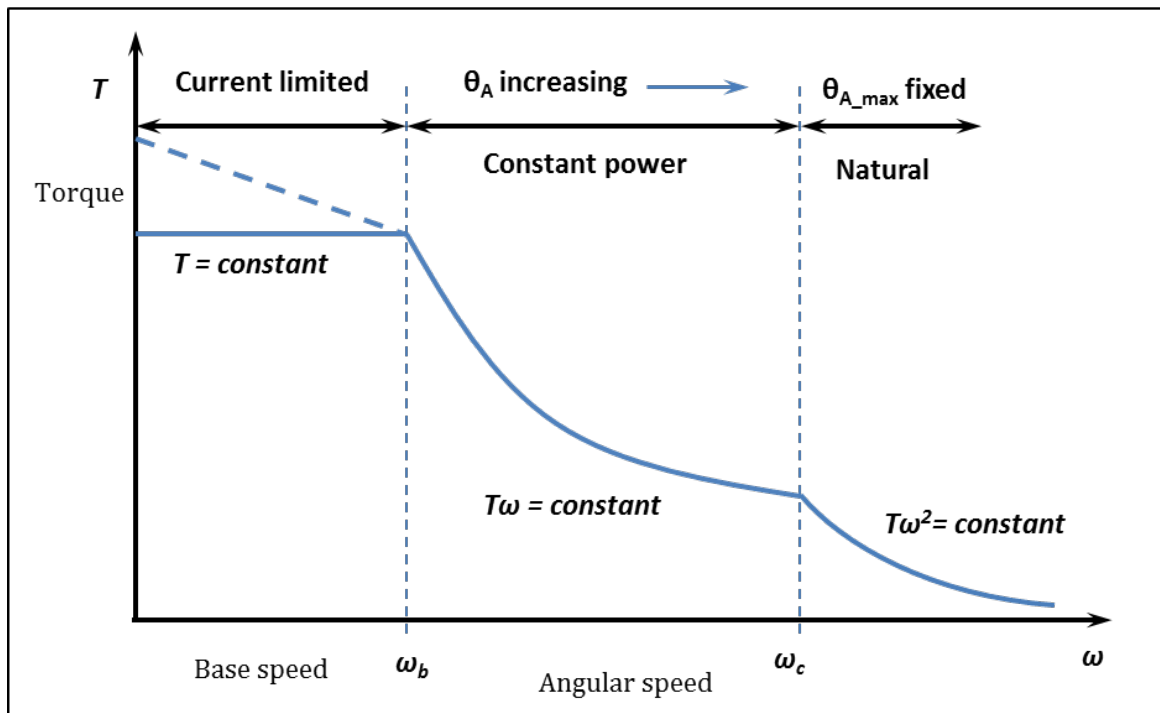


Figure 47: General speed-torque characteristic of SR motor. Adapted from [93]

For SR machine to operate in the constant power range a timing (also termed “turn-on angle”) at which transistor switches of the SR motor drive start conducting the excitation current with respect to rotor position must be determined. This timing will be a function of rotational speed of the SR motor. Same will apply to a linear SR machine where rotor angle will be replaced with an equivalent linear translator displacement. The exact analytical determination of

optimal conduction angle is difficult in practise due to the magnetic nonlinearity [96], however since the 3D flux-linkage map is readily available for that particular SR machine the determination of optimum AoA can be found by sweep of the AoA parameter with respect to instantaneous torque at that particular angular speed. Therefore the general speed-torque curve up to the critical speed ω_c , will be as shown in Fig. 48.

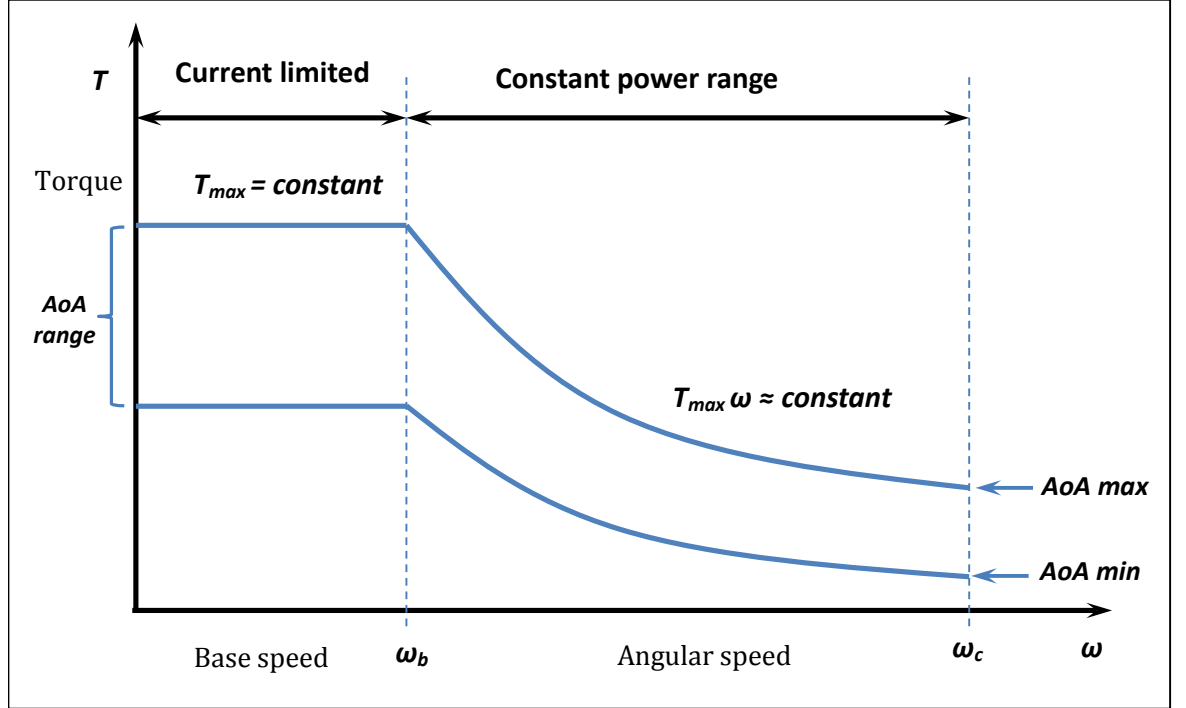


Figure 48: Speed-torque envelopes resulting from AoA parameter sweep.

As can be seen from Fig. 48 the sweep of AoA results in speed-torque envelope and such envelopes will, in general, be of the same characteristic shape for all SR machines. The end of phase current conduction cycle, the turn-off angle (or commutation angle), is assumed to always coincide with full alignment of the excited stator and rotor or translator pole (it is certainly possible to optimise the turn-off angle in addition to the AoA, but this is not considered in this study). Therefore for the present study the AoA is taken as a parameter, within a certain range which will depend on the number of machine phases and major dimensions of the magnetic circuit of the machine. Provided all of this information is available a sweep of the AoA is performed with respect to electromagnetic force for a range of translator speeds of the SR machine.

5.1.3 SR Machine Output Power Curves

In a similar way to the turn-on angle determination the mechanical output power characteristic curves of the SR machine will also be directly affected by the turn-on angle. As noted in [97], [98] traction motor application for electric and hybrid vehicle technology requires as wide a constant power curve as possible, shown in Fig. 48, with the prescribed machine specifications. Therefore, the sweep of AoA parameter serves second important purpose of determination of the width of the constant power curve with respect to mechanical speed of the machine. Of course the speed-power curve will now become a speed-power envelope following the AoA definition from Fig. 48. These results are indispensable in design of traction motors for pure electric and hybrid electric vehicles that operate in essentially constant power range for acceleration and gradability performance as extensively discussed in [35], [50], [97], [99]–[101] amongst others.

5.1.4 Optimization of SR Machines using Genetic Algorithm

Given that a suitable magnetic model of SR machines is available it is possible to incorporate the magnetic model into the proposed design search and optimization cycle as in Fig. 2. For the present study a genetic algorithm (GA) based optimization [102] is considered as it directly benefits from computationally cheap to evaluate surrogate model, which the currently proposed improved flux tubes and slices method is. For the present study a constrained multi-objective optimization with a certain number of continuous design variables was used which maximises certain objective functions. In order to maximize the specified objective functions it is first necessary to express these as negative objective functions which is equivalent to a maximization problem in GA [102]. In order to be consistent with the vocabulary used in GA based optimization literature the objective functions to be maximized will be referred to as minimization problems in the current report.

To start with the constrained multi-objective GA optimization of the SR machines it is important clearly define objective functions to be optimized and associated equality and inequality constraint functions. Two objective functions to be optimized were defined, and therefore will result in a 2D Pareto front [102], as follows. First, minimize output torque value at a specified base speed of the machine. Namely

$$f(T_{\omega})_{\min} = -T_{\omega} = -\frac{\partial W}{\partial \theta} \quad (37)$$

where the right hand side in (37) denotes the surface area between aligned and unaligned flux-linkage curves [78] as in Fig. A1 in Appendix A. Optimizing this objective function will result in torque-dense machine. The second specified objective function; optimize the constant power-speed range of the SR machine. The meaning of the term constant power-speed range is defined in Fig. 49.

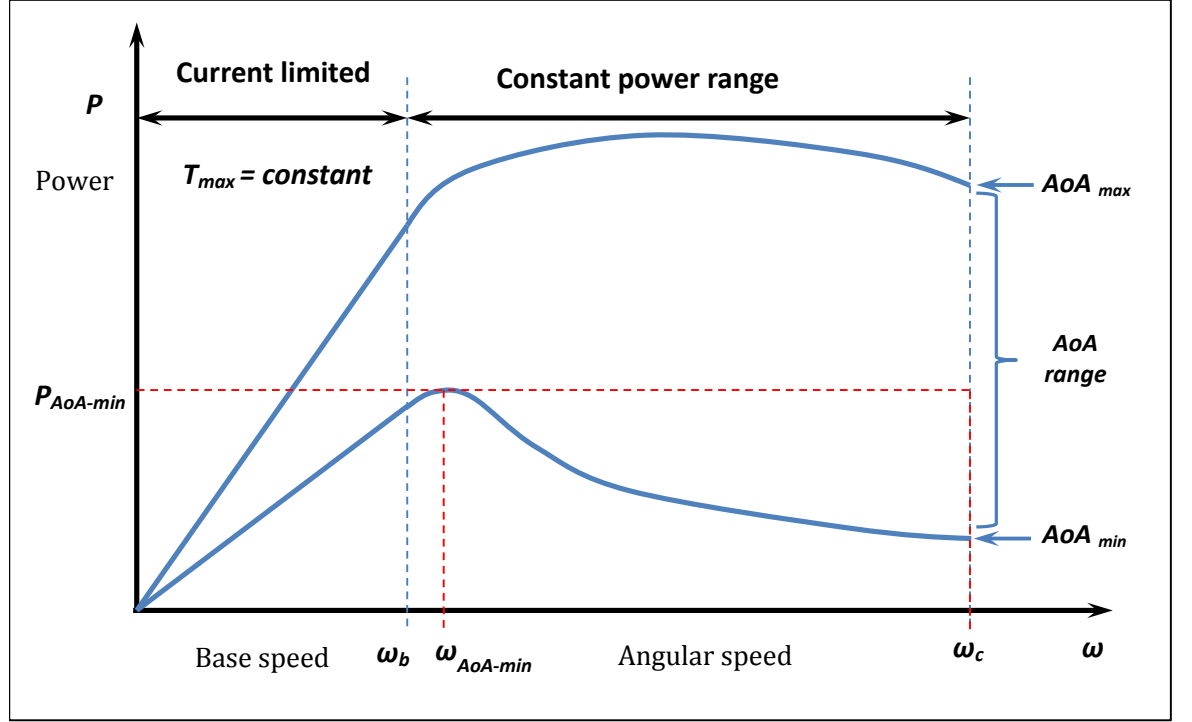


Figure 49: Graphical representation of the GA objective function

In other words; the output power at the minimum AoA value is found and is multiplied by the angular speed range over which this power level can be sustained by the machine, the product thus obtained is minimized using the GA. Referring to Fig. 27 and Fig. 49 this objective function can be expressed as

$$f(P, \omega)_{\min} = -P_{AoA-\min} \times (\omega_c - \omega_{AoA-\min}) \quad (38)$$

It is certainly possible to achieve much higher output power levels as seen from the general speed-power envelope in Fig. 49, but the specified objective function (38) will indicate the minimum amount of power available with the minimum AoA value given minimum speed range. Expression (38) is therefore very conservative and as such it is anticipated will enable unbiased comparison of the different SR

machine designs being optimized and will increase the range of solutions available on the resulting Pareto front.

5.2 Translating Switched Reluctance Machine Analysis and Design Results

5.2.1 LSRM Analysis – Defining the Variables

Table 6 summarizes the LSRM topology (as presented in Section 3.1) geometric design variables and their associated numeric ranges used in the flux tubes and slices based multi-objective GA optimization.

Table 6: GA optimization parameters and their numeric ranges of the three LSRM topologies

	LSRM 12-8		LSRM 16-12		LSRM 16-20	
	min	max	min	max	min	max
Outer diameter, OD (mm)	200	260	200	260	200	280
Inner diameter, ID (mm)	120	180	120	180	120	180
Translator back iron thickness, t (mm)	7	20	6	20	10	20
Translator pole height, t_h (mm)	5	20	5	15	5	15
Stator pole height, s_h (mm)	30	60	30	60	30	60
The pole width, β (degrees, mech.)	8	13	9	12	5	7
Number of turns per coil, N (integer)	50	120	50	100	50	120

A generic LSRM geometry diagram, Fig. A4, has been annotated with the selected design variables and for clarity and reference placed in Appendix A. As can be seen from the above table the numeric values of the selected design variables are varied over wide ranges in order to enable the search within as wide a design space of the selected SR machine topologies as practicable with the given improved flux tubes and slices approach and GA based optimization routine.

As is always the case with the GA based optimization it is necessary to specify the size of populations to be generated by the GA solver. Using the trial and error approach it has been found that the randomly generated population of 50 individuals is more than adequate for this particular investigation and the number of generations was set to 7 for all three machine topologies. Furthermore a specification of elitism score was set to 0.333 which signifies that 33.3% of the

Flux Tubes and Slices Based SR Machine Analysis and Design Optimization Results

randomly obtained elite individuals in each population will be taken as parents for the subsequent generations. This setting reduces the number of suboptimal individuals from being carried over into the subsequent generations and speeds-up the convergence of the algorithm [102]. Finally in order to be able to reproduce all the optimization runs the initial random number seed was recorded. These GA optimization settings are summarized in Table 7.

Table 7: GA based optimization settings for the LSRM topologies

LSRM GA Optimization Settings	
Number of individuals	50
Number of generations	7
Elitism score	0.333
Random number for reproducibility	yes

5.2.2 LSRM Flux Linkage Analysis Results

Using the improved flux tube modelling approach the following flux-linkage functions were obtained and are shown in Fig. 50, for the LSRM geometry shown in Fig. 20, having 16 stator and 20 translator poles as defined in Table 6.

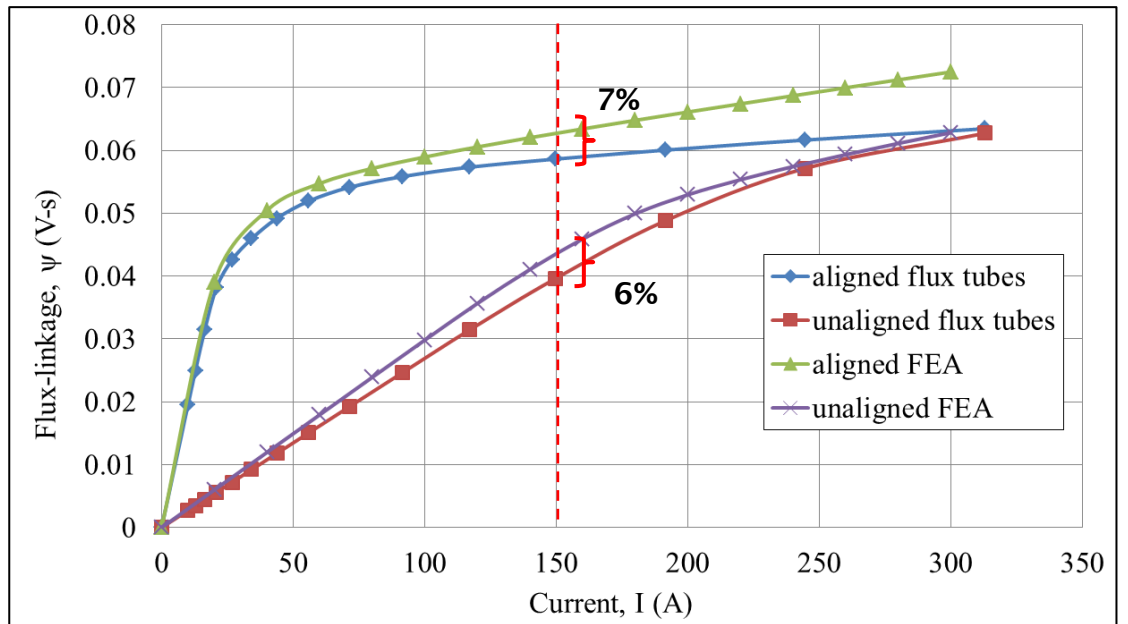


Figure 50: Flux-linkage map of the 16-20 LSRM obtained with flux tubes and slices approach and FEM

Chapter 5

In order to preserve the consistent modelling the number of parallel flux tubes m and tube slices n in the model was set equal to 9. The flux-linkage functions, obtained using the flux tubes method, are compared to FEM simulations of the same LSRM machine in Fig. 50.

Fig. 50 indicates that, in general, there is close agreement of the two methods up to a certain phase excitation current level for each flux linkage function. After this level the flux tube modelling results underestimate the flux-linkage functions of the aligned and unaligned translator cases. As can be expected; this error, which is 7% lower for the aligned case, arises from the simplifying assumptions made in the flux tube modelling process whereby it was assumed that the LSRM is ideal and does not produce any magnetic leakage flux under high levels of phase excitation currents. Furthermore, the unaligned case flux-linkage function in Fig. 50 indicates that such important effects as onset of magnetic saturation are also captured with the improved flux tube approach. Although the saturation effects at the unaligned translator position are quite well defined they will not impact the machine performance as the rated machine current was set to 150A which is below the region of saturation. Flux-linkage curves for the additional two LSRM machine topologies have been obtained and for brevity are placed in the Appendix A. From the visual inspection of these figures it can be deduced that the flux tube approach is accurate for these two additional LSRM topologies as well.

The unaligned translator position flux-linkage function of the improved flux tube method is representative of a general flux-linkage function for this translator position in that it is near-linear function with respect to excitation current, as in Fig. 50. As can be seen from the figure; it is certainly possible to saturate the machine iron parts at the unaligned translator position so that the unaligned case flux-linkage curve becomes highly non-linear, however for this to happen the current levels would be too high for any practical purposes. The unaligned case flux-linkage function, shown in Fig. 50, is lower compared to the FEM obtained flux-linkage curve by 6% but is of higher accuracy of the alternative flux tube modelling approaches described in the literature review chapter of this work.

The following important conclusions can be made with respect to Fig. 50; both the aligned and unaligned flux-linkage functions obtained with the flux tube method preserve the true shapes of the flux-linkage functions as obtained with FEM. This fact, already observed and reported in literature [78] and evident from Fig. 51, has far reaching implications and greater importance – when determining

instantaneous torque and phase current waveforms of the machine – than the exact flux-linkage numerical answer at only saturated or only unsaturated SR machine states. The striking similarity of the instantaneous current and torque values in Fig. 51 confirms this.

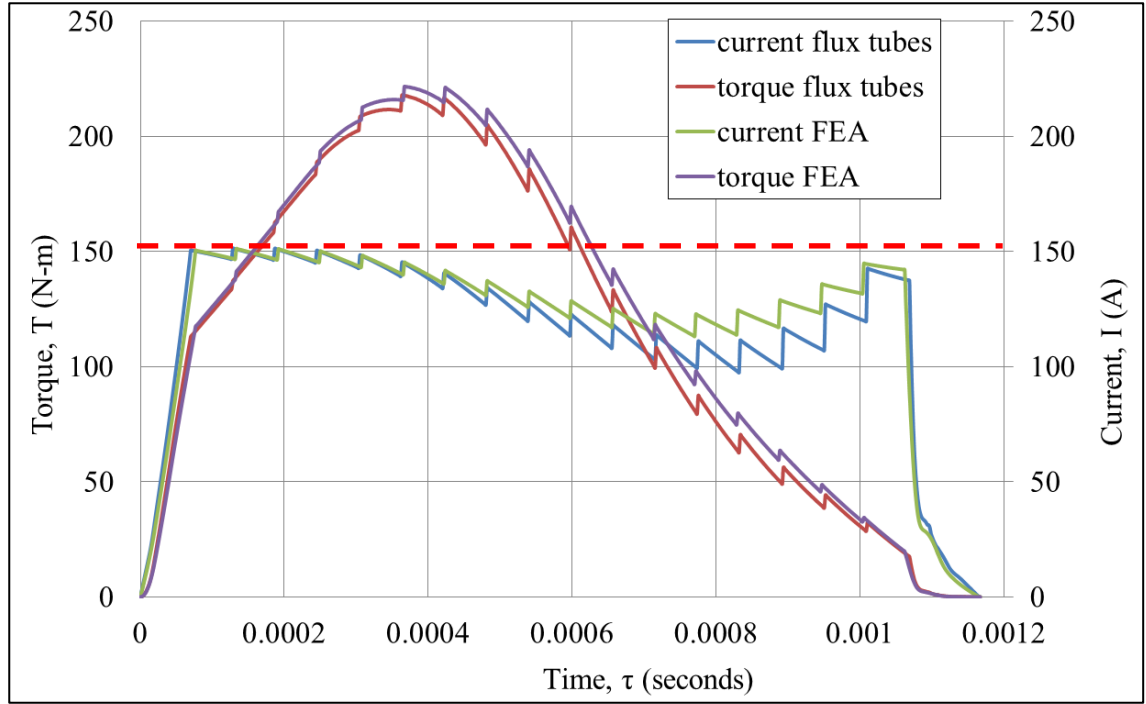


Figure 51: Comparison of instantaneous current and torque waveforms obtained with the flux tube method and FEM at the rated machine speed of 1000 rpm.

Therefore, the analytical errors derivation of the flux tube and slices method given in expressions (20) and (28) (or Table 3 more generally) confirm that the geometric errors associated with the flux tubes can be averaged, if need be, for the purposes of model calibration without loss of the predictive capabilities of the flux tube method. However, all LSRM topology results indicate that the calibration of the flux tubes and slices model was not required in terms of the accuracy of the instantaneous phase current and torque profiles in Fig. 51.

5.2.3 LSRM Optimum Angle-Of-Advance Determination

Utilising the improved flux tube approach the determination of optimum AoA was performed for the analysed LSRM along the lines of Fig. 48. The obtained flux-linkage map pertinent to the analysed LSRM was completed by utilisation of the interpolation method described in [92]. For ease of interpretation and comparison of the AoA analysis results the LSRM was converted from the linear to its

equivalent rotary domain as described in [63]. Fig. 52 shows the relationship between output electromagnetic torque values with respect to rotational speed values of the machine with the AoA taken as a parameter. Also included in the figure is the constant torque and constant power characteristics. These speed-torque curves are customarily termed SR machine torque envelopes [17].

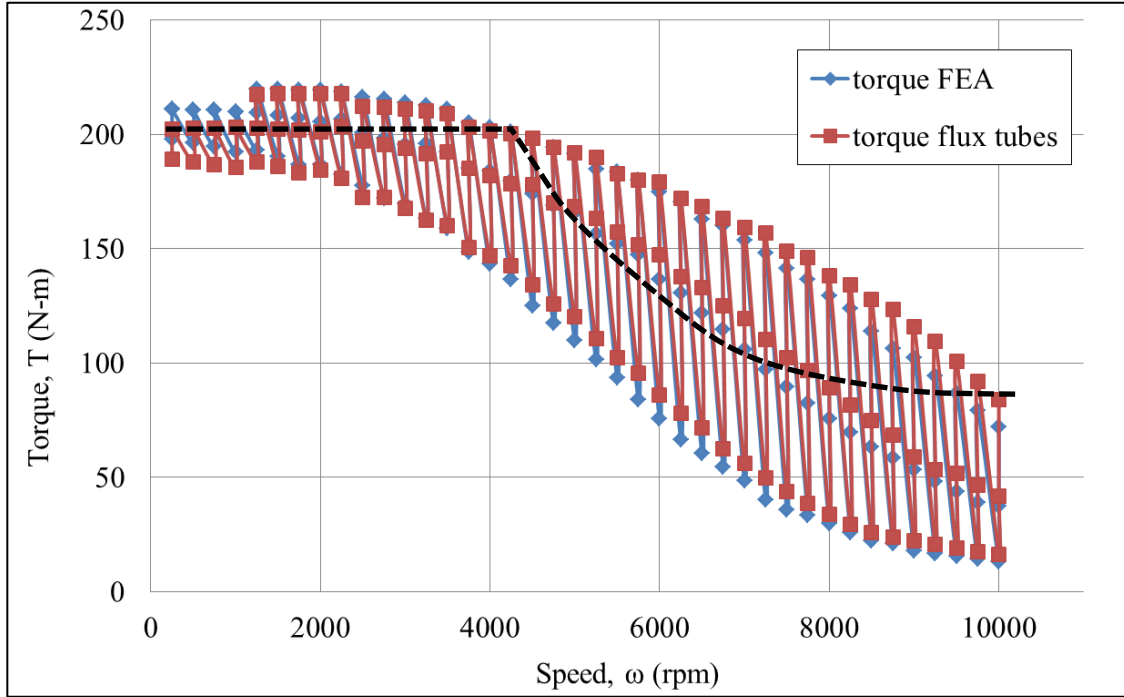


Figure 52: Speed-torque envelopes of the 16-20 LSRM obtained with the improved flux tube approach and FEM

From the above figure it is evident that the obtained torque values with the improved flux tube method compare very well with the FEM results and over the wide speed range. Information in Fig. 52 enables the constant electromagnetic torque and constant power regions of the machine, those specified in Fig. 47, to be found by graphical method if required. These regions are shown in Fig. 52 as dashed lines with the constant torque value set at 200 N-m. It then follows that in order to achieve these two regions the AoA must vary as a function of speed.

According to the design requirements of the LSRM the constant torque value up to the base mechanical speed, ω_b , as in Fig. 47 would be a known specified value. From this information the constant torque line can be drawn on the speed-torque envelope, Fig. 52, and where this line intersects the maximum AoA curve such point would specify the base speed of the machine as defined in Fig. 48. Next, the highest AoA value at which greatest output torque value occurs at the

maximum mechanical speed is the desired end coordinate point for the torque curve which obeys the relationship

$$T \times \omega = \text{constant} \quad (39)$$

where T is average torque and ω is mechanical speed. However, in general this relationship will not be satisfied automatically for SR machines at this coordinate point. Iterative method (graphical or otherwise) is needed to determine the maximum speed at which the torque will obey the hyperbolic relationship of $T = \text{constant}/\omega$. Once such point is determined the complete speed-torque characteristic curve can be constructed for the SR machine. If it is found that this curve does not satisfy the performance requirements of, for example, electric or hybrid vehicle traction motor the whole optimization process is repeated with updated machine dimensions and or other machine design variables as in Fig. 2. Such design process is repeated until an SR machine with satisfactory speed-torque envelope is obtained.

5.2.4 LSRM Output Power Curves Determination

Following the same line of reasoning as for the optimum AoA determination it follows that the output mechanical power of the SR machine will also directly depend on AoA. Fig. 53 shows the superimposed speed-power envelopes obtained with the flux tube method and FEM with the sweep of the AoA parameter.

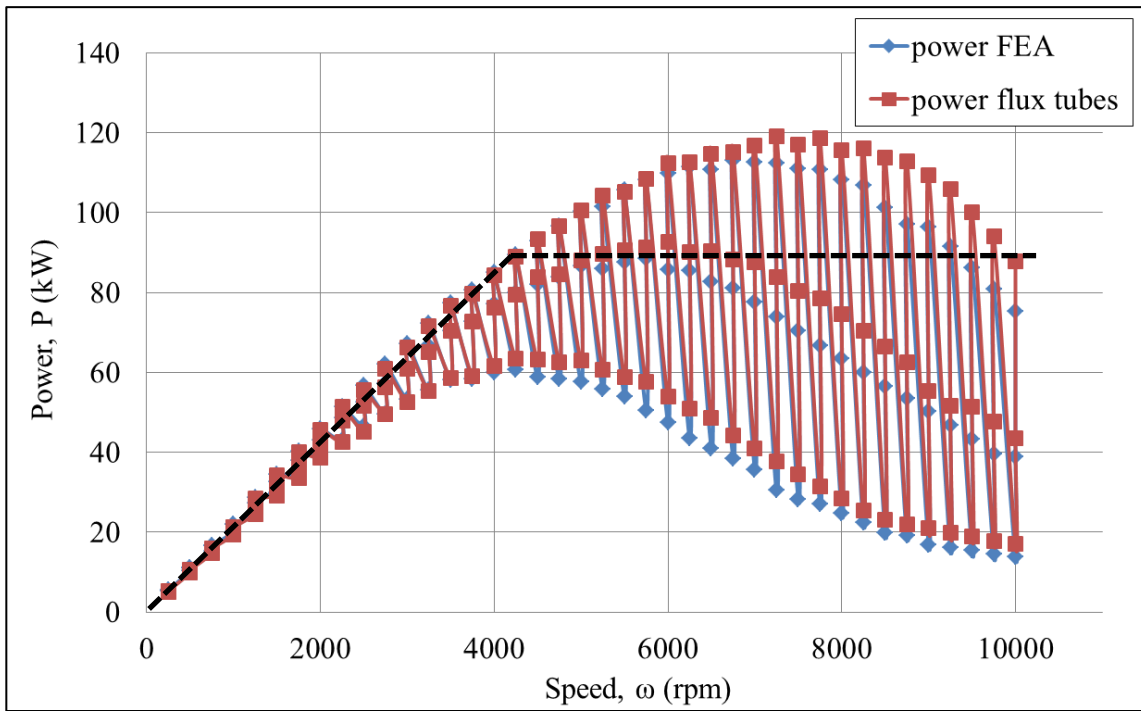


Figure 53: Speed-power envelopes of the 16-20 LSRM obtained with the flux tubes approach and FEM

From the comparison of power envelopes in Fig. 53, obtained with the flux tube method and FEM, it can be seen that the flux tubes method predictions of the output power are very similar to the FEM results over the wide speed range. Of course it directly follows that if the speed-torque envelopes are predicted quite accurately, as in Fig. 52, then the power envelopes will also be of similar accuracy.

From the SR machine design performance requirements or specifications the constant power value will be a known specified quantity. By knowing this value it is then possible to construct a straight line on the output power envelope, corresponding in this case to 88 kW value in Fig. 53, and the lowest mechanical speed at which this line crosses the output power curves is obtained. This speed value can be treated as the point at which constant output torque value starts to obey the hyperbolic relationship stated in (39). Alternatively this intersection point can be regarded as the base speed point, ω_b , as defined in Fig. 47. For vehicular traction applications the traction power requirement is such that the torque value should be constant from zero up to the base mechanical speed. Therefore the machine output power should be increasing linearly with respect to mechanical speed up to the base speed in order to achieve gradability and controllability requirements of the vehicle [103]. This straight line must be below output power curves obtained by the sweep of the AoA parameter, which is

Flux Tubes and Slices Based SR Machine Analysis and Design Optimization Results represented as a sloping dashed line in Fig. 53, to ensure that the SR traction system is able to deliver this power without overheating.

From the preceding analysis it is seen that the optimum AoA will vary with respect to speed, therefore this information will be needed in order to accurately control the SR machine. For example, if the machine is to be designed as a traction motor or generator then the AoA values will completely describe the machine performance for a given mechanical speed (positive or negative) in addition to the phase current values. From Fig. 53 it is apparent that such output power determination approach represents difficulty when deciding which AoA value should be used in the linearly increasing output power range because it appears that all AoA values can be used at that particular mechanical speed. Therefore there is ambiguity present when deciding which AoA would be used by a microcontroller of the SR machine. The only viable solution in this type of scenario is to have a lookup table of all the AoA values for each mechanical speed as well as power demand of the machine. Once such lookup table is available it can be permanently stored in microcontroller memory and each AoA value determined on output power demand instantly, as described in [104], thus avoiding lengthy real time calculations which can put performance limit on the machine operation.

The power envelopes of the additional two LSRM topologies defined in Table 6 have been obtained by use of the flux tubes and slices technique and for brevity are placed in the Appendix A.

5.2.5 LSRM GA Optimization and Pareto Front

As was stated in Section 5.1.4 the GA optimization will result in 2D Pareto front of the optimized LSRM as there were two objective functions specified, namely (37) and (38). After the constrained multi-objective GA optimization was performed for the 16-20 LSRM the Pareto front of the two objectives was constructed as shown in Fig. 54.

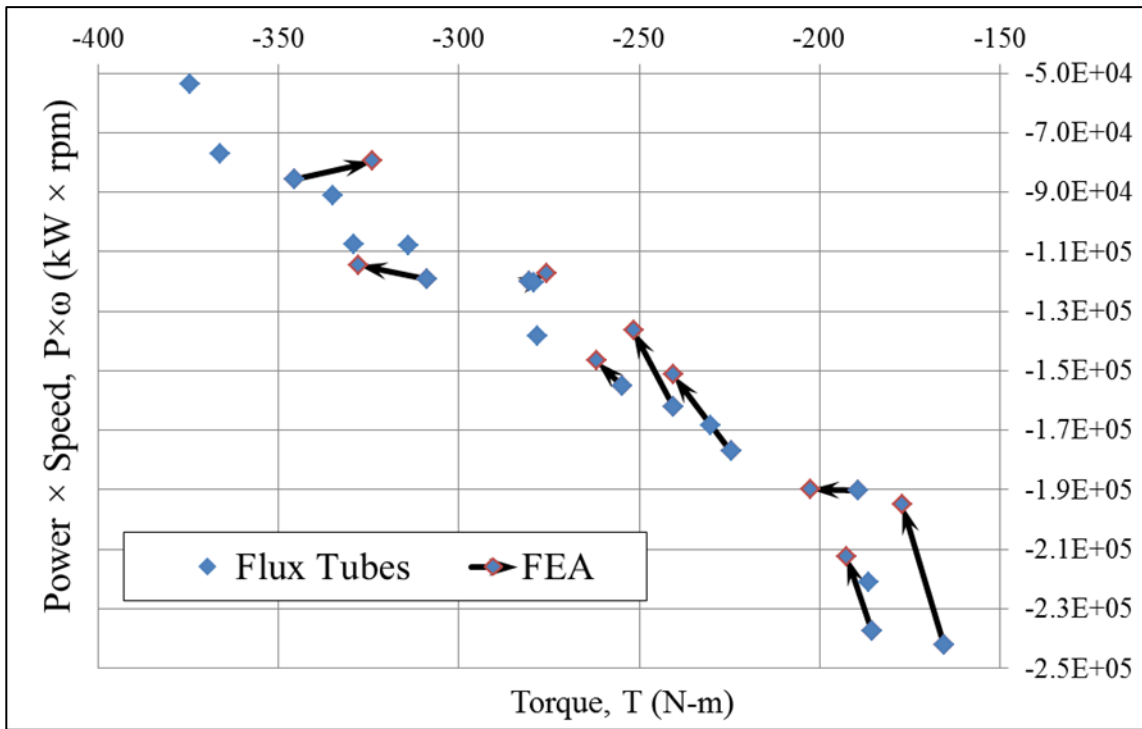


Figure 54: GA optimization Pareto front of the 16-20 LSRM obtained with the flux tube method and FEM

Inspection of Fig. 54 reveals that in general there is a trade-off between the maximum amount of torque available from the SR machine and the wide speed range over which the minimum power can be produced. This should be expected as the very definition of the Pareto front [102] necessitates this to be so. Therefore, all the resulting SR machine designs, in Fig. 54 are near-optimal, now it is a matter of choice which one particular machine design is most suitable for a given application. Of course the resulting Pareto front in Fig. 54 is pertinent to the GA settings which were defined and summarized in Table 6 and Table 7. Quite different data points would have been produced if even a single option from Table 7 was changed. However, it does not mean that the new Pareto front would have resulted in drastically different front compared to Fig. 54, but only the position of the data points on the Pareto front.

In order to check the Pareto front data point accuracy of the flux tube based optimization certain number of these points was reanalysed with FEM. This was performed so that like-for-like comparison could be made of the improved flux tube method and FEM results when the two methods are used in conjunction with GA based optimization. Fig. 54 compares the selected data points of the flux tubes method and FEM. It can be deduced that there is a Pareto front drift of the flux tubes generated design points with respect to the FEM front. By visual inspection of the figure it is seen that the flux tubes approach consistently under-

Flux Tubes and Slices Based SR Machine Analysis and Design Optimization Results

predicts the average torque values, with only a few exceptions, and over-predicts the power-speed product objective function in all the cases. The numerical accuracy and consistency afforded by the flux tubes method is encouraging and is indicative that the method can be applied to the GA based SR machine optimization with reasonable confidence. Table 5 compares the flux tube results accuracy of the two objective function values to those found with FEM.

Table 8: Numerical Error analysis of the 16-20 LSRM GA optimization results

LSRM design number		Average Torque (N-m)	Flux Tubes error (%)	Power \times Speed (kW rpm)	Flux Tubes error (%)
2	Flux Tubes	-280	1.75	-119886	2.25
	FEM	-275.5		-117243	
7	.	-309	-5.76	-119322	4.17
	..	-327.8		-114543	
8	.	-185.2	-3.69	-237551	11.79
	..	-192		-212482	
9	.	-346	6.67	-85719	7.75
	..	-324		-79548	
10	.	-240	-4.46	-162004	18.87
	..	-251.6		-136277	
13	.	-255	-2.69	-154987	5.67
	..	-261.8		-146658	
14	.	-166	-6.42	-242169	24.14
	..	-177		-195065	
15	.	-189	-6.46	-190073	0.11
	..	-203		-189851	
18	.	-225	-6.60	-176848	16.85
	..	-240.4		-151336	
Average error (%)	Flux tubes		-3.1		10.2

General flux tubes error trend in Table 8 indicates that if the average torque values are under predicted then the power-speed product will be over predicted. Therefore the general output power envelopes, as in Fig. 49, will be shifted to the right and downwards relative to FEM based power envelopes, if the former curves are obtained with the improved flux tube method. This shift of the power envelope will be proportional to the predicted torque error terms in Table 8. In effect this error will tend to indicate a machine with lower output torque but higher maximum mechanical speed at which maximum power is attained. However, the error terms in Table 8 can be mitigated by the suggested error reduction strategy whereby the flux tubes obtained aligned and unaligned flux-linkage functions, as in Fig. 50, are calibrated with respect to the same flux-linkage functions obtained with FEM. The calibration parameter is subsequently applied to all the flux tubes based GA generated designs. This strategy, as argued

in [70], is most likely to be effective when the GA generated population size is large, which in this study was set to 50 individuals, and the number of generations is sufficiently large.

The computational accuracy and consistency of the flux tube method is evident. Furthermore the computational efficiency of the flux tube approach is also important and should be compared with the FEM approach. As was stated above the total number of individuals (SR machine designs) generated by the current GA based optimization was

$$\text{total number of designs} = \text{population size} \times \text{number of generations} = 50 \times 7 = 350 \quad (40)$$

Furthermore, the GA optimization terminated as all the design constraints were satisfied at the last generation. The GA optimization has terminated successfully, obtained Pareto front of which is shown in Fig. 54, and the simulation time of 117 minutes was recorded. Therefore the time required to generate and fully analyse each SR machine design instance in the GA study, on average, was

$$\text{design simulation time} = \frac{\text{total simulation time}}{\text{total number of designs}} = \frac{7042(\text{seconds})}{350} \approx 20(\text{seconds}) \quad (41)$$

In contrast to the above answer each of the replicated flux-linkage maps obtained using FEM, as in Fig. 50, of the selected designs from the obtained Pareto front in Fig. 54 required, on average, 120 seconds to compute including the meshing time of each instance. Therefore, the FEM based analysis is markedly slower compared to the flux tube approach, yet order of magnitude more accurate and generally more versatile, also remembering that the time required to obtain the information in Fig. 52 and Fig. 53 was not accounted for in the FEM timing.

Pareto fronts and numerical error tables of the additional two LSRM topologies are placed in Appendix A.

5.3 Rotating Switched Reluctance Machine Analysis and Design Results

The rotating SR machine analysis and optimization based on the flux tubes and slices approach proceeds in much the same way as described in the previous section. However, since the radial flux SR machine geometry, as described in Section 3.2.1, contains slightly larger number of geometric parameters these

Flux Tubes and Slices Based SR Machine Analysis and Design Optimization Results should be described in detail explaining their significance. This helps to assess their impact on the optimization of the SR machine and its performance.

5.3.1 Rotary SR Machine Analysis – Defining the Variables

Table 9 summarizes the rotary SR machine (as presented in Section 3.2) geometric design variables used in the flux tubes and slices based electromagnetic analysis of the two particular designs, namely SRM1 and SRM2. The machine data is taken from literature [2] where it was already shown the performance of this particular machine through FEM analysis. Therefore, this particular analysis is performed first to ascertain if the flux tubes and slices method yields adequate and accurate results compared to FEM based analysis for a known machine design.

Table 9: Rotary 18/12 SR machine design variables. Adapted from [2].

18/12 SR Machine Design Parameters	SRM1	SRM2
Outer diameter (mm)	269	269
Stack length (mm)	135	135
Air gap length (mm)	0.5	0.5
Iron core material	10JNEX900	10JNEX900
Wire diameter (mm)	0.95	0.6
Wire turns (turns)	13	17
Wire parallel turns (turns)	13	22
Slot fill factor (%)	54.1	57.0
Current, peak (Apk)	380	320
Max. current density (A/mm ²)	24 (24)	33 (33)
RMS current (@1200rpm) (Arms)	241 (240)	204 (206)
Max Torque (@1200rpm) (N-m)	354 (340)	415 (400.4)
Number of phases	3	3
() indicate measured values		

Table 10 summarizes the rotary SR machine geometric design variables and their associated numeric ranges used in the flux tubes and slices based multi-objective GA optimization. The initial values in the table are from Table 9 SRM2 machine design as this design was denoted as superior compared to the SRM1 design [2] through FEM analysis. Therefore this particular design was chosen as a starting point (seed) for the generation of all the subsequent designs in the GA optimization.

Table 10: Rotary 18/12 SR machine geometric design variables and their ranges

18/12 SR Machine Design Paramete	Initial Value	Value Range
Stator Outer Diameter, OD (mm)	269	269
Back Iron Thickness, t_b (mm)	17.25	5 - 25
Rotor Pole Height, h_r (mm)	19.5	10 - 30
Stator Pole Height, h_s (mm)	27	10 - 50
Stator Pole Angle, β_1 (degrees)	11	6 - 12
The Pole Root Angle, β_2 (degrees)	11	6 - 12
Shaft Diameter, s_d (mm)	100	80 - 160
Wire Turns, N (turns)	17	5 - 50
Stack Thickness (mm)	135	135
Air Gap Length g (mm)	0.5	0.5
Number of Phases (n)	3	3
Peak Phase Current (A _{pk})	320	320
DC Supply Voltage (V)	500	500

A generic rotary SR machine geometry diagram, Fig. A3, has been fully annotated with the selected design variables and for clarity and reference is placed in Appendix A. As can be seen from the above table the numeric ranges of the selected design variables are varied extensively in order to enable the search within as wide a design space of the selected SR machine topology as practicable with the given improved flux tubes and slices approach and GA based optimization routine.

The GA based optimization of the rotary 18-12 SR machine topology with a specified size of populations to be generated by the GA solver was undertaken. Using the trial and error approach it was found that the randomly generated population of 100 individuals is adequate for this particular investigation, bearing in mind that the number of design variables in Table 10 is quite high, and the number of generations was set equal to 13 for the rotary 18-12 SR machine topology. Furthermore a specification of elitism score was set to 0.333 which signifies that 33.3% of the randomly obtained elite individuals in each population will be taken as parents for the subsequent generations. Finally, in order to be able to reproduce all the optimization runs the initial random number seed was recorded. These GA optimization settings are summarized in Table 11.

Table 11: GA based optimization settings for the rotary 18/12 SR machine topology

Rotary 18/12 SR Machine GA Optimization Settings	
Number of individuals	100
Number of generations	13
Elitism score	0.333
Random number for reproducibility	yes

5.3.2 Rotary SR Machine Flux Linkage Analysis Results

As a starting point of the electromagnetic analysis of the rotary 18/12 SR machine topology the aligned and the unaligned flux-linkage functions were found using the flux tubes and slices method and these are compared with the flux linkage functions found with FEM in Fig. 55. In order to preserve the consistent modelling process the number of parallel flux tubes m and tube slices n in the model was set equal to 9.

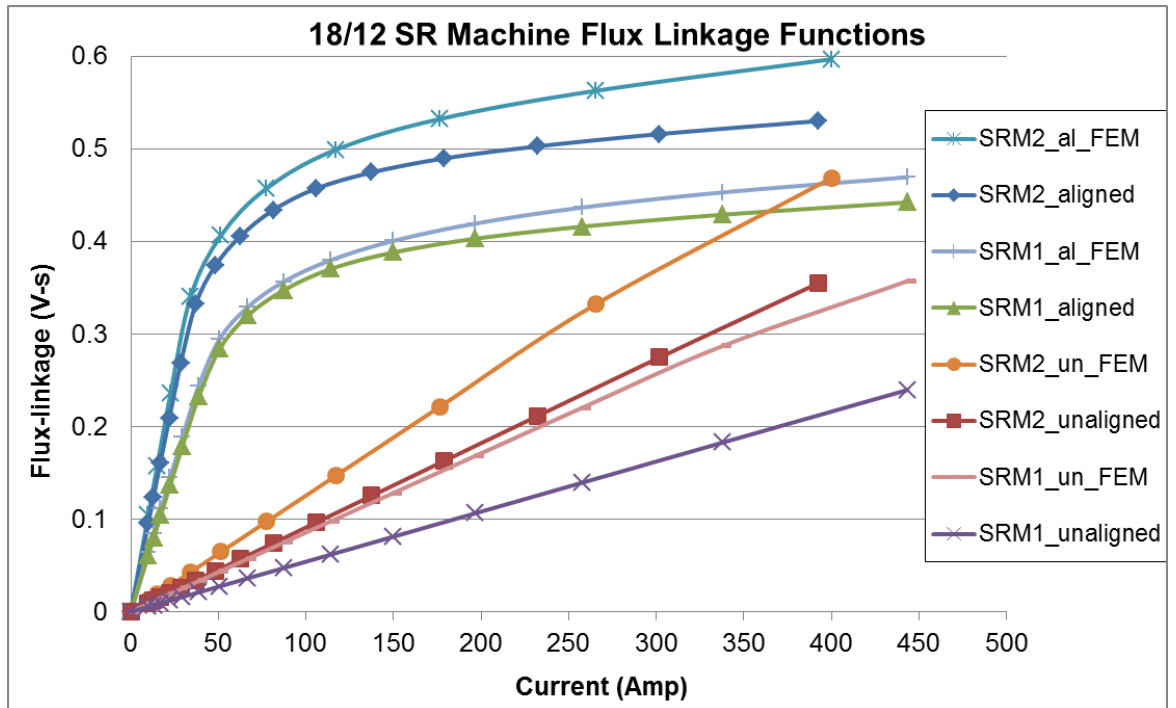


Figure 55: Comparison of the aligned and unaligned flux-linkage functions of the 18/12 SR machine

The flux-linkage functions in Fig. 55 are for the two SR machine designs whose design parameters are listed in Table 9, also remembering to note the different peak current values for the two SR machine design in the table.

The visual comparison of the results in Fig. 55 indicates quite clearly that the errors of the respective flux-linkage functions are somewhat large. Although it should be noted that the SRM2 design flux-linkage functions obtained with the two alternative methods enclose roughly the same areas between them which effectively means that the average torque and *rms* phase current values will be of comparable numeric values. Same reasoning does not apply for the SRM1 machine flux-linkage in Fig. 55 since the aligned functions of the two methods are almost coincident whereas the unaligned functions are far apart.

Therefore, from Fig. 55 it is clear that the construction of the flux tubes and slices, as described in Section 3.2, have introduced the geometric errors, namely the cross-sectional area error α and the cord length error λ , into the reluctance values of the two flux linkage functions. Most likely reason for the introductions of the two geometric errors are the non-rectilinear geometric features of the rotary SR machine magnetic circuit as well as the complex shape of the unaligned air gap flux path. These factors make it far more difficult to fit accurate flux tubes to rotary SR machines compared to simpler rectilinear geometries of LSRM. The present results in Fig. 55 necessitate the calibration of the reluctance values obtainable with the flux tubes and slices method with respect to FEM results. However, since it was decided to use the SRM2 design as the seed design in the multi-objective GA based design optimization study the calibration of the flux tube model was made with respect to this design. Furthermore the SRM2 design was indicated as superior design compared to SRM1 design in the original work in [2].

Figure 56 presents the calibrated flux tubes and slices flux linkage functions with respect to FEM results.

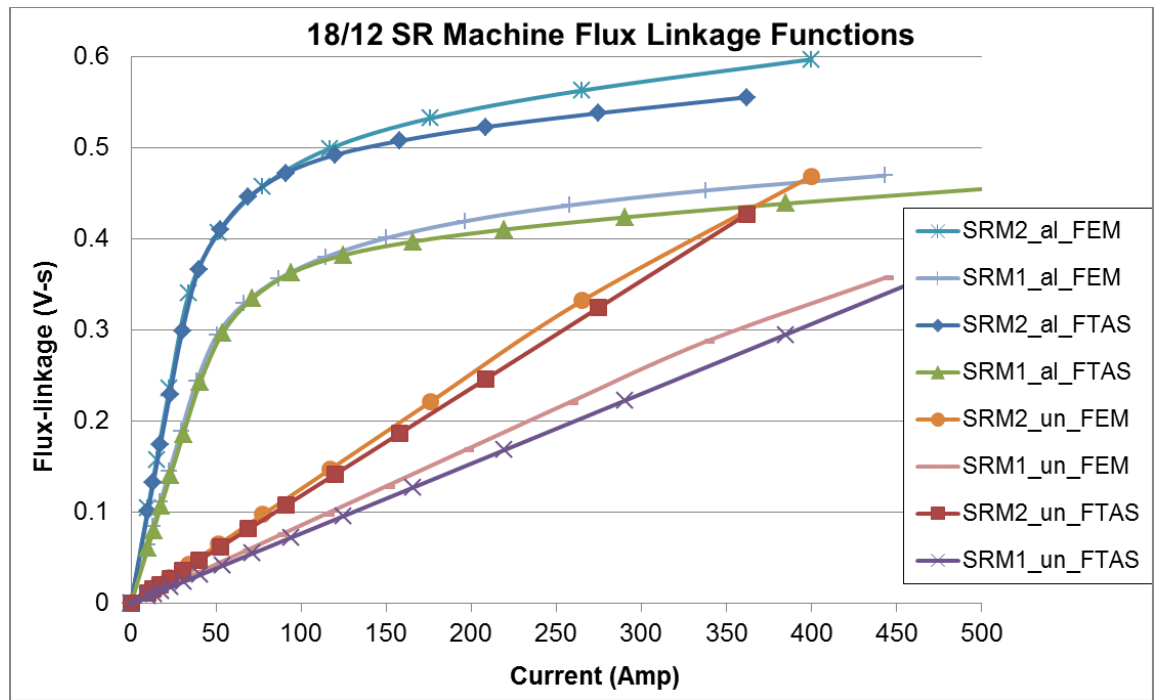


Figure 56: Calibrated flux tubes and slices flux linkage functions with respect to FEM results

The aligned and unaligned flux linkage functions of the SRM2 design were scaled by a factor of 1.17 and 1.25 respectively. Effectively, all the tube cross-sectional areas were increased by 17% and 25% for the aligned and unaligned cases respectively. However, since the flux tubes and slices method has fairly flexible flux tube cord generation capabilities based on cubic-spline interpolation the cord length calibration was not undertaken.

Further observation of the flux tubes and slices results is that both flux linkage functions for the SRM2 design do not capture the leakage flux effects that are otherwise clearly visible in the FEM results plot in Fig. 27 and Fig. 28. For the aligned case at approximately 150A the flux tubes and slices method starts deviating from the FEM result mostly due to the absence of the leakage flux effect in the former method. In the real magnetic circuit the leakage flux tends to increase the aligned flux linkage, i.e. tends to decrease the reluctance, since the leakage flux takes least resistant path thus reducing the saturation of the other flux paths. On the contrary flux tubes and slices method has all the flux tubes fixed for all the phase current excitation levels.

In addition to the calibration of the SRM2 design the calibration of the SRM1 design was also accomplished and the results are shown alongside in Fig. 56. As before the aligned and unaligned flux linkage functions obtained with the flux tubes and slices method were scaled by a factor of 1.22 and 1.5 with respect to

the FEM results. In effect, all the cross-sectional areas were increased by 22% and 50% for the aligned and unaligned flux linkage functions respectively. Similar trend emerges for the SRM1 design flux linkage functions obtained with the calibrated flux tubes and slices method. The leakage flux is not captured and therefore the values are underestimated somewhat beyond the 150A phase current level in Fig. 56.

Further question arises if we compare the calibration parameters of the cross-sectional areas for the SRM2 and SRM1 machine designs. As a first consideration it would appear that same calibration parameters would produce the same scaling effect of the flux linkage functions of the two rotary 18-12 SR machine designs as in Fig. 56. The aligned flux linkage scaling factors of the two SR machine designs are of comparable magnitude. Yet, for the unaligned flux linkage functions for the two SR machine designs the scaling factor has a difference of 2. The reason for this discrepancy can be identified by examining Fig. 57 for the unaligned rotor position of the SRM1 rotary 18-12 SR machine.

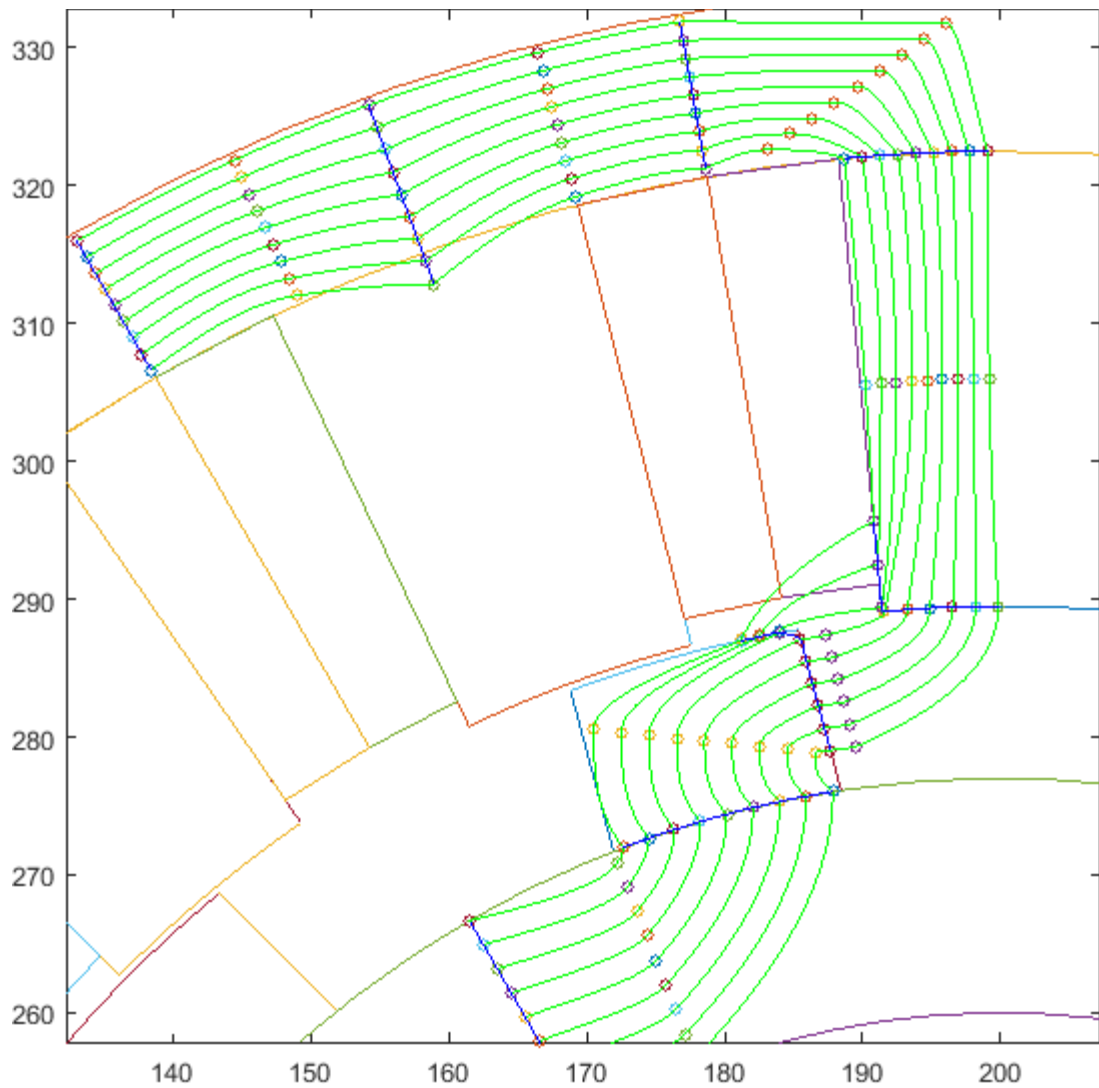


Figure 57: Unaligned air gap flux tube distribution of SRM1 18-12 SR machine

It is apparent that the SRM1 design results in less realistic flux distribution compared to SRM2 design in Fig. 27. However, it can also be seen that SRM1 design incorporates smaller rotor poles compared to SRM2 design. For this reason and since the particular slices defining the air gap flux paths were fixed to the rotor pole geometry the calibration parameter for the unaligned rotor position of the two designs differs substantially. This is far from the ideal scenario, but it will be seen in the subsequent sections of the report that the flux tubes and slices method can still produce meaningful and accurate results even when the geometric parameters are varied over a substantial range of values. However, the numerical results can be improved if the geometric parameters of the machine are chosen to vary between upper and lower levels recommended in literature in [71] and [105] for example.

In addition to the direct comparison of the flux linkage curves of the uncalibrated as well as calibrated flux tubes models in Fig. 55 and Fig. 56 the instantaneous

Chapter 5

current and torque profiles have been generated as a post-processing step in the 18-12 SR machine design analysis. Two figures were used to capture the differences in the results prior to the flux tubes and slices model calibration and after the calibration as shown in Fig. 58 and Fig. 59 respectively for the rotational speed of 1250 (rpm).

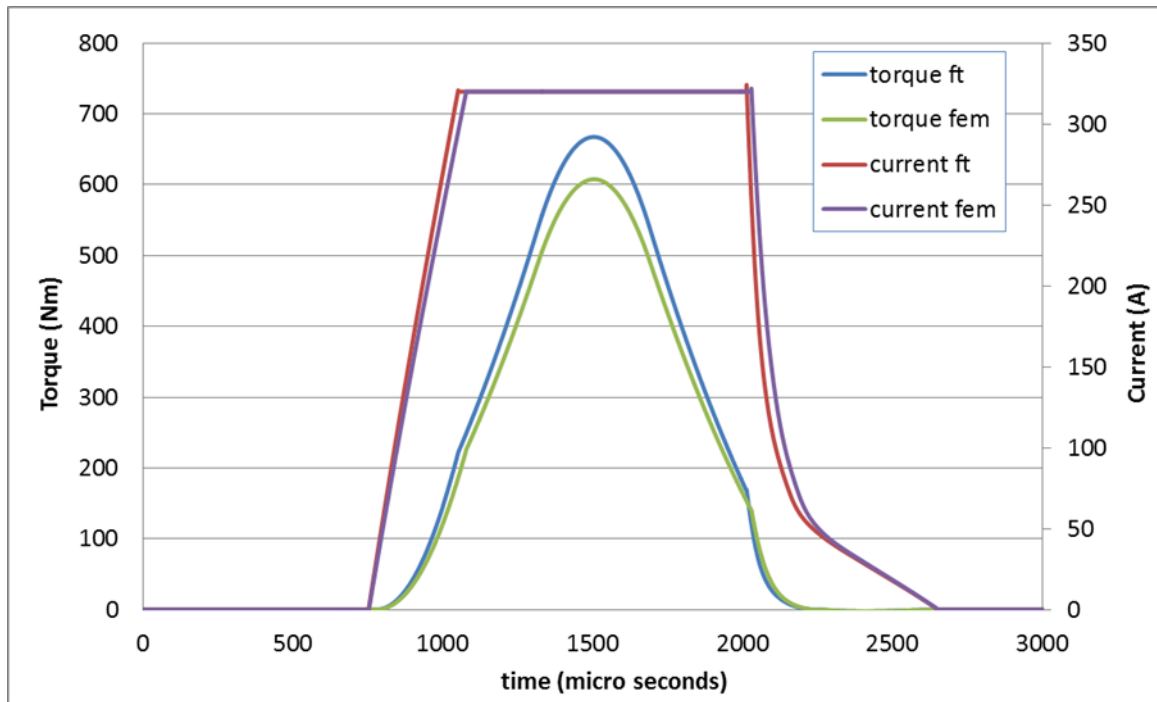


Figure 58: Uncalibrated flux tubes and slices based instantaneous current and torque profiles of the 18-12 rotary SR machine compared to FEM

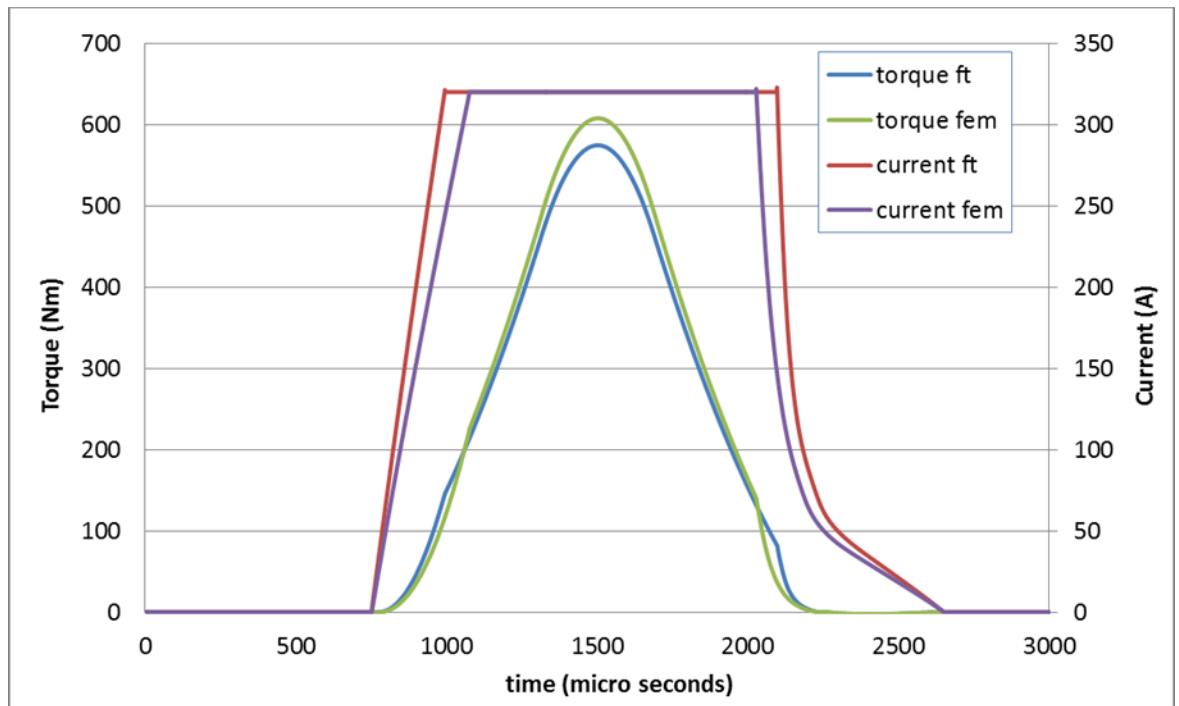


Figure 59: Calibrated flux tubes and slices based instantaneous current and torque profiles of the 18-12 rotary SR machine compared to FEM

From the above two figures it can be inferred that the difference between the pairs of curves is noticeable with the instantaneous torque profile being overestimated in the uncalibrated case whereas it is underestimated in the case of the calibrated model. The effect of overestimation is of course less desirable as it produces unrealistic designs in the large number of designs generated as in GA optimization for example. Furthermore, both Fig. 58 and Fig. 59 depict the instantaneous torque at a particular rotational speed of the machine and are likely to deviate further as the mechanical speed is increased and AoA parameter is varied. However, the visualisation of such deviations would require exhaustive sweep of the speed and AoA parameters [106] which is not attempted here since instead the average torque envelopes were produced for the comparison in the following section.

5.3.3 Rotary SR Machine Optimum Angle-Of-Advance Determination

Utilising the improved flux tubes and slices approach the determination of optimum AoA was performed for the analysed rotary SR motor along the lines of Fig. 48. The obtained flux-linkage map pertinent to the analysed SR motor was completed by utilisation of the interpolation method described in [84] which was shown in Fig. 26. Figure 60 presents the relationship between output average electromagnetic torque values with respect to rotational speed values of the SR

machine with the AoA taken as a parameter. These speed-torque curves are termed SR machine torque envelopes.

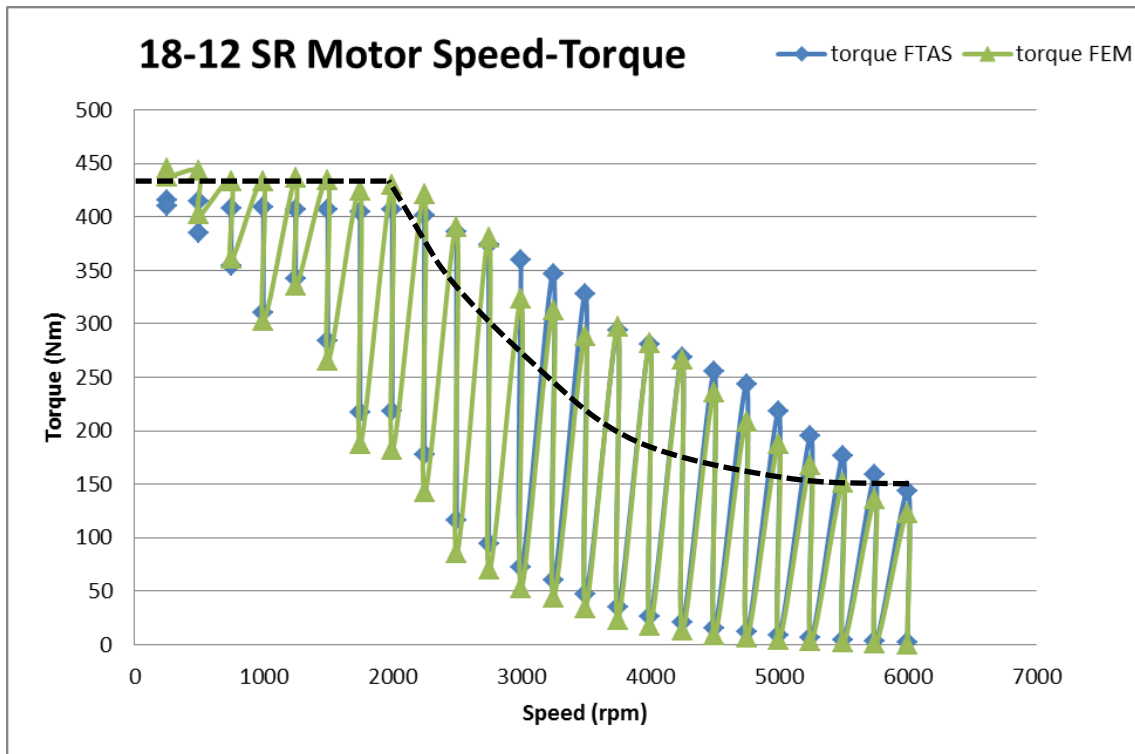


Figure 60: Speed-torque envelopes of the 18-12 rotary SR motor obtained with the improved flux tube approach and FEM

From the above figure it is evident that the obtained torque values with the improved flux tube method compare very well with the FEM results and over the wide speed range for the rotary SR machine. Information in Fig. 60 enables the constant electromagnetic torque and constant power regions of the machine, those specified in Fig. 47, to be found by graphical method if required. These regions are shown in Fig. 60 as dashed lines with the constant torque value set at approximately 410 N-m. It then follows that in order to achieve these two operating regions the AoA parameter must be adjusted as a function of speed between the minimum and maximum values.

5.3.4 Rotary SR Machine Output Power Curves Determination

As has been already inferred from the LSRM case presented earlier for the optimum AoA determination it follows that the output mechanical power of the rotary SR machine will also be directly dependent on the AoA. Fig. 61 shows the

Flux Tubes and Slices Based SR Machine Analysis and Design Optimization Results

superimposed speed-power envelopes obtained with the flux tubes and slices method and FEM with the maximum and minimum values of the AoA parameter.

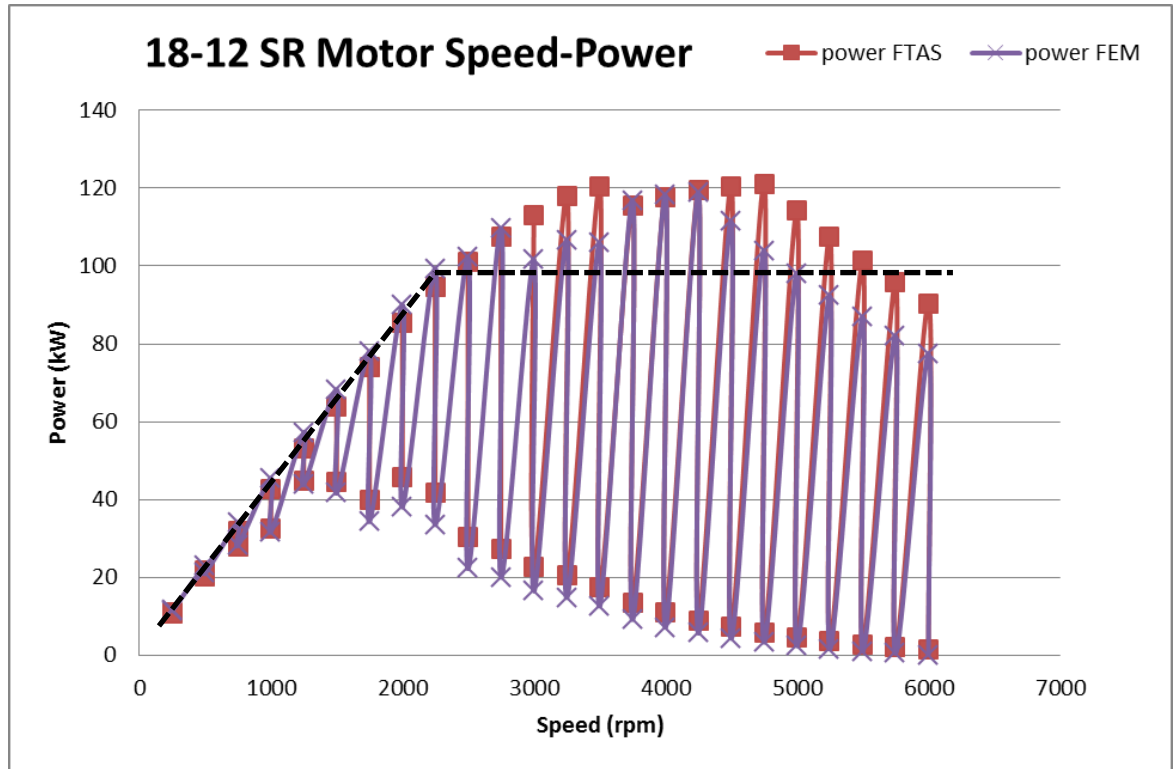


Figure 61: Speed-power envelopes of the 18-12 rotary SR motor obtained with the flux tubes and slices approach and FEM

From the comparison of the power envelopes in Fig. 61, obtained with the flux tubes method and FEM, it can be seen that the flux tubes method predictions of the output power are very similar to the FEM results over the wide speed range. Of course it directly follows that if the speed-torque envelopes are predicted quite accurately, as in Fig. 60, then the power envelopes will also be of similar accuracy.

From the rotary SR machine design performance requirements or specifications the constant power value will be a known specified quantity. By knowing this value it is then possible to construct a straight line on the output power envelope, corresponding in this case to 90 kW value in Fig. 61, and the lowest mechanical speed at which this line crosses the output power curves is obtained. This speed value can be treated as the point at which constant output torque value starts to obey the hyperbolic relationship stated in (39). Alternatively this intersection point can be regarded as the base speed point, ω_b , as defined in Fig. 47. For vehicular traction applications the traction power requirement is such that the torque value should be constant from zero up to the base mechanical speed.

Therefore the machine output power should be increasing linearly with respect to mechanical speed up to the base speed in order to achieve gradability and controllability requirements of the vehicle [95]. This straight line must be below output power curves obtained by the sweep of the AoA parameter, which is represented as a sloping dashed line in Fig. 61, to ensure that the SR traction system is able to deliver this power without overheating.

From the preceding analysis it is seen that the optimum AoA will vary with respect to speed, therefore this information will be needed in order to accurately control the SR machine. For example, if the machine is to be designed as a traction motor or generator then the AoA values will completely describe the machine performance for a given mechanical speed (positive or negative) in addition to the phase current values. From Fig. 61 it is apparent that such output power determination approach represents computational difficulty when deciding which AoA value should be used in the linearly increasing output power range which calls for goal seeking optimization routines. Once the AoA values are known the values can be stored in the computer memory and would subsequently be used by a microcontroller of the SR machine. The only viable solution in this type of motor control scenario is to have a lookup table of all the AoA values for each mechanical speed as well as power demand of the machine. Once such lookup table is available it can be permanently stored in microcontroller memory and each AoA value determined on output power demand instantly, as described in [96], thus avoiding lengthy real time calculations which can put performance limit on the machine operation [107].

5.3.5 Rotary SR Machine GA Optimization and Pareto Front

The multi-objective optimization of the 18-12 rotary SR machine with the given design variables in Table 9 was performed and a 3D pareto front obtained as shown in Fig. 62.

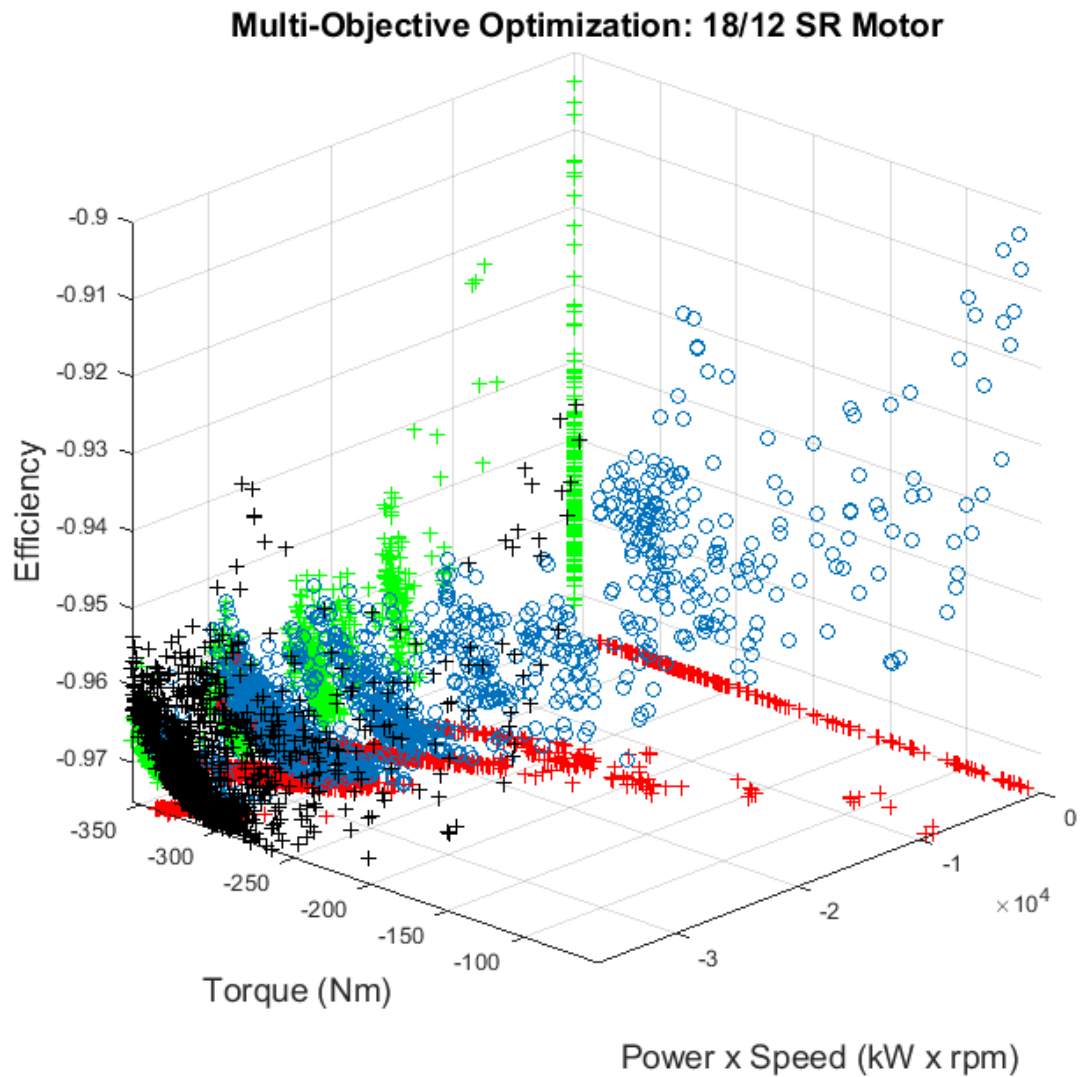
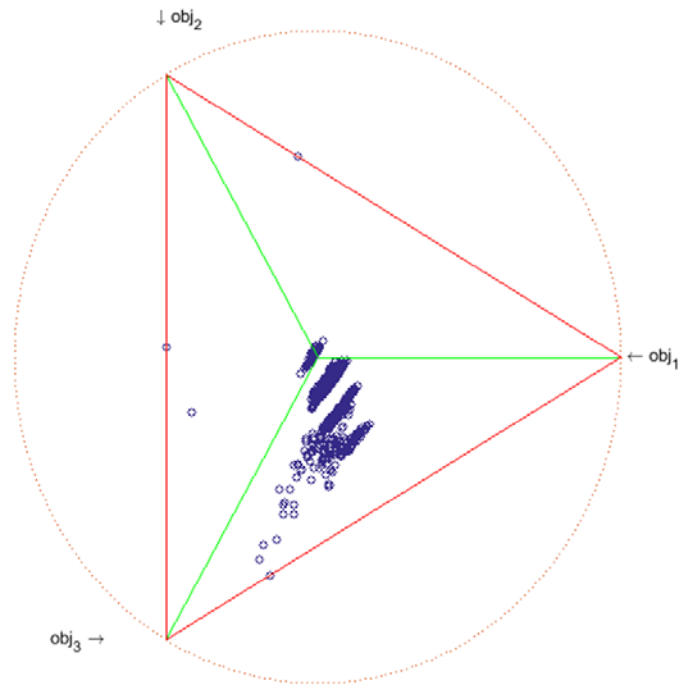


Figure 62: GA optimization Pareto front of the 18-12 rotary SR motor obtained with the flux tube method

In order to better visualise the 3D pareto front in Fig. 62 the 3D-RadVis technique [108], a particular multi-dimensional radial visualisation technique, was utilised to represent the front more succinctly as shown in Fig. 63.

Radial Coordinate Visualization. 3-Objective Optimization
levels per machine design plotted in 2D space.
Figure shows this data is not separable in 2D space



Radial Coordinate and Distance (d) Visualization. 3-Objective Optimization
levels per machine design plotted in 3D space for
1317
design points

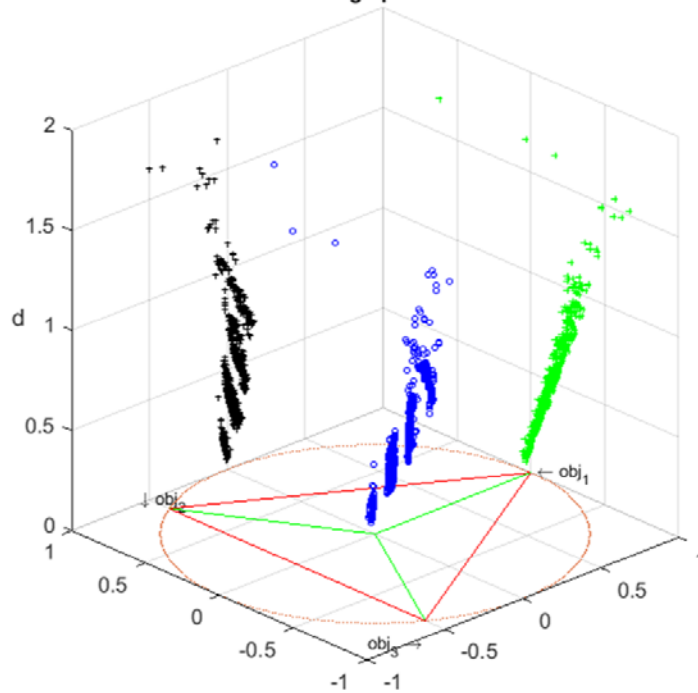


Figure 63: 3D-RadVis technique used to visualise the GA obtained 3D pareto front of the 18-12 rotary SR machine

In Fig. 63 all free objectives resulting from each of the generated rotary SR machine designs in Fig. 62 were scaled to a unity, with the smallest objective represented by zero and the largest objective being represented by one, and were plotted on a radial plot. In addition the pareto front distance d which represents the distance to the utopian pareto frontier of each SR machine design was calculated as can be seen on the lower part of Fig. 63. The SR machine designs with the smallest pareto front distance d are normally selected first. Such plot can now be very effectively used to select strictly non-dominated designs from the entire cohort, one at a time, or in multiples and if such designs are found to be non-satisfactory in other variables they are discarded. Then the entire scaling process of the objectives is repeated again and the pareto front distance d is recalculated for each remaining design thus exposing new strictly non-dominated machine designs [108].

As has been accomplished in the case of the LSRM optimization some of the rotary SR machine designs from the pareto front in Fig. 63 were randomly selected for further comparison with FEM analysis in order to check the accuracy afforded with the flux tubes and slices method as would be performed in the proposed design cycle of Fig. 2. The absolute error comparison of the randomly selected SR machine designs between the alternative methods is shown in Fig. 64.

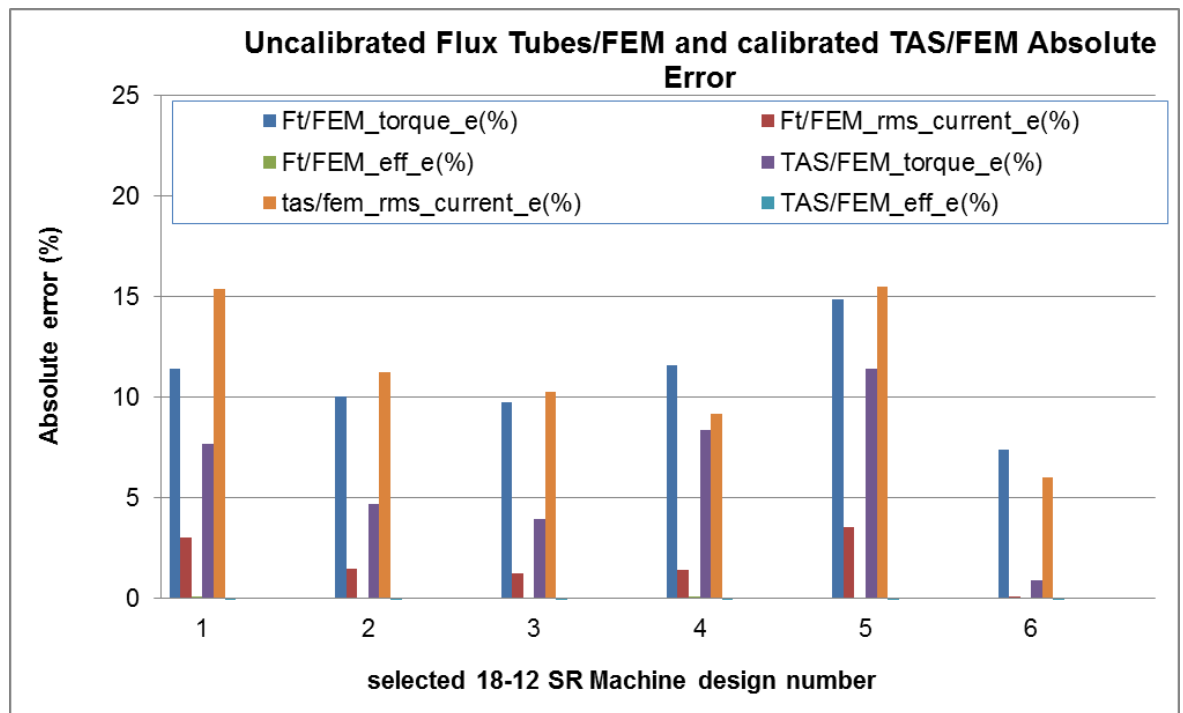


Figure 64: Numerical error analysis of the 18-12 rotary SR motor GA optimization results obtained with the uncalibrated and calibrated flux tubes and slices method and FEM

Chapter 5

Figure 64 indicates that the uncalibrated flux tubes and slices method produces torque values that are in error compared to FEM results at 11% mark on average across the randomly selected designs from Fig. 63. The *rms* current of the uncalibrated method is in very good agreement with the FEM results as well as the efficiency, both much less than 5% on average. On the contrary, the calibrated flux tubes and slices method results have the torque values in much better agreement with FEM results at 6% mark on average across the selected designs. However, the *rms* current of the calibrated method is now worse, within 11% mark on average across the selected designs. The efficiency values are again in very good agreement with the FEM results since the efficiency was optimized at the specified and fixed base speed of the rotary SR machine as in Table 9.

Therefore it could be concluded that no single calibration strategy can wholly minimize the relative errors of all the objectives being optimized simultaneously compared to FEM results. However, it is still possible to select the flux tubes and slices model calibration strategy which enables effective error minimization of the objectives of interest. For example, once such choice could be made purely on the consideration of the particular objective being selected for optimization. Thus, if the *rms* current is being optimized for thermal considerations of the machine then the uncalibrated model could be used whereas if the average torque values are being optimized then the calibrated model should be preferred. The computational accuracy and consistency of the flux tube method in this particular rotary 18-12 SR machine optimization task is less clear compared to the LSRM design optimization case. This could be due to the point expressed earlier regarding the sensitivity of the flux tubes and slices method with respect to certain design variables of the rotary SR machine and shown in Fig. 57.

In addition to the numerical accuracy of the flux tubes and slices method for the rotary 18-12 SR machine design the computational efficiency of the flux tube approach is also important and should be compared with the FEM approach. The total number of individuals (18-12 SR machine designs) generated by the current GA based optimization was

$$\text{total number of designs} = \text{population size} \times \text{number of generations} = 100 \times 13 \approx 1317 \quad (42)$$

including the seed designs passed on to the GA routine.

Furthermore, the GA optimization terminated as all the design constraints were satisfied at the last generation. The GA optimization has terminated successfully,

Flux Tubes and Slices Based SR Machine Analysis and Design Optimization Results obtained Pareto front of which is shown in Fig. 62, and the simulation time of 548 minutes was recorded which is approximately 9 hours of simulation time. Therefore the time required to generate and fully analyse each rotary 18-12 SR machine design instance in the GA study, on average, was

$$\text{design simulation time} = \frac{\text{total simulation time}}{\text{total number of designs}} = \frac{32905(\text{seconds})}{1317} \approx 25(\text{seconds}) \quad (43)$$

In contrast to the above answer each of the replicated flux-linkage maps obtained using FEM, as in Fig. 64, of the selected designs from the obtained Pareto front in Fig. 62 required, on average, 110 seconds to compute including the meshing time of each instance. Therefore, the FEM based analysis is markedly slower compared to the flux tube approach, yet order of magnitude more accurate and generally more versatile, also noting that the time required to obtain the post-processed information as in Fig. 60 and Fig. 61 not being accounted for in the FEM timing whereas it was included in the flux tubes and slices computations.

5.4 Chapter Summary

The preceding chapter results and findings can be summarised as follows.

From the flux linkage curves obtainable with the proposed flux tubes and slices method it is understood that the accuracy of such curves will directly impact the instantaneous phase current and torque profiles of any topology SR machine be it translating or rotating machine. However, the close comparison of the LSRM instantaneous current and torque waveforms obtained with the flux tubes and slices method were seen to be in close agreement with the FEM results. Same observation is present to a lesser extent for the analysed 18-12 rotary SR machine topology where the calibrated and non-calibrated flux tubes and slices models were compared to FEM results of the flux linkage curves.

In a similar fashion the average torque values computed with the AoA as a parameter showed close agreement with the FEM results for both the rotary and translating SR machine topologies over wide speed range of operation of the respective machine topologies. Such results are encouraging as they indicate that the practical design optimization task of the SR machine can be rapidly performed with the flux tubes and slices method.

More in depth sensitivity analysis of the design variables of both machines with respect to the accuracy of the results is likely to reveal which machine design

Chapter 5

parameters have the biggest impact on the numerical accuracy of the design objectives being optimized with the flux tubes and slices method.

Chapter 6 Discussion and Conclusions

Having performed a number of distinct topology SR machine design optimization tasks and having obtained the optimization results it is now possible to draw general conclusions on the proposed improved flux tubes and slices method as applied to the rapid analysis and design of magnetically non-linear SR machines.

6.1 Results Discussion

6.1.1 Flux Tubes and Slices Model Sensitivity Discussion

The improved flux tubes and slices model sensitivity results presented in Chapter 4 can now be placed into perspective when the modelling approach is used for rapid optimization of SR machines.

The sensitivity results have indicated that the flux tubes and slices method accuracy depends heavily on the two geometric error terms introduced during the equipotential slice placement stage of the modelling. The errors thus created can, nevertheless, be controlled in order to reduce the numerical error of the final reluctance values or to improve the computational speed of the solution or both.

The numeric discrepancy of the aligned rotor position reluctance, and therefore the flux linkage values, are only weakly affected by the number of the parallel flux tube paths m in the magnetic circuit as was demonstrated in Section 4.3.1. Thus the flux tube based modelling of the aligned position can proceed with the minimum number of parallel flux tubes, however this choice must be made with respect to the complexity of the shape of the magnetic circuit being analysed in order to capture the true shape of the circuit. Capturing the true geometry of the magnetic circuit is likely to be more effective with a larger number of parallel flux tubes.

The numeric discrepancy of the aligned rotor position reluctance, and therefore the flux linkage values are, in addition to the above discussion, only weakly affected by the number of the flux tube path cord subdivisions n in the magnetic circuit as was demonstrated in Section 4.3.1. This fact therefore warrants the reduction of the number of slices n to the smallest possible values, however making sure that the magnetic circuit shape is captured accurately given the selected number of subdivisions n . On the other hand, it should be noted that the

number of subdivisions n will also affect the apparent saturation levels of the circuit and should be increased to ensure accurate estimation of the saturation when the phase current levels are at their maximum for the flux linkage functions.

In a similar way it is recognised that the unaligned rotor position modelling using the flux tubes and slices method will be affected to a variable degree by the number of tubes m and slice subdivisions n . From the results in Section 4.3.2 it appears that the unaligned flux linkage function is insensitive to the number of slice subdivisions n and therefore this number can be kept low to speed-up the solution time. However, same effect cannot be achieved with the smallest number of parallel flux tubes and therefore the number m should be increased. It appears that the unaligned air gap flux distribution would benefit from the larger number of parallel tubes whereas the rest of the magnetic circuit can be, drawing on the indication of the fully aligned position results, modelled with a minimum number of parallel flux tubes since the saturation effects are small as shown in Table 5.

From the preceding discussion and the results in Chapter 4 it is certain that the flux tubes and slices method can further benefit from the variation of the parameters m and n in order to improve the computing speeds whilst controlling the numeric error effectively. This is the preferred way of modelling with the flux tubes and slices due to the introduced rapid design optimization cycle in Fig. 2. Therefore it can be stated that flux tubes and slices method is highly dependent and is subject to the actual implementation of the model for a particular geometry and will perform distinctly, in terms of accuracy, for each magnetic circuit case. Therefore it is beneficial to pay particular attention when constructing the flux tubes and slices model for a particular SR machine magnetic circuit geometry as these choices will impact the analysis results obtainable from the rapid SR machine design optimization cycle proposed in Fig. 2.

6.1.2 SR Machine Optimization Results Discussion

The LSRM and rotary SR machine topology results presented in Section 5.2 and 5.3 can now be discussed as follows.

The LSRM topology design optimization results obtained with the improved flux tubes and slices modelling in Section 5.3 indicate that the method compares well to the FEM results in terms of the numerical accuracy. The flux linkage functions of all the considered LSRM topologies were seen to be in good agreement with

the FEM results and no calibrations to compensate for the geometric modelling errors α and λ of the flux tubes and slices method were necessary. The average torque and power envelopes of the LSRM were close to the FEM results as well. This is encouraging since the flux tube construction task can be performed with relative ease and efficiency, compared with the alternative MEC methods [109], and the optimization results checked at the final stages of the proposed design cycle in Fig. 2 only to ascertain if the selected optimized designs are indeed close to the FEM results.

The considered rotary SR machine topology design optimization results obtained with the improved flux tubes and slices modelling in Section 5.3 indicate that the method is of comparable accuracy to the FEM results. However, contrary to the LSRM optimization case the rotary 18-12 SR machine model required the calibration of the flux tubes in order to produce results of a known SR machine design found with the FEM analysis. The calibration of the flux tubes and slices model of the rotary 18-12 SR machine subsequently enabled accurate optimization to be performed. The optimization results indicated that the calibration can help to mitigate effectively the discrepancies occurring in the optimized machine average torque values as obtained from the multi-objective pareto front. Furthermore, the calibration of the flux tubes and slices model also introduced the uncertainty in the obtained *rms* phase current values of the selected optimized SR machines. Given the large number of design variables and their associated wide numeric ranges of the rotary 18-12 SR machine topology to be optimized the *rms* current results suggest that in addition to the calibration of the model the numeric ranges of the variables could be reduced to minimize the discrepancy of the resulting *rms* current values.

From the preceding discussion points the following can be summed up.

It appears that the simpler and largely rectilinear geometry of the LSRM topologies considered in this study had the major effect on the flux linkage results accuracy obtained with the flux tubes and slices method. Both the aligned and unaligned translator cases of the considered LSRM topologies produced relatively accurate numeric result of the respective flux linkage functions. On the contrary the slightly more complicated aligned case magnetic circuit geometry of the considered rotary SR machine topology required noticeable calibration parameter to be introduced so that the FEM and flux tubes and slices results were of comparable values. Finally, the fairly complicated unaligned magnetic circuit geometry, and the air gap region more specifically, of the rotary SR machine was

found to require substantial calibration parameter in order for the flux linkage functions to be comparable with the FEM results.

Most likely cause of the flux linkage discrepancies between the flux tubes and slices method and FEM analysis for the rotary SR machine is that the flux tubes method uses the fixed equipotential slices of the tubes which can deviate from the true flux tubes if the machine design variables are varied over substantial range of values as was the case for the optimization case presented in Section 5.3. Therefore in order to minimize the likelihood of the need to calibrate the flux tubes and slices method it is beneficial to reduce the numeric ranges of the SR machine geometric design variables which impact the unaligned air gap geometry of the machine. Alternatively it is possible to prescribe certain rules that enable the unaligned air gap flux tube distributions to adjust, but more specifically the defined equipotential slices to adjust, subject to the changes in the geometric proportions of the air gap itself. Under such formulation the flux tubes and slices method, it is anticipated, will produce highly accurate flux linkage values comparable to the FEM results over wide range of geometric parameters variation as would be desirable in an extensive design optimization process proposed in Fig. 2.

Finally, the following important point can be drawn regarding the flux tubes and slices capability of accurate electromagnetic modelling of SR machine.

Since the calibration parameters for the rotary 18-12 SR machine topology were fixed from the start of the optimization exercise in Section 5.3 the number of generated GA individuals was relatively large. Therefore, the introduced calibration parameter was sufficient not to produce the machine designs that are far from the multi-objective pareto front. This observation has a very important practical implication that the flux tubes and slices calibration is unambiguous and is needed only once prior to the rapid optimization itself. This is one of the main advantages of the flux tubes and slices method compared to the previously discussed alternative reduced order computational methods.

6.2 Conclusions

From the methodology and results chapters of the report the following conclusions with regards to the proposed improved flux tubes and slices modelling approach can be made as follows.

The improved flux tubes and slices approach reduces substantially the ambiguity of construction of magnetic flux tubes in electromechanical devices operating on the purely reluctance torque principle. The method also reduces the required minimum number of geometric parameters of the modelled electromechanical device necessary for the accurate expression of the flux tube distribution compared to published manual field modelling methods.

Accurate determination of the flux tube cord lengths is possible with the improved flux tube method since all the information needed to achieve this is available in the mathematically descriptive form of cubic-splines. Computationally efficient numerical integration is then performed to find the flux tube cord lengths accurately. Therefore almost exact cord length value can be found for all assumed flux tubes compared to only average cord length values of alternative MEC methods. This particular capability of the flux tubes method tends to minimize the error terms in (20) and (28) which have the direct impact on the reluctance values of the complete magnetic circuit. Furthermore, average cross-sectional areas of the flux tube segments can also be found readily from the slices placed across the flux tube paths, which were placed for the construction of the flux tubes in the first place, at a small number of locations of the magnetic circuit of electromechanical device.

Complete flux-linkage map, including the magnetic saturation effects, can be constructed for an SR machine using the flux linkage values obtained with the improved flux tube method. Accuracy of the method is seen, in general, to be in close agreement with FEM results of the studied four distinct SR machine topologies and a large number of geometries. Although not applied specifically to tractive electromagnets and actuators it is believed that the flux tubes and slices method is equally applicable to such devices. The method has a potential to account for the magnetic leakage flux effects, around phase windings, occurring at high levels of excitation current at the aligned and the unaligned translator or rotor position.

The novel flux tubes and slices method can be readily used for rapid optimization of the AoA parameter to determine optimum values of the parameter with respect to mechanical speed and instantaneous torque of the SR machine in question. Knowledge of the optimal values of AoA parameter is essential and enables characteristic output torque curve for a specific SR machine to be found which is necessary for the precise control of the machine. If the SR machine design requirements are such that constant power curve is necessary for its application,

e.g. electric vehicle traction motor, then this power curve can be obtained once the AoA parameter sweep has been performed. Thus the improved flux tube approach enables the constant power curve construction and optimization to be performed with increased computational efficiency.

Coupling of the new flux tube method with optimization techniques has been performed since the method is computationally efficient and relatively accurate. These advantages can be exploited during initial search and optimization stages where large design response surface must be searched for a candidate SR machine design. In such optimization tasks the usefulness of computational efficiency of the method can outweigh the approximate, yet consistent, results the model generates. This particular flux tubes and slices feature suggests economical use of computing resources.

The proposed rapid analysis and design cycle of SR machines, Fig. 2, has been validated against order of magnitude more accurate FEM based design and analysis tool. Novel topology SR machine design has been generated by using the improved flux tube method which was combined with GA based optimization. Subsequently the selected number of obtained optimal designs was reanalysed with an FEM approach. The comparison of the results revealed that the improved flux tube method can be used to search optimal designs rapidly, consistently and with accuracy approaching that of 2D FEM. Thus, the aim of the modelling approach to complement the FEM analysis has been achieved.

Finally, the following conclusions can be drawn with regards to the research objectives spelled out in Section 1.3.

The reduced order computational methods for the analysis of electromagnetic fields were reviewed in Chapter 2 and their advantages and disadvantages identified in the context of the SR machine modelling. The newly proposed flux tubes and slices method was formulated which incorporates many of the advantages of the alternative computational techniques; this was demonstrated in Chapter 3. The main features of the improved and extended flux tubes and slices approach are the automatic generation of the flux tubes and slices by use of the cubic-splines and by the use of combinations of straight line and circular arc segments. This approach showed superiority in terms of the manual effort required when constructing the geometric features of the modelled magnetic fields. Furthermore, the proposed flux tubes and slices approach was formulated analytically and it was demonstrated in Section 3.3 that the method is numerically

robust and can be effectively controlled in terms of the minimization of the numerical errors afforded by the method. Finally, it was shown in Section 5.2 and Section 5.3 that the method can be effectively applied to the wide range of practical SR machine topologies for the rapid electromagnetic analysis and design.

6.3 Scientific Contributions

The presented research work has contributed to the advance of knowledge in the scientific field of reduced order computational methods applicable to the rapid electromagnetic analysis and design of SR machines.

The present research contribution to the advance of knowledge in the scientific field of reduced order computational methods can be summed-up as follows.

- A number of electromagnetic field modelling paradigms from the existing reduced order computational techniques were combined into substantially improved flux tubes and slices formulation. The main feature of the flux tubes and slices formulation is the automated generation of the flux tubes and slices using cubic-splines for the construction of tubes and a combination of straight lines and circular arc segments for the automatic construction of the slices. This technique, not explored previously, has shown a significant advantage compared to the similar electromagnetic field modelling approaches in terms of the time required to construct such geometric features in the magnetic circuits of SR machines. This advantage is evident in the ferromagnetic and magnetically linear regions of the machine and for the aligned and unaligned rotor positions.
- The cubic-spline based flux tubes and slices formulation enables the electromagnetic analysis of ferromagnetically non-linear as well as linear regions of an SR machine circuit.
- The cubic-spline based flux tubes and slices analytic formulation enables the derivation of the geometric error parameters of the method. The geometric error parameters indicate that the numeric error accuracy of the proposed method can be adjusted thus controlling the accuracy of the final results. It is shown that the same geometric error factors are present in the alternative MEC based reduced order computational methods used for electromagnetic field analysis.

- The cubic-spline based flux tubes and slices formulation enables dual bound estimation of the inductance values of the analysed non-linear SR machine electromagnetic circuits in the linear and the non-linear regions. The dual bounds capability of the proposed flux tubes and slices method enables the effective numerical error minimization and the error control strategies given the uncertainty of the final results.
- The proposed reduced order computational method of flux tubes and slices was demonstrated to be computationally efficient and accurate compared to the industry standard FEM when the cubic-spline modelling techniques were used and therefore the method is a viable complement to such advanced computational analysis techniques.

The following scientific publications were generated as a result of the present research work, in collaboration with other contributors, and full copies of the publications are placed in the Appendix B and in the list of references where appropriate.

1. A. Stukys and J. Sykulski, 'Rapid Multi-Objective Design Optimization of Switched Reluctance Motors Exploiting Magnetic Flux Tubes', IET Sci. Meas. Technol., Nov. 2017.
2. A. Stukys and J. K. Sykulski, 'An Efficient Design Optimization Framework for Nonlinear Switched Reluctance Machines', IEEE Trans. Ind. Appl., vol. 53, no. 3, pp. 1985–1993, May 2017.
3. A. Stukys, M. Rotaru, and J. K. Sykulski, 'A refined approach exploiting tubes of flux for analysis of linear switched reluctance motors', Int. J. Appl. Electromagn. Mech., vol. 51, no. s1, pp. S13–S21, Apr. 2016.
4. Stukys, A., Mohammadi, M. H., Lowther, D. and Sykulski, J. (2017), "Rapid electromagnetic analysis and design using flux tubes", 21st International Conference on the Computation of Electromagnetic Fields, COMPUMAG2017 Daejeon, Korea, Republic of. 18 - 22 Jun 2017. 2 pp.

Chapter 7 Extensions and Future Work

Given that the proposed improved flux tube method is suitable for rapid analysis and design of SR machines, including novel topology SR machines, it is proposed to realise the full potential of this particular reduced order computational technique to a wider variety of design search and optimization problems of electromechanical devices.

Firstly, from the evident usefulness of the improved flux tube modelling approach it is imperative to apply such technique to as wide a range of SR machine topologies as practical within given time constraints. Such exercise will enable new understanding to be gained with respect to those novel topology machines and their extents of performance studied effectively. For example, the improved flux tube approach together with the proposed rapid analysis and design optimization cycle, Fig. 2, can be applied to the extensively studied classical SR machines such as the three and four phase radial flux machines. However, the new approach would enable 3D or higher dimensional GA based optimization to be undertaken. In other words, the classical radial flux machine topology would be subjected to a much more rigorous GA based optimization with at least three or more objective functions and numerous design constraints – something that has not been achieved to date. In addition to the more classical SR machines there are many novel topology SR machines proposed which are not amenable to the effective FEM based design as these topologies have not been analysed extensively. Furthermore, it is believed that the improved flux tube approach is suitable for the analysis and design of synchronous reluctance machines which are rapidly gaining popularity. This exercise would offer new understandings to be gained of what is thought to be comprehensively researched machine. Therefore a holistic understanding of these machines can be afforded with the proposed flux tubes and slices based analysis and design techniques.

Secondly, due to the marked computation time savings afforded with the proposed analysis and design cycle, Fig. 2, and the flux tube approach in comparison with FEM only approach it seems that a logical step would be to investigate the quasi – 3D or full 3D capability of the flux tube modelling to see if computational speed gains can be made but with the preserved accuracy, intuitiveness and simplicity of the original approach compared to 3D FEM models. Of course this would necessitate moderate extensions of the flux tube approach

by adding the third dimension. This is likely to be nontrivial exercise, however if it is assumed that the full 3D flux tube approach can offer same numerical accuracy as 2D as well as computational efficiency then it seems to be worth the effort required to formulate and implement such model. To start with such exercise the geometries of the analysed machines could be simplified, yet 3D, and such important effects as 3D magnetic leakage flux included. The computational speed gains of 3D flux tube modelling capability, therefore, are very attractive.

Given the above mentioned opportunities in the rapid electromagnetic analysis and design optimization of SR machines the following capabilities of the flux tubes and slices approach are envisaged conceptually to be of immediate importance and are discussed in the proceeding sections.

7.1 On the Capability of 2D Leakage Flux Estimations using Flux Tubes and Slices Modelling Techniques

The 2D leakage flux estimation with the proposed flux tubes and slices method can be performed as follows.

As was stated in the modelling section of this report the LSRM and rotary SR machines modelled with the improved flux-tube method were assumed to be ideal machines in that the leakage flux was not included in the flux tubes analysis. This simplifying assumption was made in order to test the fidelity of the improved flux tubes and slices method for low to medium excitation current levels only. This is because the SR machines produce none or negligible levels of leakage flux at even moderate excitation current. It is seen that the FEM obtained results, in general, are reproduced with the improved flux-tube method. However, it is also observed that the flux tubes method does not reproduce the flux-linkage values exactly at higher excitation currents as indicated in Fig. 65.

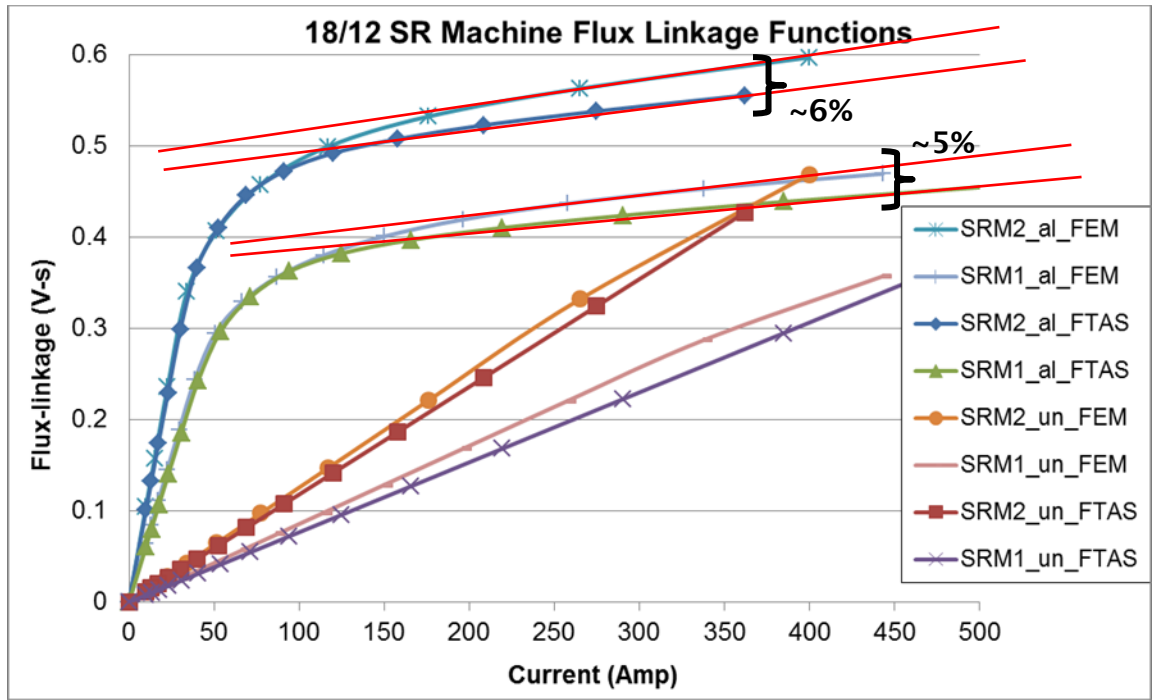


Figure 65: Leakage flux effect on the accuracy of the modelled flux linkage curves for the rotary 18-12 SR machine

Therefore there is an opportunity to improve the flux tubes and slices modelling approach further in order to be able to model LSRM and rotary SR machines at all excitation currents with reasonable confidence and accuracy since the 2D leakage flux effects were seen to be important [63]. Therefore the next stage of the flux-tube model improvement could be directed towards the construction of a method whereby the leakage flux effects occurring around the excited stator poles of the aligned position are taken into account.

The following approach dealing with the leakage flux modelling around the excited stator poles of SR machines with concentrated windings is considered a candidate method and is based on methods and techniques presented in [60], [72] and [71]. Figure 66 shows the initially considered LSRM topology with the flux tube distribution sketch pertinent to the machine geometry when the machine is operating at a low level of excitation current.

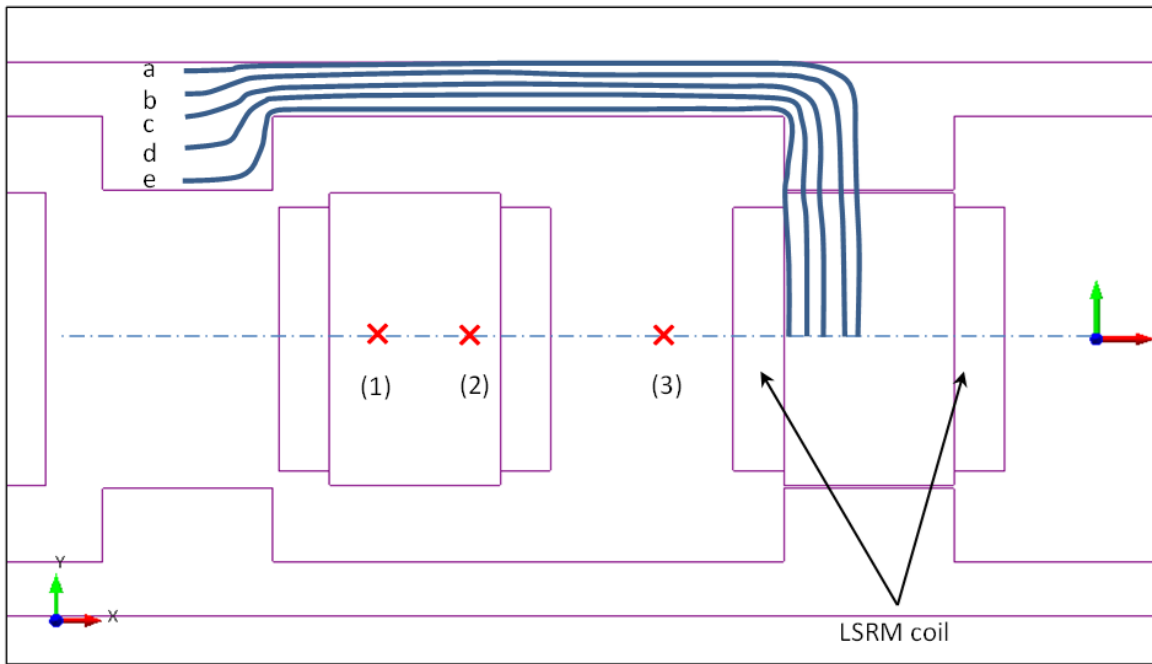


Figure 66: Ideal LSRM flux tube distribution under low levels of excitation current

Provided that the distribution of the probable flux paths for the given geometry is known, either from general FEM analysis or prior experience, it will be possible to obtain the flux-linkage function for a range of excited coil current levels as was demonstrated with the improved flux-tube method in this report. But to model the leakage flux paths which are not, in general, known *a priori* it is necessary to revisit the Roters [72] definition of the probable flux paths as implicitly stated in the literature review section of this report and restated explicitly here for convenience: provided that most (i.e. 80%) of the flux tubes are modelled in the immediate vicinity of the air gap this will accurately represent large proportion of the air gap permeance. This statement can be generalised and applied to the leakage flux path permeance or reluctance estimation. Therefore it is assumed that: provided that most (i.e. 80%) of the leakage flux tubes are modelled in the magnetic circuit this will accurately represent large proportion of the leakage flux path reluctance value in the flux-linkage function.

Resting on the aforementioned assumption it is then necessary to construct the probable coordinate points through which the leakage flux paths are likely to cross under increase levels of the excitation current. With the prior knowledge of the leakage flux distributions, specifically from Fig. 20 in Chapter 3, the following three approximate coordinate points are selected for the probable leakage flux paths as shown in Fig. 67.

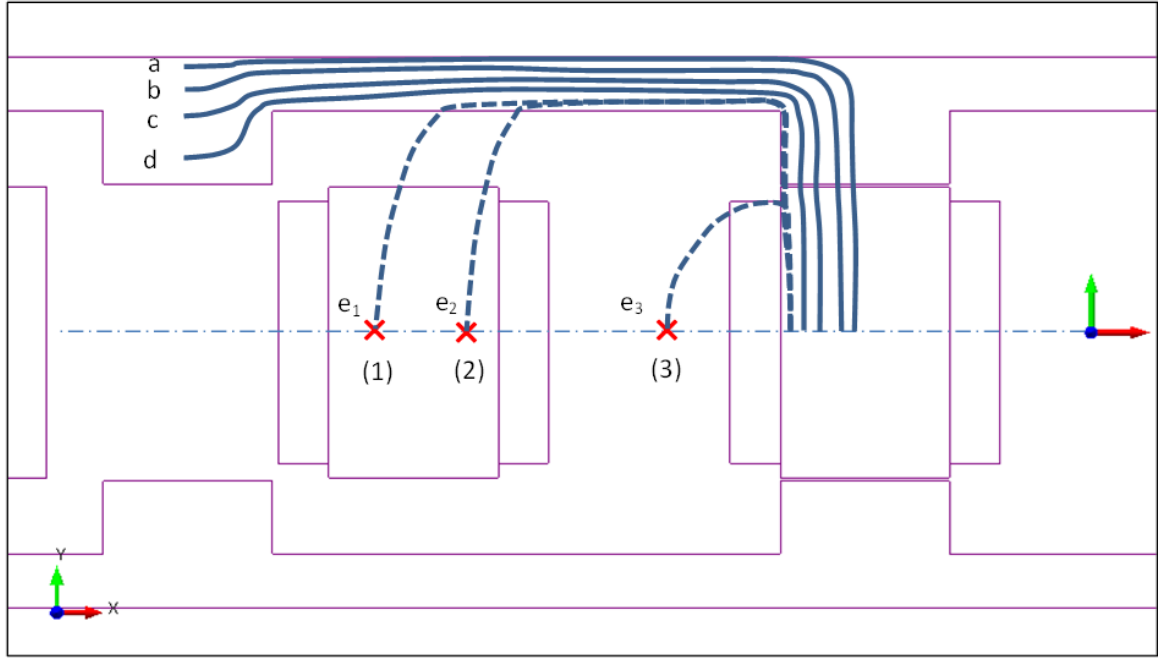


Figure 67: LSRM with the probable leakage flux paths

In general the initial path e , in Fig. 66, will be linked with all of the excited coil turns and the current level in the turns and therefore can be expressed in terms of the applied mmf as:

$$T_p \times I = F_e \approx 0.5 \times H_{sp} l_{sp} + H_g l_g + H_{rp} l_{rp} + H_{ry} l_{ry} \quad (44)$$

Where T_p , I , F_e , H and l are turns per pole, coil current, magneto-motive force, magnetic field intensity and length of the flux path segment respectively. The subscripts denote segments of the machine: stator pole, air gap, rotor pole and rotor yoke respectively. The relationship is only approximately equal to the applied mmf due to the numerical approximations. All the geometric quantities for this flux path will be known and therefore reluctance values for each flux path segment will be found in the iron parts as:

$$r_i = \frac{H_i l_i}{B_i A_i} \quad (45)$$

And in the air gap region:

$$r_g = \frac{l_g}{\mu_0 A_g} \quad (56)$$

Where B is the magnetic field density and A is average cross-sectional area of the flux path segment. And because this flux path is composed of individual flux tube segments connected in series the total reluctance of the path will be:

$$R_e = \sum r_i + r_g \quad (47)$$

Furthermore, this mmf equation will be written for the rest of the flux paths depicted in Fig. 66. Because all the paths in the figure are in parallel the total mmf will be the same, or approximately same, for each flux path, namely:

$$F_e = F_a = F_b = F_c = F_d \quad (48)$$

So finally it is possible to express the flux-linkage function for the aligned case as:

$$\lambda = \frac{T_p F_e}{R_{Total}} = \frac{T_p^2 I}{R_{Total}} \quad (49)$$

Now, if the original flux path denoted as e in Fig. 66 is assumed to leak through the rotor yoke then the first likely coordinate point it will cross is that denoted by position (1) in Fig. 67. The original flux-tube then becomes e_1 and is composed of flux path segment in the iron part in series with the leakage flux path segment in the air region as well as stator pole piece. Following this shift to the e_1 flux path all the remaining flux paths in Fig. 67 are repositioned in the iron parts of the machine and their geometric quantities recomputed. The mmf of the circuit will stay the same and therefore the excitation current, and the original flux path mmf equation will take into account the new segments of the flux path as follows:

$$F_e = F_{e1} \approx 0.5 \times H_{sp} l_{sp} + H_g l_g + H_{rp} l_{rp} + 0.7 \times H_{ry} l_{ry} + H_{g1} l_{g1} + 0.5 \times H_{sp} l_{sp} \quad (50)$$

The total reluctance of this new path, path e_1 , has changed compared to the original path, path e reluctance. If this new reluctance is calculated and is found to be lower compared to the original path reluctance then the new path is a better approximation of the leakage flux path. And the total reluctance of the updated flux paths will also change and will be lower. Therefore:

$$R_{e_new} < R_e = \sum r_i + r_g \quad (51)$$

And the total new flux linkage for this case will be:

$$\lambda_{new} > \lambda = \frac{T_{ph} F_e}{R_{Total}} \quad (52)$$

The above calculations can be repeated by updating the leakage flux path coordinates and recalculating all the variables and if again it is found that the new

reluctance of the entire path is lower; therefore that flux path is kept and the new flux-linkage function computed. This new flux-linkage function will be higher in magnitude compared to the old flux-linkage function for the same excitation current level. Finally, the total flux-linkage function for that particular stator-rotor alignment case will be higher than the flux-linkage of the ideal machine and will give more accurate output torque and power values for the SR machine since the stored magnetic field energy will be represented more accurately.

It could be argued that such computational procedure can be lengthy, however it is clear that the proposed 2D leakage flux computational procedure should only be applied to excitation current levels in between 0.8 and 1.2 *p.u.*. Therefore it is only necessary to apply this technique to two or three excitation current instances that fall between the stated *p.u.* current limits of an SR machine and the rest of the points can be accurately interpolated for complete flux-linkage function at that particular stator-rotor alignment instance.

7.2 On the Capability of Modelling 3D Flux Distributions using Flux Tubes and Slices Techniques

The topic of modelling the 3D flux distribution effects in SR machines has been undertaken in the past in order to assess the importance and influence of the 3D magnetic fields with respect to the machine performance. The 3D flux distribution problem can be split into the two distinct cases for the SR machine technology, namely that of the aligned and the unaligned rotor position. Both cases are important as the 3D flux distributions in the magnetic circuit of an SR machine affect the performance of the machine since the 3D flux linkage map can be enlarged or decreased dependent on the relative impact of the 3D effects [110]. Some novel 3D leakage flux reduction strategies have been proposed [3], however the nature of the active suppression of the leakage flux appears to be constraining rather than liberating the design choices of the SR machine topology.

In some specific cases it has been found that the 3D flux distributions, including the 3D leakage flux effects in close proximity to the stator phase coils, are not very significant [111], [112] and that their effects can be relatively accurately estimated during the design stage by treating the problem in 2D and adding the estimated 3D leakage correction factors [104]. These results were suggested for the classical radial flux SR machines with the stator outer diameter to core stack

length ratio equal or smaller than 1. Therefore, if the radial flux SR machine has its core stack length larger than the outer diameter of the stator the 3D leakage flux and therefore the 3D flux distributions within the magnetic circuit of the machine can be treated effectively and accurately as a 2D magnetic field problem with appropriately selected correction factors if such are available or can be easily inferred from the prior experience [104].

However, the challenge of assessing the impact of the 3D flux distributions is markedly different when even the simple classical radial flux SR machine has the aspect ratio of the outer stator diameter to the core stack length much lower than 1 [113]. This particular geometric ratio of the SR machines is generally favoured in the automotive electric propulsions applications which command compact axial length machines. Under such design conditions the practical SR machine can deviate markedly from its performance predictions obtained with 2D FEM [114]. The situation can be even more uncertain for the many novel topology translating and rotating SR machines which were discussed in Chapter 1. Under such design requirements the novel topology SR machines must be analysed using extremely slow 3D FEM analysis tools, as was noted in Fig. 1, that are not at all intuitive especially if, for example, the parametrised studies of the SR machine geometries are to be performed for fine tuning of the design.

One possible solution to the above posed problem of 3D based parametrised magnetic analysis and design of SR machines could potentially be attempted with the proposed flux tubes and slices approach. That is the 3D electromagnetic fields can, potentially, be very rapidly constructed for the purpose of quasi-3D static electromagnetic field solutions in SR machine circuits using the present flux tubes and slices approach. Since it has been demonstrated, in Section 4, that the computational speed-up of the 2D flux tubes and slices method scales quite effectively with respect to the number of the parallel flux tubes m in the circuit, this can be an indication that the method could also be suitable for the approximations of the 3D flux distributions in the SR machine circuit. Further advantage of the conceptual 3D based flux tubes and slices approach would be the possibility to estimate the dual bounds of the resulting reluctance values [76] thus increasing the confidence of the 3D based analysis results accuracy.

The success of the 3D, or quasi-3D, based flux tubes and slices method would be largely dependent on the specifics of implementation of the method, however, since in principle the leakage flux modelling was discussed to be easily implementable in the flux tubes and slices approach based on the cubic-splines,

the 3D flux tubes method would offer some very attractive computational performance features and advantages compared to, for example, the 3D FEM approach as conceptually summarised in Table 12 for the accurate estimation of the flux linkage functions.

Table 12: Feature comparison table of the 3D flux tubes and slices approach and 3D FEM for the Optimization of SR machines

SR Machine Design Optimization Approaches ¹					
	Computing Speed (sec.)	Memory Size (Giga Bytes) ⁸	Model Setup Time (sec.) ⁷	Relative Accuracy (%) ⁵	Software Cost ⁶
Flux Tubes (optimized) ²	2 (0.4)	< 2	< 600	> 90	free (open source)
FT-TAS (optimized) ²	10 (2)	< 2	< 600	> 90	free (open source)
3D FT-TAS	< 600	< 2	< 600	> 95	free (open source)
2D FEM ^{3,4}	> 80	4	> 600	> 95	yearly renewal fee
3D FEM ^{3,4}	> 3600	6	> 3600	100	yearly renewal fee

Table colour scheme: green > yellow > amber > red

Table assumptions:

1. SR machine design optimization using Genetic Algorithm or similar
2. Optimized coding including parallel computing techniques
3. 2D/3D geometric modelling capability not considered
4. Computing speeds excluding FEM meshing time
5. Computing accuracy potential relative to 3D FEM which it is assumed to be capable of 100% accuracy
6. Software cost as an identifier only between open source and commercial license
7. Model setup time in terms of all the processes but short of solution meshing and computations
8. Memory size on the computer hard drive including the software and the results storage
9. Results post-processing software requirements not considered

The computational advantages of the conceptual 3D flux tubes and slices implementation for the analysis and design of SR machines is compelling not only from the computing speed and numerical accuracy point of view. Additionally, there are usually further requirements placed on the magnetic field analysis software when the particular design methodology is chosen for the computationally intensive SR machine design tasks. Table 12 lists further 3D based magnetic analysis software and hardware considerations and compares these objectively against generally accepted FEM techniques.

From Table 12 it is clear that the conceptual 3D flux tubes and slices based magnetic analysis approach is very compelling especially if the listed advantages

of the method are placed into perspective with Fig. 1 and the proposed rapid SR machine design optimization cycle in Fig. 2.

One particular 3D implementation of the flux tubes and slices approach is shown in Fig. 68 whereby 2D slice planes are used instead of the equipotential slices, which were introduced in the 2D based flux tubes and slices model in Chapter 3, for the subdivision of 3D space.

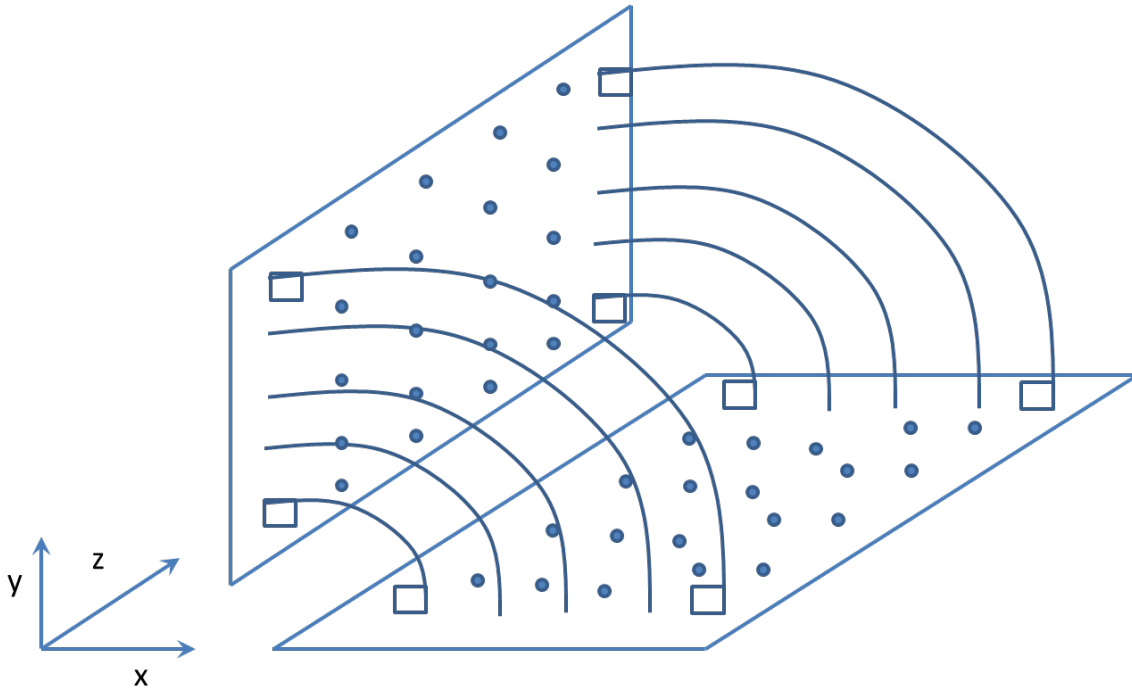


Figure 68: Proposed exemplary 3D flux distribution implementation using the flux tubes and slices approach

The particular implementation shown in Fig. 68 can be somewhat likened to the similarly proposed construction of the closed flux paths techniques for the post-processing stages of the results obtainable with 3D FEM based computer software [115]. Likewise, the 3D construction of the flux tubes would be accomplished with the appropriate placement of 2D slice planes and a prescribed number of points of the parallel flux tubes defined with the parameter m in Fig. 29, Chapter 3.

The 3D flux tubes and slices technique offers further modelling advantages of the 3D magnetic circuits of SR machines. First, the generally present geometric redundancy of the symmetry of the machine, as might be in the case of 3D FEM analysis, would be reduced to a single symmetry segment which could subsequently be modelled with the template-like 3D flux tube planes. In this way the custom generation of slice planes as in Fig. 68, for each new magnetic circuit

geometry, could be avoided and only the major machine circuit geometric dimensions used. Effectively, the slicing of the computational 3D geometry with the 2D flux tube planes are comparable to the mesh control and the meshing of the 3D geometry itself with the 3D FEM approach – labour and time intensive task. The 2D flux tube based plane subdivision would offer the unparalleled economy of the 3D model preparation time which in 3D FEM case is often substantial as shown in Table 12. Therefore it is envisaged that the 3D flux tubes and slices formulation will play an increasingly important part in the 3D based electromagnetic analysis of SR machines.

7.3 On the Capability of Modelling Flux Distributions in Synchronous Reluctance Machines using Flux Tubes and Slices Techniques

Since the usefulness of the flux tubes and slices technique for the electromagnetic analysis and design of SR machines has been demonstrated in terms of computational accuracy and speed of solution it is also of interest to investigate other electric machine technologies that operate wholly or partially on the reluctance torque principle.

One such technology of increasing industrial importance is the synchronous reluctance machine (SynRel) which is able to produce the useful torque by use of purely the reluctance torque created in the air gap and no permanent magnets [116]. The topologies of the SynRel machine technology are numerous, but one particular radial flux machine example is shown in Fig. 69.

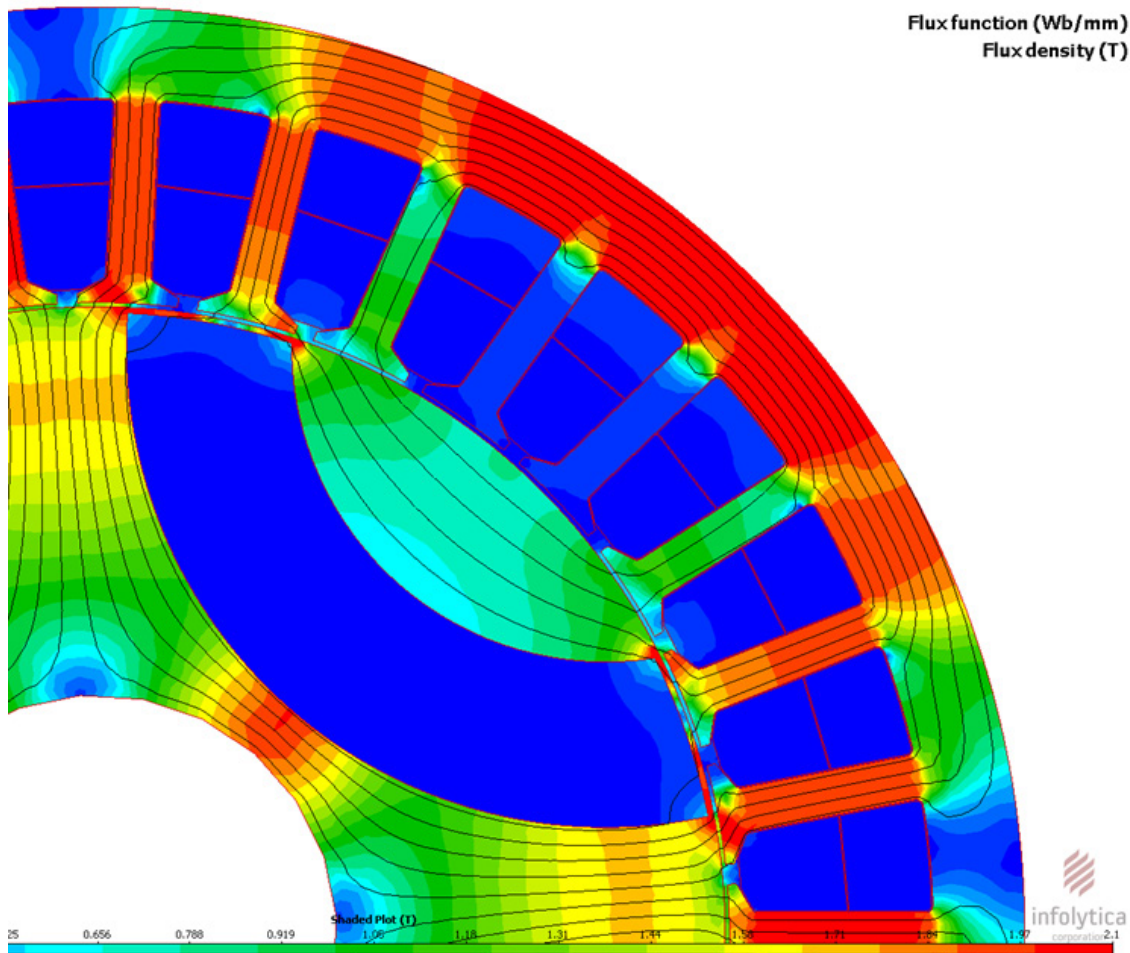


Figure 69: Typical radial flux fractional slot synchronous reluctance machine.
Taken from [117]

As can be seen from the general magnetic flux distribution within the SynRel machine circuit obtained with 2D FEM analysis it appears that the next closest comparison of the distribution could be made with the radial SR machine flux distribution as in Fig. 27 and Fig. 28 for example. It also follows that since the SynRel machine can operate purely on the reluctance torque in the air gap it will also be liable to the increased levels of ferromagnetic saturation, as seen during the normal operation of SR machines, which in turn will result in the highly non-linear electromagnetic torque over one electrical cycle. This calls for the highly capable FEM analysis with large number of time stepping instances in order to fully capture the instantaneous torque profile over the rotor movement of interest. Further challenges are due to the parametrised geometric study of SynRel machines in order to maximise their torque-per-ampere (TPA) and power factor performance metrics [118].

To overcome the exclusive requirement of the FEM based magnetic analysis in such SynRel optimization studies the improved flux tubes based method was adapted as shown in Fig. 70 for the machine geometry of Fig. 69.

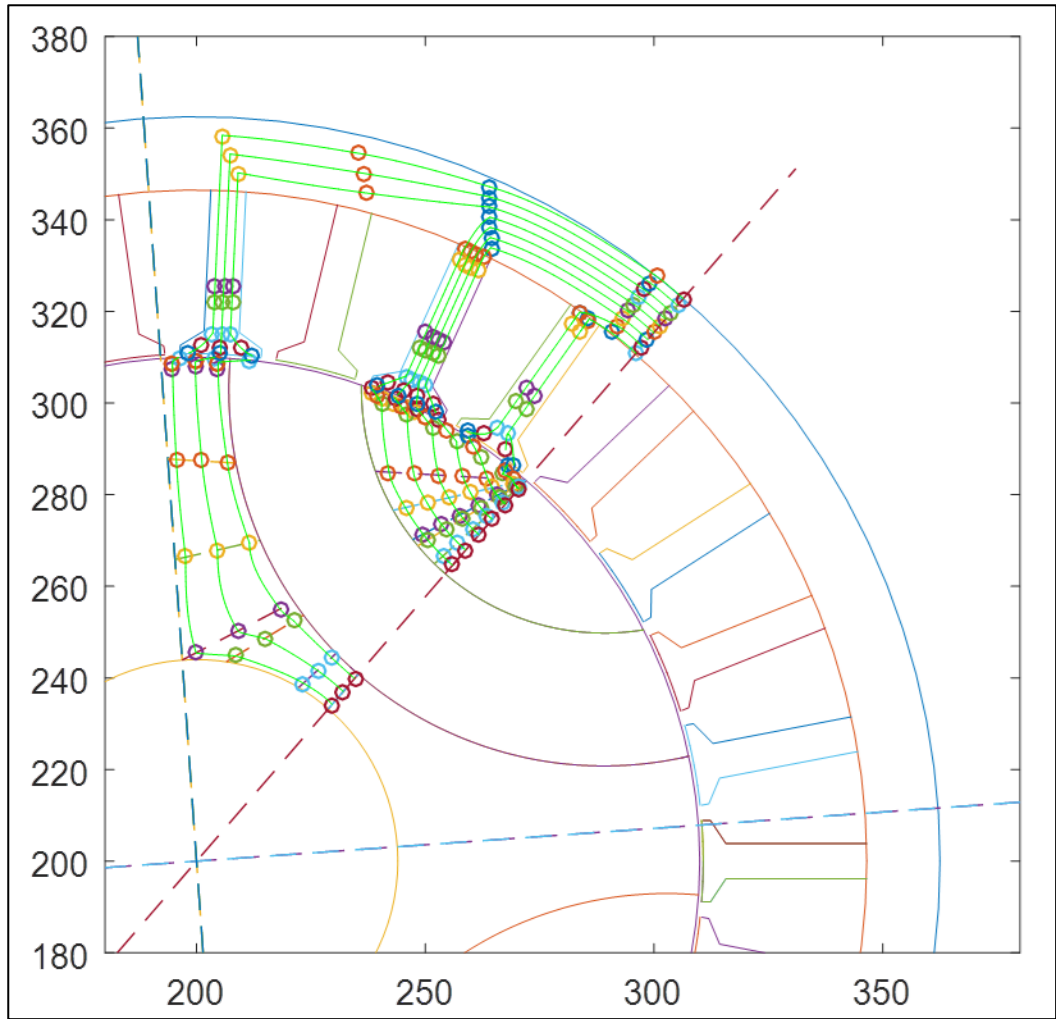


Figure 70: The radial flux fractional slot synchronous reluctance machine flux distribution of flux tubes method. Taken from [117]

Preliminary results of such parametrised SynRel machine optimization studies indicate that the flux tubes method can be very effectively employed for the SynRel machine technology [117]. Therefore the future effort to develop the flux tubes and slices formulation for the electromagnetic analysis of SynRel machines is also of practical importance.

Appendix A

The Appendix A contains flux-linkage functions, speed-torque envelopes and speed-power envelopes of the analysed SR machines obtained with the flux tube method and compared to FEM analysis. Also included are the GA based optimization Pareto fronts and the results error comparison tables.

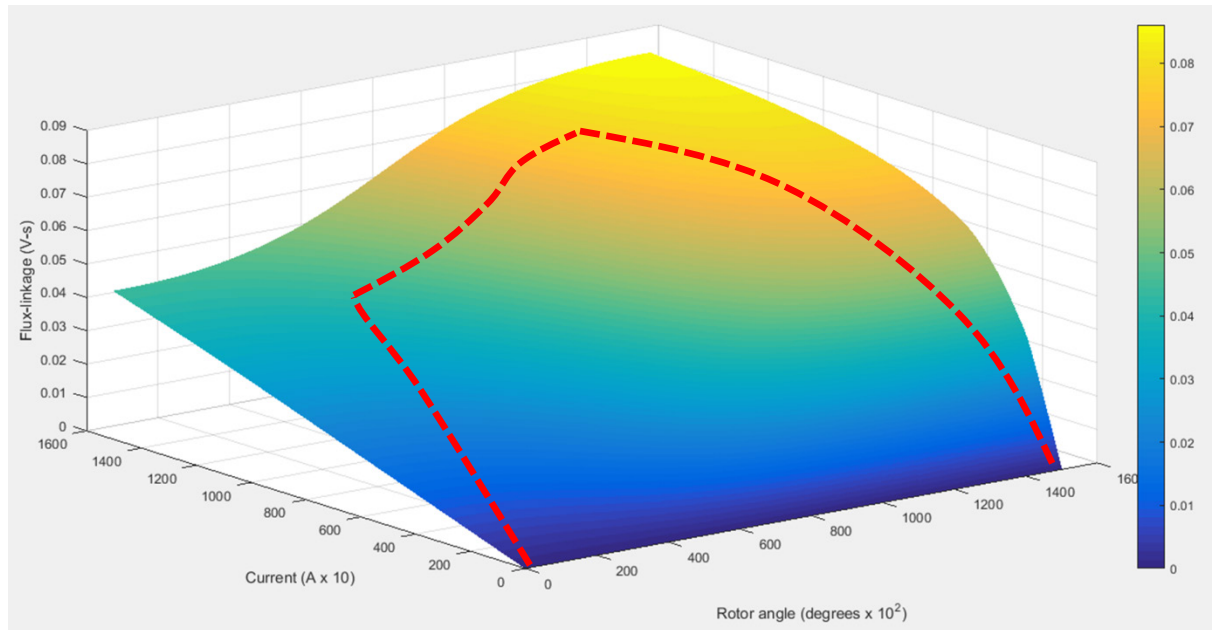


Figure A 1: Generic 3D flux-linkage map of SR machine

The bellow figure has been adapted from [63] and is associated with Fig. 29 and Fig. 30 and equations (12) to (32).

Appendix A

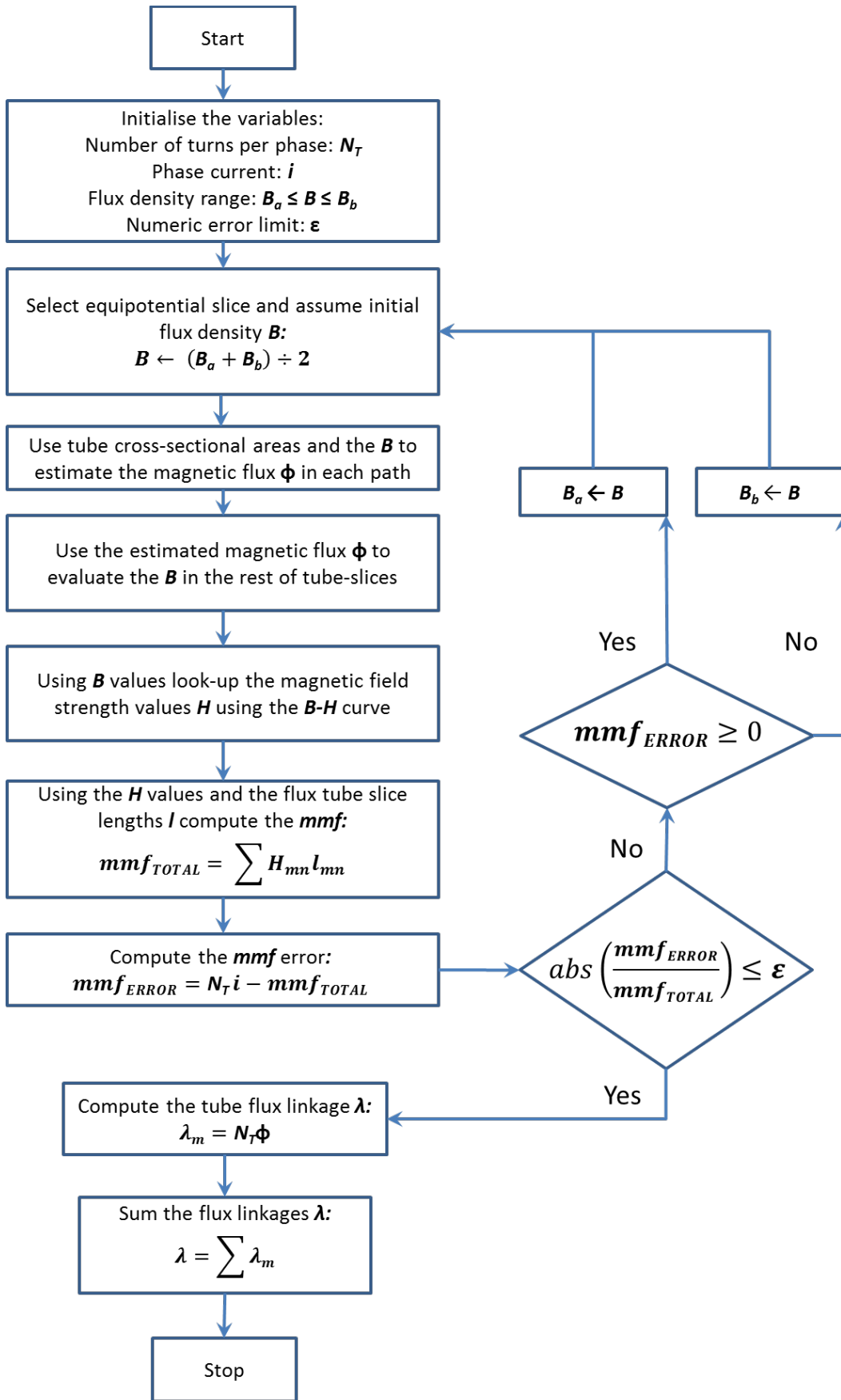


Figure A 2: Bisection root finding method based computational algorithm as used for the improved flux tubes and slices method. Adapted from [63]

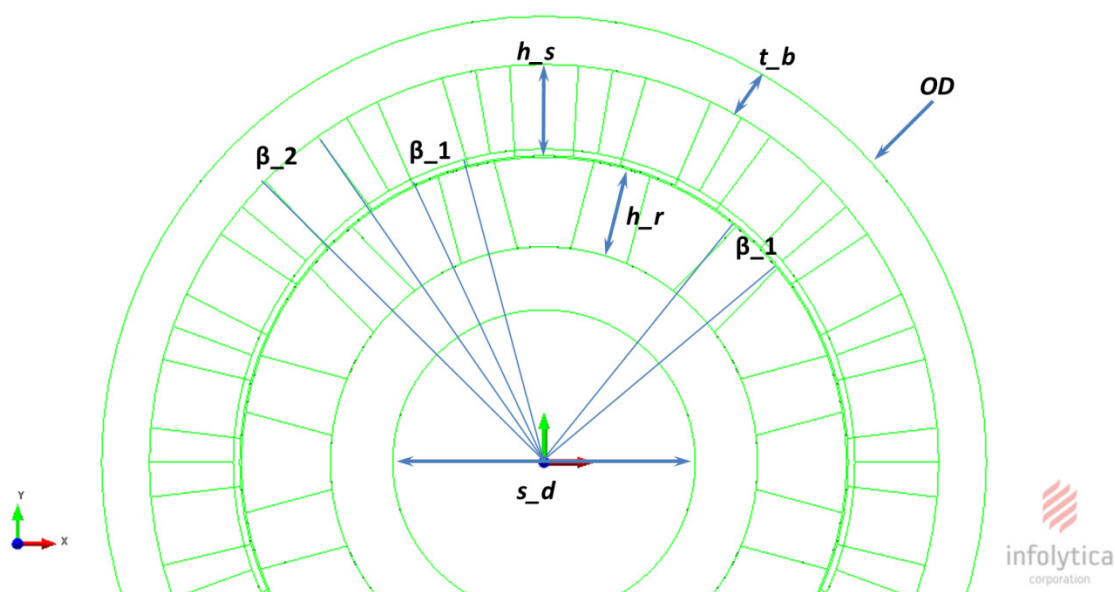


Figure A 3: Geometric information of the rotary 18-12 SR machine used for the sensitivity analysis

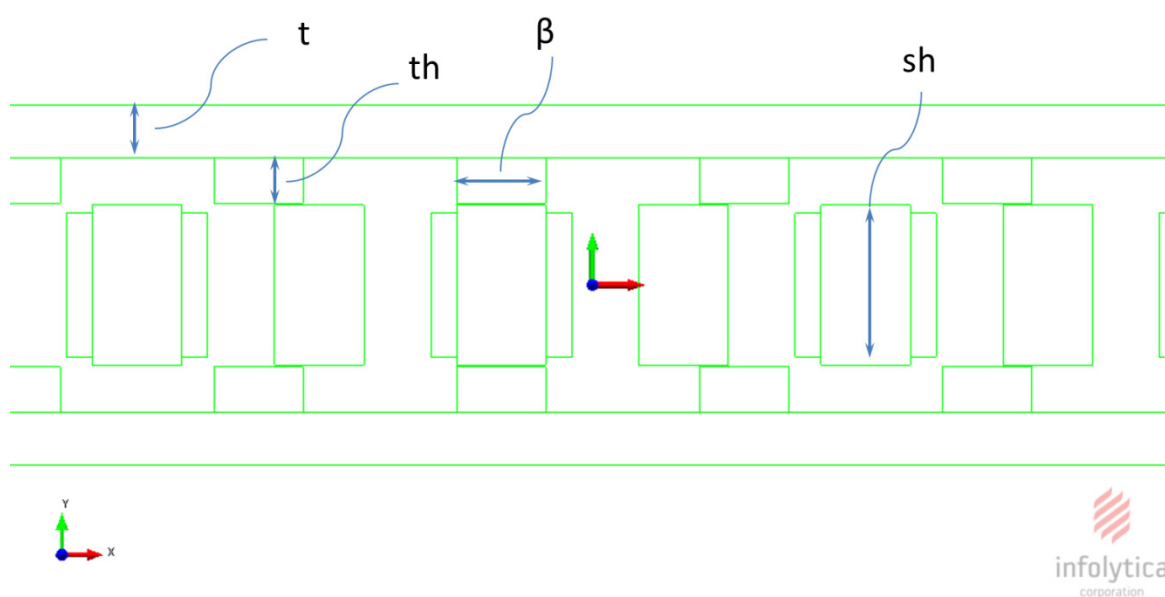


Figure A 4: Selected geometric variables of the LSRM

Appendix A

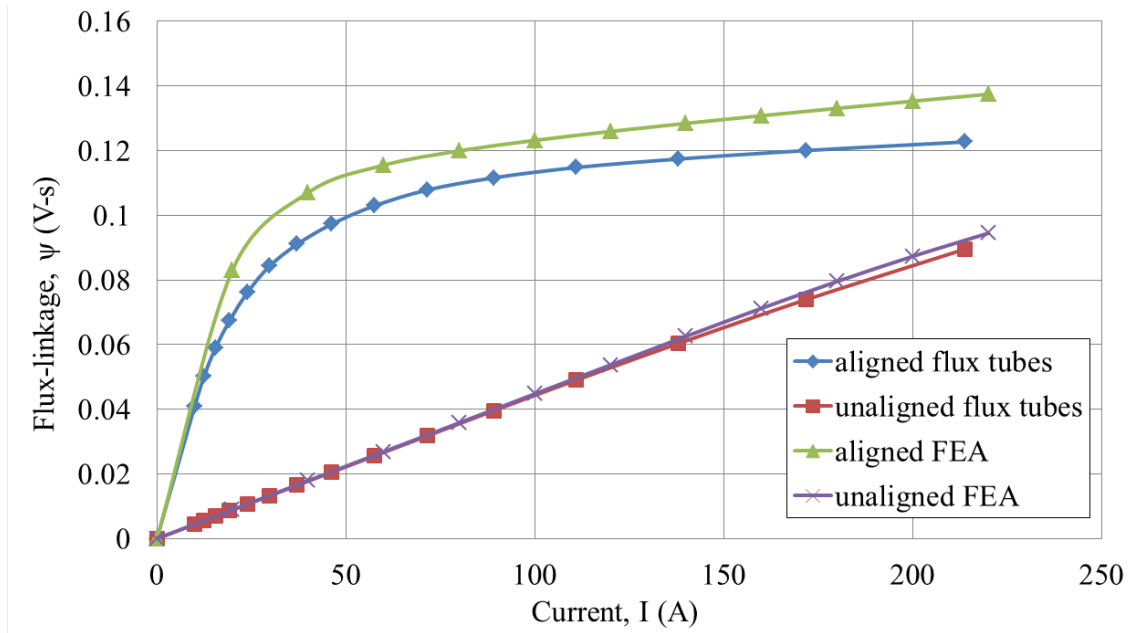


Figure A 5: Flux-linkage map of the 16-12 LSRM obtained with the improved flux tube approach and FEM

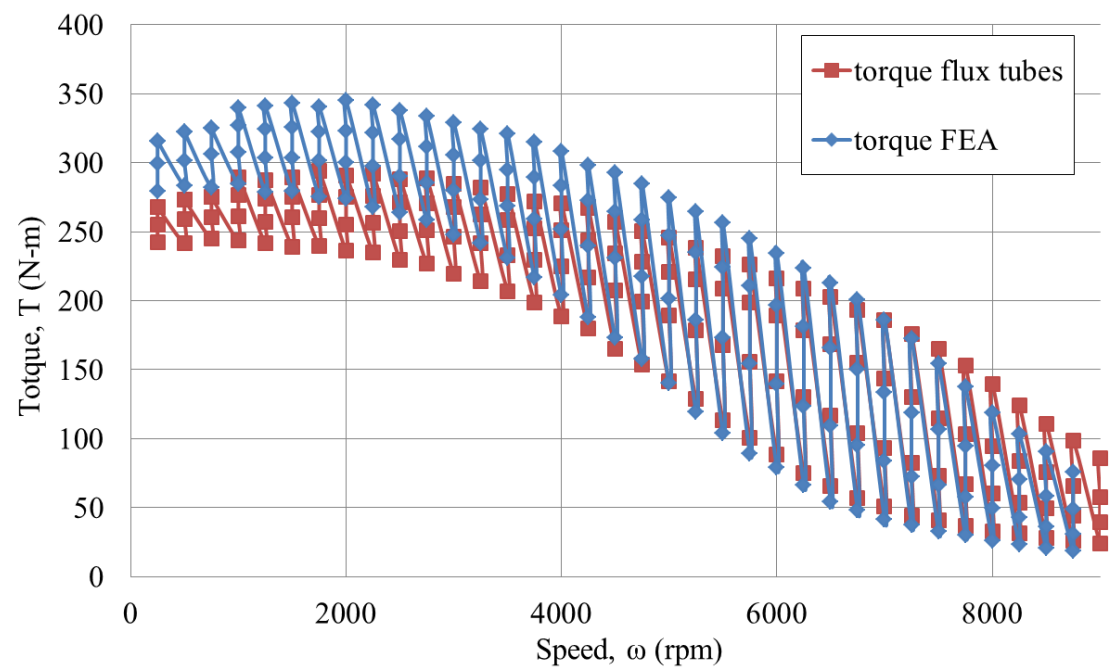


Figure A 6: Speed-torque envelopes of the 16-12 LSRM obtained with the improved flux tube approach and FEM

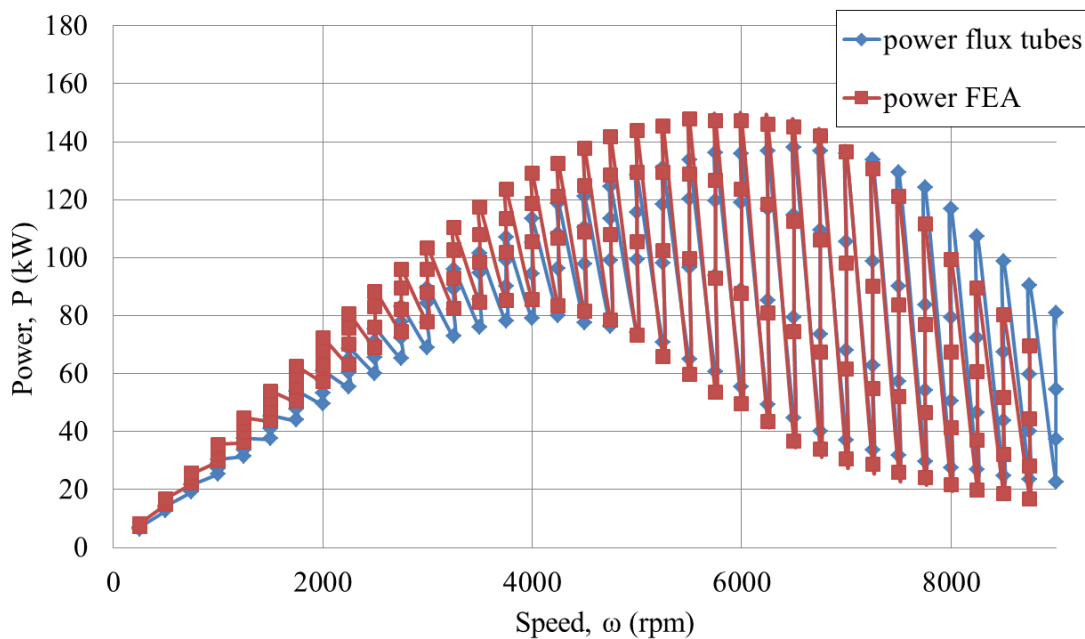


Figure A 7: Speed-power envelopes of the 16-12 LSRM obtained with the improved flux tube approach and FEM

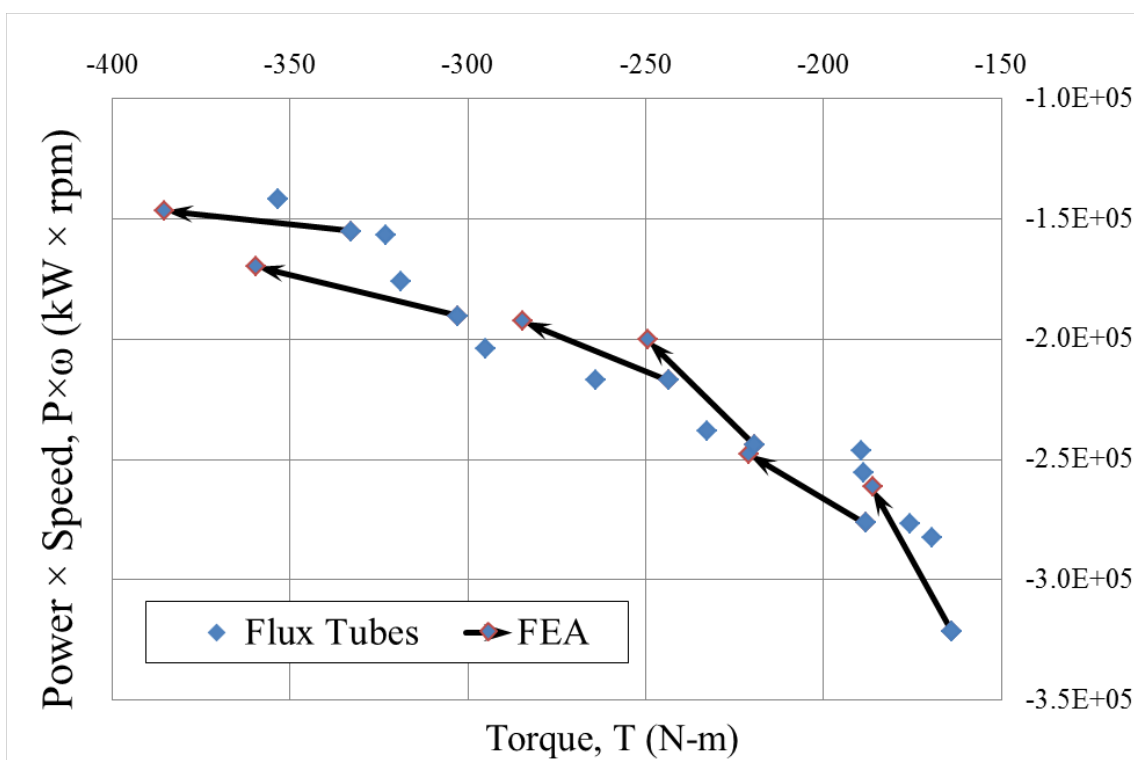


Figure A 8: GA optimization Pareto front of the 16-12 LSRM obtained with the flux tube method and FEM

Appendix A

Table A 1: Numerical error analysis of the 16-12 LSRM GA optimization

LSRM design number		Average Torque (N-m)	Flux Tube error (%)	Power \times Speed (kW rpm)	Flux Tube error (%)
2	Flux Tubes	-243	-14.49	-217144	12.86
	FEM	-284.6		-192386	
6	.	-219	-12.10	-243797	21.82
	..	-249.5		-200120	
7	.	-188	-14.90	-276306	11.59
	..	-221.1		-247603	
10	.	-333	-13.61	-155212	5.89
	..	-385.5		-146575	
12	.	-303	-15.78	-190248	11.97
	..	-359.6		-169906.4139	
16	.	-164	-11.96	-321471	22.93
	..	-186		-261508	
Average error (%)	Flux Tubes		-13.8		14.5

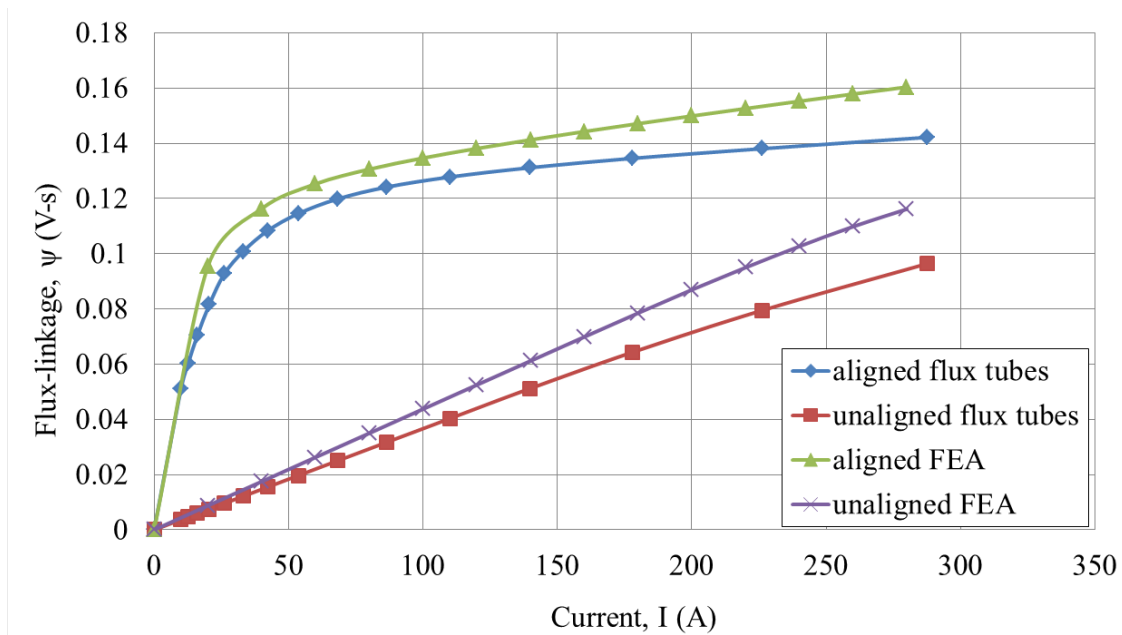


Figure A 9: Flux-linkage map of the 12-8 LSRM obtained with the improved flux tube approach and FEM

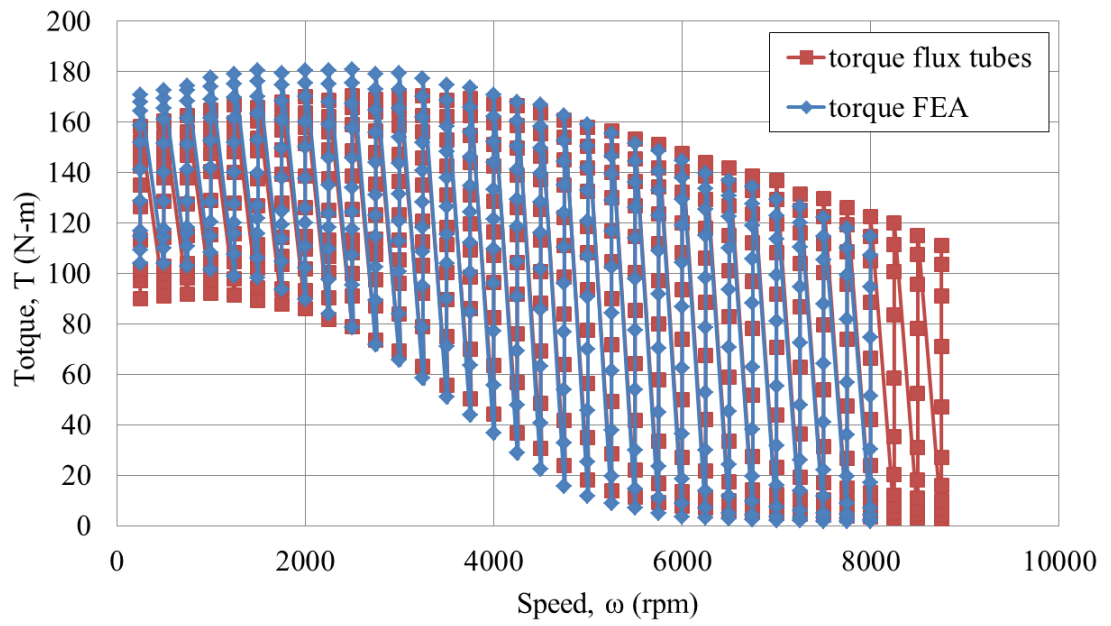


Figure A 10: Speed-torque envelopes of the 12-8 LSRM obtained with the improved flux tube approach and FEM

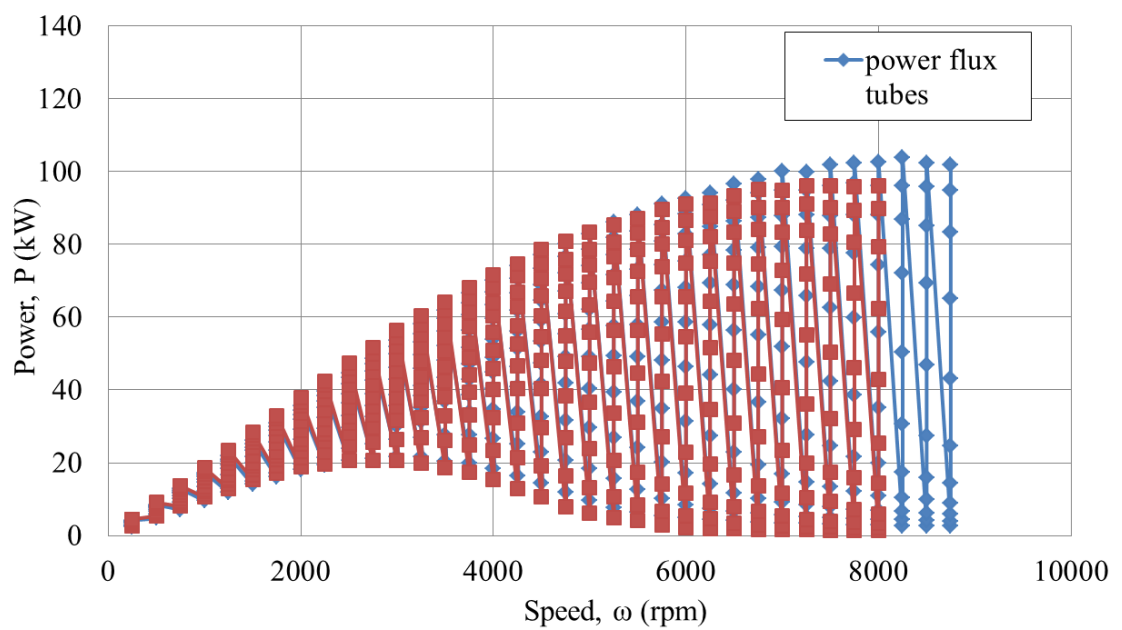


Figure A 11: Speed-power envelopes of the 12-8 LSRM obtained with the improved flux tube approach and FEM

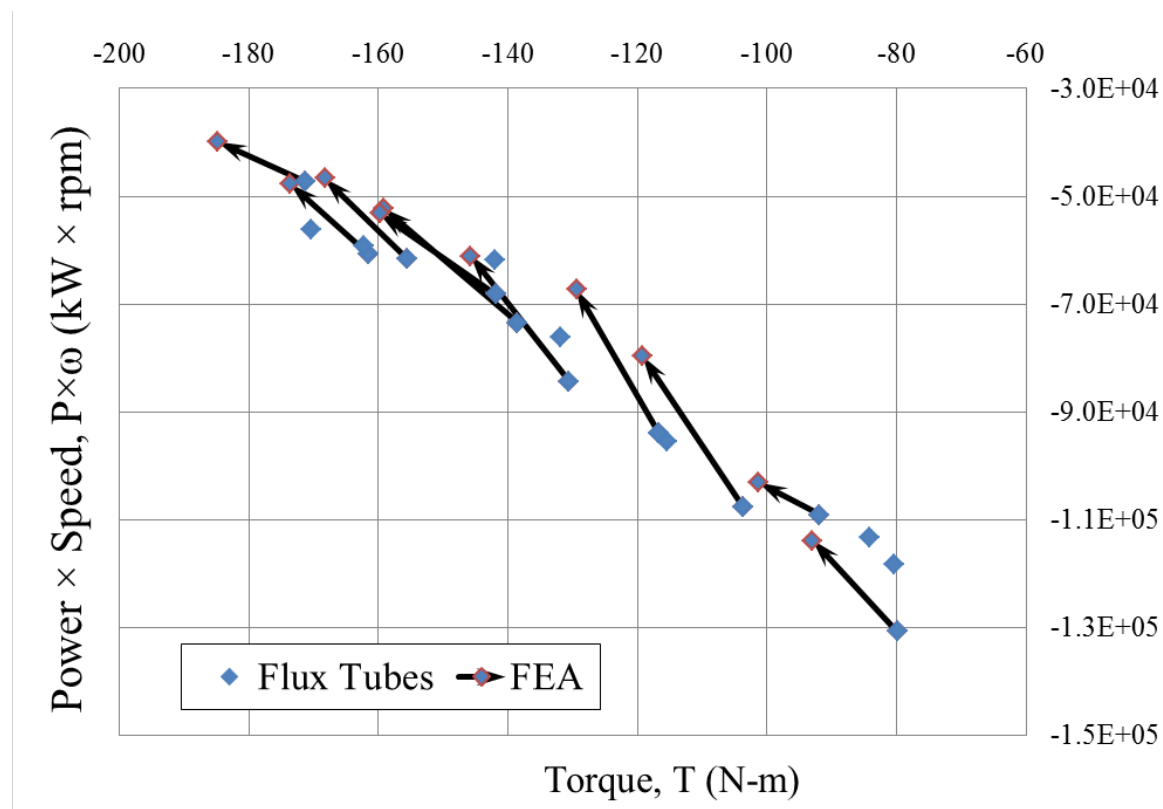


Figure A 12: GA optimization Pareto front of the 12-8 LSRM obtained with the flux tube method and FEM

Table A 2: Numerical error analysis of the 12-8 LSRM GA optimization

LSRM design number		Average Torque (N-m)	Flux Tube error (%)	Power \times Speed (kW rpm)	Flux Tube error (%)
3	Flux Tubes	-80	-14.16	-130708	14.81
	FEM	-93		-113846	
4	.	-92	-9.21	-109091	5.73
	..	-101.3		-103179	
5	.	-156	-7.54	-61560	32.15
	..	-168.3		-46583	
7	.	-161	-7.00	-60732	27.16
	..	-173.6		-47759	
8	.	-139	-12.88	-73468	40.68
	..	-159		-52223	
10	.	-171	-7.38	-47207	18.58
	..	-184.9		-39809	
11	.	-142	-11.21	-68067	27.87
	..	-159.8		-53231	
12	.	-131	-10.39	-84327	38.03
	..	-145.8		-61091	
15	.	-117	-9.89	-94056	39.92
	..	-129		-67221	
16	.	-104	-13.09	-107694	35.31
	..	-119		-79593	
Average error (%)	Flux Tubes		-10.3		28.0

Appendix B

The Appendix B includes the published versions of the parts of the thesis.

Rapid Multi-Objective Design Optimization of Switched Reluctance Motors Exploiting Magnetic Flux Tubes

Aleksas Stukys*, Jan Sykulski

Department of Electronics and Computer Science, University of Southampton, Southampton, UK
*A.Stukys@soton.ac.uk

Abstract: The magnetic design of Switched Reluctance (SR) motors is inherently a hierarchical process. The design cycle progresses through distinct stages where the accuracy improves but computing times increase greatly, thus it often becomes impractical to furnish extensive multi-objective optimization required to accomplish the optimal design. In order to enable rapid and accurate optimization of SR motors an improved reduced-order computational method of flux tubes is implemented to complement and practically replace the time consuming 2D finite element based magnetic analysis. The paper demonstrates how the use of the improved flux tubes approach to evaluate objective functions results in substantially faster while still accurate multi-objective optimization of SR motors.

1. Introduction

Switched Reluctance (SR) machines are often regarded as having the simplest mechanical design [1]-[3] compared to other conventional electric machines, such as permanent magnet dc, synchronous reluctance or induction, as they are brushless and have no permanent magnets (PM) or windings on the rotor. These design features make SR machines well suited to a wide range of applications where variable speed operation is required, such as general traction or pump drives. Moreover, the mechanical robustness of SR machines offers cheaper maintenance and better tolerance to harsh environments in which other types of machines cannot operate.

Since SR motors are capable of operating in both constant torque and constant power regimes over a wide speed range [4], [5], this operating feature also makes them suitable for the automotive propulsion applications, where the absence of permanent magnets is considered necessary since this industry is very cost sensitive and insists on immunity from unforeseen material price fluctuations, as experienced by PM materials [6]. However, the absence of PM parts makes the SR machines much more difficult to control [7] due to their nonlinear torque-per-ampere characteristic. This operational nonlinearity is a result of the nonlinear magnetic characteristic as the machine's magnetic circuit becomes heavily saturated even during steady-state operation [8].

Considering that SR machines are very nonlinear, they require complex analysis and robust design procedures to adequately predict their performance. Until now a rather limited success has been achieved in terms of accurate analytical design procedures for SR machines [9], [10] to provide satisfactory quantification of the machine performance. Most of the magnetic analysis and design is nowadays performed by numerical simulations based on a finite element method (FEM) in order to capture the detailed shape and allow for magnetic nonlinearity. The FEM based solutions can be accurate; however, they are time consuming and lack the intuitive insight into the cause-and-effect relationships between numerous machine design parameters. Moreover, the FEM solutions give only part of the

information needed to fully describe the performance; this necessitates extensive post processing of the results using specialist software. Lengthy FEM solver based design computations resulted in the previous FEM based Differential Evolution (DE) optimization attempts to be rather restricted in terms of the number of objective function calls, with most such investigations taking more than 10 hours to complete and the number of design points explored being limited to about 200 [11] – with simultaneous three objectives to be optimized this number of design points appears to be insufficient. Furthermore, the same difficulty is encountered with the use of Design of Experiments (DoE) based optimizations as the number of objective function calls based on FEM solver is large even if the number of design objectives is less than 3 [12]. Single design-objective based optimizations have shown some success in the past for the machines which exhibited good initial design configurations, i.e. were known to be good designs prior to the single-objective optimization, such as torque ripple minimization [13]. On the other hand, an optimization approach using only a small number of machine design parameters and design objectives is unlikely to result in an optimal design, as a large design space is normally needed to avoid local optima. These conflicting requirements naturally lead to the concept of a hierarchical design as depicted by the inverted pyramid of Fig. 1.

The hierarchical design process summarized in Fig. 1 indicates that at each subsequent optimization step the design space of a particular electromechanical device may be reduced as the confidence in the predicted performance grows following the outcome of the previous design stage. The clear distinctions between the different design paradigms in the pyramid emphasize that accuracy generally improves as we use more elaborate analysis tools at the expense, however, of significantly increased computational effort. Thus there is a need for both approximate (but fast) modelling tools at the early stages of the design, to explore the large design space, while homing in on a particular area identified as the likely location of the global optimum allows for the use of more time consuming simulation tools as fewer design points need to be considered. In the context of electromechanical devices this stage is often further split

This article has been accepted for publication in a future issue of this journal, but has not been fully edited.
Content may change prior to final publication in an issue of the journal. To cite the paper please use the doi provided on the Digital Library page.

into preliminary 2D steady state FEM simulations followed by the most computationally intensive transient 3D FEM solutions. The challenge here is to ensure a smooth transition between the models without the loss of important information, especially that stepping 'back' in the modelling (from more to less accurate models) may sometimes be required if an area outside the currently localized optimum needs to be explored further. Associated with this is the issue of selecting the most appropriate optimization algorithms, as the simple but fast models may be run many times while with the FEM based simulations we aim at reducing the number of objective function calls. Thus there may be several internal communication links between the different levels in the pyramid. The design of a SR motor falls neatly into the paradigm discussed above where a careful balance needs to be achieved between the speed of computation and accuracy of the solution.

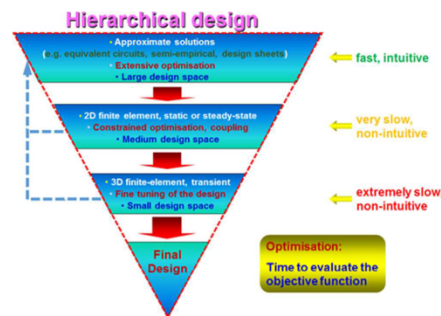


Fig. 1. The concept of a hierarchical design of electromechanical devices.

This paper proposes to improve the efficiency of analysis and design optimization of the radial flux SR machine by adapting the improved reduced order computational method of flux tubes. The flux tube method – which has already been successfully applied to translating SR machines as reported in [14] and [15] – complements and enhances the hierarchical design paradigm of Fig. 1 by reducing the need for hard choice between solution time and accuracy early on in the design process, while still allowing to arrive at a near-optimal design. Therefore the importance of the intermediate stage (one which is very slow and non-intuitive) in the hierarchical process of Fig. 1 is diminished since the enhanced accuracy of the approximate but fast solution based on flux tubes can be directly utilized in the final design stage with substantial savings in computational resources.

The reduced order computational method of flux tubes is a well-established technique [16]; however, its application to the design of SR machines has not been pursued and in the past the design process relied heavily on the manual work of the designer [3], [17]–[19]. In this paper an improved and extended version of the flux tube method is proposed whereby the original flux tube modelling is combined with tubes-and-slices (TAS) techniques [20], resulting in a substantial reduction of manual work of an analyst or a designer, while improving the computing speed

and making the accuracy comparable to 2D FEM. It is argued that this approach makes it particularly appropriate in everyday engineering practice in design offices.

The reminder of the paper is organized as follows. In Section 2 the application of the improved flux tube method, with emphasis on computing speed and accuracy, is illustrated using an example of a prototype SR motor with published measured performance data. In Section 3 a detailed discussion follows related to the robustness of the improved flux tube method. Section 4 describes an application of the flux tube method to a multi-objective optimization of the SR motor for automotive traction application. In Section 5 the proposed SR machine design optimization cycle is discussed, Fig. 12, and demonstrated how it complements and enhances the conventional design process of Fig. 1. Finally, Section 6 contains the conclusions and suggested future research direction in the field of rapid multi-objective optimization of SR machines and other electric machines using the flux tubes.

2. THE FLUX TUBE MODELLING APPROACH

In this section the proposed improved flux tube method is applied to a 50kW radial flux 18/12 SR motor intended for automotive traction application, as published in [4], where most of the design and optimization was achieved using FEM. A prototype was built and a full dynamometer test performed in order to measure its torque output over a wide speed range. The machine was subsequently redesigned to improve its performance compared to the initial version. The relevant data for both machines (SRM1 and SRM2) is listed in Table 1.

Table 1 SR Motor Design Variables and Test Results (adapted from [4]).

Design Parameters	SRM1	SRM2
Outer diameter [mm]	269	269
Stack length [mm]	135	135
Air gap length [mm]	0.5	0.5
Iron core material	10JNEX900	10JNEX900
Wire diameter [mm]	0.95	0.6
Wire turns [turns]	13	17
Wire parallel turns [turns]	13	22
Slot fill factor [%]	54.1	57.0
Current, peak [A]	380	320
Max. current density [A/mm ²]	24 (24)	33 (33)
RMS current (@1200rpm) [Arms]	241 (240)	204 (206)
Max Torque (@1200rpm) [Nm]	354 (340)	415 (400.4)
Number of phases	3	3

() denote test results

As the geometries and other data for both SR machines are known, including material properties and electric loading, a 2D FEM analysis of the SRM2 design was performed in order to visualize the magnetic flux distribution within the magnetic circuit of the machine. Fig. 2 illustrates a general solution for the SRM2 design at a peak current as specified in Table 1. The flux tube modelling approach will now be explained in detail.

2

This article has been accepted for publication in a future issue of this journal, but has not been fully edited.

Content may change prior to final publication in an issue of the journal. To cite the paper please use the doi provided on the Digital Library page.

The flux tube modelling of the SR machine starts with a general inspection of the 2D FEM solution, as illustrated in Fig. 2, and in particular inspection of the flux function distributions within the magnetic circuit. The equipotential lines – along which the magnetic field density is constant, or approximately constant – are chosen in such a way so that the complete magnetic circuit can be fully subdivided along its length. Subsequently, the magnetic circuit is segmented into the identified equipotential slices as shown in Fig. 3, while taking full advantage of the machine symmetry.

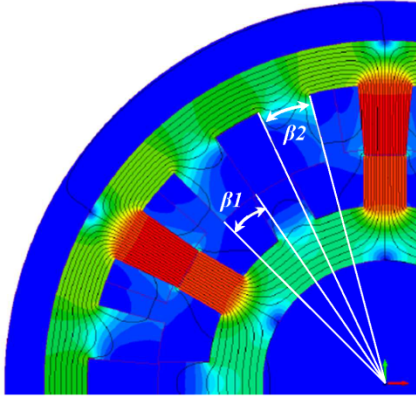


Fig. 2. 2D FEM solution for the 18/12 three phase SRM2 design at the aligned rotor position.

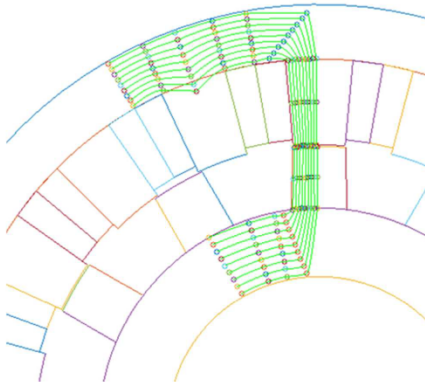


Fig. 3. Subdivision of the SRM2 magnetic circuit into equipotential slices at the aligned rotor position using flux tubes methodology.

The equipotential slices in Fig. 3 are fixed to the given machine geometry by associating the slices with the machine geometric parameters and therefore are free to vary as the machine geometry is varied.

Once the subdivision into the equipotential slices is complete the equipotential slices are mapped into rows of coordinate points between which the smooth and continuous cubic-spline interpolations are performed automatically in order to approximate, as closely as possible, the true magnetic flux function lines, as those in Fig. 2. Thus the resulting smooth line segments in Fig. 3 along the path of the magnetic circuit represent magnetic flux tubes of equal flux inside them. The knowledge of the constructed flux tube geometric properties, as well as material properties in which they occur, enables accurate estimation of the flux linkage functions for a particular SR machine geometry and prescribed electric loading. The flux linkage function for both the aligned and unaligned rotor positions of the SR machine can be defined analytically as

$$\psi = \frac{N^2 \cdot I}{R} \quad (1)$$

where N is the number of conductor turns, I is the electric current and R is the magnetic reluctance of the magnetic circuit in which the flux tubes are established [16]. Therefore the numerator in (1) is a known quantity as the number of turns and the current are both given. Consequently the only unknown value in (1) is the magnetic reluctance of the magnetic circuit which – in the most general case – is a nonlinear quantity and varies as a function of the current. It transpires that the fitted flux tubes in Figs. 3 and 6 give close estimates of the reluctance values R for both rotor positions. We will demonstrate how the magnetic reluctance is estimated and the reasons behind the numerical robustness of the flux tube method in Section 3. Using (1) the flux linkages are found for both rotor positions for the two SR machine designs considered in Table 1 and are shown in Fig. 4.

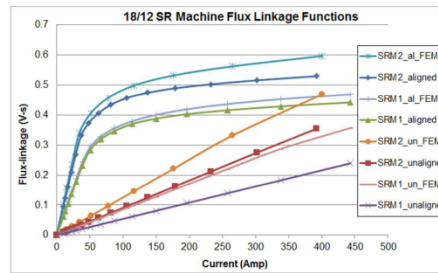


Fig. 4. The flux linkage functions for the SRM1 and SRM2 SR machine designs obtained with the flux tubes method and from the 2D FEM.

The unaligned flux linkage function of Fig. 4 for the SR machine may be estimated by constructing a flux tube model for the unaligned magnetic circuit, as shown in Fig. 6. A similar as before visual inspection of the FEM field plot of Fig. 5 is undertaken first in order to locate approximate equipotential magnetic field density contours which serve as equipotential slices of the magnetic circuit. Once such equipotential magnetic field density slices are found,

This article has been accepted for publication in a future issue of this journal, but has not been fully edited. Content may change prior to final publication in an issue of the journal. To cite the paper please use the doi provided on the Digital Library page.

constructed and converted into coordinate points, the automatic generation of flux tubes for the unaligned rotor position can be performed as shown in Fig. 6. Next, the total reluctance R of the flux tubes is found from the geometric information about the flux tubes and is used in (1) to find the flux linkage of the unaligned rotor position as in Fig. 4.

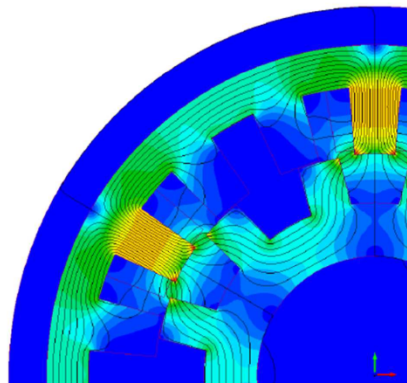


Fig. 5. 2D FEM solution for the 18/12 three phase SRM2 design at the unaligned rotor position.

The visual comparison of flux function distributions in Figs. 5 and 6 reveals that in Fig. 6 the flux tubes are not exactly replicated, but only approximately. However, the numerical comparison of the results obtained from the relevant distributions, as presented in Fig. 4, indicates that the flux tube method gives values sufficiently close to the associated 2D FEM results.

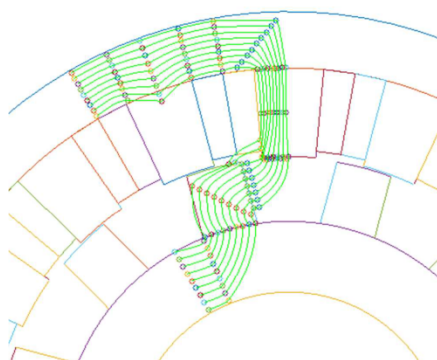


Fig. 6. Subdivision of the SRM2 magnetic circuit into equipotential slices at the unaligned rotor position using flux tube methodology.

It should be noted at this point that the flux tube based flux linkage estimation took 1s compared to 45s in the case of the 2D FEM aligned case which was the faster of the

two FEM cases, not taking into account the FEM model geometry preparation and solver setup time. Fig. 4 indicates that both of the SRM2 machine flux linkage functions are underestimated compared to the FEM based solutions. The aligned flux linkage function of flux tubes is underestimated by around 11% and the unaligned by 24% at the 400A current level which is above the peak current limit of the machines as specified in Table 1. The underestimation of the flux tube based analysis results is due to the fact that the flux tube method constrains the flux tube paths which are then fixed for all operating current levels of the machine, whereas in the 2D FEM based solution the flux tubes are positioned in such a way as to minimize the path reluctance for each current level. In other words, the leakage flux was not incorporated into the flux tube model. The flux linkage value discrepancies in Fig. 4 may be attributed to the absence of the leakage flux in the flux tube model. As a partial remedy, to account for the discrepancies in the flux linkage values quoted above and in Fig. 4, two calibration parameters (aligned and unaligned) were introduced, both proportional to the errors, in order to minimize the likely numerical errors from the subsequent flux tubes based simulations.

Having obtained the flux linkage functions for the SRM2 machine design, as detailed in Table 1, the complete flux linkage map of the machine can be efficiently and accurately constructed using the gauge curve fitting techniques as detailed in [1]. Therefore it is not necessary to model the intermediate rotor position flux functions. Once the complete flux linkage map of the SR motor is available, the speed-torque and output power characteristics of the machine can be obtained, given that the operating voltage, current and firing angles are known. The characteristics analysis is performed as a flux-tubes post-processing step and thus the post-processing times are not measured since they do not depend on the magnetic field analysis times. In order to compare the result from the flux tube method with the measurements cited in [4] the SRM2 motor performance was evaluated at a rated machine speed of 1200 rpm. The flux tube based flux linkage map gives rise to the torque value of 420Nm at the rated machine speed, an overestimate by 5% compared with the measurement, but very close to the result from the FEM analysis. Moreover, the estimated RMS value of the current for the SRM2 machine at the rated speed is 220A, a 7% overestimate compared with the measurement. Overall the very fast estimates based on the flux tube method appear to be close, from the practical point of view, to the experimental results and comparable to those obtained from the much more computationally expensive 2D FEM.

3. Accuracy and Robustness of the Flux Tube Method

The flux tube method was first formulated analytically in [16]; it is possible to derive equations governing the accuracy of the numerical approach based on this method. A detailed account of the derivations may be found in [15], a summary is given below.

Assume a system of tubes arranged in parallel to each other to occupy an arbitrary shaped 3D space as in Fig. 7. Let each such tube contain a magnetic flux ϕ due to a difference in magnetic potentials V_a and V_b at a known

4

This article has been accepted for publication in a future issue of this journal, but has not been fully edited.

Content may change prior to final publication in an issue of the journal. To cite the paper please use the doi provided on the Digital Library page.

distance l_{ab} apart. If the flux tubes are subdivided into slices of arbitrary length along their entire length (between the nodes V_a and V_b) the cross-sectional area of each such slice of each tube can be replaced by an average

$$A_j \leftarrow \frac{1}{2}(A_j + A_{j+1}), \quad j = 1, 2, \dots, n \quad (2)$$

where the arrow indicates a substitution. Magnetic flux will of course exist in both the magnetic parts of the machine (iron) and in the air gap, the latter usually the more important from the point of view of the total *mmf* requirements. In terms of error analysis it is helpful to consider the air gap and iron parts separately as the final expressions are somewhat different.

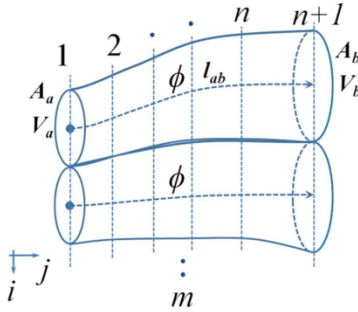


Fig. 7. A system of magnetic flux tubes arranged in parallel.

3.1. Flux Tubes in the Air Gap

The magnetic reluctance of each tube is approximated by

$$R_{ab} = r_j = \sum_{j=1}^n \frac{l_j}{\mu_0 \cdot A_j} \quad (3)$$

where l_j is the length of each component sub-tube (with the ends defined by the appropriate slices). The higher the number of subdivisions (n) the better chance to approach the true value of the reluctance R as in (1), providing the tube paths are positioned correctly, with tubes arranged in parallel. Following this line of reasoning it was shown in [15] that the total reluctance of the system of tubes in air, as in Fig. 7, will be given by

$$\frac{1}{R_{parallel}} = \sum_{i=1}^m \left(\sum_{j=1}^n \frac{l_j}{\mu_0 \cdot A_j} \right)^{-1} \times \frac{(1+\alpha)}{(1+\lambda)} \quad (4)$$

where α is an average error for the flux tube areas and λ is an average error for the flux tube lengths, both of which can be numerically positive, negative or zero. The meanings of these errors may be explained with the help of Fig. 8, where a flux tube will be, in most cases, only approximately close to the shape of the 'true' tube (i.e. obtained from a 2D FEM). This may be captured by the following expressions

$$A_j \cdot \varepsilon_{A_{av}} = A_j + A_j \cdot \alpha; \quad l_j \cdot \varepsilon_{l_{av}} = l_j + l_j \cdot \lambda. \quad (5)$$

where the relevant errors ε have been averaged.

A substitution into (3) and application of the basic formula for a parallel connection of reluctances ultimately leads to the expression (4); as already mentioned the full derivation may be found in [15].

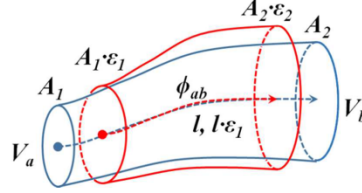


Fig. 8. An approximation of a tube introducing the errors in length and area.

Considering the implications of (4) it emerges that if both errors were positive, or both negative, at the same time, the resultant error would benefit from some cancellation effect, as it is the ratio of the two errors that matters. The worst case scenario will occur when the areas are overestimated and the lengths are underestimated, or vice versa. The result in (4) also indicates that the errors will not affect the resultant value of the reluctance dramatically as even if the area and the length errors were both around 10% and of opposite sign, the overall error in the reluctance value would be limited to around 20%. Moreover, such an error would occur only if all the modelled flux tubes experienced the worst case scenario simultaneously.

3.2. Iron Circuit Flux Tubes

A similar argument may be applied to the system of flux tubes in the magnetic parts of the machine resulting in the expression

$$R_{parallel} = \left(\sum_{i=1}^m \left(\sum_{j=1}^n \frac{H_{ij} \cdot l_{ij}}{B_{ij} \cdot A_{ij}} \right)^{-1} \right)^{-1} \cdot (1+\pi) \cdot (1+\lambda). \quad (6)$$

where π denotes an error introduced due to the uncertainties in the magnetization data of the magnetically nonlinear material [15], which can be in the region of $\pm 10\%$ as typically found in laboratory measurements and λ denotes an average error for the flux tube lengths, as in (5).

The repercussions of (6) are somewhat different than for the tubes in the air gap, as encapsulated by (4), as this time the cancellation of errors will occur when the component errors are of opposite sign. At the same time it transpires that the area error α is no longer important, whereas the error in magnetization data needs to be considered. The worst case scenario occurs when both errors in (6) are of the same sign.

Following the above discussion it is now possible to explain why the flux linkage functions in Fig. 4 – obtained from the approximate distributions in Figs. 3 and 6 – give results close to the 2D FEM analysis. As the local errors given in (5) for the modelled tubes will vary from point to

This article has been accepted for publication in a future issue of this journal, but has not been fully edited.
Content may change prior to final publication in an issue of the journal. To cite the paper please use the doi provided on the Digital Library page.

point in the magnetic circuit, the total error is likely to be small thanks to the mentioned cancellation effects in (4) and (6). This leads to an encouraging observation regarding the improved flux tube formulation that the method does not require any particular calibration and will perform satisfactorily in practical situations. To ensure the accuracy the number of slices n in (2) should be kept at a reasonable level, depending on the geometry of the magnetic circuit. The robustness of the flux tube method is therefore assured.

4. MULTI-OBJECTIVE OPTIMIZATION USING FLUX TUBES

The analysis of the SR machine based on flux tubes has been shown to be fast and accurate for practical purposes, making the method an ideal choice for rapid initial optimization. To illustrate the optimization process the SRM2 machine from Table 1 had been selected for further improvements while the design constraints were kept fixed as originally imposed in [4]. The design variables with associated ranges and constraints for the multi-objective optimization undertaken are shown in Table 2.

Table 2 Parameters for the 18/12 SR Machine Optimization

Design Parameters	Initial Value	Value Range
Stator Outer Diameter	269	269
Back Iron Thickness	17.25 mm	5 - 25 mm
Rotor Pole Height	19.5 mm	10 - 30 mm
Stator Pole Height	27 mm	10 - 50 mm
Stator Pole Angle, β_1	11 degrees	6 - 12 degrees
The Pole Root Angle, β_2	11 degrees	6 - 12 degrees
Shaft Diameter	100 mm	80 - 160 mm
Wire Turns	17 turns	5 - 50 turns
Stack Thickness	135 mm	135 mm
Air Gap Length	0.5 mm	0.5 mm
Number of Phases	3	3
Peak Phase Current	320 A	320 A
Supply DC Voltage	500 V	500 V

In the table the stator pole angles are as defined in Fig. 2 whereas the rotor pole angle was equal to β_1 .

Given that the flux tube method takes only 3s to construct the complete flux linkage map of the investigated SRM2 SR machine, and noting that the number of design variables is quite high, the evolutionary design optimization routine based on Genetic Algorithm (GA) [21] was considered the best choice since the algorithm directly benefits from accurate and fast-to-evaluate objective functions as provided by the flux tube functions. The capability to perform constrained multi-objective optimization was a further incentive to select GA for this task.

Three objective functions for the SR machine were defined. The first objective was to maximize the average torque at a rated machine speed of 1200rpm, as originally specified in [4]. Secondly, the speed range over which rated constant power could be sustained by the machine was also to be maximized; this objective function is measured in units of kW×rpm. Finally, the third objective function was selected to maximize the machine efficiency at the rated speed of 1200rpm.

The GA based constrained multi-objective optimization routine was configured as follows. The

population size of 100 individuals was chosen and the number of generations set to a value of 30. Therefore in total 3,200 individuals were generated in order to optimize the three simultaneous objectives, for the seven design variables and subject to six constraints, as detailed in Table 2. The GA solver was passed an 'elitism score' of 30% – effectively limiting the count of elite parents (individuals) to 30% of the total population in a given generation. The elitism score prevents too large a number of suboptimal machine designs from being carried over into subsequent generations [21].

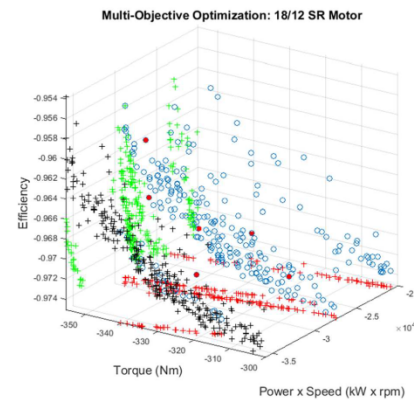


Fig. 9. 3D scatter plot of the three objective function design points (circles) and the projections of Pareto fronts onto each plane (plus markers).

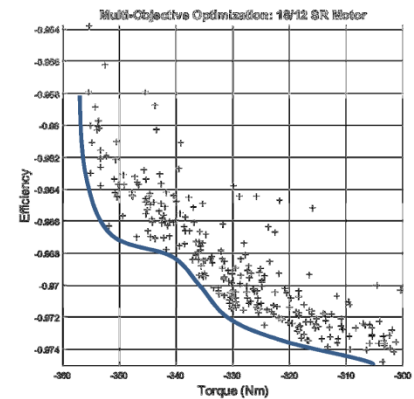


Fig. 10. 2D plot of the two objective functions with the approximate projection (solid line) of 3D Pareto front onto the plane.

Once the optimization task, using the GA, was complete the optimized three objectives for the 18/12 SR machine were simultaneously visualized as a 3D scatter plot

6

This article has been accepted for publication in a future issue of this journal, but has not been fully edited.

Content may change prior to final publication in an issue of the journal. To cite the paper please use the doi provided on the Digital Library page.

for ease of interpretation, as shown in Fig. 9. It should be noted that the complete GA simulation took 131551s, which is roughly 37 hours; therefore each individual took, on average, approximately 42s to evaluate all three objectives.

Visual interpretation of the 3D cloud of points in Fig. 9 is aided by the projected pareto fronts on each of the three planes. One such pareto front projection on the torque-efficiency plane of Fig. 9 is shown as Fig. 10 for clarity.

The concave pareto front on the torque-efficiency plane can be clearly seen as it is essentially continuous. Thus it can be deduced that the machine design trade-off between efficiency and torque must be made – as is always the case. That is, a higher torque will inevitably imply lower efficiency, and vice versa. The concavity of the pareto front on the torque-(power/speed) plane of Fig. 9 is less pronounced, which is largely due to the discontinuities of the design points on that particular pareto front. However, it is still possible to observe that the projected red plus markers onto the plane roughly indicate concavity; this implies that a high torque machine necessitates a lower constant power/speed product compared to a low torque machine. The pareto front could have resulted in a much more coherent and continuous front if either the number of individuals or the elitism score, or both, of the GA were set to a higher number [21]. The usual technique of obtaining a well-defined pareto front with the GA based optimization is of course through trial and error of the mentioned parameters, but this was not the main goal of this exercise. Furthermore, the current optimization task was to explore possible improvements upon the earlier machine design as reported in [4]. Finally, the pareto front on the efficiency-(power/speed) plane is almost linear and has little effect on the efficiency of the machine, as seen in Fig. 9. This was to be expected since the efficiency estimation was for the fixed base-speed of the machine and was thus a function of the torque only.

For the computing time comparison it was recorded that the FEM simulations of the representative machine geometries took approximately 140s each to complete – taking into account the parallel speedup of two computing cores. Assuming less than ideal parallel speedup of only 1.8 times, rather than 2.0, the average FEM solution time was approximately 252s – thus achieving at least six times the speedup with the flux tube based method compared to the FEM based solution. The speedup result is consistent with the previously undertaken flux tubes based GA optimization [15]. Further advantage of using flux tubes based optimization is that the requirement for extensive computing software and hardware is minimal as the method can be implemented with any modern computer scripting language such as Octave [22].

Returning to the point made in Section 2 regarding the accuracy of the flux tubes based SR machine analysis, it is now necessary to enquire if the same statement is true for the design optimization as well, as analysis and design are not the same tasks. The errors stemming from the flux tube based optimization for the torque, efficiency and *rms* current are displayed in Fig. 11 for several arbitrarily selected designs from Fig. 9 (red circles). The selection of points was random so as not to favour any particular design – it is a simple test to estimate average errors of the flux tube based method. As can be seen the discrepancies between the flux tube estimates and 2D FEM solutions are not large. It

emerges that the averaged errors for the selected number of designs are 11%, 2% and less than 1% for the torque, current and efficiency, respectively.

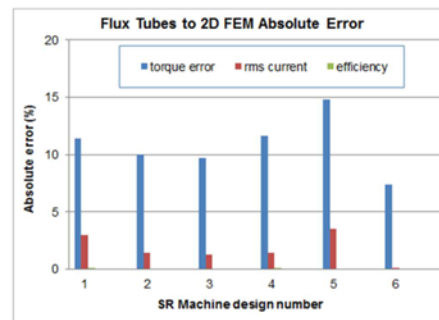


Fig. 11. Flux tubes method absolute error (%) of torque, efficiency and rms current for the randomly selected SR machine designs from Fig. 9.

It can be argued therefore that the flux tubes based optimization furnishes objective functions which are accurate for the purpose of rapid initial design optimization of SR machines. It is reiterated here that the flux tubes accuracy can be controlled, and therefore increased, by selecting a larger number of flux tube slices n , while there were only $n = 15$ such slices in Figs. 3 and 6 – a very coarse subdivision compared to a fine subdivision in the case of FEM solutions.

5. FLUX TUBE BASED DESIGN OPTIMIZATION CYCLE

We can now revisit the concept of the hierarchical design, as depicted in Fig. 1 of Section 1, in the context of the SR machine design and the proposed flux tube approach. The basic steps in the original hierarchy in Fig. 1 will normally be followed as there is little choice in the provision of magnetic analysis techniques that are fast, intuitive and accurate at the same time. Thus in order to fully explore the available machine design space within acceptable computing times the designer is forced to follow the specified sequence. The flux tube approach, however, offers new opportunities due to its numerical error robustness and fast computations. The overall flux tube accuracy is not sufficient for the method to completely replace the more precise but time consuming 2D FEM, but does allow for the notion of rapid design to be introduced. This is elaborated upon in the flowchart of Fig. 12; it should be noted, however, that this flowchart describes a proposed design cycle, rather than suggesting a particular optimization algorithm. The advocated cycle defines a new paradigm in the rapid design of SR machines.

This article has been accepted for publication in a future issue of this journal, but has not been fully edited.
Content may change prior to final publication in an issue of the journal. To cite the paper please use the doi provided on the Digital Library page.

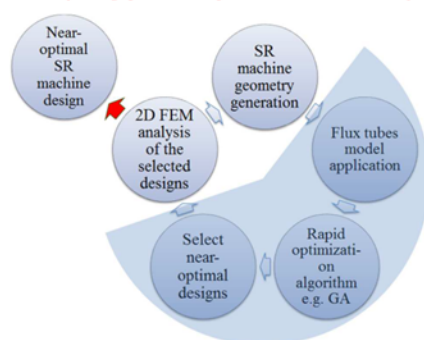


Fig. 12. Proposed rapid SR machine design cycle incorporating the flux tubes based modelling.

The rapid design process in the proposed cycle starts with the definition of the geometry of the SR machine and creation of the flux tube model (steps described in Section 2). After the flux tubes have been generated the model can be combined with a rapid optimization algorithm – as indicated by the third step in Fig. 12. Once the optimization based on the flux tube method has been completed the near-optimal designs are chosen, those which appear the closest to the design goals for a particular application – this is step four in the design cycle. The selected designs, arrived at by way of flux tube model optimization, are reanalysed with an order of magnitude more accurate method (but at the same time much slower and non-intuitive) such as 2D FEM. If the FEM solutions confirm that the selected flux tube based designs are indeed near-optimal, the rapid design optimization cycle can conclude, as the near-optimal SR machine design is found and confirmed – this is the final step of the design cycle. However, if the 2D FEM indicates too large an error of all the selected designs, then the whole design cycle can be repeated in an iterative fashion until a satisfactory accuracy has been accomplished.

The proposed SR machine rapid design optimization cycle of Fig. 12 can now be put into perspective in relation to the hierarchical design of Fig. 1. The shaded segment in Fig. 12, which encompasses the three distinct design steps, can now – with its favourable qualities of fast and intuitive computations – largely replace the middle stage in the hierarchical design pyramid in Fig. 1, that is essentially replace the slow and non-intuitive 2D FEM solutions, since the numerical accuracy of the flux tube method was shown to be sufficient to guide the rapid initial optimization task to its successful completion. The same statement is emphasized in the proposed design cycle in Fig. 12, where the 2D FEM is not completely excluded, but is used sparsely. Another way of describing the process would be to say that the flux tube method complements the FEM by taking over the main burden of the computational effort. Thus the synergy of the various design methods and approaches is enhanced through appropriate combination of very fast and very accurate methods. Ultimately significant savings in computing resources and reduced computing times may be achieved at the most crucial stage of the SR machine design

process, where the design space is still very large. Although the FEM computations are not completely eliminated, they are drastically reduced.

6. Conclusions

The following conclusions can be drawn regarding the rapid multi-objective optimization of SR motors assisted by the flux tubes modelling approach. First, as has been demonstrated by an example, the design cycle can be significantly shortened while preserving the original large design space. As a result substantial savings in computing resources and simulation times can be accomplished without loss of accuracy and avoiding the risk of missing the global optimum. Finally, the machine designer is presented with a fast, intuitive and practical optimization tool – one which can be utilized without elaborate computational resources.

Future implementations of the proposed flux tube based method are likely to include more elaborate representation of the flux tubes to model the leakage flux, as well as the design of synchronous reluctance machines where, similarly to the SR machines, the challenges of time consuming nonlinear magnetic simulations hinder the design process.

7. Acknowledgments

This work is kindly supported by an EPSRC grant (EP/G03690X/1).

8. References

- [1] T. J. E. Miller, *Switched Reluctance Motors and Their Control*. Oxford University Press, Oxford UK, 1993.
- [2] T. J. E. Miller ed., *Electronic Control of Switched Reluctance Machines*. Newnes Power Engineering Series, 2001.
- [3] R. Krishnan, *Switched Reluctance Motor Drives: Modeling, Simulation, Analysis, Design, and Applications*. CRC Press LLC, Boca Raton Florida, 2001.
- [4] M. Takeno, A. Chiba, N. Hoshi, S. Ogasawara, M. Takemoto, and M. Azizur Rahman, "Test results and torque improvement of the 50-kW switched reluctance motor designed for hybrid electric vehicle," *IEEE Trans. Industry Applications*, vol. 48, pp. 1327-1334, August 2012.
- [5] N. Schofield, S. A. Long, D. Howe, and M. McClelland, "Design of a switched reluctance machine for extended speed operation," *IEEE Transactions On Industry Applications*, vol. 45, no. 1, January/February 2009.
- [6] J. D. Widmer, R. Martin, and M. Kimiabeigi, "Electric vehicle traction motors without rare earth magnets," *Sustainable Materials and Technologies*, 3, pp. 7-13, Elsevier, 2015.
- [7] K. M. Rahman, B. Fahimi, G. Suresh, A. V. Rajarathnam, and M. Ehsani, "Advantages of switched reluctance motor applications to EV and HEV: design and control issues," *IEEE Trans. on Industry Applications*, vol. 36, no. 1, January/February 2000.
- [8] J. M. Stephenson and J. Corda, "Computation of torque and current in doubly salient reluctance motors from nonlinear magnetisation data," *IEE Proc.*, vol. 126, no. 5, May 1979.

This article has been accepted for publication in a future issue of this journal, but has not been fully edited.

Content may change prior to final publication in an issue of the journal. To cite the paper please use the doi provided on the Digital Library page.

- [9] R. Krishnan, R. Arumugam, and J. F. Lindsay, "Design procedure for switched reluctance motors," *IEEE Trans. on Industry Applications*, vol. 24, no. 3, pp. 456-461, June 1988.
- [10] T. J. E. Miller, "Nonlinear theory of the switched reluctance motor for rapid computer-aided design," *IEE Proc.*, vol. 137, no. 6, Nov. 1990.
- [11] M. Balaji and V. Kamaraj, "Evolutionary computation based multi-objective pole shape optimization of switched reluctance machine", *Electrical Power and Energy Systems* vol. 43 pp. 63–69, Elsevier, 2012.
- [12] C. Ma and L. Qu, "Multiobjective Optimization of Switched Reluctance Motors Based on Design of Experiments and Particle Swarm Optimization," Paper 294, DigitalCommons@University of Nebraska – Lincoln, 2015.
- [13] Y. K. Choi, H. S. Yoon, and C. S. Koh, "Pole-shape optimization of a switched-reluctance motor for torque ripple reduction," *IEEE Trans. Magn.*, vol. 43, no. 4, pp. 1797–1800, 2007.
- [14] A. Stukys, M. Rotaru, and J. K. Sykulski, "A refined approach exploiting tubes of flux for analysis of linear switched reluctance motor," *International Journal of Applied Electromagnetics and Mechanics*, vol. 51, pp. S13-S21, IOS Press, 2016.
- [15] A. Stukys and J. K. Sykulski, "An efficient design optimization framework for nonlinear switched reluctance machines," *IEEE Trans. Industry Applications*, vol. 53, no. 3, pp. 1985-1993, February 2017.
- [16] H. C. Roters, *Electromagnetic Devices*, John Wiley & Sons Inc., 1941.
- [17] L. Byeong-Seok, "Linear switched reluctance machine drives with electromagnetic levitation and guidance systems," Doctoral Thesis, Virginia Polytechnic Institute and State University, November, 2000.
- [18] U. S. Deshpande, J. J. Cathey, and E. Richter, "High-force density linear switched reluctance machine," *IEEE Transactions On Industry Applications*, vol. 31, pp. 345-352, no. 2, March/April 1995.
- [19] C. A. Vaithilingam, N. Misron, M. R. Zare, I. Aris, and M. H. Marhaban, "Computation of electromagnetic torque in a double rotor switched reluctance motor using flux tube methods," *Energies*, 5, pp. 4008-4026, DOI:10.3390/en5104008, 2012.
- [20] J. K. Sykulski, "Dual field modeling using tubes and slices," *Advances in Engineering Software*, vol. 21, pp. 21-26, Elsevier Science Limited, 1995.
- [21] D. E. Goldberg, *Genetic Algorithms in Search, Optimization & Machine Learning*. Addison-Wesley, 1989.
- [22] GNU Octave, <https://www.gnu.org/software/octave/>, accessed 10 April 2017.

An Efficient Design Optimization Framework for Nonlinear Switched Reluctance Machines

Aleksas Stukys and Jan K. Sykulski, *Fellow, IEEE*

Abstract – A new computationally efficient paradigm for the design and analysis of switched reluctance machines is proposed. At the heart of the rapid analysis and design methodology is the reduced order computational method based on a flux tube model which has been refined and extended. It is demonstrated how the improved model enables consistent and accurate analysis and design optimization. Instead of an analytical derivation, an automatic generation of cubic splines is introduced to model the magnetic flux. The flux linkage functions obtained from the improved flux tube method indicate that the method offers good accuracy compared to finite element based analysis, but with significantly improved computational efficiency. The approach is applicable to translating and rotating switched reluctance machines of various topologies and therefore enables rapid design search and optimization of novel topologies.

Index Terms -- nonlinear switched reluctance machine, magnetic circuit analysis, flux tube modeling, optimization.

I. NOMENCLATURE

A : cross-sectional area
 B : magnetic field density
 H : magnetic field strength
 l : flux tube cord length
 R : total magnetic circuit reluctance
 r : individual flux tube reluctance
 N : number of conductor turns
 t : tube, flux
 I : electric current
 V : magnetic field potential at a node
 α : flux tube cross-sectional area error
 ψ : flux linkage
 λ : flux tube cord length error
 π : magnetic field strength error
 μ : magnetic permeability
 ε : average error
 ϕ : magnetic flux
 $\hat{\cdot}$: estimated value

II. INTRODUCTION

SWITCHED reluctance (SR) machines have attracted substantial attention due to their simple and robust construction. SR machines are as versatile, from application point of view, as the well-established induction, DC, and brushless permanent magnet electric machines. The SR technology spans the following topologies: radial flux [1], axial flux [2], transverse flux rotating machines [3], [4],

translating (linear) machines [5], [6], and tubular translating (linear) machines [7]. SR machine application areas are as diverse as the more traditional electric machine technologies mentioned earlier. For example, the radial and axial flux machines have been used in many industrial drives, traction motor and pumping applications [8]–[10]. The novel SR linear machines have been used as magnetic propulsion and levitation devices for railway systems in transportation [11]. The tubular linear SR machines were successfully tested in medical applications as artificial heart pump actuators [12].

However, analysis and design of SR machines is a complex task compounded by their non-linear behavior. Despite some effort [13] the analysis and design calculations have not yet been developed into intuitive analytical tools comparable to the methods available for the more established types of machines, such as induction or permanent magnet. The main difficulty with the analysis and design of SR machines is the magnetic nonlinearity caused by the heavily saturated iron parts of the machine circuit. The non-saturating SR machines, as used in some niche applications, are not considered here.

Given the wide variety of topological arrangements of SR machines, which is expected to grow in the future as the demand for the new applications increases [14], it is vital to establish computationally efficient analysis and design methods. The aim is to make the design task more systematic which in turn will open new application areas for the versatile SR electric machine technology.

Reduced order computational methods, the most notable example being the magnetic equivalent circuit (MEC) approach, have been successfully employed in the past to various types of electric machines [15]. The main advantage of the MEC based models is that they are relatively accurate given their computational efficiency. The finite element analysis (FEA) is very useful for accurate analysis of the established electric machine technologies, but it does not offer the cause-and-effect insight when novel and unfamiliar machine topologies are being considered [16]. Therefore, bearing in mind the advantages of the MEC based analysis methods, the design cycle is proposed as illustrated in Fig. 1.

The starting point (red rim) in Fig. 1 is where a novel topology SR machine is identified and considered for a certain application because it meets some particular requirements imposed by the application, for example: cost, volume and mass, mechanical, etc. Next, the improved flux tube based method [17], [18], which we propose in this paper, is employed to construct the electromagnetic model of the machine and is subsequently used in conjunction with a design search and optimization algorithm, e.g. the genetic algorithm (GA) [19]. Once a set of near optimal solutions

This work is supported by an EPSRC grant (EP/G03690x/1).

A. Stukys and J. K. Sykulski are with the Department of Electronics and Computer Science, University of Southampton, Southampton SO17 1BJ, United Kingdom (e-mail: A.Stukys@soton.ac.uk / jks@soton.ac.uk).

(i.e. a Pareto front) is obtained from the previous design cycle step, a few designs are identified for further optimization using an order of magnitude more accurate analysis technique, such as FEA. If FEA confirms that indeed these designs are near optimal, the design cycle can conclude as the machine which satisfies all the design constraints has been found (green rim). If, however, the FEA proves otherwise, the knowledge and insights gained from the flux tube modelling step are fed back into the novel topology machine generation step and the design cycle is repeated.

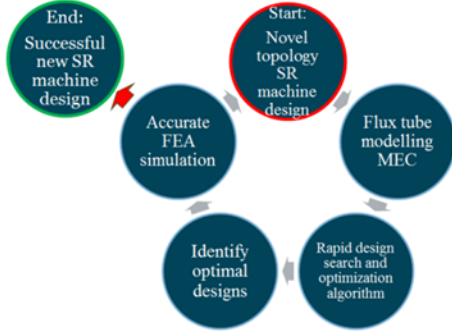


Fig. 1. The proposed SR machine design cycle using a reduced order computational method of flux tubes.

III. FLUX TUBE MODELING

MEC based modeling has been successfully used in the past for rapid analysis of induction and permanent magnet AC machines [20], as well as for SR machines [21]–[23]. In this paper we propose an improved flux tube model for analysis and design of SR machines, which offers computational efficiency and simplicity compared to the traditional analytical derivation of flux tubes as in [23].

First it is necessary to define what is meant by the term flux-tube. Referring to Fig. 2, a flux-tube will have an arbitrary length and an arbitrary cross-sectional area defining a tube in which the magnetic flux is established due to the unequal magnetic potentials V_a and V_b .

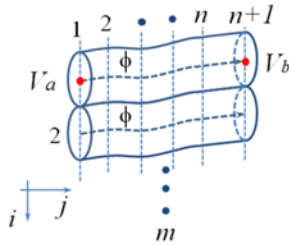


Fig. 2. A system of flux tubes in parallel.

The trajectory of the tube, between the two nodes, can be approximated by a combination of straight line and circular arc segments. The material property, in which the flux-tube exists, is defined by magnetic permeability and will, in

general, vary as a function of the magnetic potential along the tube. If the material is air then the permeability of free space is substituted, otherwise the magnetization curve of the material must be used. To form a system of flux tubes in three-dimensions (3D) the tubes are combined to fill the entire 3D space.

Accurate magnetic reluctance estimation of the flux tubes is important as this will determine the flux-linkage functions of the SR machine defined as [16]

$$\psi = \frac{N^2 \cdot I}{R}. \quad (1)$$

In the most general terms, and referring to Fig. 2, the flux tube reluctance can be expressed as

$$R_{ab} = \frac{V_a - V_b}{\phi} = \int_0^l \frac{1}{\mu(a, b, l) \cdot A(l)} dl. \quad (2)$$

The flux-linkage functions is all that is needed to describe the SR machine performance, specifically the speed-torque curve for a rotary machine or thrust force and corresponding linear speed values for a translating machine. From these characteristics the machine output power can readily be found. The procedure will now be illustrated by an example.

A. A Flux Tube Modeling Example

The analysis of SR machines hinges on the ability to accurately estimate the aligned and unaligned flux-linkage functions as given in (1), which for the saturable machines are always nonlinear for a range of excitation currents [24]. Again, this task is fairly easily accomplished with FEA based methods; however, this approach may be computationally inefficient if a near optimal design of novel and unfamiliar topology machine is sought. Here we propose a method based on the flux tube approach. We will show how to obtain the flux linkage functions for an SR machine by constructing approximate flux tube distributions. It is important to note that this approach is equally applicable to the modeling of rotating and translating SR machines.

To illustrate the improved flux-tube based modeling a translating (linear) switched reluctance machine (LSRM) is considered. Fig. 3 shows a typical LSRM geometry and the resulting magnetic field distribution obtained from an industry standard FEA. Due to the simple geometric (2D planar) and spatial arrangement of the machine the magnetic flux lines can be approximated using cubic-spline representations of flux-tubes of the true flux paths.

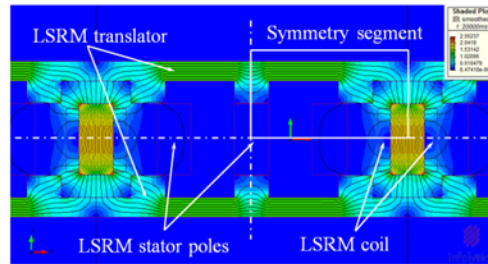


Fig. 3. A double translator linear SR machine topology.

We start by inspecting the general flux function contour and magnetic field density plot obtained from a standard 2D FEA analysis shown in Fig. 3. Next, due to symmetry, we reduce the analyzed magnetic circuit to that of symmetry segment shown in Fig. 3. The proposed flux-tube analysis relies on the ability to approximate the true flux tubes in the magnetic circuit under study using smooth cubic splines.

Zooming into the symmetry segment of the LSRM shown in Fig. 4, we recognize after visual inspection that in most electric machine magnetic circuits of practical importance there will exist the magnetic field equipotential regions.

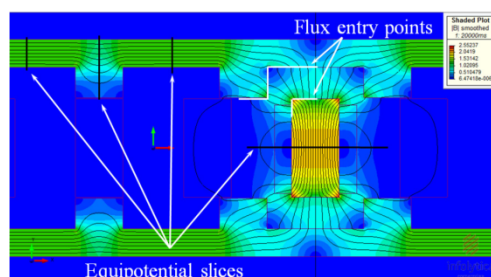


Fig. 4. Subdivision of the symmetry segment into flux tube slices.

Utilizing this knowledge we can manually construct equipotential slices across the flux paths of the magnetic circuit. Up to this stage we were able to subdivide the circuit into four such slices as shown in Fig. 4. However, an attempt to fit smooth and continuous cubic spline approximations of the real flux tubes between any two neighboring slices using single set of intermediate points would result in large interpolation errors along the flux paths. This is because the actual flux tubes have geometric discontinuities between the slices. Therefore, it is necessary to subdivide the flux tubes along their lengths even further. It is possible to do so by recognizing the very important property of the flux tubes that the flux tubes normally enter magnetic material at a right angle to its surface. Thus we are able to construct manually further slices, this time along the magnetic material surfaces, termed 'flux entry points' as in Fig. 4. Once the flux tube subdivision into slices is complete, the automatic cubic spline interpolation can be performed, as illustrated in Fig. 5.

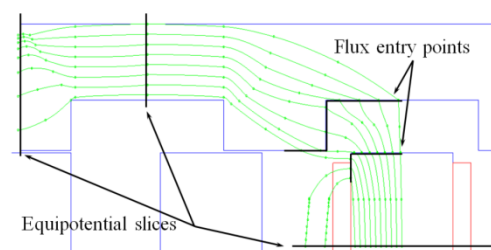


Fig. 5. Cubic-spline approximations of the flux paths for the unaligned translator position.

The automatic cubic spline generation task can be performed by any computer scripting language which supports the automatic cubic spline generation task and offers at least basic graphic plotting capability. Such functionality is offered by MATLAB, Python and Octave, amongst others, including some open source codes. A simple flowchart in Fig. 6 will assist in this task.

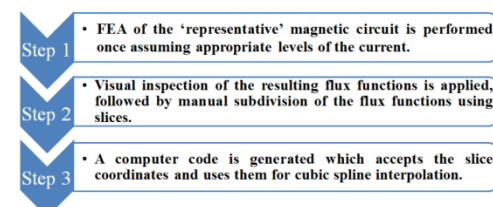


Fig. 6. Flowchart showing how cubic splines can be generated.

As evident from the preceding discussion and Fig. 4, some prior experience and applying engineering judgment are essential and will be helpful when choosing the most representative and convenient coordinate points for the cubic spline interpolation.

Using similar equipotential slice and flux entry points placement techniques the aligned translator position flux-tube approximations are obtained as in Fig. 7. Again, experience and judgement are needed in order to accurately replicate the true flux paths using cubic-spline approximations.

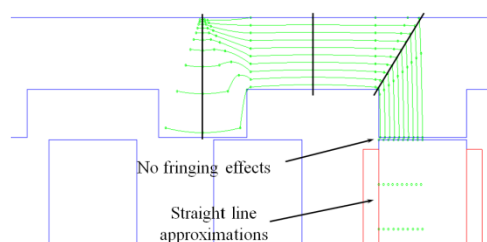


Fig. 7. Aligned translator position flux tubes obtained using cubic-splines.

Some simplifying assumptions are made when fitting the splines in Fig. 7, in particular that there are no fringing or leakage flux effects near the aligned rotor and stator poles as would be expected in a practical machine. Moreover, the energized stator pole flux tubes are approximated using straight lines rather than cubic-splines. Again, this is an approximation, but the resulting errors were found tolerable. Furthermore, the entire flux tube modeling of the machine is considered to be 2D in nature. Consequently, such important 3D effects as conductor winding 'end effects' are not captured by the flux tube method, but neither would this be achieved using the 2D FEA method. As was stated before, the flux tube method is used for rapid initial design search and optimization task and is not intended to replace the more accurate computational techniques such as 3D FEA.

Finally, once the cubic spline approximations to the true

flux tube paths are complete, their individual reluctances can be found from (2) as all the geometric information about the tubes is known from the polynomial equation coefficients, specifically the cross-sectional areas, cord lengths and material properties. Therefore, flux linkage functions, as given by (1), for these two translator cases are readily found.

B. Accuracy and Robustness of Flux Tube Modeling

In order to illustrate the accuracy and robustness of the flux tubes method, from computation and numerical error propagation point of view, analytical formulation is employed. Figure 2 is used to describe what is meant by the system of flux tubes.

1) *Air Gap Reluctance*: From Fig. 2 it is assumed that the flux tube system is in the air gap or other non-magnetic region of the SR machine. The flux tubes have been subdivided into n slices along their lengths and cross-sectional areas of each such slice averaged

$$A_j = (A_j + A_{j+1})/2, \quad j = 1, 2, \dots, n \quad (3)$$

Therefore, the individual reluctance of each of the m flux tubes can be expressed as

$$R_{ab} = r_i = \sum_{j=1}^n \frac{l_j}{\mu_0 \cdot A_j}. \quad (4)$$

Now, because the system of flux tubes in Fig. 2 is arranged in parallel, the total reluctance will be

$$\frac{1}{R_{parallel}} = \frac{1}{r_1} + \frac{1}{r_2} + \dots + \frac{1}{r_m} = \sum_{i=1}^m \left(\sum_{j=1}^n \frac{l_j}{\mu_0 \cdot A_j} \right)^{-1}. \quad (5)$$

As argued in the previous section, the resulting flux tube system of Fig. 5 approximates the FEA solution in Fig. 4 well, but is not exact. The flux tubes method considers discretized systems rather than continuous. Thus it is necessary to take two neighboring cross-sectional areas of each tube-slice and average them to produce a mean value for that particular flux-tube slice as in (3). This averaging of cross-sectional areas, however, will introduce some numerical error. The error itself will vary from slice to slice, and from tube to tube, and even from system to system. Taking into account the numerical error thus created, (4) can be expressed as follows

$$r'_i = \frac{l_1 \cdot \epsilon_{i1}}{\mu_0 \cdot A_1 \cdot \epsilon_{A1}} + \frac{l_2 \cdot \epsilon_{i2}}{\mu_0 \cdot A_2 \cdot \epsilon_{A2}} + \dots + \frac{l_n \cdot \epsilon_{in}}{\mu_0 \cdot A_n \cdot \epsilon_{An}}. \quad (6)$$

It is assumed that each error term ϵ in (6) will be in the region of, and unlikely to exceed, ± 1.1 for the averaged cross-sectional areas and cord lengths of each slice. If the number of terms n in (6) is increased, the errors resulting from the estimated cord lengths and cross-sectional areas of the tube slices can be averaged, namely

$$r'_i = \left(\frac{l_1}{\mu_0 \cdot A_1} + \frac{l_2}{\mu_0 \cdot A_2} + \dots + \frac{l_n}{\mu_0 \cdot A_n} \right) \times \frac{\epsilon_{iav}}{\epsilon_{Aav}}. \quad (7)$$

For convenience, the averaged errors of the cross sectional areas and cord lengths of each slice in (7) can be written as

$$A_j \cdot \epsilon_{Aav} = A_j + A_j \cdot \alpha; \quad l_j \cdot \epsilon_{lav} = l_j + l_j \cdot \lambda. \quad (8)$$

It is now possible to show what impact the errors of the estimated geometries will have on the reluctance value of the whole system of tubes of Fig. 2. Rewriting (6) in terms of (8)

$$\begin{aligned} r'_i &= \frac{l_1 \cdot (1 + \lambda)}{\mu_0 \cdot A_1 \cdot (1 + \alpha)} + \frac{l_2 \cdot (1 + \lambda)}{\mu_0 \cdot A_2 \cdot (1 + \alpha)} + \dots + \frac{l_n \cdot (1 + \lambda)}{\mu_0 \cdot A_n \cdot (1 + \alpha)} = \\ &= \left(\sum_{j=1}^n \frac{l_j}{\mu_0 \cdot A_j} \right) \times \frac{(1 + \lambda)}{(1 + \alpha)} \end{aligned} \quad (9)$$

and rewriting (5) in terms of (9)

$$\frac{1}{R'_{parallel}} = \sum_{i=1}^m \left(\sum_{j=1}^n \frac{l_j}{\mu_0 \cdot A_j} \right)^{-1} \times \frac{(1 + \alpha)}{(1 + \lambda)} \quad (10)$$

results in the total reluctance of the system of tube-slices in series and combined in parallel to be

$$R'_{parallel} = \left(\sum_{i=1}^m \left(\sum_{j=1}^n \frac{l_j}{\mu_0 \cdot A_j} \right)^{-1} \right)^{-1} \times \frac{(1 + \lambda)}{(1 + \alpha)}. \quad (11)$$

The result in (11) indicates that the estimated parallel reluctance of the air gap tubes will scale linearly with the quotient of the two errors. Thus it could be argued that if the two error terms are both positive or both negative this will tend to minimize the total error of the parallel reluctance. The worst case scenario occurs if the two errors are of equal magnitude but opposite sign, that is the cross-sectional areas are underestimated whilst the cord lengths of the tubes are overestimated, or vice versa. Even the worst case scenario is considered to be tolerable provided the errors α and λ are not larger than $\pm 10\%$ as stated earlier. Under such conditions the total error can be no more than $\pm 22\%$.

2) *Iron Circuit Reluctance*: In a similar way the reluctance of the magnetically nonlinear iron circuit of the SR machine can be estimated and effects of errors accounted for. Consider Fig. 2 again, this time however with the magnetic permeability no longer constant but varying according to the magnetization curve of the material. Therefore (4) may be rewritten, taking saturation into account, as

$$R_{ab} = \frac{H_{ab} \cdot l_{ab}}{B_{ab} \cdot A_{ab}} = r_i = \sum_{j=1}^n \frac{H_j \cdot l_j}{B_j \cdot A_j}. \quad (12)$$

Assuming that the flux of each tube is of constant value the magnetic field density occurring at each slice is

$$B'_j = \frac{\phi}{A'_j} = \frac{\phi}{A_j(1 + \alpha)} \quad (13)$$

and from (13) the following can be deduced

$$\begin{aligned} \text{if } \alpha > 0 \text{ then } B'_j &< B_j \\ \text{if } \alpha < 0 \text{ then } B'_j &> B_j. \end{aligned} \quad (14)$$

In other words, if the error is positive the magnetic field density will be underestimated compared to the true value and vice versa. From the magnetization curve of Fig. 8 it

follows that the relationship between the erroneous magnetic field density estimate and the resulting magnetic field strength can be stated as

$$\begin{aligned} \text{if } B'_j < B_j \text{ then } H'_j < H_j \\ \text{if } B'_j > B_j \text{ then } H'_j > H_j. \end{aligned} \quad (15)$$

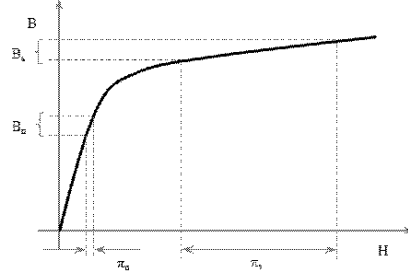


Fig. 8. A typical magnetization curve of a saturable iron circuit and the resulting worst case errors in the non-saturated and saturated regions.

The resulting erroneous magnetic field strength for each of the flux-tube slices along the lines of (8) can be expressed, for convenience, as

$$H'_j = H_j + \pi \cdot H_j = H_j (1 + \pi) \quad (16)$$

The estimated values in the denominators of (12) imply that

$$B'_j \cdot A'_j = \frac{\phi}{A'_j} \times A'_j = \frac{\phi \times A_j (1 + \alpha)}{A_j (1 + \alpha)} = \phi \quad (17)$$

which is trivial, however it does show that the estimated flux, that is the denominator in (12), is not affected by the cross-sectional area error α .

Equation (12) can now be expressed in terms of (16), also remembering to include the tube slice cord length error term derived earlier, as follows

$$\begin{aligned} r'_i &= \frac{H_1 \cdot (1 + \pi) \times l_1 \cdot (1 + \lambda)}{B_1 \cdot A_1} + \\ &+ \frac{H_2 \cdot (1 + \pi) \times l_2 \cdot (1 + \lambda)}{B_2 \cdot A_2} + \dots + \\ &+ \frac{H_n \cdot (1 + \pi) \times l_n \cdot (1 + \lambda)}{B_n \cdot A_n} = \\ &= \left(\sum_{j=1}^n \frac{H_j \cdot l_j}{B_j \cdot A_j} \right) \times (1 + \pi) \cdot (1 + \lambda) \end{aligned} \quad (18)$$

and the parallel reluctance of the system of tubes in the iron circuit is

$$\begin{aligned} R'_{parallel} &= \\ &= \left(\sum_{i=1}^m \left(\sum_{j=1}^n \frac{H_j \cdot l_j}{B_j \cdot A_j} \right)^{-1} \right)^{-1} \cdot (1 + \pi) \cdot (1 + \lambda). \end{aligned} \quad (19)$$

Equation (19) indicates that the cross-sectional area estimation error α has no influence on the final result of the

total reluctance of the iron circuit. However, a new error term appears in (19) due to the estimation of magnetic field strength from the non-linear iron magnetization curve. Therefore, the total saturating iron reluctance will scale as a product of the two errors. In contrast to the total air gap reluctance, as in (11), the iron circuit reluctance value is affected less by the equal magnitude but opposite signs of the errors (that is when one is positive and the other is negative). The worst case scenarios occur when both error terms are of equal magnitude and either both positive, or both negative.

Attention is now turned towards the discussion of the errors in (19) when the iron circuit is in the non-saturated and when it is in the fully saturated regions of the magnetization curve since steady-state SR machine operation takes place in both of these regions. As can be seen from Fig. 8, the error term for the magnetic field strength will be very small when the flux-linkage values of the SR machine are estimated at low phase excitation currents. The situation is very different when flux-linkage values of the SR machine are estimated at high phase excitation current levels where most of the iron circuit is fully saturated. At this condition the π error term is significantly larger, even if uncertainty associated with the magnetic field density value is the same as in the non-saturated region.

Due to the magnetic circuit design of the SR machine used here for illustrative purposes, the air gap and iron circuit components are arranged magnetically to be in series. Thus for the both the aligned and unaligned flux-linkage function estimations, the reluctances given by (11) and (19) will be additive, while the error terms for the unaligned flux-linkage curve will be order of magnitude smaller compared to the error terms of the aligned flux-linkage curve. This effect is due to the point made above, but to repeat: the saturated reluctance error of the aligned SR machine circuit will be exacerbated due to error terms in (19), whereas in (11) the error will be negligible as the air region's length is small as in Fig. 7. On the other hand, the reluctance error of the unaligned SR machine circuit will be made worse due to increased error terms in (11) as the air-gap region's length is large, whereas in (19) the error will be relatively much smaller because of the non-saturated state of the iron as in Fig. 5.

The preceding error analysis of the flux tube approach, and in particular expressions (11) and (19), can be directly compared to the 'tubes-and-slices' (TAS) method used to analyze electric and magnetic fields in linear media [25]. The analytical TAS derivation, in addition to using the tubes, makes use of the construction of a system of slices along the lines of Fig. 2, leading to the creation of dual bounds. The tubes result in a lower bound of the permeance, whereas the slices result in an upper bound. There is similarity to the calculation of a resistance or capacitance, with the analogue of the permeability, μ , being the conductivity, σ , or permittivity, ϵ , respectively. The bounds are guaranteed and thus the true answer always lies between the two values. Taking an average often results in a good numerical approximation.

It may be possible to adapt the flux tube approach if the

resulting error of the system of tubes is to be minimized. A possible strategy is to compare the flux-linkage function based on a particular flux-tube system with a FEA solution and use the numerical error found to correct the subsequently generated systems of flux tubes. Such a strategy would be likely to be most effective when a large number of flux tube systems is being generated, as in GA based optimization.

IV. FLUX TUBE BASED ANALYSIS RESULTS

The proposed flux tube model has been applied to a wide range of SR machine geometries to test if the new method consistently and accurately predicts the performance. To accomplish this, six machine design parameters were selected and varied in order to generate distinct machine geometries. Referring to Fig. 3, the following variables were designated: translator back iron thickness, translator pole height, stator pole height, the pole width, number of turns per coil, machine stack thickness. Table I lists the ranges of the design parameters of the machine.

TABLE I
DESIGN PARAMETERS OF THE 16/20 SR MACHINE

Design Variable	Value	Value Range
Back Iron Thickness	13 mm	6 - 20 mm
Translator Pole Height	14 mm	5 - 15 mm
Stator Pole Height	33 mm	30 - 60 mm
The Pole Width	6.7 degrees	5 - 7 degrees
Number of Turns	57 turn	50 - 100 turn
Stack Thickness	35 mm	10 - 70 mm
Air Gap Thickness	0.5 mm	0.5 mm
Number of Phases	4	4
Peak Phase Current	150 A	150 A
Supply DC Voltage	2.0 kV	2.0 kV

Fig. 9 compares the aligned and unaligned flux-linkage functions, assuming flat-topped current profile as in [16], obtained with the improved flux tube method and using commercial FEA for the design values in Table I.

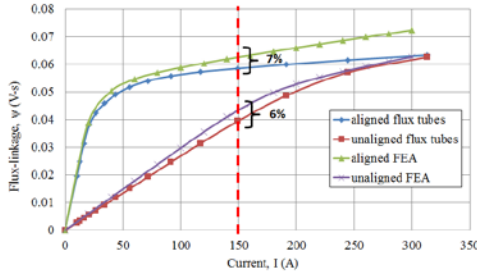


Fig. 9. Flux-linkage functions using the flux-tube method and FEA.

The unaligned flux-linkage functions from both methods compare very well and even such effects as the onset of saturation at higher phase currents, 150A and slightly above, are also captured by the flux tube model. Clearly the unaligned flux-linkage function is linear up to the peak flat-topped current, 150A in this case. Therefore the saturation effects and, more importantly, the numerical discrepancy

from the FEA result will not affect the machine performance prediction in any noticeable way.

The aligned flux-linkage functions obtained from the two methods show some numerical discrepancies, although they are not large. Assuming that the aligned flux-linkage function obtained using FEA software is correct, the flux tube method underestimates the value by 7% at the peak current of 150A. The error is reassuringly low, bearing in mind that the flux tube model of Fig. 7 used only 12 flux-tube slices, which is a coarse subdivision compared to the fine mesh used in FEA. Even more importantly, the aligned flux-linkage function obtained by the flux tube method preserves the 'true' shape of the aligned flux-linkage function as obtained with FEA. This fact, already observed and reported in literature [24] and evident from Fig. 10, has far reaching implications and greater importance – when determining instantaneous torque and phase current waveforms – than the exact numerical answer at only saturated or only unsaturated machine states.

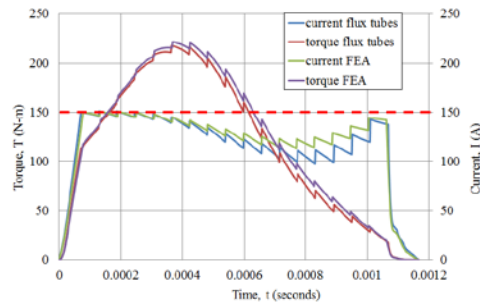


Fig. 10. Comparison of current and instantaneous torque waveforms obtained with the flux tube method and FEA.

Finally – as expected – the accuracy of the approximate prediction becomes worse in the heavily saturated region of the aligned position in Fig. 9, but this is of no practical consequence as the operating current is above the peak value; this part of the curve has been included for completeness, but should be disregarded in the context of the design process.

The instantaneous current and torque waveforms in Fig. 10 were extracted from the resulting flux-linkage map which was constructed with the aid of the gauge curves as described in detail in [24]. The principal equation for the instantaneous torque calculation is given by

$$T = \frac{\partial W}{\partial \theta} \quad (20)$$

where the expression on the right hand side denotes the surface area of the generated flux-linkage map which is proportional to the torque [26].

Consequently, from a visual comparison of the functions in Fig. 9 and the resulting instantaneous torque and current waveforms in Fig. 10, it is evident that the numerical discrepancies are not as significant compared to the discrepancies in similarity of shapes. Drawing the knowledge gained from the above presented analytical derivation of the flux tube method, it is now clear that the answer given by

(19) is more sensitive to the estimated magnetic field strength values in the saturated region than to the non-saturated region of Fig. 8. In this particular case the total circuit reluctance is overestimated, which is conservative, giving the lower aligned flux-linkage function as in Fig. 9.

The instantaneous torque and phase current waveform comparison is important when assessing the improved flux tube method accuracy. Similarly, it is very useful to compare the speed-torque characteristics of the translating SR machine. The machine geometry is first converted from the translating machine domain to the rotating machine domain, as described in [16], to facilitate ease of comparison. Fig. 11 compares speed-torque characteristic envelopes obtained by the flux-tube method and FEA for a range of current firing angles, also referred to as advance angles in [16], computed at each 250 rpm speed increment.

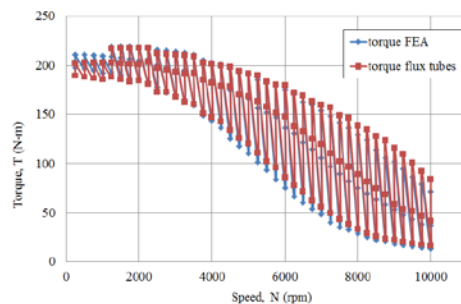


Fig. 11. Speed-torque envelopes of the flux tube method and FEA.

Again, from the visual comparison of superimposed speed-torque envelopes, it is evident that the flux tube method accurately and consistently predicts the average torque values, consistent with the FEA results, over a wide speed range. The influence of the current firing angles on the average instantaneous torque values in Fig. 11 cannot be underestimated. For instance, it can be seen that the average instantaneous torque values up to the 1000 rpm speed mark coincide with the previous firing angle average instantaneous torque values. However, once the speed increases past this point, the increase in firing angle values results in the increase of the average instantaneous torque values. As the speed increase continues towards the maximum value, the gain in torque is no longer followed by the increased firing angle value since the back *emf* of the machine approaches that of the DC supply. Much more elaborate discussion regarding the importance of the firing angles on the control aspects of SR machines is given in [8] and [16].

In a similar way the speed-power envelopes for the range of current firing angles of the SR machine are compared in Fig. 12.

As argued in this paper, the method of the flux tubes has been demonstrated to possess the necessary consistency and accuracy, while being general in scope of applications. It can be applied to rotating SR machines and to a wide range of SR machine topologies more generally.

A possible enhancement of the method might include a

direct incorporation of the dual bounds concepts by adding a second calculation based on slices, as in the original tubes-and-slices approach [25]. This enhancement also sets apart the proposed improved flux tube method from the general MEC techniques in terms of numerical error minimization. However, this needs to be considered with care as the additional effort and associated extended computing times may not necessarily be justified since the application of flux tubes alone appears to provide sufficient accuracy while preserving computational efficiency necessary for the rapid design purposes of Fig. 1.

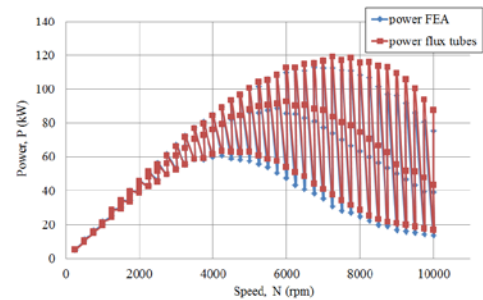


Fig. 12. Speed-power envelopes of the flux tube method and FEA.

Finally, it should be noted that the purpose of this work is to improve the practicality of the design process, normally relying on finite element modeling, by supplementing it with a much more computationally efficient methodology exploiting semi-analytical flux-tube field description. The appropriateness of the finite element analysis approach has been proven before, including experimental verification. In this work we focus on improving the speed of numerical analysis while preserving the original level of accuracy.

V. FLUX TUBE BASED OPTIMIZATION RESULTS

The proposed flux tube method has been combined with a rapid design search and optimization algorithm in order to perform an extensive sweep of the parameters space for the selected translating SR machines. For this task the constrained multi-objective GA was chosen, as the algorithm benefits directly from the computationally efficient flux tube model. The first objective function to be minimized was chosen to be the average instantaneous torque; optimizing this objective should result in a torque-dense machine. The second objective function was chosen to be the product of two quantities: the maximum power attained at the minimum firing angle, as in Fig. 12, and the speed range over which this power level can be sustained by the machine. The second objective has been selected in order to optimize the speed-power range the given machine can deliver – an important metric for the electric traction motor application.

The resulting 2D Pareto front for the machine considered in this study is shown in Fig. 13. The light-blue data points in Fig. 13 were obtained with the flux tube based GA optimization. Here the number of individuals in a randomly

generated population was set to a value of 50 and the number of generations to a value of 7 in order to achieve good convergence of the Pareto front. Furthermore, a specification of the elitism score of 33% was set, which effectively means that only this percentage of all the optimized individuals will be selected as parents for the subsequent generations. The low elitism score was chosen in order to reduce the number of suboptimal individuals from being carried over into the subsequent generations and therefore increases the convergence of the optimization [19].

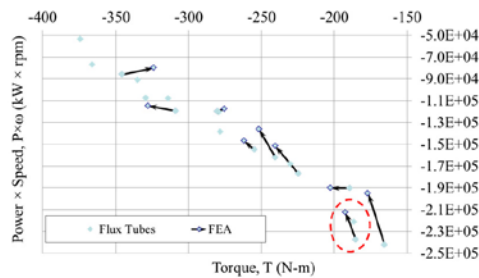


Fig. 13. SR motor Pareto fronts of the flux tube method and FEA.

The resulting flux tube based Pareto front in Fig. 13 was inspected and a number of the design points selected in order to re-compute these with FEA. The highlighted machine design in Fig. 13 and Table I has been already compared in the previous section and showed that the agreement between two methods was very close for the initial design search and optimization purposes. Fig. 13 indicates that the other selected machine designs were also re-evaluated with FEA and indicate that both objective functions give close numerical answers. An important point regarding the flux tube based method is that in order to generate a single data point on the Pareto front in Fig. 13 takes, on average, 20 seconds to compute. Therefore the speed-up of the flux tube method compared to FEA is around tenfold meaning that the flux tube based method is 10 times faster than FEA, while producing average torque results within $\pm 6\%$ of the FEA results.

An important point to note from the proposed design cycle in Fig. 1, and also Fig. 13, is as follows. Once the magnetic circuit of the selected SR machine topology is constructed along the lines of Fig. 5 and Fig. 7, the optimization routine is invoked which produces the Pareto front as in Fig. 13. Subsequently, according to the design process in Fig. 1, the favored machine design points are selected by a design engineer and reanalyzed using an order of magnitude more accurate analysis method, such as FEA. If FEA confirms that the selected Pareto front designs are near optimal, the design cycle can conclude, because the near optimal machine design has been obtained. The purpose of including the machine analysis in the previous section was to demonstrate the computational accuracy of the flux tube method compared to FEA. Consequently, since the flux tube method is numerically accurate, the analysis part from the previous

section can be used in the early stages of the design process as well.

Finally, the advantages of the proposed design cycle of Fig. 1 are evident as it has been demonstrated that the computational efficiency of the proposed flux tube method is high whilst the computational accuracy approaches that of the FEA. Therefore it is recommended that the proposed design and optimization cycle of Fig. 1 is used in the initial design optimization stages where the machine performance is not yet known well enough and the design space of the numerous design parameters is too large to be efficiently explored by using the FEA only. In this way the suboptimal designs can be eliminated from further consideration early on in the design optimization process and the expensive computational resources concentrated on the design stage once the certainty of suitability of the novel topology machine performance is established.

VI. FLUX TUBE MODEL APPLICATIONS

Since the flux tube method has been demonstrated to be well suited to the analysis and design of nonlinear and highly saturable switched reluctance machines, it is realistic to expect that the same approach would be applicable to modeling of other electric machines operating on the reluctance torque principle. Some examples of such machines include synchronous reluctance [27] and variable reluctance or stepper motors [23]. As synchronous reluctance machines are magnetically strongly nonlinear and have similar features to SR machines – such as no windings or permanent magnets on the rotor part, salient rotor structure, etc. – their magnetic analysis will be similar to SR motors. Furthermore, the contemporary design and analysis of synchronous reluctance machines is based almost exclusively on time consuming FEA – hence the need for fast and accurate modeling techniques becomes even more urgent. Therefore, provided that the manual subdivision of the magnetic circuit of the synchronous reluctance machine into equipotential slices – following the methodology explained in Section III – can be accomplished, the direct and quadrature axis inductance values of the machine can be conveniently found with the flux tube approach. Recognizing this advantage, this research was initiated in order to investigate the flux tube based modeling capability in application to the synchronous reluctance machine rapid analysis and design purposes.

VII. CONCLUSIONS

The paper has introduced a new analysis and design paradigm in application to SR machines. It is believed that the proposed design cycle will enable systematic and computationally efficient effort to be expended when novel and unfamiliar topology SR machines are considered for new applications. To speed up the design search and optimization task an improved flux tube modeling has been proposed. The improved method enables rapid analysis and design of electromechanical devices, in particular efficient estimation of flux-linkage functions used to describe the operation of SR machines. It has been demonstrated that the flux tube method can relatively accurately and consistently predict these flux

linkage functions, including such effects as magnetic saturation and flux leakage. It is concluded that the inaccuracies generated by the flux tube method are small and do not introduce unacceptable errors in the values of predicted currents and torques, both instantaneous and average. Therefore the method is suitable for rapid initial design search and optimization of SR machines of various topologies.

VIII. REFERENCES

- [1] M. Takeno, A. Chiba, N. Hoshi, S. Ogasawara, M. Takemoto, and M. Azizur Rahman, "Test results and torque improvement of the 50-kW switched reluctance motor designed for hybrid electric vehicle," *IEEE Trans. Industry Applications*, vol. 48, pp. 1327-1334, Aug. 2012.
- [2] A. Labak, and N. C. Kar, "Novel approaches towards leakage flux reduction in axial flux switched reluctance machines," *IEEE Trans. on Magnetics*, vol. 49, no. 8, August 2013.
- [3] Y. Li, H. Li, and Z. Liu, "Design and implement of novel transverse flux switched magnetic energy motor combined with control system," *Proceedings of IEEE International Conference on Mechatronics and Automation*, August 4-7, Takamatsu, Japan 2013.
- [4] I. A. Viorel, M. Crivii, L. Lowenstein, L. Szabo, and M. Gutman, "Direct drive systems with transverse flux reluctance motors," *ACTA Electrotechnica*, vol. 45, pp. 33-40, no. 3, 2004.
- [5] L. Byeong-Seok, "Linear switched reluctance machine drives with electromagnetic levitation and guidance systems," *Doctoral Thesis, Virginia Polytechnic Institute and State University*, November, 2000.
- [6] U. S. Deshpande, J. J. Cathey and E. Richter, "High-force density linear switched reluctance machine," *IEEE Transactions On Industry Applications*, vol. 31, pp. 345-352, no. 2, March/April 1995.
- [7] I. Mahmoud, and H. Rehaouia, "Design, nonlinear modeling and performances of a biomedical system," *Int. J. of Applied Electromagnetics and Mechanics*, vol. 50, no. 1, pp. 127-143, 2016.
- [8] W. F. Ray, P. J. Lawrenson, R. M. Davis, J. M. Stephenson, N. N. Fulton, and R. J. Blake, "High-performance switched reluctance brushless drives", *IEEE Trans. On Industry Applications*, vol. IA-22, pp. 722-730, no. 4, Aug. 1986.
- [9] RapidSR, Ricardo [Online]. Available at: www.ricardo.com.
- [10] SRDrives Ltd. [Online]. Available at: www.srdrives.com.
- [11] L. Kolomeitsev, D. Kraynov, S. Pakhomov, F. Rednov, E. Kallenbach, V. Kireev, T. Schneider, and J. Bocker, "Linear switched reluctance motor as a high efficiency propulsion system for railway vehicles," *Int. Symp. on Power Electronics, Electrical Drives, Automation and Motion, SPEEDAM 2008*.
- [12] J. Llibre, N. Martínez, P. Leprince and B. Nogarede, "Analysis and modeling of linear-switched reluctance for medical application", *Actuators*, vol. 2, pp. 27-44, 2013.
- [13] R. Krishnan, R. Arumugam and J. F. Lindsay, "Design procedure for switched reluctance motors," *IEEE Trans. on Industry Applications*, vol. 24, no. 3, pp. 456-461, June 1988.
- [14] E. El-Kharashi, "Improving the energy conversion process in the switched reluctance motors," *Int. J. of Applied Electromagnetics and Mechanics*, vol. 41, no. 4, pp. 375-387, 2013.
- [15] V. Ostovic, *Dynamics of Saturated Electric Machines*. ISBN-13: 978-1-4613-8935-4, New York, Springer-Verlag, 1989.
- [16] R. Krishnan, *Switched Reluctance Motor Drives: Modeling, Simulation, Analysis, Design, and Applications*. ISBN: 0849308380, CRC Press LLC, Boca Raton Florida, 2001.
- [17] A. Stukys, M. Rotaru and J. K. Sykulski, "A refined approach exploiting tubes of flux for analysis of linear switched reluctance motor", *International Journal of Applied Electromagnetics and Mechanics*, vol. 51, pp. 00-00, IOS Press, 2016.
- [18] A. Stukys and J. K. Sykulski, "Analysis and design framework for nonlinear switched reluctance machines" *XXII Int. Conf. on Electrical Machines*, 2016.
- [19] D. E. Goldberg, *Genetic Algorithms in Search, Optimization & Machine Learning*. Addison-Wesley, 1989.
- [20] M. Amrhein and P. T. Krein, "3-D magnetic equivalent circuit framework for modeling electromechanical devices," *IEEE Trans. on Energy Conversion*, vol. 24, pp. 397-405, no. 2, June 2009.
- [21] H.C. Roters, *Electromagnetic Devices*, John Wiley & Sons Inc., 1941.
- [22] J. Corda and J.M. Stephenson, "Analytical estimation of the minimum and maximum inductances of a double-salient motor," *Proc. of Int. Conf. on Stepping Motors and Systems*, Leeds, pp. 50-59, Sept. 1979.
- [23] J. F. Tabriz and J. W. Finch, "Two-Dimensional leakage flux estimation in switched reluctance motors," *Fourth Int. Conf. on Electrical Machines and Drives*, 1989.
- [24] T. J. E. Miller, "Nonlinear theory of the switched reluctance motor for rapid computer-aided design," *IEE Proc.*, vol. 137, no. 6, Nov. 1990.
- [25] J. K. Sykulski, "Dual field modeling using tubes and slices", *Advances in Engineering Software*, vol. 21, pp. 21-26, Elsevier Science Limited, 1995.
- [26] J. M. Stephenson and J. Corda, "Computation of torque and current in doubly salient reluctance motors from nonlinear magnetisation data", *IEE Proc.*, vol. 126, no. 5, May 1979.
- [27] T. Matsuo and T. Lipo, "Rotor design optimization of synchronous reluctance machine" *IEEE Trans. on Energy Conversion*, vol. 9, no. 2, pp. 359-365, Jun. 1994.

IX. BIOGRAPHIES

Aleksas Stukys received the B.Sc. degree in Mechanical Engineering from Oxford Brookes University, Oxford, UK, in year 2009. He received the M.Sc. degree in Advanced Engineering Design in year 2011 from the same institution. After a number of years working in automotive industry as an engineer he returned to academia to pursue the doctoral degree at the Institute for Complex Systems Simulation, School of Electronics and Computer Science, University of Southampton, Southampton, UK. His research interests span the fields of propulsion systems, including electric traction motors; their modeling, simulation and design for the electric and hybrid vehicles and for the sustainable transport in general. This research also includes the modeling, design and control aspects of switched reluctance machines and traction systems.

Jan Sykulski is Professor of Applied Electromagnetics at the University of Southampton, UK. His personal research is in development of fundamental methods of computational electromagnetics, power applications of high temperature superconductivity, simulation of coupled field systems and design and optimization of electromechanical devices. He has published over 370 scientific papers and co-authored four books. He is founding Secretary of International Compumag Society, Visiting Professor at universities in Canada, France, Italy, Poland and China, Editor of IEEE Transactions on Magnetics, Editor-in-chief of IET SMT, Editor-in-chief of COMPEL (Emerald) and member of International Steering Committees of several international conferences. He is Fellow of IEEE (USA), Fellow of the Institution of Engineering and Technology (IET), Fellow of the Institute of Physics (IoP), Fellow of the British Computer Society (BCS), Doctor Honoris Causa of Université d'Artois, France, and has an honorary title of Professor awarded by the President of Poland.

A REFINED APPROACH EXPLOITING TUBES OF FLUX FOR ANALYSIS OF LINEAR SWITCHED RELUCTANCE MOTORS

Stuikys A., Rotaru M. and Sykulski J. K.

ECS, University of Southampton, Southampton SO17 1BJ, United Kingdom, A.Stuikys@soton.ac.uk

Abstract – A field modelling approach is presented exploiting approximate magnetic flux distributions. The method is an extension of flux-tubes and tubes-and-slices techniques. A combination of an equivalent magnetic circuit approach with improved description of relevant flux paths allows for a computationally efficient algorithm suitable for design optimization. The method is illustrated using an example of a linear switched reluctance motor and validated using finite element simulations.

Introduction

A linear switched reluctance motor (LSRM) has applications in magnetic guidance and levitation systems for transportation and automation systems, rod actuator control mechanisms for nuclear reactors and other types of high force density linear actuators in hostile environments. The LSRM can be designed using similar equations as for a radial flux SR motor [1]. Due to the importance of pole tip saturation the modelling requires methods that can accurately capture and quantify such saturation effects [2]. The approach taken in this paper builds on an old flux-tubes modelling technique [3], used successfully to analyse tractive electromagnets and SR machines [1-5]. Flux-tube approximations based on cubic-splines are introduced to improve the accuracy of the flux-tubes approach. The method is further extended by incorporating some concepts of the ‘tubes and slices’ (TAS) approach [6]. The proposed model overcomes some restrictions reported in [7] regarding distribution of flux-tubes (also known as equiflux or isoflux paths) in the air-gap region of the LSRM. As always with such techniques, prior knowledge and experience of the designer are beneficial.

Modelling Approach

The model exploits the symmetries (Fig. 1) where the shaded magnetic flux plot has been obtained using standard finite element analysis (FEA). In the selected symmetry segment the cubic-spline representation has been applied to match the actual flux tubes distribution with the aid of careful positioning of equipotential lines (Fig. 2). By visual inspection of Fig. 2 it is possible to locate equipotential lines on the shaded plot as indicated by the straight lines termed ‘slices’ in reference [6] – these slices will be orthogonal to all the modelled flux paths in the respective parts of the machine. From Fig. 2 it is evident that if an attempt were made to fit smooth and continuous cubic-spline segments between the aforementioned equipotential slices, given only three coordinate points between them, there would be large interpolation errors introduced due to geometric discontinuities and abrupt points of inflection that describe the true flux paths. Therefore it is necessary to subdivide the remaining flux path segments (in between the equipotential lines) further to facilitate accurate cubic-spline interpolation. This is achieved by recognising the very important property of magnetic flux paths that was successfully used in the TAS method [6], namely that each flux path enters magnetic material at a right angle (i.e. normal) to the surface of the material. Once the flux lines are in the material they will follow paths of lowest reluctance. Such magnetic flux path entry points are indicated in Fig 2.

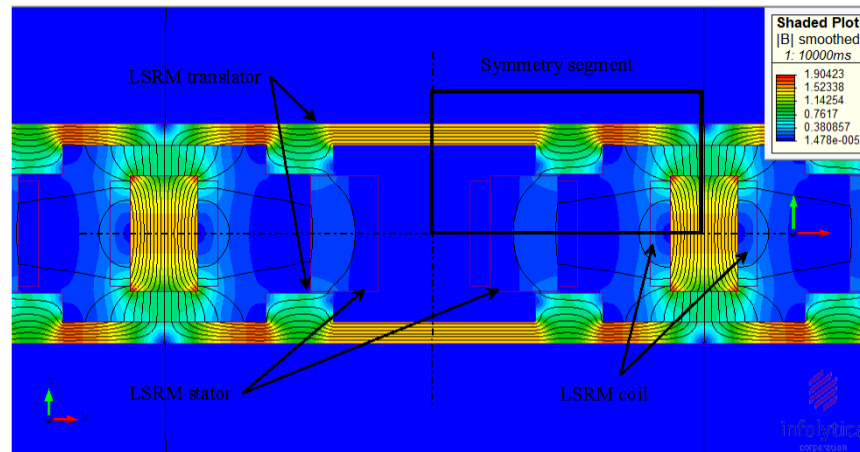


Fig. 1. Magnetic flux plot for a symmetry segment of the LSRM for the unaligned position.

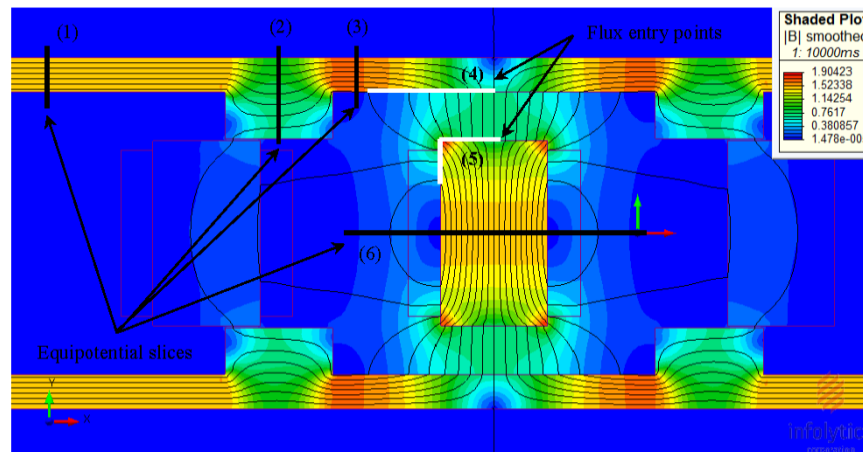


Fig. 2. Magnetic flux plot for a segment of the LSRM for the unaligned position.

Figure 3 demonstrates that some of the flux paths can be reasonably accurately approximated by only the three coordinate points, whereas others will require a minimum of four such points. Comparison of Fig. 2 and Fig. 3 reveals that the segment between slice 2 and slice 3 cannot be accurately interpolated by only three sets of coordinate points. Furthermore, the flux path segment between these two slices contains equipotential magnetic field lines which are not straight lines, but a combination of straight lines as well as circular arcs. To keep the complexity of expressing the flux paths in this particular segment to a minimum, simplified straight line approximations of equipotential magnetic field slices were used (although a more rigorous and accurate method would require construction of other than straight line slices in these regions). This enables simplified mathematical functions of the coordinate points to be defined associated with only major machine dimensions. This simplification might appear to be fairly crude, yet by revisiting the “probable flux path” formulation in reference [3] the justification of this simplification can be made if the final results are in close agreement with more accurate magnetic field analysis techniques.

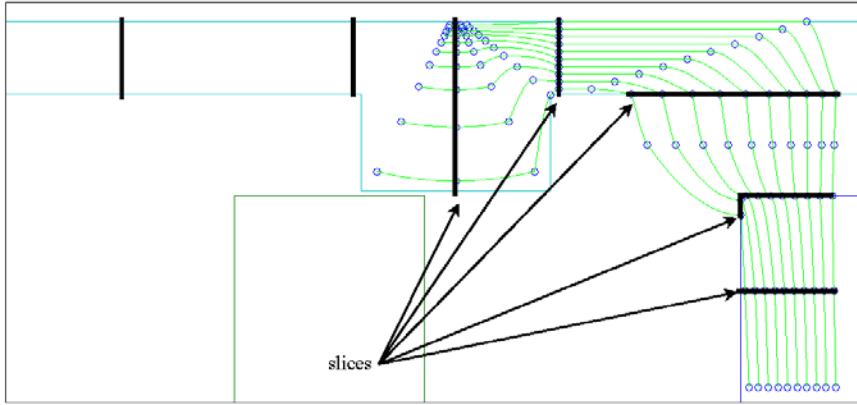


Fig. 3. Cubic-spline based approximation applied to the selected segments of LSRM for the unaligned case.

Once the cubic-spline based flux tubes are constructed, and their cord lengths and average cross-sectional areas computed, the magneto-motive force (mmf) applied to the excited stator polepiece can be found [1] as

$$T_p \times I = F_e \approx 0.5 \times H_{sp}l_{sp} + H_g l_g + H_{rp}l_{rp} + H_{ry}l_{ry} \quad (1)$$

where T_p , I , F_e , H and l are conductor turns per pole, coil current, mmf, magnetic field intensity and cord length of the flux path segment, respectively. The subscripts in (1) denote segments of the machine: stator pole, air gap, rotor pole and rotor yoke respectively. The relationship is only approximately equal to the applied mmf due to the numerical approximations as described in [1]. For the current study the mmf error was reduced to 1%, or less, of the final iteration before simulation was complete. All the geometric quantities for the constructed flux paths will be known and therefore the reluctance values r_i for each flux path segment may be found in the iron parts [1]

$$r_i = \frac{H_i l_i}{B_i A_i} \quad (2)$$

and in the air gap region

$$r_g = \frac{l_g}{\mu_0 A_g} \quad (3)$$

where B is the magnetic field density and A is average cross-sectional area of the flux path segment. Moreover, because the flux paths are composed of individual flux tube segments connected in series and form complete flux path combined in parallel, the total reluctance R of the complete flux path will be

$$\frac{1}{R} = \sum \frac{1}{\sum r_i + \sum r_g} \quad (4)$$

Having computed the total reluctance of the flux paths, the flux-linkage function, denoted by λ , can be found [1]

$$\lambda = \frac{T_p F_e}{R} \quad (5)$$

The important air gap region, for the unaligned translator position, can be further refined to include a larger number of slices (Fig. 4) to provide dual bounds estimate of the air gap reluctance as in the standard TAS approach [6].

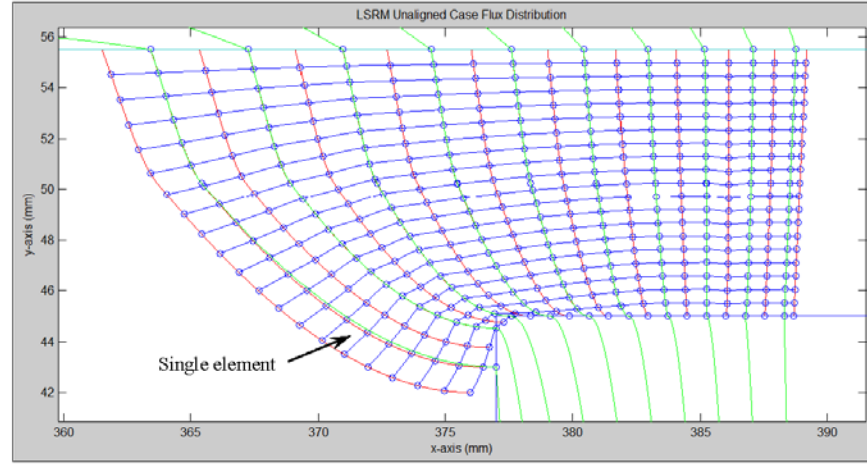


Fig. 4. Approximate subdivision of the LSRM air gap region into tubes of flux and slices of equipotentials.

In order to get the exact upper and lower bound values of the reluctance of the air gap this region must be subdivided in such a way so that the slices of equipotential lines are orthogonal to the tubes of flux they cut across. As the number of flux tubes and equipotential slices tends towards infinity the orthogonality condition can be approached. However, in practice it is not necessary to approach such a limit as the solution accuracy will converge asymptotically towards the exact values [6] as the number of tubes and slices grows larger. The demonstrated subdivision level of the air gap region, for the unaligned translator position, into tubes of flux and slices of magnetic field equipotentials approximates this region into a system of curvilinear squares. This subdivision enables determination of upper and lower bound values of reluctance of the air gap region thus increasing confidence in the solution of the flux-linkage function with respect to excitation current.

To compute the total reluctance R_t of the flux tubes in the air region, a number of which is denoted by m , connected in parallel, the following formula is used [6]

$$R_t = \left[\sum_{i=1}^m \left(\sum_{j=1}^n \frac{l_j}{\mu_0 A_{tj}} \right)^{-1} \right]^{-1} \quad (6)$$

where each block has length l_j and area A_{tj} , and the formula will give the upper bound value for the reluctance. To compute the total reluctance R_s of the flux slices in the air region, a number of which is denoted by n , connected in series, the following formula is used [6]

$$R_s = \sum_{j=1}^n \left(\sum_{i=1}^m \frac{\mu_0 A_{ti}}{l_j} \right)^{-1} \quad (7)$$

and this formula gives the lower bound of the reluctance of the region.

The aligned translator case of the LSRM is shown in Fig. 5 with the probable flux tubes distribution based on cubic-spline approximations as described earlier. It is assumed that flux tubes within the excited stator pole are straight vertical lines for all levels of current, although it is known from the FEA analysis that this is only an approximation as the constant flux lines assume shapes other than straight lines under higher levels of excitation currents. It is further assumed that the air gap region, for the aligned translator case, is ideal with no fringing effects. Again, this is only an approximation since the FEA analysis shows some fringing and leakage flux under increased levels of excitation current. All such approximations of assumed flux paths will introduce some errors in final result of the flux-linkage function, yet the complete flux-linkage map will be - to a large extent - insensitive to these errors as described in reference [8].

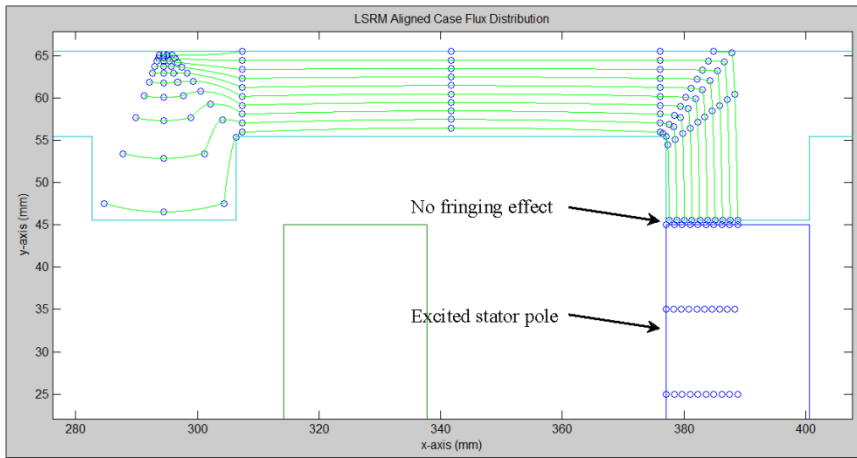


Fig. 5. Aligned translator position probable flux tubes distribution for the LSRM.

Results

The improved flux-tube modelling technique has been implemented as an algorithm for performance analysis of LSRM to estimate flux-linkage functions with respect to excitation current (Fig. 6), taking translator position as a parameter. The estimated flux-linkage for the unaligned position is in good agreement with FEA, whereas for the aligned case further model refinement is necessary for accurate determination of the function at higher levels of excitation current. The main contributing factor to the over-estimation of the flux-linkage function for the aligned translator case is that the machine is modelled without taking leakage flux or fringing flux effects into account, as in Fig. 5. In other words, the machine was assumed to have an ideal flux-tube distribution pattern for the whole range of coil currents. It can be seen that this assumption consistently over predicts the flux-linkage function for the aligned translator case of the analysed machine.

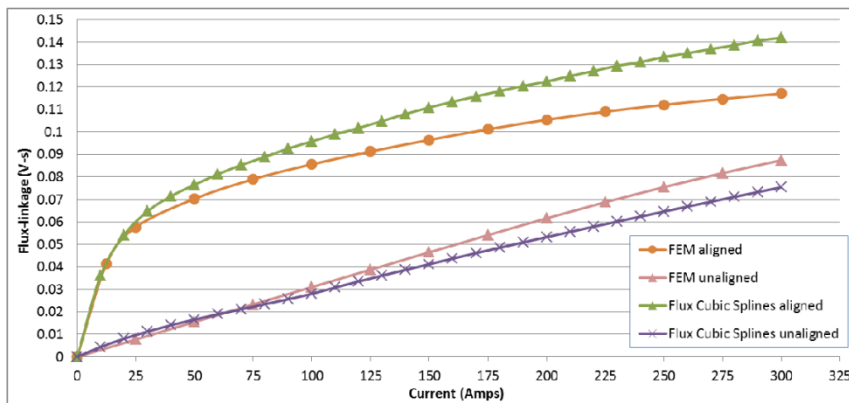


Fig. 6. Flux linkages for the aligned and unaligned positions using flux cubic-splines and FEA.

The unaligned translator position flux-linkage function of the improved flux-tube method is representative of general flux-linkage function for this translator position in that it is a near-linear function with respect to excitation current. It is certainly possible to saturate machine iron parts at the unaligned position so that the unaligned case flux-linkage function becomes non-linear; for this to happen, however, the current levels would be too high for any practical purposes. The unaligned case flux-linkage function, shown in Fig. 6, is 14% below the curve obtained from FEA at the current level of 300 amperes, which is 1.2 times higher than the specified design current of the machine. This result is of similar accuracy compared with the alternative flux-tube modelling approaches described in references [1-5].

The TAS refinement of the new flux-tube method was used to obtain the dual bounds approximations of the reluctance values of the air-gap region for the unaligned translator position of the LSRM. Fig. 7 shows the flux-linkage function obtained from this analysis.

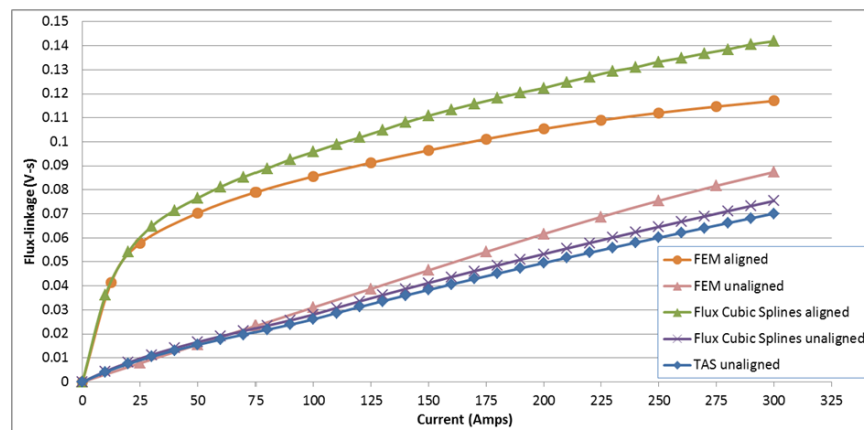


Fig. 7. Flux-linkage functions for the aligned and unaligned translator instances including the unaligned instance obtained with TAS refinement

As was stated before, the dual bound approximations of the unaligned case flux-linkage function provide useful results which can be used to select a more conservative design from the two alternative answers. Alternatively, the two results can be combined to give an averaged value with upper and lower limits serving as a guarantee that this average value is in between the limits.

The improved flux-tube method was tested for consistency of resulting flux-linkage functions when geometry parameters of the analysed LSRM were varied. It is known, from [9], that by increasing the translator pole height, in other words the air-gap length for the unaligned translator position, it is possible to reduce the unaligned flux-linkage level and thus increase the surface area of the entire flux-linkage map. This has a positive impact on the machine performance as it results in higher tractive force output compared to a machine which has a smaller air-gap region, as shown in Fig. 8, for the unaligned case of machine geometry #1.

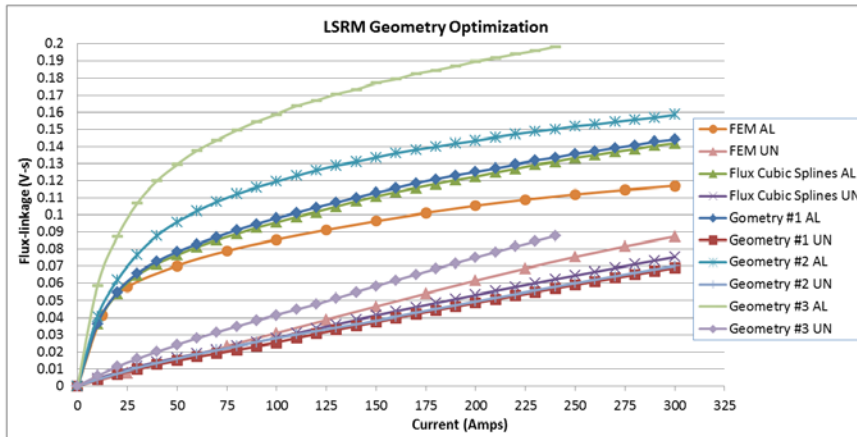


Fig. 8. Flux linkages for the aligned and unaligned positions using flux cubic-splines and FEA.

By following the switched reluctance machine design guidelines in [10], further improvements in the LSRM performance are possible. For example, by increasing the back-iron thickness of the translator parts of the machine, the aligned translator position flux-linkage function is increased markedly for a given ampere-turn parameter value of the machine. This effect is shown for the analysed machine geometry #2 aligned translator case (Fig. 8). Finally, the new flux-tube method can be used to optimize the conductor-turns parameter of the LSRM. For illustration purposes the initial 48 turn coil of the machine was changed to 60 turns with the ampere-turn parameter being held constant. The flux-tube method indicates that the machine flux-linkage function is increased substantially as shown for the geometry #3 aligned translator case (Fig. 8). This result was to be expected since the flux linkage is a function which increases in proportion to the number of conductors linked with the flux paths [1]; therefore, by increasing the number of turns, the surface area of the complete three-dimensional flux-linkage map is enlarged. This enlargement results in a considerable increase in the tractive force of the machine, but reduced excitation current levels compared to the original conductor-turns value.

Discussion and Conclusions

From the methodology and results sections of the paper the following conclusions with regard to the improved flux-tube modelling method can be drawn.

- The improved flux-tube modelling approach reduces the ambiguities in the construction of flux-tubes in electromechanical devices, compared to previous techniques. The uncertainty regarding which machine dimensions should define the coordinate points through which each flux path should pass also clarified. The proposed approach also reduces the required number of geometric parameters of the modelled electromechanical device necessary to establish an accurate mathematical expression for the flux-tubes distribution, compared to the equivalent field modelling methods.
- Accurate determination of the flux-tube cord lengths is possible with the improved flux-tube method since all the information needed to achieve this is available in the form of cubic splines. Computationally efficient numerical integration is then performed to find the cord lengths. Therefore an exact cord length value can be found for all assumed flux-tubes compared to average cord length values used in the equivalent field modelling methods.
- A complete flux-linkage map, including the magnetic saturation effects, can be constructed for an SR machine using the new flux-tube method. The results obtained from the method are in good agreement with the finite element analysis. However, the new method does not

account for leakage flux or fringing flux effects, around phase windings, occurring at high levels of excitation current.

- d) Further improvements to the proposed flux-tube modelling approach will be beneficial in providing better accuracy of flux-linkage representation at high levels of excitation current when the leakage flux becomes considerable. This leakage flux reduces the available useful output power levels of a given machine and should be taken into account for more accurate machine characterisation.

Incorporating the proposed flux-tube method into design optimization algorithms is possible and advantageous since the method is computationally efficient, with a complete three-dimensional flux-linkage map construction taking 50 seconds to compute. A comparable FEA analysis was found to require 250 seconds to achieve the same flux-linkage map, however with inherently much higher accuracy. This computational advantage of the proposed flux-tube method can be exploited during initial optimization and search stages when a large design space must be explored. During this stage of design optimization the computational efficiency of the method can outweigh the approximate nature of the results.

References

- [1] R. Krishnan, Switched Reluctance Motor Drives: Modelling, Simulation, Analysis, Design, and Applications, CRC Press LLC, Boca Raton Florida, 2001.
- [2] J. M. Kokernak and D. A. Torrey, Magnetic Circuit Model for the Mutually Coupled Switched-Reluctance Machine, IEEE Transactions on Magnetics, Vol. 36, No. 2, March 2000.
- [3] H. C. Roters, Electromagnetic Devices, 1st Edition, 1941, John Wiley & Sons Inc.
- [4] J. Corda and J. M. Stephenson, Analytical Estimation of the Minimum and Maximum Inductances of a Double Salient Motor, International Conference on Stepping Motors and Systems, The Department of Electrical and Electronic Engineering, University of Leeds, 1979.
- [5] U. S. Deshpande, J. J. Cathey and E. Richter, High-Force Density Linear Switched Reluctance Machine, IEEE Transactions on Industry Applications, Vol. 31, No. 2, March/April 1995.
- [6] J. K. Sykulski, Dual Field Modelling Using Tubes and Slices, Advances in Engineering Software, Vol. 21, pp. 21-26, Elsevier Science Limited, 1995.
- [7] T. J. E. Miller, Nonlinear theory of the switched reluctance motor for rapid computer-aided design, IEE Proceedings, Vol. 137, No. 6, November 1990.
- [8] J. M. Stephenson and J. Corda, Computation of torque and current in doubly salient reluctance motors from nonlinear magnetisation data, in Proceedings IEE, Vol. 126, No. 5, May 1979.
- [9] P.J. Lawrenson, J.M. Stephenson, P.T. Blenkinsop, J. Corda and N.N. Fulton, Variable-speed switched reluctance motors, in IEE Proceedings, Vol. 127, Pt. B, No. 4, July 1980.
- [10] T. J. E. Miller, Switched Reluctance Motors and Their Control, ISBN: 0198593872, Oxford University Press, Oxford, UK.

Rapid Electromagnetic Analysis and Design using Flux Tubes

A. Stuijks¹, M. H. Mohammadi², D. A. Lowther² *Fellow, IEEE*, and J. K. Sykulski¹ *Fellow, IEEE*

¹Electronics and Computer Science, University of Southampton, Southampton, SO16 1BJ, UK, a.stuijks@soton.ac.uk

²Department of Electrical and Computer Engineering, McGill University, Montreal, Canada

A reduced order numerical computational method based on flux tube modelling is proposed for the rapid electromagnetic analysis and design of electromechanical energy transducers using an example of a synchronous reluctance machine. The flux tube method is applied to establish flux linkage functions facilitating fast and accurate inductance estimation. The practical advantage is that the approach does not require precalculation of the air gap flux functions using computationally expensive methods such as finite elements. Initial results indicate that the method can predict, reliably and accurately, the flux distribution in the magnetic circuit, thus ultimately enabling efficient estimation of the inductance, and is suitable for rotational and translational synchronous reluctance machines.

Index Terms—Flux tube model, electric machine optimization, synchronous reluctance machine, nonlinear magnetic circuits.

I. INTRODUCTION

FLUX TUBES, a reduced order numerical method, are well suited to the magnetic field analysis of switched reluctance (SR) motors [1], [2]. The AC counterparts of SR machines are referred to as synchronous reluctance machines (synchRM), while both operate on the reluctance torque principle and share many features. In particular, both require direct and quadrature axis inductances, L_{ds} and L_{qs} , to quantify the electromechanical energy conversion capacity and power factor, as given by [3]

$$\text{torque index} = L_{ds} - L_{qs}; \quad \text{saliency ratio} = L_{ds} / L_{qs}. \quad (1)$$

An analytical estimation of the inductances is difficult due to magnetic nonlinearity. However, once the quantities are found the torque of the synchRM machine can be expressed as [3]

$$T_e = \frac{3}{2} \cdot \frac{n_p}{2} (L_{ds} - L_{qs}) I_{ds} \cdot I_{qs} \quad (2)$$

where n_p is the number of rotor poles and I_{ds} denotes direct and quadrature phase currents. It follows that the larger the torque index and/or the saliency ratio, the higher the torque T_e .

In this paper, the flux tube method is applied to the magnetic analysis of a synchRM for rapid design purposes.

II. SYNCHRONOUS RELUCTANCE MACHINE DESIGN PROBLEM

Details of the machine under consideration will be given in the full version. For illustrative purposes, Fig. 1 shows the initial finite element method (FEM) results of the flux lines and magnetic field density at the direct axis rotor position.

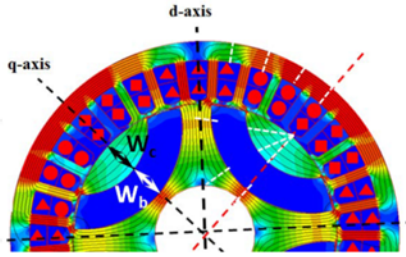


Fig. 1. FEM analysis contour plots for the fractional slot synchRM.

For the purpose of this study, all design variables are fixed except for the rotor carrier and rotor barrier widths, W_c and W_b respectively. The machine can be analysed using commercial software; however, exploring the synchRM response surface of average torque using (2) in a two-parameter design space would require numerous FEM solutions. One way of reducing computational effort is to use the magnetic equivalent circuit (MEC) based method [4], although the reported approach was still reliant on FEM simulation of the air gap flux distribution. We propose an alternative approach, based on flux tubes, which requires no precalculated air gap flux functions.

In order to investigate the effects of varying the two design parameters on the saliency ratio (1) and torque (2), a full factorial sampling was performed using FEM to compute the average torque for each design with fixed current magnitude; the corresponding response surface is shown in Fig. 2.

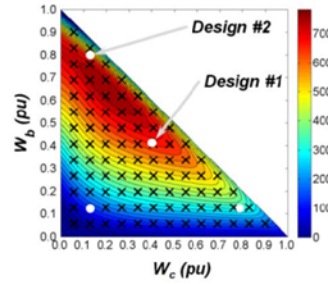


Fig. 2. Average torque response surface of the 33-slot 4-pole synchRM.

The response surface of Fig. 2 is constrained so that the two design variables of Fig. 1 are positive and do not intersect with other rotor poles. Each of the 90 sample points was evaluated thoroughly using the Maximum-Torque-Per-Ampere control strategy to find the optimal advance angle. Therefore, the response surface is three-dimensional, bound by the convex feasibility triangle. It transpires that the maximum value of the average torque is skewed towards a higher W_b . Unfortunately, the FEM based full-factorial exploration of the response surface requires substantial computational resources to achieve desired accuracy in a reasonably short time period.

III. FLUX TUBE MODELLING APPROACH

The general application of the flux tube method to the magnetic analysis of saturable SR machines was reported in [1], [2]. In this study, we extend the treatment to the synchRM machine, also analysed independently using FEM. The objective is to obtain a synchRM which would deliver similar performance to a PM synchronous machine. This machine is far more difficult to analyse using analytical or MEC methodology due to its lack of symmetry, as it is a fractional slot machine (33 slots, 4 poles). The symmetrical synchRM geometry was analysed previously using MEC techniques [4] and is not repeated here.

Proper application of the flux tube model to a particular geometry relies on the ability to recognize the existing flux function patterns; the FEM based analysis (see Fig. 1) may be helpful in this respect. Once the representative machine design FEM analysis is completed, the flux tube paths may be subdivided using equipotential slices – these will approximately coincide with the magnetic field density contours. The approximate slice positions are indicated as white dashed lines in Fig. 1. Subsequently, the slices are used as sets of coordinate points between which the smooth and continuous cubic splines are fitted.

The flux tube modelling starts with transforming the rotary to translating domain of the machine geometry as shown in Fig. 3, where the red line is the same symmetry line as in the chosen quadrant in Fig. 1.

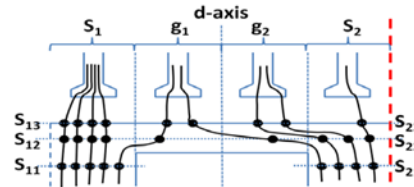


Fig. 3. Rotational to translational domain transformation of the synchRM.

The rotor region is subdivided into three horizontal slices S_i to facilitate accurate flux tube representation using cubic splines. Details of how to set up the flux tubes will be given in the full version. Once the flux tube modelling is complete the translational geometry domain is transformed back into the rotational domain with the final model illustrated by Fig. 4.

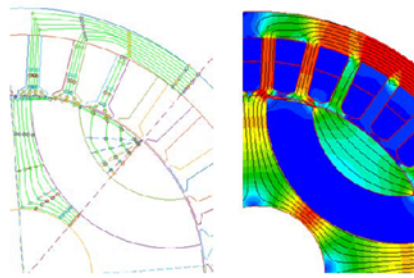


Fig. 4. The flux tube model of the chosen design (Design #1 in Fig. 2).

Using the flux tube model, the machine can be analysed by varying the two rotor geometric parameters, using the same full factorial sampling plan as in Fig. 2, so as to establish the highest inductance region of the direct rotor position for all possible variations of the two design parameters.

IV. FLUX TUBE MODELLING RESULTS

The design space of possible proportion combinations of the flux carrier and flux barrier widths of the rotor were explored using the flux tube model. The results indicate that the model can consistently generate the flux distribution within the machine magnetic circuit. For example, the flux function distribution for an alternative design is shown in Fig. 5.

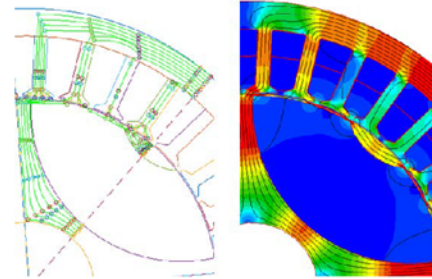


Fig. 5. The flux tube model for an alternative design (Design #2).

The above comparisons reveal that the flux tube method can roughly, but consistently, locate the highest direct inductance region with a very small computational effort (time needed to create all flux tube plots for full factorial sampling was 210s compared with 8.2 hours using 4 parallel processes of FEM simulations). Even extreme designs can be accurately mapped using the flux tube method as shown by Fig. 5. However, the reported analysis is not yet complete as the quadrature rotor axis flux tube results are also needed to compute the average torque using (2) – those will be reported in the full version together with the discussion of the saliency ratio.

V. CONCLUSIONS

The flux tube method has been applied to a fractional slot synchronous reluctance machine. Preliminary results suggest that the flux tube approach is a feasible and efficient alternative to FEM for modelling the complex flux functions.

REFERENCES

- [1] A. Stukys, M. Rotaru and J. K. Sykulski, "A refined approach exploiting tubes of flux for analysis of linear switched reluctance motor," *International Journal of Applied Electromagnetics and Mechanics*, vol. 51, IOS Press, 2016.
- [2] A. Stukys and J. K. Sykulski, "An efficient design optimization framework for nonlinear switched reluctance machines," *IEEE Trans. Industry Applications*, accepted for publication, 2017.
- [3] T. Matsuo and T. Lipo, "Rotor design optimization of synchronous reluctance machine," *IEEE Trans. Energy Conversion*, vol. 9, no. 2, pp. 359-365, Jun. 1994.
- [4] G. B. Mariani, A. Besri, N. Voyer, C. Chillet, M. Fassetet, and L. Garbuio, "Synchronous reluctance motor multi-static MEC model," *IBCON2015-Yokohama*, Yokohama, Japan, 2015.

Compumag 2017

Daejeon, Korea

UNIVERSITY OF
Southampton

Institute for Complex Systems Simulation ICSS

Rapid Electromagnetic Analysis and Design using Flux Tubes

A. Stuijks¹, M. H. Mohammadi², D. A. Lowther² *Fellow, IEEE*, and J. K. Sykulski¹ *Fellow, IEEE*

¹EEE Research Group, University of Southampton, Southampton, United Kingdom. E-mail: A.Stuijks@soton.ac.uk, J.K.Sykulski@soton.ac.uk
²Department of Electrical and Computer Engineering, McGill University, Montreal, Canada

Abstract - A reduced order numerical computational method based on flux tube modelling is proposed for the rapid electromagnetic analysis and design of electromechanical energy transducers using an example of a synchronous reluctance machine. The flux tube method is applied to establish flux linkage functions facilitating fast and accurate inductance estimation. The practical advantage is that the approach does not require precalculation of the air gap flux functions using computationally expensive methods such as finite elements. Initial results indicate that the method can predict, reliably and accurately, the flux distribution in the magnetic circuit, thus ultimately enabling efficient estimation of the inductance, and is suitable for rotational and translational synchronous reluctance machines.

Modelling, Analysis and Design Methodology

Fig. 1. Usual electromechanical design approach (left) and the proposed rapid synRM design approach using a reduced order computational method of flux tubes.

torque index = $L_{q0} - L_{d0}$;

saliency ratio = L_{q0} / L_{d0} .

$$(1)$$

$T_e = \frac{3}{2} \cdot n_p (L_{d0} - L_{q0}) I_{d0} \cdot I_{q0}$.

$$(2)$$

Fig. 2. Performance indices and the average torque response surface of the synRM evaluated at 91 data points

Fig. 3. Subdivision of the symmetry segments into flux tube slices at the q-axis rotor position of the 33-slot 4-pole synchronous Reluctance Machine (synRM).

$$\psi = \frac{N^2 \cdot I}{R} \quad (3)$$

$$R_{ab} = \frac{V_a - V_b}{\phi} = \int_0^l \mu(a, b, l) \cdot A(l) \cdot dl \quad (4)$$

$$R_{ab} = r_a = \sum_{j=1}^n \frac{l_j}{\mu_0 \cdot A_j} \quad (5)$$

$$\frac{1}{R_{parallel}} = \frac{1}{r_1} + \frac{1}{r_2} + \dots + \frac{1}{r_m} = \sum_{j=1}^m \left(\sum_{i=1}^n \frac{l_j}{\mu_0 \cdot A_j} \right)^{-1} \quad (6)$$

Fig. 4. A system of flux tubes in parallel and the governing equations.

Tentative Results and Optimization

Fig. 5. Cubic-spline approximations of the flux paths for the d-axis rotor position.

Fig. 6. The q-axis inductance response surface using FEA and the flux tube method.

Fig. 7. The d-axis inductance response surface using FEA and the flux tube method.

Fig. 8. Torque index ($L_{q0} - L_{d0}$) calculated using two FEA evaluations per point: one at 0°, the other at 90°, and the flux tube method. Total solution time ~8 hour (left), ~200 seconds (right)

Conclusions:

- A new analysis and design paradigm in relation to nonlinear fractional slot synchronous Reluctance Machines has been proposed.
- To speed up the design search and optimization task an improved flux tube modelling has been introduced.
- The improved method enables rapid analysis and design of electromechanical devices, i.e. rapid estimation of torque index response surface used to describe the operating performance of the synRMs.
- The flux tube method rapidly and consistently predicts the inductance response surface, including the effects of magnetic saturation of the machine.
- The method is suitable for rapid initial design search and optimization of magnetically nonlinear synRMs.
- Further study is needed to make the flux tubes method suitable for design and optimization of general slot-pole combination synRMs.

Glossary of Terms

None.

List of References

- [1] S. A. Nasar, 'D.C.-switched reluctance motor', *Proc. Inst. Electr. Eng.*, vol. 116, no. 6, p. 1048, 1969.
- [2] M. Takeno, A. Chiba, N. Hoshi, S. Ogasawara, M. Takemoto, and M. A. Rahman, 'Test Results and Torque Improvement of the 50-kW Switched Reluctance Motor Designed for Hybrid Electric Vehicles', *IEEE Trans. Ind. Appl.*, vol. 48, no. 4, pp. 1327–1334, Jul. 2012.
- [3] A. Labak and N. C. Kar, 'Novel Approaches Towards Leakage Flux Reduction in Axial Flux Switched Reluctance Machines', *IEEE Trans. Magn.*, vol. 49, no. 8, pp. 4738–4741, Aug. 2013.
- [4] L. Unnewehr and W. Koch, 'An Axial Air-AP Reluctance Motor for Variable Speed Applications', *IEEE Trans. Power Appar. Syst.*, vol. PAS-93, no. 1, pp. 367–376, Jan. 1974.
- [5] Y. Li, H. Li, and Z. Liu, 'Design and implement of novel Transverse Flux Switched Magnetic Energy Motor combined with control system', 2013, pp. 1675–1680.
- [6] 'I. A. Viorel, M. Crivii, L. Lowenstein, L. Szabo, and M. Gutman, "Direct drive systems with transverse flux reluctance motors," ACTA Electrotechnica, vol. 45, pp. 33-40, no. 3, 2004.'
- [7] 'L. Byeong-Seok, "Linear switched reluctance machine drives with electromagnetic levitation and guidance systems," Doctoral Thesis, Virginia Polytechnic Institute and State University, November, 2000.'
- [8] U. S. Deshpande, J. J. Cathey, and E. Richter, 'A high force density linear switched reluctance machine', 1993, pp. 251–257.
- [9] 'J. Corda and E. Skopljak, "Linear switched reluctance actuator", 6th Int. Conf. on Electric Machines and Drives, Oxford UK, IET, September 1993.'
- [10] I. Mahmoud and H. Rehaoulia, 'Design, nonlinear modelling and performances of a biomedical system', *Int. J. Appl. Electromagn. Mech.*, vol. 50, no. 1, pp. 127–143, Jan. 2016.
- [11] N. Radimov, N. Ben-Hail, and R. Rabinovici, 'Switched Reluctance Machines as Three-Phase AC Autonomous Generator', *IEEE Trans. Magn.*, vol. 42, no. 11, pp. 3760–3764, Nov. 2006.
- [12] R. Jøger, S. S. Nielsen, P. O. Rasmussen, and K. Kongerslev, 'Development and analysis of U-core switched reluctance machine', 2016, pp. 1–8.
- [13] C. C. Chan, 'Single-phase switched reluctance motors', *IEE Proc. B Electr. Power Appl.*, vol. 134, no. 1, p. 53, 1987.
- [14] C.-T. Liu, Y.-M. Chen, and D.-C. Pang, 'Performance Index Evaluations of a Micro Axial-flux Switched-reluctance Motor', 2006, pp. 1–5.
- [15] E. Richter and C. Ferreira, 'Performance evaluation of a 250 kW switched reluctance starter generator', 1995, vol. 1, pp. 434–440.

List of References

- [16] T. Uematsu and R. S. Wallace, 'Design of a 100 kW switched reluctance motor for electric vehicle propulsion', 1995, pp. 411–415.
- [17] 'W. F. Ray, P. J. Lawrenson, R. M. Davis, J. M. Stephenson, N. N. Fulton, and R. J. Blake, "High-performance switched reluctance brushless drives", *IEEE Trans. On Industry Applications*, vol. IA-22, pp. 722-730, no. 4, Aug. 1986.'
- [18] 'RapidSR, Ricardo [Online]. Available at: www.ricardo.com.'
- [19] 'SRDrives Ltd. [Online]. Available at: www.srdrives.com.'
- [20] L. Kolomeitsev *et al.*, 'Linear switched reluctance motor as a high efficiency propulsion system for railway vehicles', 2008, pp. 155–160.
- [21] J.-F. Llibre, N. Martinez, P. Leprince, and B. Nogarede, 'Analysis and Modeling of Linear-Switched Reluctance for Medical Application', *Actuators*, vol. 2, no. 2, pp. 27–44, Apr. 2013.
- [22] R. Krishnan, R. Arumugan, and J. F. Lindsay, 'Design procedure for switched-reluctance motors', *IEEE Trans. Ind. Appl.*, vol. 24, no. 3, pp. 456–461, Jun. 1988.
- [23] 'A. Matveev, "Development of Methods, Algorithms and Software for Optimal Design of Switched Reluctance Drives", PhD Thesis, Technische Universiteit Eindhoven, January 2006.'
- [24] R. Krishnan, M. Abouzeid, and X. Mang, 'A design procedure for axial field switched reluctance motors', 1990, pp. 241–246.
- [25] D. W. J. Pulle and I. R. Petersen, 'A unified approach to switched reluctance drive modeling: application to an axial flux (SRAF) motor', 1998, vol. 2, pp. 1681–1686.
- [26] Miller, T.J.E. and McGilp, M.I., *PC-SRD User's manual, Version 7.0, SPEED Laboratory, University of Glasgow, 1999.*
- [27] 'M. Besbes, B. Multon, 2004. MRVSim code : Logiciel de simulation pour l'aide au dimensionnement des MRVDS et de convertisseur. IDDN.FR.001.430010.000.S.C.2004.000.30645.'
- [28] H. C. Lovatt, 'Analytical model of a classical switched-reluctance motor', *IEE Proc. - Electr. Power Appl.*, vol. 152, no. 2, p. 352, 2005.
- [29] N. T. Shaked and R. Rabinovici, 'New procedures for minimizing the torque ripple in switched reluctance motors by optimizing the phase-current profile', *IEEE Trans. Magn.*, vol. 41, no. 3, pp. 1184–1192, Mar. 2005.
- [30] M. R. Benhadria, K. Kendouci, and B. Mazari, 'Torque Ripple Minimization of Switched Reluctance Motor Using Hysteresis Current Control', 2006, pp. 2158–2162.
- [31] S. I. Nabeta, I. E. Chabu, L. Lebensztajn, D. A. P. Correa, W. M. da Silva, and K. Hameyer, 'Mitigation of the Torque Ripple of a Switched Reluctance Motor Through a Multiobjective Optimization', *IEEE Trans. Magn.*, vol. 44, no. 6, pp. 1018–1021, Jun. 2008.
- [32] K. Kiyota, T. Kakishima, A. Chiba, and M. A. Rahman, 'Cylindrical Rotor Design for Acoustic Noise and Windage Loss Reduction in Switched Reluctance

- Motor for HEV Applications', *IEEE Trans. Ind. Appl.*, vol. 52, no. 1, pp. 154–162, Jan. 2016.
- [33] C. Lin, S. Wang, and B. Fahimi, 'Efficient multiphysics modelling of vibration and acoustic noise in switched reluctance motor drives', 2014, pp. 542–548.
- [34] M. van der Giet, E. Lange, D. A. P. Corrêa, I. E. Chabu, S. I. Nabeta, and K. Hameyer, 'Acoustic Simulation of a Special Switched Reluctance Drive by Means of Field-Circuit Coupling and Multiphysics Simulation', *IEEE Trans. Ind. Electron.*, vol. 57, no. 9, pp. 2946–2953, Sep. 2010.
- [35] K. M. Rahman, B. Fahimi, G. Suresh, A. V. Rajarathnam, and M. Ehsani, 'Advantages of switched reluctance motor applications to EV and HEV: design and control issues', *IEEE Trans. Ind. Appl.*, vol. 36, no. 1, pp. 111–121, Feb. 2000.
- [36] C. Ma and L. Qu, 'Multiobjective Optimization of Switched Reluctance Motors Based on Design of Experiments and Particle Swarm Optimization', *IEEE Trans. Energy Convers.*, vol. 30, no. 3, pp. 1144–1153, Sep. 2015.
- [37] S. Kachapornku, P. Somsir, R. Pupadubsi, N. Nulek, and N. Chayopitak, 'Low Cost High Speed Switched Reluctance Motor Drive for Supercharger Applications', presented at the Electrical Machines and Systems (ICEMS), 2012 15th International Conference on, Sapporo, Japan, 2012.
- [38] E.-K. Eyhab, 'Improving the energy conversion process in the switched reluctance motors', *Int. J. Appl. Electromagn. Mech.*, no. 4, pp. 375–387, 2013.
- [39] S. R. MacMinn and W. D. Jones, 'A very high speed switched-reluctance starter-generator for aircraft engine applications', 1989, pp. 1758–1764.
- [40] Zhenyao Xu and J.-W. Ahn, 'A novel 6/5 segmental rotor type switched reluctance motor: Concept, design and analysis', 2013, pp. 582–585.
- [41] N. S. Lobo, E. Swint, and R. Krishnan, 'M-Phase N-Segment Flux-Reversal-Free Stator Switched Reluctance Machines', 2008, pp. 1–8.
- [42] M. Ruba, 'Fault-Tolerant Electrical Machines and Drives', in *Fault Diagnosis and Detection*, M. Demetgul and M. Ünal, Eds. InTech, 2017.
- [43] M. Ruba, L. Szabo, L. Strete, and I.-A. Viorel, 'Study on fault tolerant switched reluctance machines', presented at the 18th International Conference on Electrical Machines, 2008, pp. 1–6.
- [44] C. Lee, R. Krishnan, and N. S. Lobo, 'Novel Two-Phase Switched Reluctance Machine Using Common-Pole E-Core Structure: Concept, Analysis, and Experimental Verification', *IEEE Trans. Ind. Appl.*, vol. 45, no. 2, pp. 703–711, 2009.
- [45] M. T. Khor and R. Sotudeh, 'A 3-phase 12/10 asymmetrical switched reluctance motor', 2005, p. 9 pp.-P.9.
- [46] M. Abbasian, M. Moallem, and B. Fahimi, 'Double-Stator Switched Reluctance Machines (DSSRM): Fundamentals and Magnetic Force Analysis', *IEEE Trans. Energy Convers.*, vol. 25, no. 3, pp. 589–597, Sep. 2010.
- [47] R. Madhavan and B. G. Fernandes, 'A novel axial flux segmented SRM for electric vehicle application', 2010, pp. 1–6.

List of References

- [48] F. Daldaban and N. Ustkoyuncu, 'New disc type switched reluctance motor for high torque density', *Energy Convers. Manag.*, vol. 48, no. 8, pp. 2424–2431, Aug. 2007.
- [49] E. El-Kharashi, 'Design and predicting efficiency of highly nonlinear hollow cylinders switched reluctance motor', *Energy Convers. Manag.*, vol. 48, no. 8, pp. 2261–2275, Aug. 2007.
- [50] N. Schofield, S. A. Long, D. Howe, and M. McClelland, 'Design of a Switched Reluctance Machine for Extended Speed Operation', *IEEE Trans. Ind. Appl.*, vol. 45, no. 1, pp. 116–122, 2009.
- [51] J. D. Widmer, R. Martin, and B. C. Mecrow, 'Optimisation of an 80kW Segmental Rotor Switched Reluctance Machine for automotive traction', 2013, pp. 427–433.
- [52] 'S. Faid, P. Debal, and S. Bervoets, "Development of a Switched Reluctance Motor for Automotive Traction Applications", The 25th World Battery, Hybrid and Fuel Cell Electric Vehicle Symposium & Exhibition, EVS-25 Shenzhen, China, Nov. 5-9, 2010.'
- [53] I. Boldea, L. N. Tutelea, L. Parsa, and D. Dorrell, 'Automotive Electric Propulsion Systems With Reduced or No Permanent Magnets: An Overview', *IEEE Trans. Ind. Electron.*, vol. 61, no. 10, pp. 5696–5711, Oct. 2014.
- [54] J. D. Widmer, R. Martin, and M. Kimiabeigi, 'Electric vehicle traction motors without rare earth magnets', *Sustain. Mater. Technol.*, vol. 3, pp. 7–13, Apr. 2015.
- [55] 'Seaman J. (2010): Rare Earths and Clean Energy: Analyzing China's Upper Hand. ISBN: 978-2-86592-771-5. Institut Francais des Relations Internationales (Ifri), September 2010'.
- [56] S. Zhang *et al.*, 'Permanent magnet technology for electric motors in automotive applications', 2012, pp. 1–11.
- [57] M. J. Kramer, R. W. McCallum, I. A. Anderson, and S. Constantinides, 'Prospects for Non-Rare Earth Permanent Magnets for Traction Motors and Generators', *JOM*, vol. 64, no. 7, pp. 752–763, Jul. 2012.
- [58] 'IDTechEx research report "Electric Motors for Electric Vehicles 2013-2023: Forecasts, Technologies, Players.'.
- [59] M. Besharati, J. Widmer, G. Atkinson, V. Pickert, and J. Washington, 'Super-high-speed switched reluctance motor for automotive traction', 2015, pp. 5241–5248.
- [60] B. Burkhart, H. J. Brauer, and R. W. De Doncker, 'Design of a switched reluctance traction drive for Electric Vehicles', 2012, pp. 204–209.
- [61] K. Hameyer and R. Belmans, *Numerical modelling and design of electrical machines and devices*. Southampton, UK : Boston: WIT Press ; Computational Mechanics, 1999.
- [62] V. Ostović, *Dynamics of Saturated Electric Machines*. New York, NY: Springer New York, 1989.
- [63] R. Krishnan, *Switched reluctance motor drives: modeling, simulation, analysis, design, and applications*. Boca Raton, FL: CRC Press, 2001.

- [64] Wei Wu, J. B. Dunlop, S. J. Collocott, and B. A. Kalan, 'Design optimization of a switched reluctance motor by electromagnetic and thermal finite-element analysis', *IEEE Trans. Magn.*, vol. 39, no. 5, pp. 3334–3336, Sep. 2003.
- [65] D. Meeker, *Finite Element Method Magnetics (FEMM), FEMM Reference Manual*, <http://www.femm.info/wiki/Documentation/>, accessed on 5 September 2017. .
- [66] W. Jiang, M. Moallem, B. Fahimi, and S. Pekarek, 'Qualitative Investigation of Force Density Components in Electromechanical Energy Conversion Process', 2006, pp. 1113–1118.
- [67] E. Bostanci, M. Moallem, A. Parsapour, and B. Fahimi, 'Opportunities and Challenges of Switched Reluctance Motor Drives for Electric Propulsion: A Comparative Study', *IEEE Trans. Transp. Electrification*, vol. 3, no. 1, pp. 58–75, Mar. 2017.
- [68] T. Lambert, M. Biglarbegian, and S. Mahmud, 'A Novel Approach to the Design of Axial-Flux Switched-Reluctance Motors', *Machines*, vol. 3, no. 1, pp. 27–54, Mar. 2015.
- [69] A. Stukys and J. Sykulski, 'Rapid Multi-Objective Design Optimization of Switched Reluctance Motors Exploiting Magnetic Flux Tubes', *IET Sci. Meas. Technol.*, Nov. 2017.
- [70] A. Stukys and J. K. Sykulski, 'An Efficient Design Optimization Framework for Nonlinear Switched Reluctance Machines', *IEEE Trans. Ind. Appl.*, vol. 53, no. 3, pp. 1985–1993, May 2017.
- [71] T. J. E. Miller, *Switched reluctance motors and their control*. Hillsboro, OH : Oxford: Magna Physics Pub. ; Clarendon Press, 1993.
- [72] H. C. Roters, *Electromagnetic devices*. New York: Wiley, 1970.
- [73] M. Amrhein and P. T. Krein, '3-D Magnetic Equivalent Circuit Framework for Modeling Electromechanical Devices', *IEEE Trans. Energy Convers.*, vol. 24, no. 2, pp. 397–405, Jun. 2009.
- [74] 'J. Corda and J.M. Stephenson, "Analytical estimation of the minimum and maximum inductances of a double-salient motor," Proc. of Intl. Conf. on Stepping Motors and Systems, Leeds, pp. 50-59, September 1979.'
- [75] 'J. F. Tabriz and J. W. Finch, "Two-dimensional leakage flux estimation in switched reluctance motors", Fourth Int. Conf. on Electrical Machines and Drives, 1989.'
- [76] J. K. Sykulski, 'Dual field modelling using tubes and slices', *Adv. Eng. Softw.*, vol. 21, no. 1, pp. 21–26, Jan. 1994.
- [77] A. Labak and N. C. Kar, 'Designing and Prototyping a Novel Five-Phase Pancake-Shaped Axial-Flux SRM for Electric Vehicle Application Through Dynamic FEA Incorporating Flux-Tube Modeling', *IEEE Trans. Ind. Appl.*, vol. 49, no. 3, pp. 1276–1288, May 2013.
- [78] T. J. E. Miller and M. McGilp, 'Nonlinear theory of the switched reluctance motor for rapid computer-aided design', *IEE Proc. B Electr. Power Appl.*, vol. 137, no. 6, p. 337, 1990.

List of References

- [79] B. Ganji and M. H. Askari, 'Analysis and modeling of different topologies for linear switched reluctance motor using finite element method', *Alex. Eng. J.*, vol. 55, no. 3, pp. 2531–2538, Sep. 2016.
- [80] M. Amrhein and P. T. Krein, 'Magnetic Equivalent Circuit Simulations of Electrical Machines for Design Purposes', 2007, pp. 254–260.
- [81] S. D. Umans, 'Steady-state, lumped-parameter model for capacitor-run, single-phase induction motors', *IEEE Trans. Ind. Appl.*, vol. 32, no. 1, pp. 169–179, Feb. 1996.
- [82] A. Demenko and K. Hameyer, 'Field and field-circuit description of electrical machines', Power Electronics and Motion Control Conference, 2008. EPE-PEMC 13th, 2008, pp. 2412–2419.
- [83] C. Neagoe, A. Foggia, and R. Krishnan, 'Impact of pole tapering on the electromagnetic torque of the switched reluctance motor', 1997, p. WA1/2.1-WA1/2.3.
- [84] P. Hammond and J. K. Sykulski, *Engineering electromagnetism: physical processes and computation*, Repr. Oxford: Oxford Univ. Press, 1995.
- [85] D. Baldomir and P. Hammond, *Geometry of electromagnetic systems*. Oxford : New York: Clarendon Press ; Oxford University Press, 1996.
- [86] Y. A. Çengel, *Heat transfer: a practical approach*. Boston, Mass: WBC McGraw-Hill, 1998.
- [87] A. Radun, 'Analytical calculation of the switched reluctance motor's unaligned inductance', *IEEE Trans. Magn.*, vol. 35, no. 6, pp. 4473–4481, Nov. 1999.
- [88] *GNU Octave*, <https://www.gnu.org/software/octave/> , accessed 10 April 2017. .
- [89] 'Infolytica Corporation (2010). MagNet 32-bit, Version 7.4.1.4 software. Copyright © Infolytica Corporation 1998-2008.'
- [90] *RADIA V 4.1., scientific software*, Authors: O.Chubar, P. Elleaume, J. Chavanne, ID Group, The European Synchrotron, <http://www.esrf.eu/Accelerators/Groups/InsertionDevices/Software/Radia> , accessed 15 November 2017. .
- [91] M. Hazewinkel, Ed., *Encyclopaedia of mathematics: an updated and annotated translation of the Soviet 'Mathematical encyclopaedia'*. Dordrecht ; Boston : Norwell, MA, U.S.A: Reidel ; Sold and distributed in the U.S.A. and Canada by Kluwer Academic Publishers, 1988.
- [92] J. M. Stephenson and J. Čorda, 'Computation of torque and current in doubly salient reluctance motors from nonlinear magnetisation data', *Proc. Inst. Electr. Eng.*, vol. 126, no. 5, p. 393, 1979.
- [93] T. J. E. Miller, *Brushless permanent-magnet and reluctance motor drives*. Oxford : New York: Clarendon Press ; Oxford University Press, 1989.
- [94] A. Stuikeys, M. Rotaru, and J. K. Sykulski, 'A refined approach exploiting tubes of flux for analysis of linear switched reluctance motors', *Int. J. Appl. Electromagn. Mech.*, vol. 51, no. s1, pp. S13–S21, Apr. 2016.

- [95] P. Hammond, *Energy methods in electromagnetism*. Oxford: Clarendon Press, 1981.
- [96] J. J. Gribble, P. C. Kjaer, and T. J. E. Miller, 'Optimal commutation in average torque control of switched reluctance motors', *IEE Proc. - Electr. Power Appl.*, vol. 146, no. 1, p. 2, 1999.
- [97] H. C. Lovatt *et al.*, 'Design procedure for low cost, low mass, direct drive, in-wheel motor drivetrains for electric and hybrid vehicles', 2011, pp. 4558–4562.
- [98] S. Zhitkova and K. Hameyer, 'Realization of a wide speed range for an agricultural tractor', *Electrical Machines (ICEM)*, 2016 XXII International Conference, 2016, pp. 2031–2037.
- [99] J. Larminie and J. Lowry, *Electric vehicle technology explained*. Chichester: Wiley, 2003.
- [100] W. Liu, *Introduction to hybrid vehicle system modeling and control*. Hoboken: John Wiley & Sons, 2013.
- [101] C. Mi, M. A. Masrur, and D. W. Gao, *Hybrid electric vehicles: principles and applications with practical perspectives*. Chichester: Wiley, 2011.
- [102] D. E. Goldberg, *Genetic algorithms in search, optimization, and machine learning*, 30. print. Boston: Addison-Wesley, 2012.
- [103] M. Felden, P. Butterling, P. Jeck, L. Eckstein, and K. Hameyer, 'Electric vehicle drive trains: From the specification sheet to the drive-train concept', 2010.
- [104] T. J. E. Miller, Ed., *Electronic control of switched reluctance machines*. Oxford: Newnes, 2001.
- [105] P. J. Lawrenson, J. M. Stephenson, N. N. Fulton, P. T. Blenkinsop, and J. Corda, 'Variable-speed switched reluctance motors', *IEE Proc. B Electr. Power Appl.*, vol. 127, no. 4, p. 253, 1980.
- [106] J. Deskur, T. Pajchrowski, and K. Zawirski, 'Optimal control of current switching angles for high-speed SRM drive', *COMPEL - Int. J. Comput. Math. Electr. Electron. Eng.*, vol. 29, no. 1, pp. 156–172, Jan. 2010.
- [107] B. Amin, M. Masoumi, and M. Mirsalim, 'Field and Torque Calculation and Transient Analysis in Variable Reluctance Machines', *IEEE Trans. Magn.*, vol. 53, no. 9, pp. 1–9, Sep. 2017.
- [108] A. Ibrahim, S. Rahnamayan, M. V. Martin, and K. Deb, '3D-RadVis: Visualization of Pareto front in many-objective optimization', 2016, pp. 736–745.
- [109] C. Vaithilingam, N. Mison, M. Zare, I. Aris, and M. Marhaban, 'Computation of Electromagnetic Torque in a Double Rotor Switched Reluctance Motor Using Flux Tube Methods', *Energies*, vol. 5, no. 12, pp. 4008–4026, Oct. 2012.
- [110] 'Kołota, Jakub & Stepień, Sławomir. (2011). Analysis of 2D and 3D Finite Element Approach of a Switched Reluctance Motor. *Przegląd Elektrotechniczny*. 87. 188-190.'

List of References

- [111] A. M. Michaelides, 'Effect of end core flux on the performance of the switched reluctance motor', *IEE Proc. - Electr. Power Appl.*, vol. 141, no. 6, p. 308, 1994.
- [112] 'Shaikh, Abdul Basit. (1992). Three dimensional effects in diagrams for switched reluctance motors. , Proc., ICEM 92:842-848.. .'.
- [113] K. Kiyota, S. Nakano, and A. Chiba, 'An optimal ratio of outer diameter and axial length for torque improvement in switched reluctance motor', 2016, pp. 1298–1304.
- [114] K. Kiyota, T. Kakishima, H. Sugimoto, and A. Chiba, 'Comparison of the Test Result and 3D-FEM Analysis at the Knee Point of a 60 kW SRM for a HEV', *IEEE Trans. Magn.*, vol. 49, no. 5, pp. 2291–2294, May 2013.
- [115] M. Hafner, M. Schoning, M. Antczak, A. Demenko, and K. Hameyer, 'Methods for Computation and Visualization of Magnetic Flux Lines in 3-D', *IEEE Trans. Magn.*, vol. 46, no. 8, pp. 3349–3352, Aug. 2010.
- [116] T. Matsuo and T. A. Lipo, 'Rotor design optimization of synchronous reluctance machine', *IEEE Trans. Energy Convers.*, vol. 9, no. 2, pp. 359–365, Jun. 1994.
- [117] 'Stuikys, A., Mohammadi, M. H., Lowther, D. and Sykulski, J. (2017), "Rapid electromagnetic analysis and design using flux tubes", 21st International Conference on the Computation of Electromagnetic Fields, COMPUMAG2017 Daejeon, Korea, Republic of. 18 - 22 Jun 2017. 2 pp.'
- [118] M. H. Mohammadi, T. Rahman, R. Silva, M. Li, and D. A. Lowther, 'A Computationally Efficient Algorithm for Rotor Design Optimization of Synchronous Reluctance Machines', *IEEE Trans. Magn.*, vol. 52, no. 3, pp. 1–4, Mar. 2016.